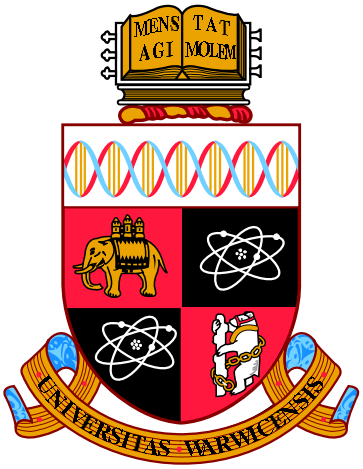

Longitudinal Dispersion in Steady and Unsteady Pipe Flow

by

James R Hart

Thesis

Submitted to the University of Warwick

for the degree of

Doctor of Philosophy

School of Engineering

May 2013

THE UNIVERSITY OF WARWICK

Contents

List of Tables

List of Figures

Nomenclature

Roman

a	Pipe radius
A	Pipe cross-sectional area
A_p	Area of concentration profile
b_D	Laser beam diameter
b_s	Beam separation distance
c	Cross-sectional mean concentration
d	Pipe diameter
d_m	Measuring volume depth
D_m	Molecular diffusion coefficient
D_r	Radial diffusion coefficient
D_t	Turbulent diffusion coefficient
D_{xx}	Longitudinal dispersion coefficient
$\overline{D_{xx}}$	Time averaged longitudinal dispersion coefficient
D_y	Vertical diffusion coefficient
E	Residence time distribution
E_b	Laser beam expansion factor
f	Darcy-Weisbach friction factor
$f(p)$	Geometric relationship for velocity profile
f_f	Fanning friction factor
f_L	Laser focal length
g	Acceleration due to gravity
G	Dimensionless discharge gradient, $G = (d^3/\nu^2)(d\bar{\bar{u}}/dt)$
h	Flow depth for open channel flow
$\hat{h}$	Estimated residence time distribution for deconvolution code
h_f	Head loss due to friction
L	Pipe length
L_d	Length required for flow to become fully developed
L_I	Length from injection point
l_m	Measuring volume depth
M	Mass of tracer

M_n	n^{th} moment
p	Dimensionless position from the centreline, $p = r/a$
P	Pressure
Q	Discharge
$\bar{Q}$	Time averaged discharge
r	Distance from centreline
Re	Reynolds Number
Re_0	Initial Reynolds Number
Re_1	Final Reynolds Number
Re_c	Critical Reynolds Number
s	Standard deviation
S	Entropy
Sc	Schmidt Number
Sc_t	Turbulent Schmidt Number
t	Time
t^*	Dimensionless time, $t^* = (t - t_0)/T$
$\bar{t}$	Temporal centroid
t_0	Initial time
T	Transient time
T_F	Dimensionless time for Fick's law to be valid
$\hat{T}$	Dimensionless time, $\hat{T} = tQ/v$
u_ϕ	Velocity in the direction ϕ
u_*	Frictional velocity
u_{*0}	Initial frictional velocity
u_{*1}	Final frictional velocity
$\bar{u}$	Cross-sectional mean velocity
$\bar{\bar{u}}$	Time averaged cross-sectional mean velocity
u^+	Dimensionless velocity, $u^+ = u_x/u_*$
U^+	Dimensionless velocity, $U^+ = u^+(\bar{u})/u_c$
$\bar{u}_0$	Initial cross-sectional mean velocity
$\bar{u}_1$	Final cross-sectional mean velocity
u_c	Maximum (centreline) velocity
u_L	Velocity distribution for laminar flow
u_r	Velocity in the direction r
u_T	Velocity distribution for turbulent flow
u_x	Velocity in the direction x
v	Volume
x	Longitudinal distance
$\bar{x}$	Spatial centroid
y	Distance from pipe's wall
y^+	Dimensionless distance from the wall, $y^+ = yu_*/\nu$
Y^+	Dimensionless distance from the wall, $Y^+ = y^+(\bar{u})/u_c$

Greek

α	Laminar to turbulent transition factor
γ	Dimensionless discharge gradient, $\gamma = (d/u_{*0})(1/\bar{u}_0)(d\bar{u}/dt)$
ϵ	Characteristic size of pipe roughness
λ	Pseudo or integration time
λ_l	Laser wave length
μ	Dynamic viscosity
ν	Kinematic viscosity
ν_t	Turbulent kinematic viscosity
ξ	Weighting factor for lagrangian function
σ	Density
$\sigma_x^2(t)$	Spatial variance
$\sigma_t^2(x)$	Temporal variance
τ	Shear stress
τ_t	Turbulent shear stress

Acknowledgments

I am extremely grateful to Professor Ian Guymer, for taking me on in the first place, and for his continued support and guidance throughout the project. His meticulous approach has greatly forwarded the work.

I am also extremely grateful for the technical support of Ian Baylis, who built and maintained the experimental facility. The project would have been much more difficult if it hadn't been for his technical input and work rate.

I would also like to thank Dr Virginia Stovin and Fred Sonnenwald from The University of Sheffield, for providing technical support with the project, specifically with the Deconvolution code.

My family; Dad and Mom, Pa Pa and Grandma, Granddad and Nanny, Nanny 'M', Andy, and Kriss and Sam, who have provided me with constant support throughout the project, for which I am very grateful.

And finally, the project would not have been possible without the financial support of Dad and Mom, Nanny 'M', Granddad and Nanny and Pa Pa and Grandma.

Declarations

I declare that the work in this thesis has been composed by myself and no portion of the work has been submitted in support of an application for another degree or qualification of this or any other university or other institute of learning. The work has been my own except where indicated and all quotations have been distinguished by quotations marks and the sources of information have been acknowledged.

Abstract

The longitudinal dispersion coefficient describes the change in characteristics of a solute cloud, as it travels along the longitudinal axis of a flow. Within potable water networks, it is important to be able quantify this parameter, to predict the fate of solutes introduced into the network. Current water quality models assume steady, highly turbulent flow [Tzatchkov et al., 2009]. However, this assumption is not valid for the network's periphery, where water leaves the main network and comes to the point of consumption. Here, the flow can be both unsteady and turbulent, transitional or laminar [Buchberger et al., 2003; Blokker et al., 2008, 2010].

Taylor [1954] proposed a now classical expression to predict the longitudinal dispersion coefficient within steady, turbulent pipe flow. However, experimental data has shown significant deviation from his prediction for $Re < 20000$.

Within the present work, new experimental data is presented for steady and unsteady flows for a range of discharges corresponding to $2000 < Re < 50000$. From this experimental work, results describing the mixing processes through steady and unsteady turbulent and transitional pipe flow are presented, as well as an explanation as to why Taylor's theory fails to predict experimental data for $Re < 20000$.

In addition, a simple numerical model is proposed for steady flow for $2000 < Re < 50000$. The model extends Taylor's analysis to predict the longitudinal dispersion coefficient in a manner more consistent with experimental data for $Re < 20000$. Furthermore, the model is extended for use within unsteady flow.

Chapter 1

Introduction

1.1 Background

When a solute is introduced into fluid flowing through a pipe, it spreads in all directions. One aspect of this process that is of key importance with regard to water quality modeling is the spreading of the solute in the longitudinal direction, along the pipe's main axis. This process leads to the change in characteristics of the contamination cloud as it travels along the longitudinal axis in the direction of the flow, from an initial state of high concentration and low spatial variance, to a downstream state of lower concentration and higher spatial variance.

Within potable water networks, it is important to quantify the changing characteristics of solutes as they travel through the network. Current water quality models for distribution networks assume steady, highly turbulent flow [Tzatchkov et al., 2009]. For highly turbulent flow, longitudinal dispersion is negligible when compared to transport by advection alone, and thus water quality models often only account for contaminant bulk advection, neglecting longitudinal dispersion altogether [Tzatchkov et al., 2009]. This assumption is valid for the majority of the flow conditions experienced in the main network. However, one part of the network for which this assumption is not valid is the network's periphery, where water leaves the main network and travels to the point of consumption [Lee, 2004]. Here, in the so called 'dead end' regions of the network, discharge is contingent upon the saprobic demand of the consumer, and hence the flow is both unsteady, and can assume any flow rate from the relatively high main network rate, through to zero in times of no demand. Within such regions, flows have been reported as being turbulent, transitional and laminar [Buchberger et al., 2003; Blokker et al., 2008, 2010]. In addition, pressure transients, caused by any change in the flow conditions (closed

valve, leaking pipe, network maintenance etc), can lead to periods of both unsteady and low flow in the main network [LeChevallier et al., 2003]. This scenario is of particular interest in water quality modeling, as negative pressure created in such pressure transients can lead to contaminant intrusion into the network through any leaks in the system [LeChevallier et al., 2003]. Thus, contaminant can be released into a low and unsteady flow. To accurately model solute transport within the network at all times, a model is required that can predict the fate of a contaminate introduced into unsteady discharges, where the discharge can vary from zero up to the main network rate.

Various mathematical models have been proposed to predict downstream concentration profiles associated with an upstream contamination event. Within these models, the key determinand of the profile's distribution is the effective longitudinal dispersion coefficient, a parameter analogous to the diffusion coefficient of Fick's second law.

Taylor [1953, 1954] developed two analytical equations to determine the longitudinal dispersion coefficient within steady laminar and turbulent pipe flow respectively. His equations are still widely used. However, experimental data has shown a significant divergence between predictions made by Taylor's equations and experimentally obtained longitudinal dispersion coefficients within turbulent flow at low Reynolds Numbers. Taylor's equation for laminar flow [Taylor, 1953] is valid for approximately Re $<$ 2000, whilst Taylor's equation for turbulent flow [Taylor, 1954] has been shown to be valid for Re $>$ 20000.

Thus, a model is required that can predict the longitudinal dispersion coefficient for steady flow for $2000 < Re < 50000$, and that can be extended for use within unsteady flow.

1.2 Aims

The main aim of the present work is to develop a model that can predict the longitudinal dispersion coefficient for steady and unsteady flow for $2000 < Re < 50000$. This model would enable quantification of the mixing processes in dead-end regions of water distribution networks. To achieve this, the present work aims to:

- Perform a detailed experimental investigation of longitudinal dispersion and the hydraulics of pipe flow for steady flow for $2000 < Re < 50000$, to understand the mixing processes occurring for steady turbulent and transitional pipe flow over this range of Reynolds Numbers.
- Develop a simple numerical model to predict the longitudinal dispersion coefficient for steady flow for $2000 < Re < 50000$, and propose a framework for which the model could be applicable for unsteady flow.
- Perform a detailed experimental investigation of the longitudinal dispersion coefficient within various configurations of unsteady flow for $2000 < Re < 50000$, to understand the mixing precesses occurring and to assess conditions under which the proposed model for unsteady flow is valid.

1.3 Thesis Structure

- Chapter 2 comprises a literature review that presents all background work and relevant literature on the problem. Chapter 2 concludes with a summary of the present literature, along with a set of more detailed aims in light of the literature review.
- Chapter 3 presents the development of a numerical model to predict the longitudinal dispersion coefficient for steady flow for $2000 < Re < 50000$. A framework is also proposed by which the model for steady flow may be applicable for unsteady flow.
- Chapter 4 gives a detailed explanation of the experimental facility used for all laboratory tests, as well as an overview of the test programs undertaken within the work.
- Chapter 5 presents all results for steady flow. The Chapter first presents experimental results for the hydraulics of steady flow for $2000 < Re < 50000$, to establish the various flow regimes occurring through this range of discharges

for the facility used for all tests. The Chapter then presents experimental results for longitudinal dispersion for $2000 < Re < 50000$. Finally, the Chapter uses the hydraulic data presented to set parameters for the numerical model proposed in Chapter 3, and validates the results of the model against the results for the longitudinal dispersion coefficient within steady flow.

- Chapter 6 presents results for tracer experiments within transient, unsteady flow. Longitudinal dispersion coefficients are obtained from experimental results, and conditions are assessed under which the model for the longitudinal dispersion coefficient within unsteady flow is valid.
- Chapter 7 presents the work's main conclusions.
- Chapter 8 considers possible further work on the problem highlighted by the present work.

Chapter 2

Literature Review

2.1 Introduction to Longitudinal Dispersion

Longitudinal dispersion can be defined as the spreading of a solute introduced into a flow along the flow's longitudinal axis. The primary mechanism of longitudinal dispersion is differential advection caused by the radial distribution of the flow's longitudinal velocity. When fluid flows through a pipe at a given discharge and corresponding cross-sectional mean velocity, the velocity of the flow is not constant with respect to radial position across the pipe. The magnitude of the velocity changes from the maximum velocity obtained at the pipe's centreline, through to zero at the pipe's wall. This effect is due to viscous forces associated with the pipe's boundary. The radial distribution of the longitudinal velocity is known as the velocity profile [Benedict, 1980].

When a cross-sectionally well mixed tracer is introduced across a pipe, the tracer will be advected in accordance to the velocity at its corresponding radial position. Hence, tracer at the centre of the pipe will travel further in a given period of time than tracer at the boundary of the pipe, and thus the tracer disperses [Rutherford, 1994].

The tracer is further spread in all directions by the effects of molecular and turbulent diffusion. Molecular diffusion is the spreading of particles by random molecular fluctuations, whilst turbulent diffusion is the spreading of particles by random turbulent fluctuations and eddies, considered analogous to molecular diffusion [Rutherford, 1994].

The degree to which these mechanisms act to spread the tracer directly in the longitudinal direction is negligible when compared to the effects of differential advection. However, the two mechanisms are significant with regard to longitudinal

dispersion because of their ability to spread the tracer radially. As radial diffusion increases, each particle of tracer experiences a larger number of radial positions and corresponding velocities, thus reducing the effects of the differential advection. Hence, there is an inverse relationship between molecular and turbulent diffusion and longitudinal dispersion. Molecular diffusion is several orders of magnitude smaller than turbulent diffusion, and is therefore often neglected from longitudinal dispersion models where turbulent diffusion is present.

2.2 Longitudinal Dispersion within Water Distribution Networks

Current water quality models used to model longitudinal dispersion assume steady, highly turbulent flow [Tzatchkov et al., 2009]. This assumption provides a good approximation within the normal operating conditions for the main network, where the flow is steady and highly turbulent, but fails to predict longitudinal dispersion within the dead end regions of the network, or in times of pressure transients within the main network, where the flow is unsteady [Tzatchkov et al., 2009; Lee, 2004; LeChevallier et al., 2003].

Dead end regions of the network can be defined as pipelines where only one end of the system is connected to the main network, with the other end being the system's output to the consumer [Lee, 2004]. Here, the flow patten and discharge is contingent upon the sporadic demand of the customer, and thus the flow can be stagnant for large periods of time, and then move in random busts of low and unsteady discharge [Lee, 2004]. Tzatchkov et al. [2001] showed that current water quality models, which assume steady, highly turbulent flow conditions, over predict the concentration of solutes traveling through these region of the network.

Within all parts of the network, unsteady flow occasionally occurs as a result of a change in the flow conditions, such as intentional or unintentional pump stoppage, a pipe fracture or leak, or the closing of a value in a dead end system [LeChevallier et al., 2003]. In such instances, periods of unsteady discharge can be experienced in both the main network and dead end regions. Furthermore, such periods of sudden, unsteady flow can lead to large pressure transients in the pipe network [LeChevallier et al., 2003]. Pressure transients created by the sudden change in flow conditions can travel in waves of positive and negative pressure up and down the pipe [LeChevallier et al., 2003]. This scenario is of particular importance to water quality modeling as, if a pipe has a leak, negative pressure can draw non-potable water into the pipe though the leak [LeChevallier et al., 2003; Jung et al., 2007].

Thus, contaminant can be introduced anywhere in the network, at any flow rate between the main network rate and zero, into various patterns of unsteady flow. These scenarios highlight the importance of modeling longitudinal dispersion for flow rates below the main network rate, and for unsteady flow for flow rates below and at the main network flow rate.

2.3 Laminar, Turbulent and Transitional Pipe Flow

Pipe flow can be separated into three main categories; laminar, turbulent and transitional.

Laminar flow is characterised by streamline motion of the fluid, where the fluid's only velocity component is longitudinal, parallel to the boundary, and the only radial exchange is that of molecular diffusion. Within laminar flow, the ratio of internal to viscous forces is low, and thus viscous forces are dominant, damping out any perturbations introduced into the flow [Mathieu and Scott, 2000].

Turbulent flow is characterised by the chaotic motion of the fluid, where the magnitude and direction of the fluid's local velocity fluctuates randomly. Hence, there can be a velocity component and rapid exchange in any direction. Turbulent flow occurs when a certain critical flow rate is exceeded. At this point, the ratio of inertial to viscous forces is high, and thus perturbations are no longer damped out by viscous forces, but instead are amplified, leading to fully turbulent flow [Mathieu and Scott, 2000].

Transitional flow occurs near the critical flow rate. Here, the flow can be either laminar or turbulent, and is often characterised by laminar flow interrupted by periods of transient, local turbulence [Mathieu and Scott, 2000].

One useful parameter when considering the transition from laminar to turbulent flow is the Reynolds Number [Reynolds, 1883]:

$$Re = \frac{\bar{u}d}{\nu} \tag{2.1}$$

Where $\bar{u}$ is the cross-sectional mean velocity, d is the pipe's diameter and ν is the molecular kinematic viscosity.

The Reynolds Number is a dimensionless group that quantifies the ratio of viscous to internal forces within the fluid, and thus can be used to suggest the point at which the flow transitions from being laminar to turbulent. Benedict [1980] gives a broad overview of commonly observed critical points, and suggests that for Re < 2000, viscous forces are dominant and the flow is often laminar. At some point between approximately $2000 <$ Re < 4000, inertial forces become significant and

begin to cause fluctuations within the flow that can no longer be damped out by viscous forces, hence the onset of turbulence. From $4000 < \mathrm{Re} < 10000$, the flow is characterised by continuous turbulence which exhibits a strong Reynolds Number dependence. At $\mathrm{Re} > 10000$, the flow approaches a state where turbulence has only a small Reynolds Number dependence. These regimes, suggested by Benedict [1980], are summarised in Table 2.1.

Range	**Regime**	**Description**
$\mathrm{Re} < 2000$	Laminar	Laminar flow
$2000 < \mathrm{Re} < 4000$	Transitional	Intermittent turbulence
$4000 < \mathrm{Re} < 10000$	Low turbulent	Continuous turbulence, strong Re dependence
$\mathrm{Re} > 10000$	Fully turbulent	Continuous turbulence, small/negligible Re dependence

Table 2.1: *Summary of flow regimes [Benedict, 1980].*

Table 2.1 provides broad ranges for the transition from laminar to turbulent flow. The precise point at which the flow becomes turbulent is known as the critical Reynolds Number, Re_c. The exact value for the critical Reynolds Number is difficult to define, as it is a function of the configuration of a particular system, and thus is system specific.

Reynolds [1883] first investigated the critical Reynolds Number, and published data suggesting that the critical Reynolds Number occurs at $Re \approx 2020$. In a subsequent paper, Reynolds [1894] proposes that the critical Reynolds Number fell somewhere within the range $1900 < Re_c < 2000$. Further work has revealed a relatively large range of values for the critical Reynolds Number, with results falling within the range $1800 < Re_c < 2300$ [Lindgren, 1957; Leite, 1958; Wygnanski and Champagne, 1973; Darbyshire and Mullin, 1995; Faisst and Eckhardt, 2004; Eckhardt, 2009].

One of the reasons for the ambiguity in defining the critical Reynolds Number is because the actual transition mechanism is more complex than the over simplistic picture of a critical point at which the flow will transition from being fully laminar to fully turbulent. Under ideal conditions, pipe flow will remain laminar until very high Reynolds Numbers. Laminar flow had been reported as being achieved as high as $Re \approx 100000$ by Pfenniger [1961]. In fact, linear stability theory has been used to suggest that pipe flow can remain laminar up to effectively infinite Reynolds Numbers [Salwen et al., 1980; Meseguer and Trefethen, 2003].

Turbulent flow is not simply caused by obtaining a certain Reynolds Number,

but rather by a perturbation in a flow with a sufficiently high Reynolds Number to propagate the disturbance into turbulence. Below the critical Reynolds Number, disturbances caused by perturbations will be damped out, and quickly decay, such that the flow returns to being fully laminar. For low Reynolds Numbers beyond the critical Reynolds Number, a range around $2000 < Re < 2700$, perturbations will lead to turbulent puffs [Wygnanski and Champagne, 1973]. These puffs are patches of local turbulence, i.e. the flow upstream, downstream and around the puff is still laminar. Furthermore, these puffs are transient, hence the flow will eventually decay to a laminar state. Although the turbulent puffs are local, and do not expand spatially, the turbulent fraction of the flow can increase through a process of the puffs splitting, where a single puff can split to form several puffs, a phenomenon that becomes more likely as Reynolds Number increases [Avila et al., 2011]. As Reynolds Numbers increases beyond $Re \approx 2700$, turbulent puffs propagate into turbulent slugs, volumes of turbulence that occupy the entire cross-section of the pipe and expand in both the up and downstream direction, leading to fully developed turbulent flow [Wygnanski and Champagne, 1973; Avila et al., 2011; Eckhardt, 2011].

Avila et al. [2011] propose a critical Reynolds Number by considering, both experimentally and numerically, the probability of whether a turbulent puff will decay, leading to the relaminarisation of the flow, or split, leading to an increase in the flow's turbulent fraction.

For the experimental investigation Avila et al. [2011] used a 15 metre long glass pipe with an internal diameter of 4 mm, corresponding to a relatively large length of $3750d$. The system could support laminar flow up to $Re = 4400$. For each run a perturbation was introduced $250d$ from the inlet in the form of a water jet injected through a hole with a diameter of $0.2d$. The perturbation was designed to create a single turbulent puff in the flow. Two pressure sensors were used to monitor the life of the turbulent puff, one at a length $300d$ and another which could be positioned at any point along the pipe. The first sensor was used to confirm that a single puff had been created, and the second was used downstream of the first to determine the fate of the puff, i.e. if it decayed, remained the same or split.

In addition to the experimental investigation, Avila et al. [2011] considered the results of two numerical codes; a spectral-element Fourier code that solves the Navier-Stokes Equations in cartesian co-ordinates, as developed by Blackburn and Sherwin [2004], and a hybrid spectral finite-difference code that solves the Navier-Stokes Equations in cylindrical coordinates, as developed by Willis and Kerswell [2009].

For low turbulent flows near the critical Reynolds Number, the turbulent fraction of the flow only increases through the process of puff splitting. Figure 2.1 shows the experimental results of Avila et al. [2011], and the numerical results of Blackburn and Sherwin [2004] and Willis and Kerswell [2009], in terms of the probability that a turbulent puff will split with time at a given Reynolds Number, where P is the probability that a puff will split before time t, thus $1 - P$ is the probability that a puff will remain a single localised puff after time t. From Figure 2.1 it can be seen that as Reynolds Number increases, the probability of the puffs splitting increases, and thus the probability of the turbulent fraction increasing is greater.

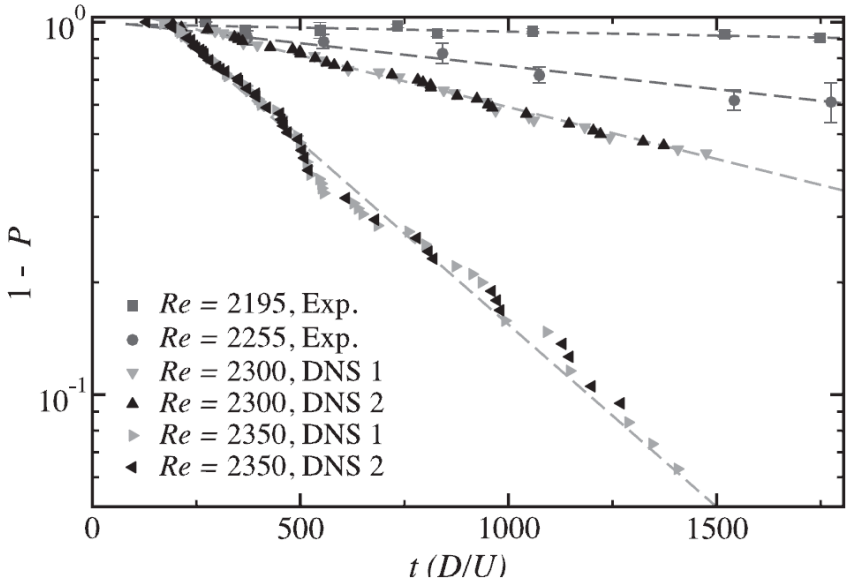

Figure 2.1: *Probability a turbulent puff will split after time t. Showing experimental data of Avila et al. [2011] and numerical data of Blackburn and Sherwin [2004] (DNS1) and Willis and Kerswell [2009] (DNS2). Figure reproduced from Avila et al. [2011].*

Figure 2.2 shows the probability of a puff splitting after traveling a given distance downstream of it origin. Here, the probability P is $P = r/n$ where r is the number of events that split and n is the total number of realisations. From Figure 2.2 it can again be seen that as Reynolds Number increases, the probability that the puff will split increases. It can also be noted that the 'S' trend in the data shows that the probability of puff splitting tends towards zero for $Re < 2000$, and tends towards unity for $Re > 2400$.

Figure 2.3 shows a comparison between the time scales for turbulence to

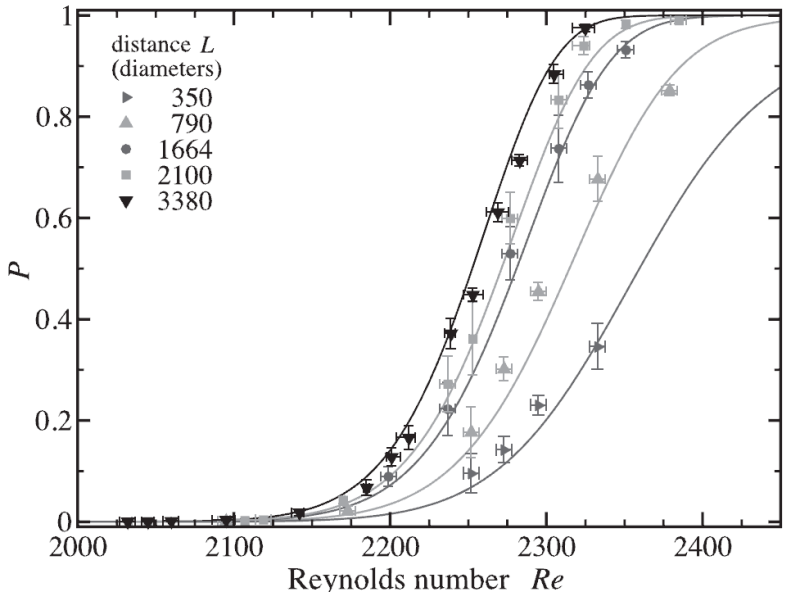

Figure 2.2: *Probability a turbulent puff will split after distance L. Showing experimental data of Avila et al. [2011]. Solid line is given by super exponential fits to the data. Figure reproduced from Avila et al. [2011]*

spread (puff splitting) to the time scales for turbulence to decay. In Figure 2.3 the trend showing the time for turbulence to spread is represented by the solid black line, which shows the time required for a puff to split in two, and the trend showing the time for turbulence to decay and re-laminarise is represented by the dashed line. Both trends are described well by an exponential function.

Avila et al. [2011] proposed the critical Reynolds Number as the point at which the two trends intersect, i.e. the point below which turbulence will likely decay, and above which turbulence will likely spread. On this basis, Avila et al. [2011] proposes a critical Reynolds Number of $Re_c \approx 2040 \pm 10$ for their system.

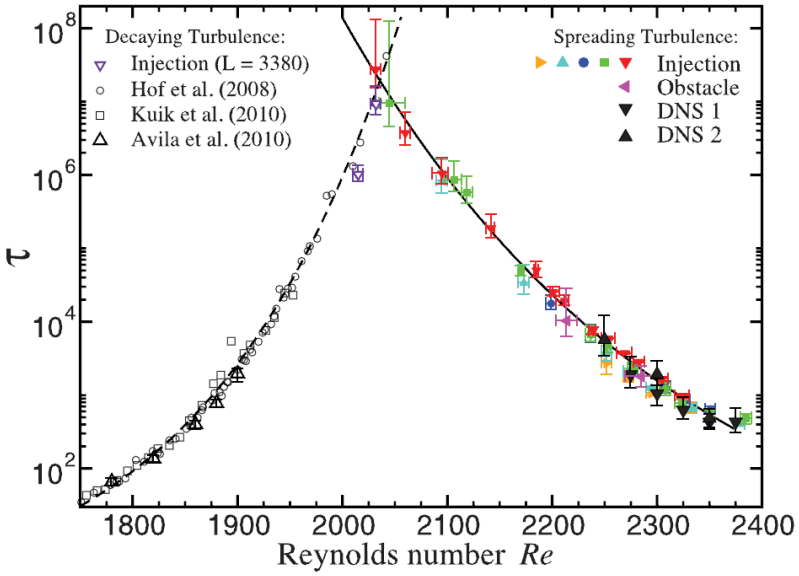

Figure 2.3: *Mean lifetime of a puff before decaying or splitting, τ, vs. Reynolds Number. Showing experimental data of Hof et al. [2008]; Avila et al. [2010]; Kuik et al. [2010]; Avila et al. [2011] and numerical data of Blackburn and Sherwin [2004](DNS1) and Willis and Kerswell [2009](DNS2). Solid line and dashed line is given by exponential fits. Figure reproduced from Avila et al. [2011]*

2.4 The Velocity Profile in Steady Pipe Flow

2.4.1 Introduction

Due to viscous forces associated with the boundary, the longitudinal velocity of fluid flowing through a pipe changes with radial position across the pipe. The longitudinal velocity varies from the maximum velocity obtained at the pipe's centreline, to zero at the pipe's wall. The distribution of the longitudinal velocity within pipe flow is described by the cylindrical version of the Navier-Stokes Equation for longitudinal velocity [Acheson, 1990]:

$$\begin{aligned} &\rho\left(\frac{\partial u_x}{\partial t}+u_r\frac{\partial u_x}{\partial r}+\frac{u_\phi}{r}\frac{\partial u_x}{\partial \phi}+u_x\frac{\partial u_x}{\partial x}\right) \\ &=-\frac{\partial P}{\partial x}+\mu\left[\frac{1}{r}\frac{\partial}{\partial r}\left(r\frac{\partial u_x}{\partial r}\right)+\frac{1}{r^2}\frac{\partial^2 u_x}{\partial \phi^2}+\frac{\partial^2 u_x}{\partial x^2}\right] \end{aligned} \tag{2.2}$$

Where ρ is fluid density, ϕ is tangential position, μ is dynamic viscosity, P is pressure and u_x, u_r and u_ϕ and the velocities in the longitudinal, radial and tangential directions respectively.

2.4.2 Laminar Flow

Laminar flow is characterised by stream line motion of the fluid, with no radial or tangential velocity. For a laminar flow to exhibit fully laminar characteristics, a certain length is required from when the flow first enters the pipe to when the flow is deemed fully developed. This is because initially, the flow will adopt characteristics associated with its previous geometry, hence the flow needs time to come under the influence of the boundary geometry of the pipe in question. The distance required for the flow to become fully developed can estimated by the following expression [White, 2008]:

$$\frac{L_d}{d} \approx 0.06Re \tag{2.3}$$

Where L_d is the length required for the flow to become fully developed.

Once the flow is fully developed, there is no velocity component in the radial or tangential direction. Furthermore, if the flow is assumed steady and uniform, there is no variation with time or distance. Hence, for steady, uniform laminar pipe flow, Equation 2.2 reduces to:

$$\frac{\partial P}{\partial x} = \mu \left[\frac{1}{r} \frac{\partial}{\partial r} \left(r \frac{\partial u_x}{\partial r} \right) \right] \tag{2.4}$$

Equation 2.4 can be solved analytically to give the velocity distribution with fully developed laminar flow as:

$$\frac{u_x}{u_c} = 1 - p^2 \tag{2.5}$$

Where p is the dimensionless position from the centreline $p = r/a$, where a is the pipes radius, and u_c is the profile's maximum velocity, assumed as the velocity at the centre line.

The velocity distribution defined by Equation 2.5 is parabolic, as shown in Figure 2.4, and is a function of radial position alone. Hence, fully developed laminar pipe flow has a velocity distribution that is independent of Reynolds Number.

The magnitude of the maximum velocity can be obtained as a function of the cross-sectional mean velocity by integrating the velocity distribution over the pipe's cross section to obtain the discharge, and then dividing through by the cross-sectional area to obtain the mean to maximum velocity ratio as:

$$\frac{\bar{u}}{u_c} = 0.5 \tag{2.6}$$

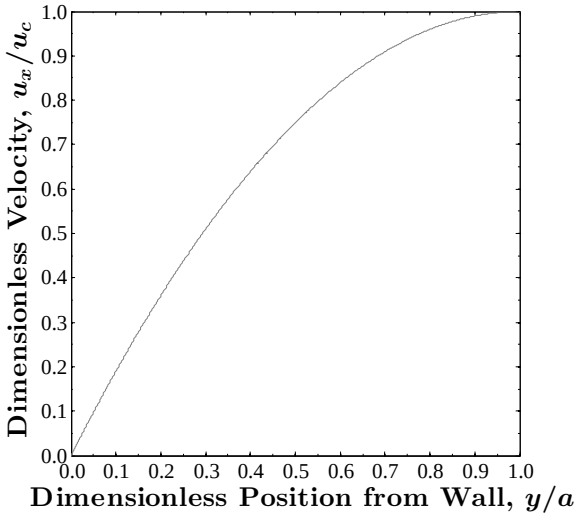

Figure 2.4: *Example of a laminar velocity profile, as defined in Equation 2.5.*

From which it can be seen that the maximum velocity within laminar pipe flow is:

$$u_c = 2\bar{u} \tag{2.7}$$

2.4.3 Turbulent Flow

Turbulent flow is characterised by random turbulent fluctuations and eddies in all directions, hence there is a velocity component in more than just the longitudinal direction. Because of this, Equation 2.2 cannot be solved analytically for turbulent flow. Hence, theoretical turbulent velocity profiles are generally numerical or empirical, and are often presented as a 'mean velocity profile', where each local velocity represents the time-averaged velocity at that point.

Turbulent velocity profiles are generally more uniform than the parabolic laminar profile, with a much larger velocity gradient near the wall. Turbulent velocity distributions are also Reynolds Number specific, becoming increasingly uniform as Reynolds Number increases [Benedict, 1980].

In his pioneering work on turbulent velocity profiles, Nikuradse [1932] measured the velocity distribution of water flowing through a pipe with an internal diameter of 10 mm. The velocity measurements were obtained using Pitot tubes with internal diameters of 0.21 and 0.3 mm respectively. Figure 2.5 shows an example of a turbulent velocity profile collected by Nikuradse [1932].

Turbulent velocity profiles are often defined in terms the dimensionless ve-

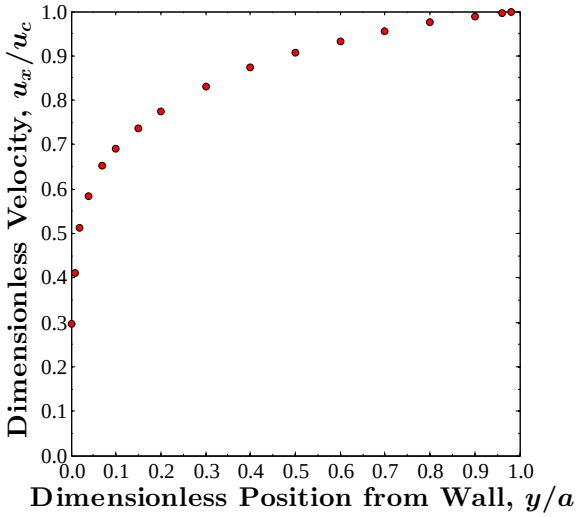

Figure 2.5: *Example of experimentally obtained velocity profile of Nikuradse [1932].*

locity and distance terms u^+ and y^+, where:

$$u^+ = \frac{u_x}{u_*} \tag{2.8}$$

and:

$$y^+ = \frac{yu_*}{\nu} \tag{2.9}$$

Where y is the actual distance from the wall and u_* is the frictional velocity, which can be defined as:

$$u_* = \bar{u}\sqrt{f/8} \tag{2.10}$$

Where f is the friction factor, which will be considered in more detail in Section 2.5.

Similarly to laminar flow, an initial length is required for a turbulent flow to become fully developed. This length is shorter than within laminar flow, and can be estimated as [White, 2008]:

$$\frac{L_d}{d} \approx 4.4Re^{1/6} \tag{2.11}$$

The velocity distribution within fully developed turbulent flow can be estimated by

a logarithmic function, where a significant portion of the profile conforms to the relationship:

$$u^+ = A + ln(y^+) + B \tag{2.12}$$

Where A and B are empirical constants.

Nikuradse [1932] used his experimental data to propose values of $A = 2.5$ and $B = 5.5$ for fully developed turbulent flow within a smooth pipe. Thus, Nikuradse proposes the turbulent velocity profile as:

$$u^+ = 2.5ln(y^+) + 5.5 \tag{2.13}$$

Figure 2.6 shows the theoretical profile of Nikuradse [1932] at $Re = 4000$ and $Re = 100000$, as defined by Equation 2.13, compared to a laminar velocity distribution, as defined by Equation 2.5.

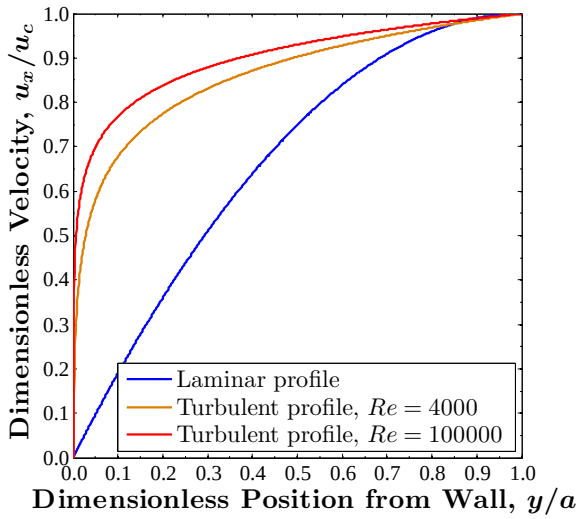

Figure 2.6: *Comparison between a laminar velocity profile, Equation 2.5, and the theoretical turbulent profile of Nikuradse [1932], Equation 2.13, at* $Re = 4000$ *and* $Re = 100000$.

Although the data of Nikuradse [1932] provides a good picture of the majority of the velocity profile, limitations within his experiments due to the size of the Pitot tubes meant that he could not measure the flow's velocity very close to the wall. Durst et al. [1995] used Laser Doppler Anemometry (LDA) to measure the velocity distribution across a pipe with an internal diameter of 50 mm. By matching the refractive index of the pipe's material to the fluid's, Durst was able to perform accurate velocity measurements very near to the wall. Through this method, Durst

was able to present data much closer to the wall than Nikuradse could by using Pitot tubes.

Figure 2.7 shows the data of Durst et al. [1995], compared to a laminar profile, Equation 2.5, and the turbulent profile of Nikuradse [1932], Equation 2.13. The figure's x-axis is in logarithmic co-ordinates to highlight the boundary layer near the wall. From Figure 2.7 it can be seen that there are three main parts to a turbulent velocity profile. The main part of the profile is the 'turbulent core', which occurs at $y^+ > 30$. In this portion of the flow, the profile is fully turbulent. Here, the profile is logarithmic besides a small region near the centreline where the profile flattens, deemed the 'wake' region. For $y^+ < 5$, even in fully developed turbulent flow, the flow remains laminar. This portion of the flow is deemed the 'laminar sub-layer'. From $5 < y^+ < 30$, the flow transitions from being laminar to fully turbulent, a portion of the flow deemed the 'buffer zone'.

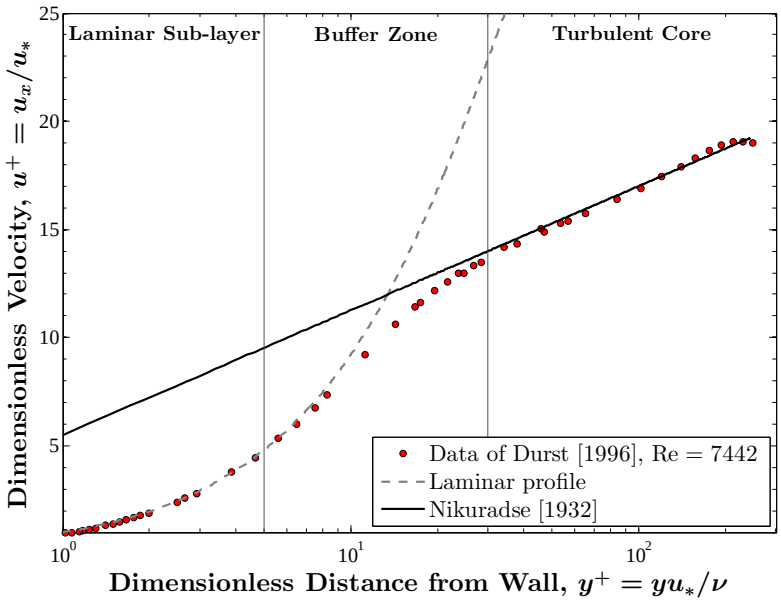

Figure 2.7: *Data of Durst et al. [1995], compared to a laminar profile, Equation 2.5, and the turbulent profile of Nikuradse [1932], Equation 2.13.*

From Figure 2.7 it can be seen that Nikuradse's profile predicts the velocity distribution reasonably for $y^+ > 30$, within the turbulent core, but poorly for the non-turbulent portion, for $y^+ < 30$.

Reichardt [1951] proposed the following expression that accounts for both

the turbulent and non-turbublent portions of the flow:

$$u^+ = 2.5ln(1 + 0.4y^+) + C_1 \left[1 - exp\left(\frac{-y^+}{11}\right) - \frac{y^+}{11}exp(-0.33y^+)\right] \tag{2.14}$$

Where C_1 is a empirical constant, found to be 7.8 by Reichardt [1951]. Thus Reichert proposed the turbulent velocity profile as:

$$u^+ = 2.5ln(1 + 0.4y^+) + 7.8 \left[1 - exp\left(\frac{-y^+}{11}\right) - \frac{y^+}{11}exp(-0.33y^+)\right] \tag{2.15}$$

Figure 2.8 shows a comparison between Reichardt's profile, as defined in Equation 2.15, and the experimental data of Durst et al. [1995]. From Figure 2.8 it can be seen that for $y^+ > 30$, within the profile's turbulent core, the profile tends towards a logarithmic distribution, but diverges in accordance with the data for $y^+ < 30$. It can also be noted that the logarithmic distribution of the profile within the turbulent core neglects the profile's wake region.

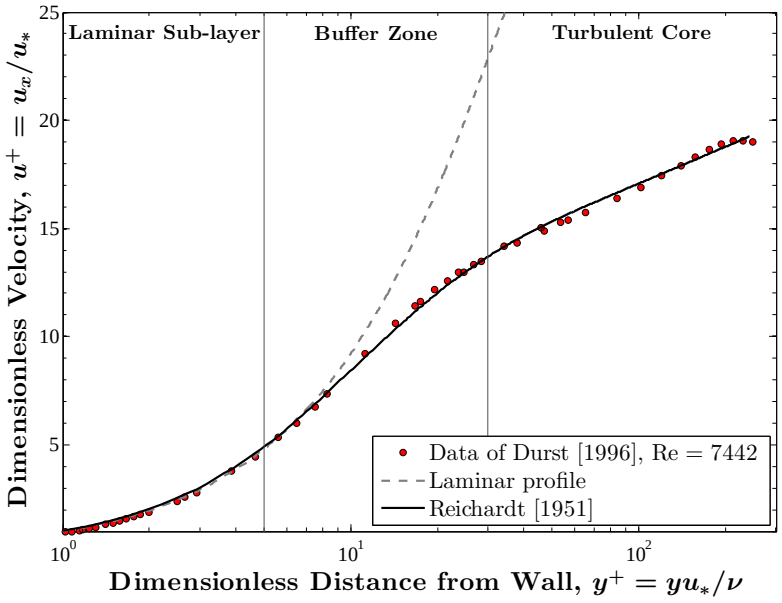

Figure 2.8: *Data of Durst et al. [1995], compared to profile of Reichardt [1951], Equation 2.15, and a laminar profile, Equation 2.5.*

Flint [1967] proposed a velocity profile that accounts for the laminar sub-layer, buffer zone, turbulent core and wake region for $6000 < Re < 100000$. He began by proposing an expression for the velocity profile for $y^+ < 150$, by re-visiting

the expression proposed by Reichardt [1951] in Equation 2.14. Flint proposed the constant C_1 as 7.3, and thus proposed the turbulent velocity profile for $y^+ < 150$ as:

$$u^+ = 2.5ln(1 + 0.4y^+) + 7.3\left[1 - exp\left(\frac{-y^+}{11}\right) - \frac{y^+}{11}exp(-0.33y^+)\right] \tag{2.16}$$

He then went on to propose the following expression for the remainder of the profile, for $y^+ > 150$:

$$u^+ = 2.5ln\left(C_2\left[\frac{1+p^2}{1+2p^2}\right]\right) + C_3 \tag{2.17}$$

Where C_2 and C_3 are constants. Flint sets the value of C_3 as 5, whereas C_2 must be set, such that the following condition is satisfied at $y^+ = 150$:

$$C_2\left[\frac{1+p^2}{1+2p^2}\right] = 1 \tag{2.18}$$

Figure 2.9 shows a comparison between Flint's profile, as defined in Equation 2.16 and 2.17, and the experimental data of Durst et al. [1995].

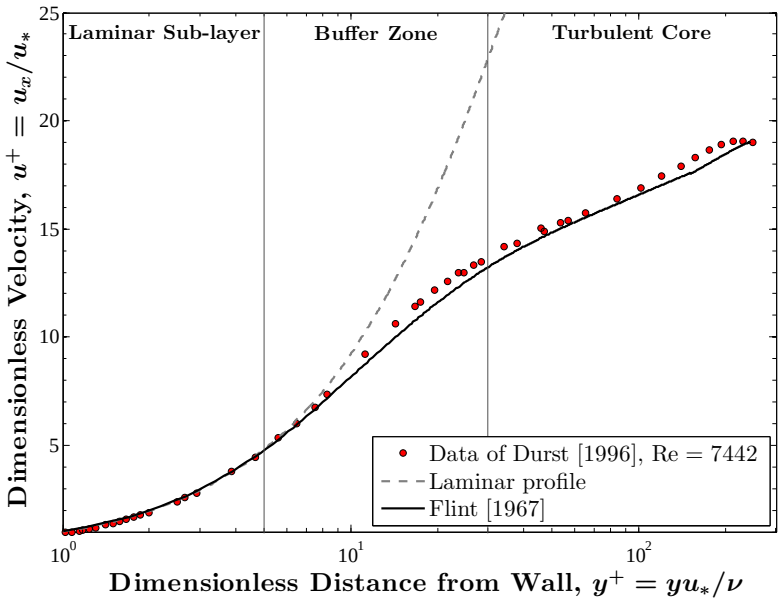

Figure 2.9: *Data of Durst et al. [1995], compared to profile of Flint [1967], Equation 2.16 and 2.17, and a laminar profile, Equation 2.5.*

2.4.4 Transitional Flow

Figure 2.6 shows a laminar velocity distribution at any Reynolds Number within the laminar range, and a turbulent velocity profile at $Re = 4000$, the approximate Reynolds Number at which the transition to fully turbulent flow generally occurs. At $Re \approx 2000$ the flow is generally laminar, and thus the velocity profile is parabolic, whereas at $Re \approx 4000$ the flow is generally fully turbulent and thus the velocity profile is approximately logarithmic, and much more uniform than for laminar flow. Thus, at some point between $2000 < Re < 4000$, the velocity profile transitions from a parabolic to a logarithmic distribution.

Senecal and Rothfus [1953] obtained experimental data in this range by measuring the velocity distribution of air flowing through two pipes with internal diameters of 12.7 and 19 mm respectively. The velocity measurements were made using three Pitot tubes with internal diameters of 0.33, 0.51 and 0.71 mm respectively.

Flint [1967] proposed an empirical expression to estimate the velocity profile for $2000 < Re < 6000$. The expression is derived by plotting experimental data within this region in terms of the dimensionless coefficients U^+ and Y^+, where:

$$U^+ = u^+ \left(\frac{\bar{u}}{u_c}\right) = \frac{u_x}{u_*}\left(\frac{\bar{u}}{u_c}\right) \tag{2.19}$$

and:

$$Y^+ = y^+ \left(\frac{\bar{u}}{u_c}\right) = \frac{y u_*}{\nu}\left(\frac{\bar{u}}{u_c}\right) \tag{2.20}$$

From this, he proposed the velocity profile for transitional flow as:

$$U^+ = ln(1 + Y^+) + 9.5\left[1 - exp\left(\frac{-Y^+}{11}\right) - \frac{Y^+}{11}exp(-0.45Y^+)\right] \tag{2.21}$$

Figure 2.10 shows a comparison between experimental data of Senecal and Rothfus [1953] and Equation 2.21.

From Figure 2.10 it can be seen that Flint's expression for the velocity profile in transitional flow predicts the data well for $2700 < Re < 4000$, but fails to fully describe the profile as the flow transitions to being laminar for approximately $2000 < Re < 2700$.

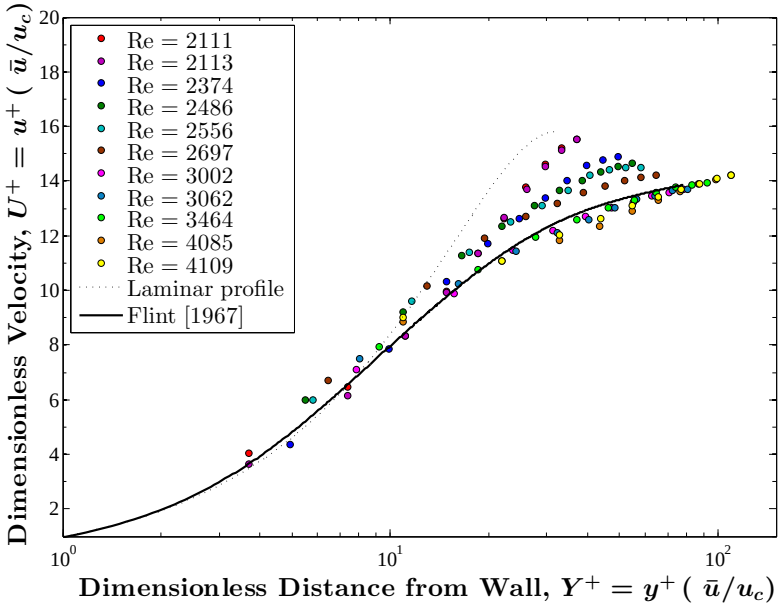

Figure 2.10: *Data of Senecal and Rothfus [1953], compared to profile of Flint [1967], Equation 2.21, and a laminar profile, Equation 2.5.*

2.5 The Friction Factor in Steady Pipe Flow

2.5.1 Introduction

The friction factor is a dimensionless coefficient that quantifies the effect of friction between the boundary and the fluid. The friction factor is closely related to wall shear stress and the frictional velocity.

The Darcy-Weisbach Equation relates friction factor to head loss [Benedict, 1980]:

$$h_f = f\left(\frac{L}{d}\right)\left(\frac{\bar{u}^2}{2g}\right) \tag{2.22}$$

Where h_f is head loss due to friction, f is the Darcy-Weisbach friction factor, L is pipe's length and g is acceleration due to gravity.

The friction factor is related to shear stress through the following expression [Benedict, 1980]:

$$\tau = \frac{f_f \rho \bar{u}^2}{2} \tag{2.23}$$

Where τ is shear stress at the wall and f_f is the Fanning friction factor, $f_f = f/4$.

Figure 2.11 shows experimentally obtained results of Saph and Schoder [1903], Nikuradse [1933] and data collected at the Universities of Princeton and Oregon, as presented by McKeon et al. [2004] for the friction factor within laminar, transitional

and turbulent smooth pipe flow.

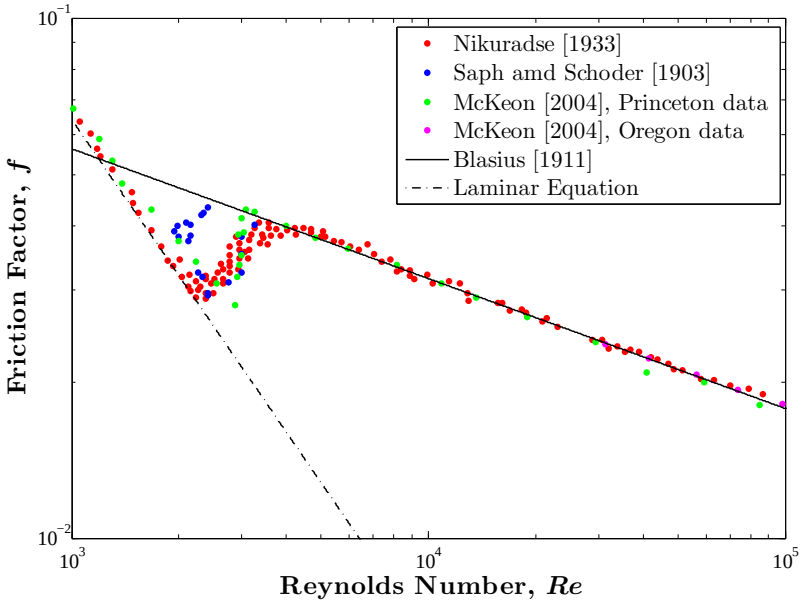

Figure 2.11: *Experimental data of Saph and Schoder [1903], Nikuradse [1933] and McKeon et al. [2004] compared to the analytical Equations for laminar flow, Equation 2.24 and the empirical Equation of Blasius [1911] for turbulent flow, Equation 2.25, for smooth pipe flow.*

2.5.2 Laminar Flow

For laminar flow, Equation 2.22 can be solved analytically to give [Benedict, 1980]:

$$f = \frac{64}{Re} \tag{2.24}$$

Within laminar flow, there is no relationship between pipe roughness and friction factor. Figure 2.11 shows a comparison between Equation 2.24 and experimental data.

2.5.3 Turbulent Flow

For turbulent flow, no analytical solution exists for the friction factor. Hence, Equations for the friction factor within turbulent flow are often empirical.

Blasius [1911] first plotted the relationship between the friction factor and Reynolds Number for smooth pipes, and proposed the following empirical relation-

ship:

$$f = \frac{0.3164}{Re^{0.25}} \tag{2.25}$$

Figure 2.11 shows a comparison between Equation 2.25 and experimental data.

Colebrook [1939] considered various experimental results for friction factors within smooth and rough pipe flow, and proposed the following implicit equation to relate the friction factor to Reynolds Number and pipe roughness:

$$\frac{1}{\sqrt{f}} = -2log\left(\frac{\epsilon/d}{3.7} + \frac{2.51}{Re\sqrt{f}}\right) \tag{2.26}$$

Where ϵ/d is the relative roughness of the pipe, where ϵ is the characteristic size of the roughness.

Moody and Princenton [1944] plotted Equation 2.24 for laminar flow, and Equation 2.26 for various values of ϵ/d within turbulent flow, as shown in Figure 2.12. This chart, known as the 'Moody Diagram', enables simple determination of the friction factor without the need to solve Equation 2.26. For smooth pipe flow, Equation 2.25 provides a reasonable estimate of the friction factor for turbulent flow, as shown in Figure 2.11.

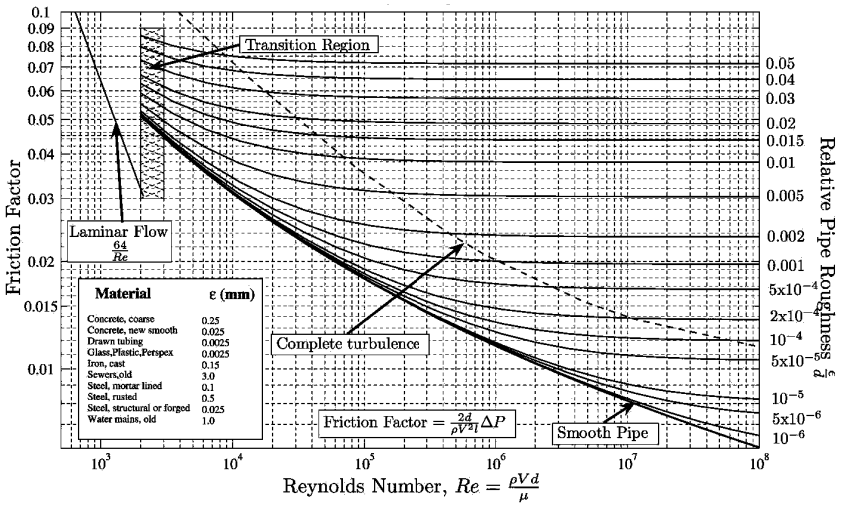

Figure 2.12: *The Moody Diagram [Moody and Princenton, 1944].*

2.5.4 Transitional Flow

From Figure 2.11 it can be seen that within laminar flow the friction factor, shown in log-log co-ordinates, decreases linearly with Reynolds Number. For fully turbulent flow the friction factor still decreases linearly with Reynolds Number, however the

magnitude of the friction factor increases sharply, as the much steeper velocity gradient near the wall within turbulent flow leads to much greater friction. From Figure 2.11 it can also be seen that there is a transitional region where the friction factor transitions from being laminar to turbulent. This region is again approximately linear, and occurs as a linear trend joining the trends for laminar and turbulent flow. However, the start, end and duration of the transition are indeterminate, and are often a function of the specific system in question.

Yang and Joseph [2009] produced a continuous expression for the friction factor for laminar, turbulent and transitional pipe flow through the use of a 'logistic dose' function. They began by considering the data of Nikuradse [1933] and McKeon et al. [2004], as shown in Figure 2.11. Initially they split the data into several regions, and fitted linear 'splines' to the data for each of the regions considered. They then use the logistic dose function to smoothly connect the various splines in a manner consistent with the data. The general form of the logistic dose function used for N number of linear splines is:

$$F_0 = P_1$$

$$F_i = F_{i-1} + \frac{P_{i+1} - F_{i-1}}{[1 + (Re/Re_{c,i})^{-m_i}]^{n_i}}$$

$$f = F_{N-1} = F_{N-2} + \frac{P_N - F_{N-2}}{[1 + (Re/Re_{c,N-1})^{-m_{N-1}}]^{n_{N-1}}} \tag{2.27}$$

Where P_i is a linear spline, $Re_{c,i}$ is the critical Reynolds Number for the linear spline i, F_i is a continuous function and m and n are constants.

Table 2.2 summarised the parameters derived by Yang and Joseph [2009] to produce a continuous function for the friction factor.

i	**Range**	**Spline**	**Equation**	$\boldsymbol{Re_c}$	**m**	**n**
0	$Re < 2320$	P_1	$f = 64/Re$	-	-	-
1	$2320 < Re < 3810$	P_2	$f = 8.3 \times 10^{-5} Re^{0.75}$	2320	50	0.5
3	$3810 < Re < 70000$	P_3	$f = 0.3164 Re^{-0.25}$	3810	15	0.5
4	$70000 < Re < 2000000$	P_4	$f = 0.1537 Re^{-0.185}$	7000	5	0.5
5	$Re > 2000000$	P_5	$f = 0.0753 Re^{-0.136}$	2000000	2	0.5

Table 2.2: *Summary parameters for continuous function for friction factor of Yang and Joseph [2009].*

Figure 2.13 shows a comparison between the continuous function of Yang and Joseph [2009], as defined in Equation 2.27, and experimental data.

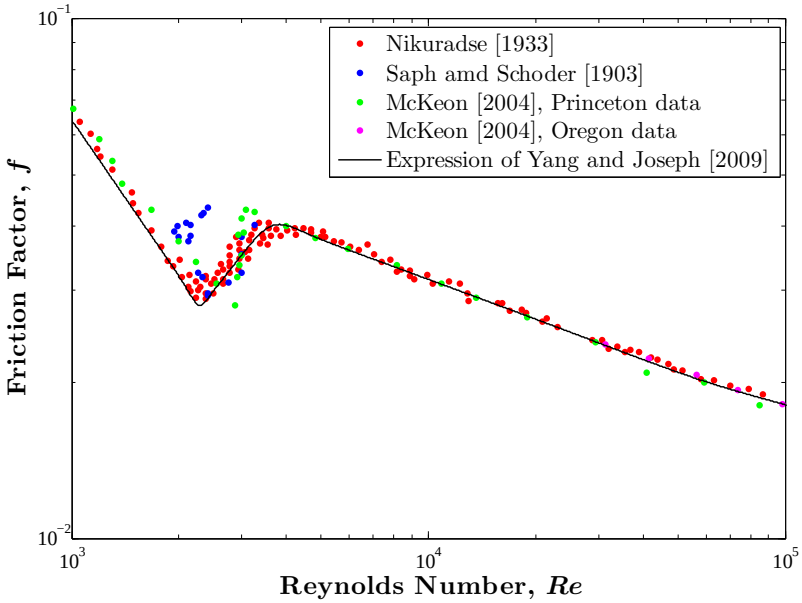

Figure 2.13: *Comparison between continuous function of Yang and Joseph [2009], as defined in Equation 2.27, and experimental data of Saph and Schoder [1903], Nikuradse [1933] and McKeon et al. [2004] compared to Equations 2.24 and 2.25 for smooth pipe flow.*

2.6 Unsteady Pipe Flow

Unsteady pipe flow can be defined as a flow where the discharge is time varying, such that $dQ/dt \neq 0$, and can be split in two general categories; oscillatory and transient.

Oscillatory flow can be defined as a flow where the mean velocity oscillates around a non zero mean value at a certain amplitude and frequency. Transient flow can be defined as a flow that is temporally unsteady, where the flow begins at a initial steady discharge, undergoes a period of unsteady transition, then assumes a final steady discharge. The unsteady transition is usually in a single direction, hence the flow can be categorised as accelerating or decelerating.

Within the present work, the type of unsteady flows being investigated are transient, thus the literature review will focuss on transient flow.

2.7 The Velocity Profile in Unsteady Pipe Flow

Kurokawa and Morikawa [1986] performed one of the first experimental investigations of the velocity profile in transient flow. Velocity profiles were obtained using

a hot film anemometer in a pipe 6 metres long with an internal diameter of 25 mm. Velocity profiles were measured whilst the flow was either accelerated from stationary to a discharge corresponding to a Reynolds Number of $Re = 73000$, or decelerating from the same discharge to stationary. A range of acceleration and deceleration rates were investigated.

Figure 2.14 shows the velocity time series of the flow's velocity at several radial positions across the pipe. Two acceleration rates are shown, 'Acceleration A', where the transient period was approximately 2.5 seconds, and 'Acceleration E', where the period was approximately 25 seconds. These acceleration rates represent the maximum and minimum rates undertaken within the experiment.

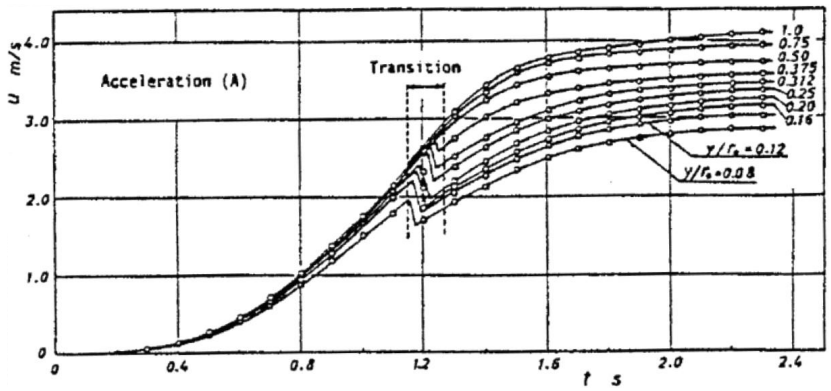

(a) Acceleration A

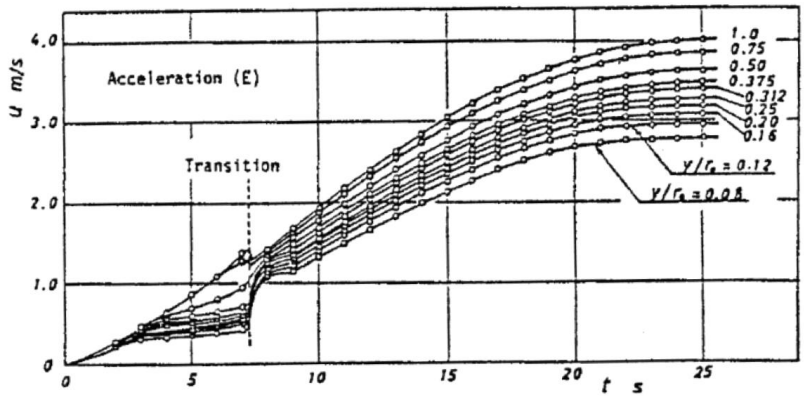

(b) Acceleration E

Figure 2.14: *Time series of velocity at several radial positions for unsteady transients Accelerations A and E. Reproduced from Kurokawa and Morikawa [1986]*

From Figure 2.14 it can be seen that there is a significant difference between the velocity time series of Accelerations A and E. As the flow is being accelerated

from stationary, there is a period of laminar acceleration, then a transition, followed by a period of turbulent acceleration. The point of transition can be seen in both time series as the point at which a sudden change occurs in the velocity magnitude and trend.

For Acceleration A, the transition to turbulence occurs at a relatively large velocity when compared with Acceleration E, and at a much larger velocity than would be expected for typical steady flow. For Acceleration A, a significant portion of the acceleration period is laminar acceleration, with a relatively low variation in velocity at each radial position. At the transition to turbulence, the variation in the velocity across the pipe increases significantly due to a sudden deceleration near the wall.

For Acceleration E, the transition to turbulence occurs at a relatively low velocity when compared with Acceleration A, but still at a higher velocity then would be expected for steady flow. For Acceleration E, the majority of the acceleration period is turbulent acceleration. For the laminar acceleration period the variation in velocity at each radial position is relatively large, compared to Acceleration A, leading up to the transition. In addition, the velocity at the transition is relatively low near the wall and relatively high at the centreline, leading to a high variation in velocity across the pipe. After the transition, the velocity near the wall accelerates and the velocity at the centreline decelerates, leading to a smaller variation in the velocity at each radial position.

Figure 2.15 shows the velocity profile for Accelerations A and E at several times in the acceleration. It can be seen that for Acceleration A, initially the velocity profile is undeveloped, where the majority of the profile is uniform with a small boundary layer. This distribution is maintained to a relatively high velocity, as the acceleration rate is high so the profile does not have time to become fully developed, thus leading to the low variation in velocity for the laminar acceleration period. For Acceleration E, given the slower acceleration leading to a longer period for the profile to develop, the velocity profile develops into a standard velocity profile in the initial acceleration phase. Both Accelerations A and E present non-conventional profiles around the transition to turbulence.

Figure 2.16 shows the velocity profile for Decelerations A and E at several times in the deceleration. It can be seen that turbulent flow is maintained through the whole range. In addition, the profiles are more conventional turbulent profiles than seen in the accelerating cases. This may be because the velocity profile was already fully developed at the start of the test, rather that having to develop within the transient period, as with the accelerating cases. The accelerating cases were

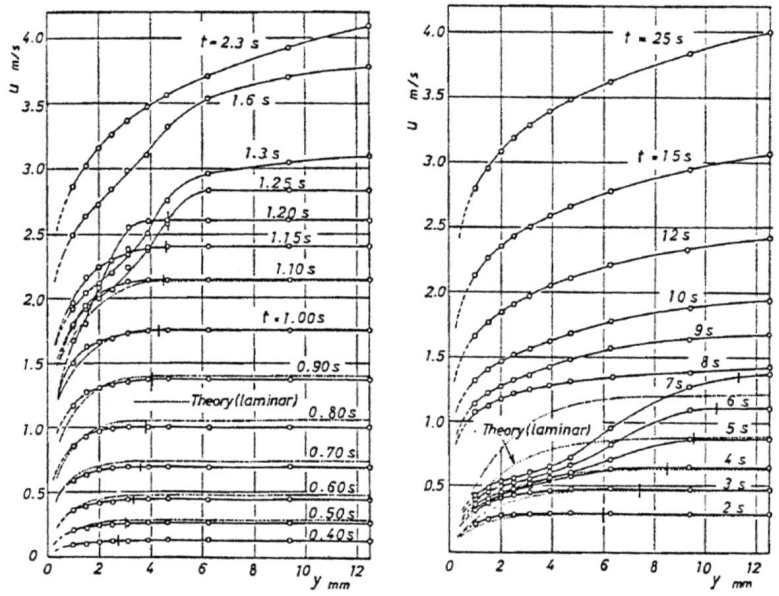

(a) Acceleration A (b) Acceleration E

Figure 2.15: *Velocity profiles at various times for unsteady transients Accelerations A and E. Reproduced from Kurokawa and Morikawa [1986]*

accelerated from stationary, leading to an artificial decrease in variation compared to an accelerating flow that was already fully developed. Furthermore, the transition point between laminar and turbulent flow caused many of the discontinuities in the accelerating profile. Thus, as there is no transition point in the decelerating flow, with turbulent flow maintained throughout the range, there are less discontinuities and hence the profiles are more conventional.

He and Jackson [2000] measured velocity profiles in turbulent transient pipe flow. Velocity profiles were obtained using a three-beam, two-component LDA system in a pipe 9 metres long pipe with an internal diameter of 50.8 mm. The measurements were undertaken upon a fully developed flow at a initial discharge and corresponding cross-section mean velocity, $\bar{u}_0$, and Reynolds Number Re_0, which was accelerated or decelerated to a final discharge and corresponding cross-section mean velocity, $\bar{u}_1$, and Reynolds Number Re_1. Considering transient flow in fully developed turbulent flow has the advantage of removing the effects of the transition to turbulence and the development period of the profile, effects that were seen to influence the results of Kurokawa and Morikawa [1986]. Thus, the only effect that is investigated is the discharge gradient upon the velocity profile.

He and Jackson [2000] consider the discharge gradient in terms of a dimen-

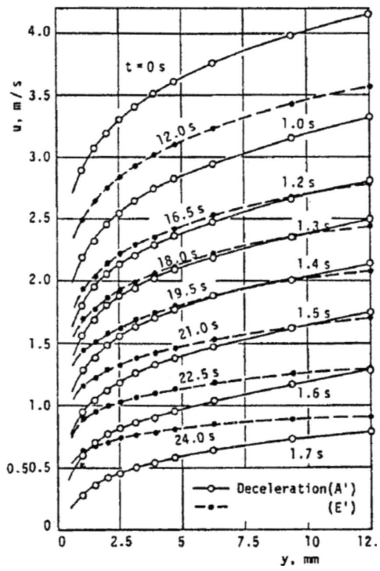

Figure 2.16: *Velocity profiles at various times for unsteady transients Decelerations A and E. Reproduced from Kurokawa and Morikawa [1986].*

sionless ramp rate parameter:

$$\gamma = \frac{d}{u_{*0}} \left(\frac{1}{\bar{u}_0} \frac{d\bar{u}}{dt} \right) \tag{2.28}$$

Where u_{*0} and $\bar{u}_0$ are the initial frictional and cross-sectional mean velocity respectively.

The form of the expression for dimensionless ramp rate, γ, gives some indication as to whether the flow is equivalent to fully developed steady flow at each discrete cross-sectional velocity, a case deemed 'pseudo-steady flow.' If $\gamma < 1$, the the flow will behave as a steady flow at each of its discrete velocities, hence the flow is pseudo-steady. If $\gamma > 1$, then the flow will diverge from pseudo-steady characteristics.

For the main test series, He and Jackson [2000] considered turbulent flow which was accelerated from an initial Reynolds Number of $Re_0 = 7000$ to a final Reynolds Number of $Re_1 = 45200$, and turbulent flow which was decelerated from an initial Reynolds Number of $Re_0 = 45200$ to a final Reynolds Number of $Re_1 = 7000$. For each configuration, several discharge gradients were considered. In further tests they considered other initial and final Reynolds Numbers.

Figure 2.17 shows how the velocity at several radial positions changes for a flow with an initial Reynolds Number $Re_0 = 7000$, which is accelerated to a final Reynolds Number of $Re_1 = 45200$, over a period of 45 seconds, corresponding to a

dimensionless ramp rate of $\gamma = 0.68$.

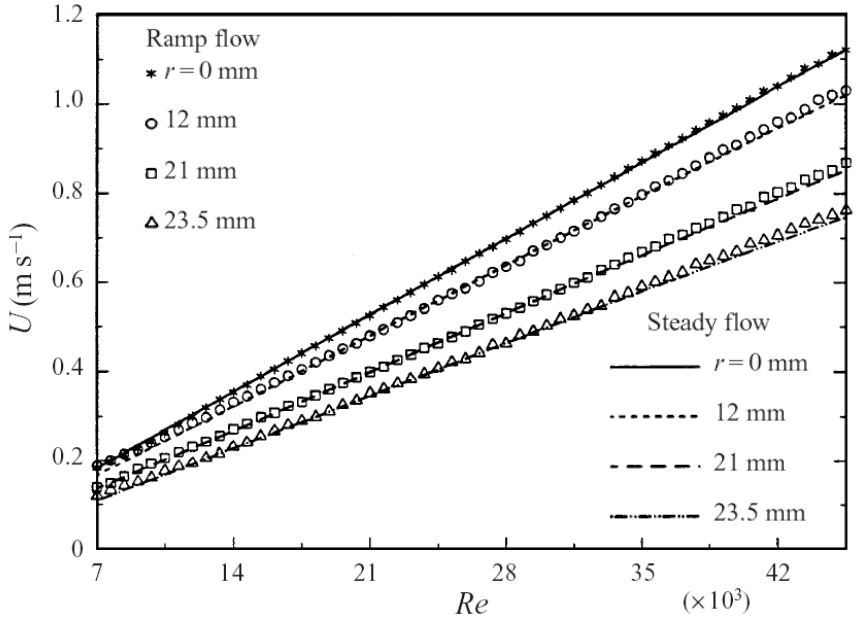

Figure 2.17: *Variation of velocity at several radial positions with Reynolds Number for $\gamma = 0.68$, compared to pseudo-steady predictions. Reproduced from He and Jackson [2000].*

It can be seen that there is no significant difference between the the velocities for $\gamma = 0.68$ and those of pseudo-steady flow.

Figure 2.18 shows the same experimental configuration, but with a acceleration period of 5 seconds, corresponding to a dimensionless ramp rate of $\gamma = 6.1$, where there is a significant deviation from pseudo-steady flow. At the pipe's centreline, after a small initial period, the local velocity is lower than the pseudo-steady value. The magnitude of the difference then decreases to the point that the local velocity of the accelerating flow crosses the local velocity of the pseudo-steady flow. This trend then continues, resulting in the local velocity for the accelerating flow becoming larger than the equivalent velocity for pseudo-steady flow. Towards the end of the acceleration, the local velocity for accelerating flow then approaches the pseudo-steady value. The magnitude of this trend decreases as the flow gets closer to the wall, to the point that at approximately halfway between the centreline and the wall, the local velocity is almost pseudo-steady. Beyond this point, the trend occurs in the opposite direction. Thus, near the wall the local velocity early in the acceleration is higher than the pseudo-steady velocity, and towards the end of the acceleration the local velocity is lower that the pseudo-steady velocity.

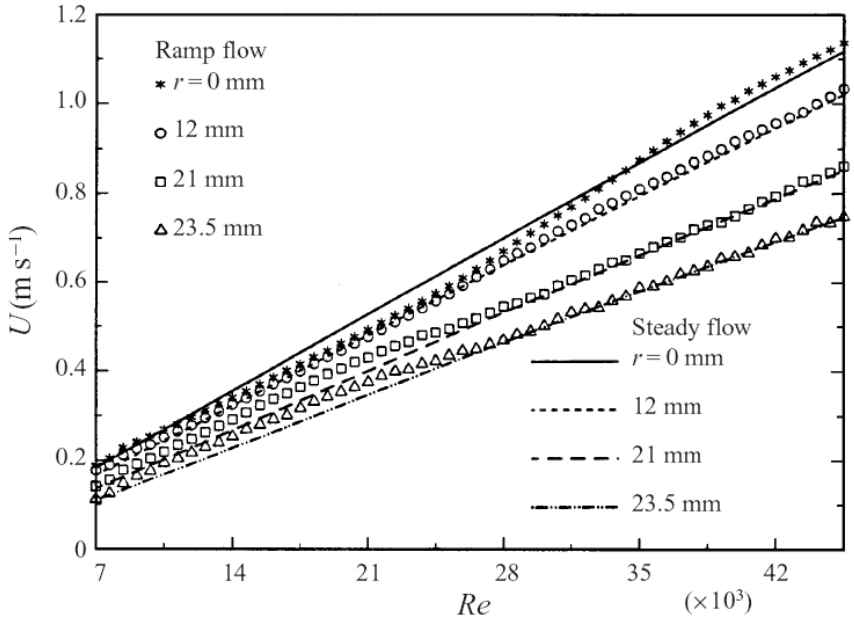

Figure 2.18: *Variation of velocity at several radial positions with Reynolds Number for $\gamma = 6.1$, compared to pseudo-steady predictions. Reproduced from He and Jackson [2000].*

Figure 2.19 shows the velocity profiles for various times throughout the experiment described above for a dimensionless ramp rate of $\gamma = 6.1$, compared to the equivalent pseudo-steady flow velocity profiles at the same time. It can be seen that the main feature of the accelerating flow at this ramp rate is that in the early stages of the acceleration, the core of the profile is more uniform than the equivalent pseudo-steady profile, and the boundary layer gradient is higher. Towards the end of the acceleration, the flow approaches pseudo-steady characteristics.

Greenblatt and Moss [2004] measured velocity profiles in transient pipe flow using a 12 metre long glass pipe with an internal diameter of 48 mm. Velocity profiles were measured in water using a single component LDA device. Greenblatt and Moss [2004] considered transients in terms of a dimensionless ramp rate parameter:

$$G = \frac{d^3}{\nu^2}\left(\frac{d\bar{\bar{u}}}{dt}\right) \tag{2.29}$$

One of the main purposes of the study by Greenblatt and Moss [2004] was to consider discharge gradients higher than had previously been investigated. Greenblatt and Moss [2004] consider three cases, Case 1 where $G = 81 \times 10^6$, Case 2 where $G = 143 \times 10^6$ and Case 3 where $G = 320 \times 10^6$. Even the lowest of these gradients is

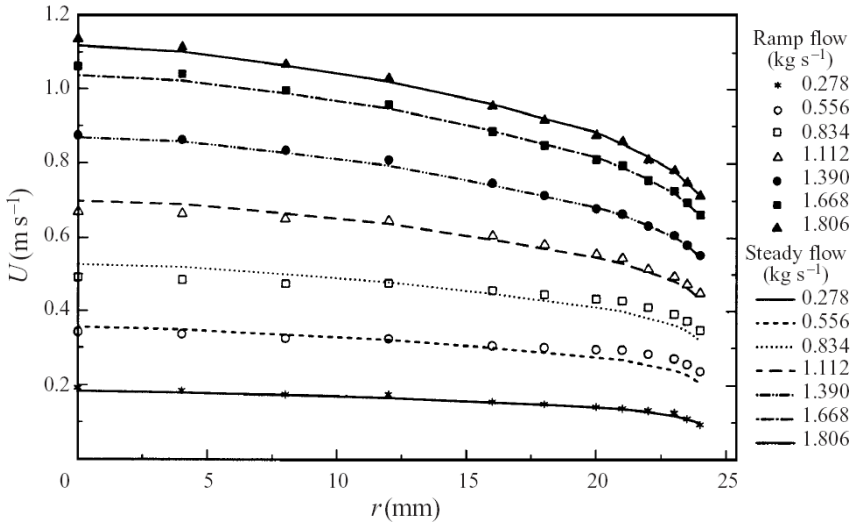

Figure 2.19: *Velocity profiles at various times for $\gamma = 6.1$, compared to pseudo-steady predictions. Reproduced from He and Jackson [2000].*

larger than any gradient considered by Kurokawa and Morikawa [1986] or He and Jackson [2000], who both considered gradients of the order $G < 70 \times 10^6$.

For easy comparison between different gradients, Greenblatt and Moss [2004] considered the time for the discharge gradients in terms of dimensionless time:

$$t^* = \frac{t - t_0}{T} \tag{2.30}$$

Where t^* is dimensionless time, t is time, t_0 is the initial time and T is the transient period.

Figure 2.20 shows the results for the velocity profile at various dimensionless times t^*, for Cases 1 and 3, and it can be seen that, due to the high discharge gradient in both cases, they deviate considerably from the pseudo-steady state. For Case 1, it can be see that early in the discharge transient, at around $t^* < 0.31$, the wake component of the velocity profile, present at around $y^+ > 300$, flattens. At a time $t^* \approx 0.49$ a kink appears in the profile at around $400 < y^+ < 800$. From $0.5 < t^* < 1$, where the transient is starting to relax, the wake component begins to re-form. Greenblatt and Moss [2004] do not present results for Case 2, but comment on its similarity to Case 1. For Case 3, the kink in the profile first occurs sooner in the transient than for Case 1, at around $t^* \approx 0.31$. Furthermore, the kink is also initially closer to the wall, first occurring at around $300 < y^+ < 400$. The propagation of this kink with time for both cases leads to considerable deviation

from the pseudo-steady turbulent core and wake regions, with an increased non-uniformity over the pseudo-steady case. This effect is exaggerated for Case 3, which experiences a much higher discharge gradient.

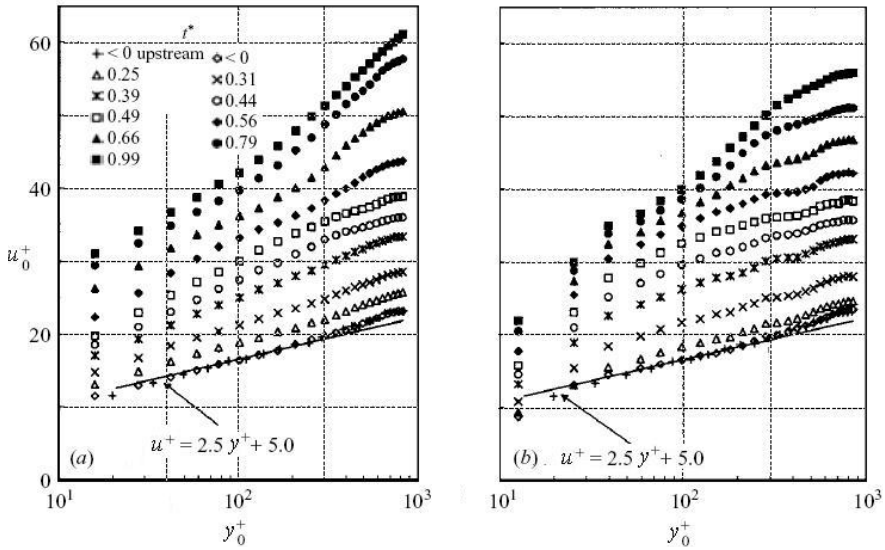

(a) Case 1 (b) Case 3

Figure 2.20: *Velocity profiles at various dimensionless times t^*, for Case 1 (a), where $G = 81 \times 10^6$, and Case 3 (b) where $G = 320 \times 10^6$. Reproduced from Greenblatt and Moss [2004].*

2.8 The Friction Factor in Unsteady Pipe Flow

In addition to measuring the velocity profile in transient flow, Kurokawa and Morikawa [1986] measured the friction factor for the same configurations of transient flow as described in Section 2.7. The friction factor was determined from the difference in pressure between two pressure transducers 6 metres apart.

Figure 2.21 shows the results for the friction factor for accelerations A and E, compared to the pseudo-steady values for the same flow conditions. Both accelerations start with the flow stationary, then accelerate at different rates to a flow rate corresponding to $Re = 73000$. See Section 2.7 for a more detailed description of the discharge configurations for accelerations A and E.

From Figure 2.21 it can be seen that for both accelerations the friction factor is larger than the pseudo-steady values for laminar acceleration. This result can be explained with reference to Figure 2.15, from which it can be seen that for the laminar accelerations A and E, it takes a certain period of time for the velocity

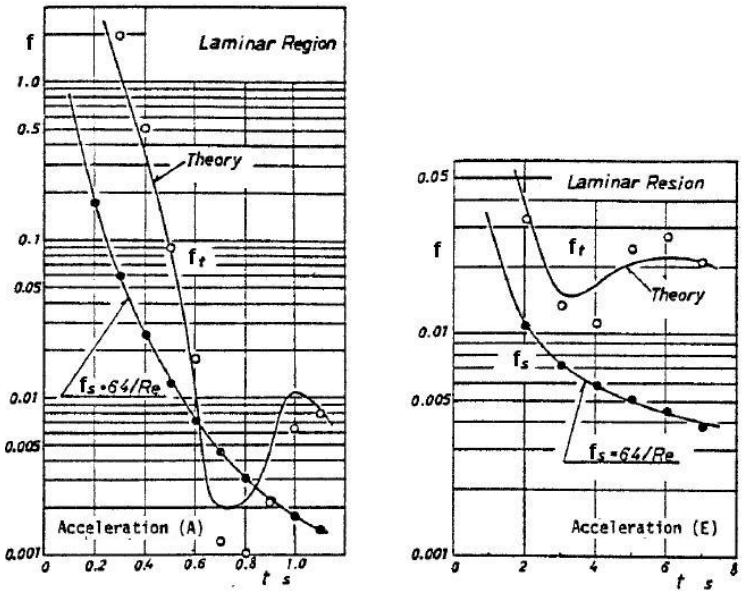

(a) Laminar acceleration range

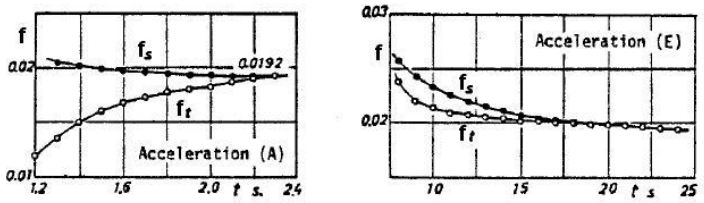

(b) Turbulent acceleration range

Figure 2.21: *Friction factor for unsteady transients Accelerations A and E, f_t, compared to pseudo-steady values, f_s. Reproduced from Kurokawa and Morikawa [1986].*

profile to become fully developed. In this initial period, the profile is more uniform than the parabola that would be expected for fully developed laminar flow. Because of the flatter profile, the velocity near the wall is much higher than for normal laminar flow, thus the shear stress at the wall is higher, leading to a increased value for the friction factor.

From Figure 2.21 it can also be seen that for both accelerations, the friction factor is larger than the pseudo-steady values for turbulent acceleration. Both values tend towards the pseudo-steady value, and acceleration E follows the same trend, but under predicts the pseudo-steady value slightly for the initial period, yet remaining close to pseudo-steady. However, for the majority of acceleration A, the friction factor is considerably different from the pseudo-steady value in both magnitude and

trend. Kurokawa and Morikawa [1986] explain this phenomena by proposing that the discharge gradient for acceleration A is so large that the majority of the pressure head is occupied by the acceleration head. Thus the remaining component of the total head left in the friction head is small, and thus the friction factor is smaller than of pseudo-steady flow.

Figure 2.22 shows the results for the friction factor for Deceleration A compared to the pseudo-steady values for the same flow. Deceleration A begins with the flow fully developed at $Re = 73000$, and the decelerates to the point that the flow is stationary. See Section 2.7 for a more detailed description of the discharge configurations for deceleration A.

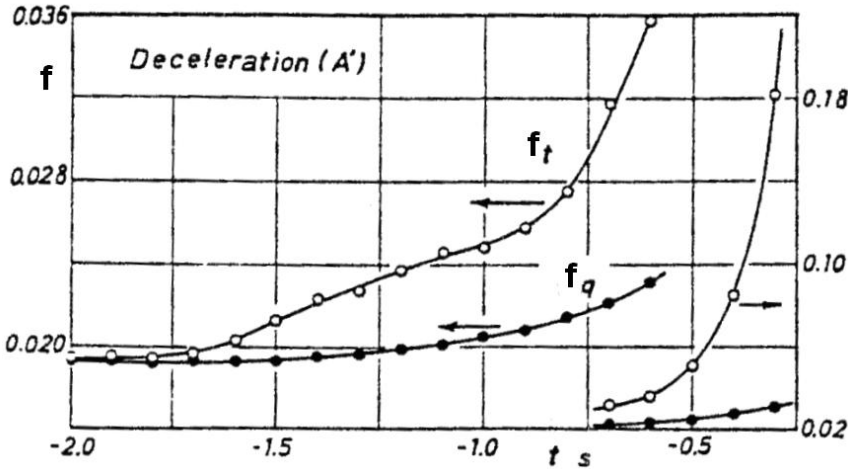

Figure 2.22: *Friction factor for unsteady transient Deceleration A, f_t, compared to pseudo-steady values, f_q. Reproduced from Kurokawa and Morikawa [1986].*

From Figure 2.22 it can be seen that the friction factor is larger than the pseudo-steady values for the whole range. Kurokawa and Morikawa [1986] comment that this trend is the same for Deceleration E, although the magnitude of the results are much close to the pseudo-steady values, however, they do not present these results. Kurokawa and Morikawa [1986] explain the larger magnitude for the friction factor in decelerating flow as the opposite explanation to accelerating flow. Namely, that acceleration head is now negative, thus the friction head becomes larger.

He et al. [2011] measured the wall shear stress, which is closely related to the friction factor, for unsteady turbulent flows for various initial Reynolds Numbers and discharge gradients. Measurements were undertaken using a 23 metre long pipe with an internal diameter of 206 mm. The wall shear stress was measured on the basis of head loss between two pressure trappings approximately 14.2 metres apart.

Figure 2.23 shows the results for the wall shear stress in unsteady flow, and shows both the relationship between the discharge gradient and initial Reynolds Number. The results show two sets of tests, one where the discharge gradient is approximately the same and initial Reynolds Number is varied (a and b), where (a) shows relationship with time and (b) shows relationship with Reynolds Number, and one where the initial Reynolds Number is approximately the same and the discharge gradient is varied, (c and d) where (c) shows relationship with time and (d) shows relationship with Reynolds Number.

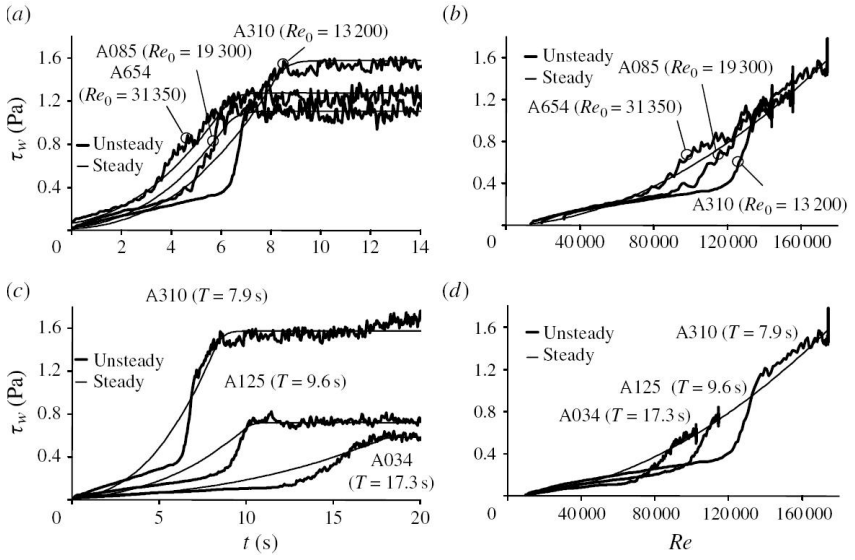

Figure 2.23: *Experimental results for relationship between wall shear stress and both time and Reynolds Number for various discharge gradients and initial Reynolds Numbers. Reproduced from He et al. [2011].*

From Figure 2.23 it can be seen that for all configurations the wall shear stress diverges from the pseudo-steady case. He et al. [2011] propose that all the results show three clear stages of the development of the wall shear stress through a discharge transient. For stage 1, the wall shear stress is initially larger than the pseudo-steady value, but then decreases, crossing the pseudo-steady value. This trend continues until the value for wall shear stress under predicts the pseudo-steady value, considerably in certain cases. Stage 2 is characterised by a rapid increase in the value for wall shear stress, such that the value goes from significantly under predicting the pseudo-steady value, to over predicting it. For stage 3, the wall shear stress tends towards the pseudo-steady value.

From Figure 2.23 (c) and (d) it can be seen that this trend is more pronounced the larger the discharge gradient, whilst Figure 2.23 (a) and (b) show the trend to

be more pronounced the lower the initial Reynolds Number.

He et al. [2011] explain these trends in terms of 'delay and recovery' of the turbulence. For stage 1, in the initial period of acceleration, the under-prediction of the wall shear stress is due to the turbulence over the cross-section remaining 'largely frozen'. In stage 2, the turbulence responds to the transient, and thus the wall shear stress rapidly increases, approaching the pseudo-steady case in stage 3.

He et al. [2008] studied shear stress in transient turbulent flows numerically using a low Reynolds Number $\kappa - \varepsilon$ model. They considered discharge transients for various gradients and initial Reynolds Numbers in fully developed turbulent flow. Figure 2.24 shows the results for the wall shear stress in unsteady flow, and shows both the relationship between the initial Reynolds Number and discharge gradient. The results show two sets of tests, one where the discharge gradient is approximately the same and initial Reynolds Number is varied (Figure 2.24 (a)), and one where the initial Reynolds Number is approximately the same and the discharge gradient is varied (Figure 2.24 (b)).

The numerical results of He et al. [2008] presented in Figure 2.24 show a similar trend to the experimental results of He et al. [2011] presented in Figure 2.23. From Figure 2.24 it can be seen that the unsteady shear stress conforms to the three stages proposed by He et al. [2011]. Further, the enhancement of these effects with both lower initial Reynolds Number and larger discharge gradient and is also shown. He et al. [2008] explain the increase in deviation from the pseudo-steady case with initial Reynolds Number in terms of the thickness of the boundary layer and the the rate of turbulent diffusion. At high Reynolds Numbers, the boundary layer is small, thus minimising the time needed for new turbulent effects to reach the wall. Further, at high Reynolds Numbers turbulent diffusion is high, thus decreasing the time for new turbulent effects to spread. He et al. [2011] gives two reasons why the deviation from the pseudo-steady state increases within higher discharge gradient. Firstly, that the higher the gradient, the higher the inertia in the flow over the pseudo-steady state. Secondly, the higher the discharge gradient, the shorter the transient, and thus, the shorter the time available for the flow to respond to the acceleration before an effective Reynolds Number is obtained.

Jung and Chung [2011] studied the friction factor with accelerating turbulent flows numerically using large-eddy simulations. They considered fully developed flow with an initial and final Reynolds Number of $Re_0 = 7000$ and $Re_1 = 35000$ respectively. The flow was accelerated at a rate of $d\bar{u}/dt = 0.2$, which was the equivalent to the gradient $\gamma = 6.1$ used by He and Jackson [2000].

Figure 2.25 shows their results for the friction factor against Reynolds Num-

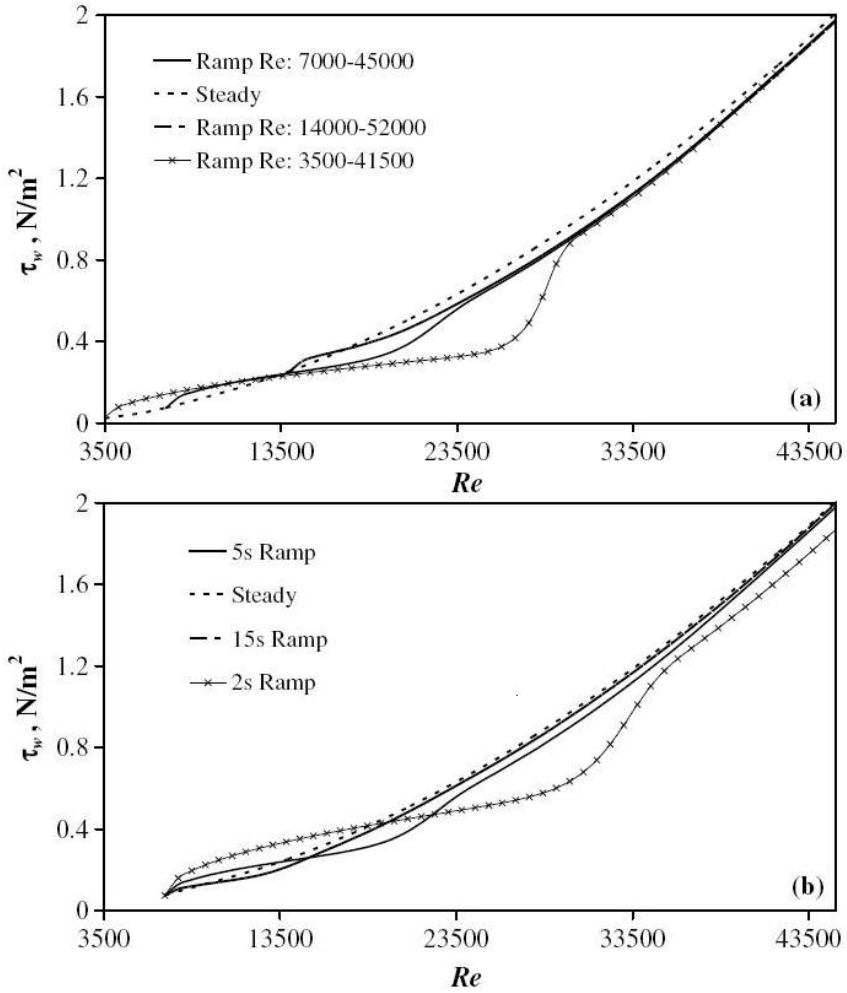

Figure 2.24: *Numerical results for relationship between wall shear stress and both time and Reynolds Number for various discharge gradients and initial Reynolds Numbers. Reproduced from He et al. [2008].*

ber compared to pseudo-steady flow. From Figure 2.25 it can be seen that there is significant divergence between the unsteady and the pseudo-steady case. Initially, the unsteady friction factor over predicts the steady trend. The magnitude of the unsteady friction factor then begins to decrease with Reynolds Number until it crosses, then goes on to under predict the steady case. At $Re \approx 21000$, the friction factor begins to rapidly approach the steady value, which it obtains at $Re \approx 28000$. From this point on the friction factor is pseudo steady. This trend is consistent with the three stages proposed by He et al. [2011].

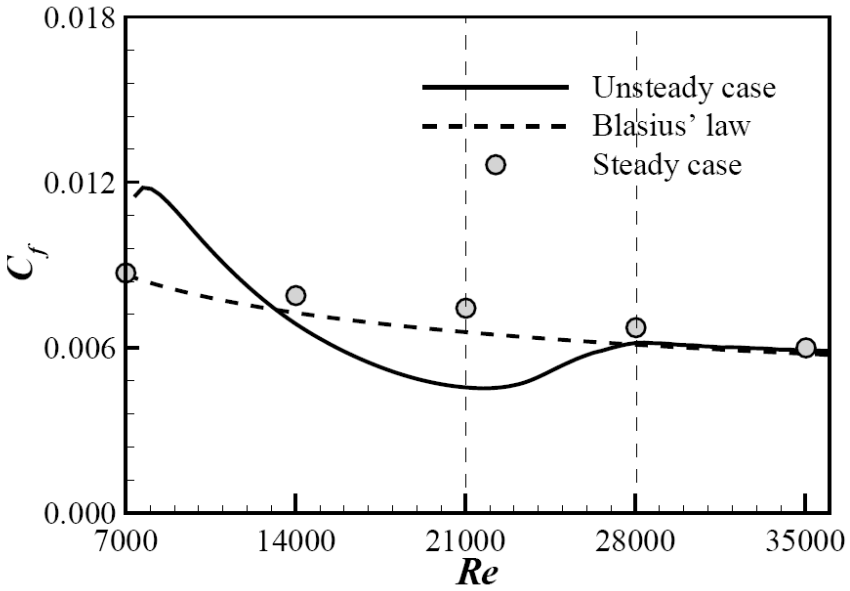

Figure 2.25: *Relationship between friction factor and Reynolds Number compared to pseudo-steady flow. Reproduced from Jung and Chung [2011].*

2.9 The Longitudinal Dispersion Coefficient

2.9.1 The Fickian Dispersion Model

If it is assumed that the radial concentration distribution of a solute, introduced into a flow, is symmetrical about the pipe's centreline, then the radial concentration distribution is given by the following Equation [Taylor, 1953]:

$$\frac{\partial c(r,x,t)}{\partial t} = D_r \left(\frac{\partial^2 c(r,x,t)}{\partial r^2} + \frac{1}{r} \frac{\partial^2 c(r,x,t)}{\partial x^2} \right) - u(r) \frac{\partial c(r,x,t)}{\partial x} \tag{2.31}$$

Where $c(r,x,t)$ is the solute's concentration at position (r,x) and time t, and D_r is the radial diffusion coefficient.

Within laminar flow, the radial diffusion coefficient is equivalent to the molecular diffusion coefficient, such that:

$$D_r = D_m \tag{2.32}$$

Where D_m is the molecular diffusion coefficient.

Within turbulent flow, the radial diffusion coefficient is the total diffusion in the radial direction, as a result of both molecular diffusion and turbulent diffusion; diffusion caused by turbulent fluctuations and transport by turbulent eddies. In this

case, the radial diffusion coefficient is:

$$D_r = D_m + D_t \tag{2.33}$$

Where D_t is the turbulent diffusion coefficient.

Taylor [1953, 1954] undertook some of the first theoretical and experimental investigation of longitudinal dispersion within pipes. He proposed that if a tracer is injected into a pipe flow, after some initial development period, an equilibrium is obtained between longitudinal differential advection and radial diffusion, at which time the cross-sectional mean concentration vs. distance profile will be Gaussian with a variance that increases linearly with time, thus conforming to Fick's second law of diffusion, such that:

$$\frac{\partial c}{\partial t} = D_{xx}\frac{\partial^2 c}{\partial x^2} - \bar{u}\frac{\partial c}{\partial x} \tag{2.34}$$

Where c is the cross-sectional mean concentration and D_{xx} is the effective longitudinal dispersion coefficient, analogous to Fick's molecular diffusion coefficient [Taylor, 1953].

Equation 2.34 is known as the advection dispersion equation. A standard solution to Equation 2.34 is [Rutherford, 1994]:

$$c(x,t) = \frac{M}{A\sqrt{4\pi D_{xx} t}} \exp\left[-\frac{(x-\bar{u}t)^2}{4D_{xx}t}\right] \tag{2.35}$$

Where A and M are cross-sectional area and mass of tracer respectively.

The time at which the Fickian model is valid is approximately equivalent to the time required for the tracer to become cross-sectionally well mixed. For laminar flow, Taylor [1953] estimated the time to be:

$$\frac{L_I}{\bar{u}} \gg \frac{a^2}{3.8^2 D_m} \tag{2.36}$$

Where L_I is the length along the pipe's longitudinal axis from injection. Sayre [1968] considered the development period in open channel flow, and found that the growth of the concentration profile's variance was linear, and thus conforms to Fick's law, at:

$$T_F = \frac{D_r t}{h^2} \approx 0.5 \tag{2.37}$$

Where T_F is a dimensionless time after which Fick's law applies and h is the flow depth of the open channel.

Lee [2004] considers the development period for pipe flow, and notes that the

Fickian model 'works well' for times:

$$T_F = \frac{D_r t}{a^2} > 0.5 \tag{2.38}$$

A result very similar to that of Sayre [1968].

Despite the fact that Sayre found the growth of the variance to be linear at $T_F \approx 0.5$, he notes that concentration profiles were still skewed well beyond this point. His numerical tests were only conducted up to $T_F = 3$, at which point his profiles were still not fully Gaussian. Rutherford [1994] notes that 'extrapolating his results one might expect tracer concentrations to become Gaussian at about $T_F = 10$' [Rutherford, 1994].

Taylor [1954] notes that the skewness of concentration profiles in turbulent pipe flow is small when:

$$\bar{u}t \gg \sqrt{4D_{xx}t} \tag{2.39}$$

Taylor also notes that within 'most cases' of turbulent pipe flow, this should be equivalent to a distance of approximately:

$$L_I \approx 100a \tag{2.40}$$

However, Taylor's analysis of turbulent pipe flow only considers highly turbulent flow, where the laminar sub-layer and buffer zone are assumed to be very small, and thus are neglected from the analysis.

2.9.2 The Longitudinal Dispersion Coefficient within the Development Zone

In the previous section it was proposed that the Fickian dispersion model given in Equation 2.34 is only valid after some initial time has lapsed. After this time, the variance of the concentration profiles is linear with respect to time and thus the Fickian dispersion model can be assumed. After the initial period, the longitudinal dispersion coefficient is constant with respect to distance and corresponding time. However, a further period is still required for the profiles to become fully Gaussian, owing to tracer being retained by the flow's laminar sub-layer [Rutherford, 1994].

Within the initial period, the longitudinal dispersion coefficient is not constant with respect to distance or corresponding time, increasing with distance from the point of injection.

Gill and Sankarasubramanian [1970] showed that Equation 2.34 can be 'use-

ful' for all times after injection, provided that the longitudinal dispersion coefficient is allowed to vary with time. Under this assumption, they propose the time dependent longitudinal dispersion coefficient for $0 < T_F < 0.5$ as:

$$D_{xx}(t) = D_{xx}\left[\, 1 - 768 \sum \frac{J_3(\lambda_n)J_2(\lambda_n)}{\lambda_n^5[J_0(\lambda_n)]^2} exp\left(\, -\lambda_n^2 \frac{D_r t}{a^2}\right)\right] \tag{2.41}$$

Where $D_{xx}(t)$ is the longitudinal dispersion coefficient as a function of time, D_{xx} is the fully developed longitudinal dispersion coefficient, independent of time, towards which the time dependent dispersion coefficient tends, $J_n(x)$ is a Bessel function of the first kind, of order n, and λ_n is root of $J_1(x)$.

Lee [2004] showed that Equation 2.41, which is complex to use, could be approximated to '99.94 %' by the following simple expression:

$$D_{xx}(t) = D_{xx}\left[\, 1 - exp\left(\, -\frac{t}{\tau_0}\right)\right] \tag{2.42}$$

Where $\tau_0 = a^2/16D_r$.

Equations 2.41 and 2.42 both refer the instantaneous dispersivity of a flow. When considering an up and a downstream concentration profile, the longitudinal dispersion coefficient obtained encompasses the mean dispersivity of the flow between the two locations. If both concentration profiles are measured after the initial period, there would be no distinction between the instantaneous and time averaged longitudinal dispersion coefficient, as after this point the longitudinal dispersion coefficient is constant with distance. However, if one or both the concentration profiles are measured within the initial period, then the longitudinal dispersion coefficient needs be calculated as the mean value of all of the possible instantaneous values over that period, as the values will change with time in the initial period before the longitudinal dispersion coefficient becomes steady.

The mean longitudinal dispersion coefficient over a period of time can be considered as:

$$D_{xx} = \frac{1}{t_2 - t_1} \int_{t_1}^{t_2} D_{xx}(t)dt \tag{2.43}$$

Where t_1 and t_2 are the start and end time respectively of the time period over which the longitudinal dispersion coefficient is averaged.

2.10 Estimating the Longitudinal Dispersion Coefficient from Experimental Data

2.10.1 The Method of Moments

The longitudinal dispersion coefficient can be obtained by considering experimentally obtained concentration vs. distance profiles in terms of their moments in the direction of the flow [Rutherford, 1994]. The general expression for the moments of a spatial tracer profile is [Rutherford, 1994]:

$$M_n(t) = \int_{-\infty}^{\infty} x^n c(x,t) dx \tag{2.44}$$

Where $M_n(t)$ is the nth spatial moment at time t and $c(x,t)$ is the cross-sectional mean concentration at time t and position x.

To determine the longitudinal dispersion coefficient, three moments are required, where $n = 0$, 1 and 2. Such that:

$$M_0(t) = \int_{-\infty}^{\infty} c(x,t) dx \tag{2.45}$$

$$M_1(t) = \int_{-\infty}^{\infty} x c(x,t) dx \tag{2.46}$$

$$M_2(t) = \int_{-\infty}^{\infty} x^2 c(x,t) dx \tag{2.47}$$

From this, the area of the spatial tracer profile can be obtained as:

$$A_p = M_0 \tag{2.48}$$

Where A_p is the area of the tracer profile.

The centroid of the spatial tracer profile can be obtained as:

$$\bar{x} = \frac{M_1}{M_0} \tag{2.49}$$

Where $\bar{x}$ is the centroid of the tracer profile.

And the variance of the spatial profile can be obtained as:

$$\sigma_x^2(t) = \frac{M_2}{M_0} - \bar{x}^2 \tag{2.50}$$

Where $\sigma_x^2(t)$ is the profile's spatial variance at time t.

On the basis of the spatial variance, the longitudinal dispersion coefficient can be obtained through:

$$D_{xx} = \frac{1}{2}\frac{d\sigma_x^2(t)}{dt} \tag{2.51}$$

Experimental concentration data is most conveniently recorded as concentration vs. time data at some fixed location. Thus, it is most convenient to consider the concentration profile in terms of its temporal variance. In a similar manner to the equations above, the temporal moments of a tracer profile can be considered as [Rutherford, 1994]:

$$M_n(x) = \int_{-\infty}^{\infty} t^n c(t,x)dt \tag{2.52}$$

Where $M_n(x)$ is the nth temporal moment at position x and $c(t,x)$ is the concentration at time t and position x.

From this it can be seen that the temporal moments of interest are:

$$M_0(x) = \int_{-\infty}^{\infty} c(t,x)dt \tag{2.53}$$

$$M_1(x) = \int_{-\infty}^{\infty} tc(t,x)dt \tag{2.54}$$

$$M_2(x) = \int_{-\infty}^{\infty} t^2 c(t,x)dt \tag{2.55}$$

The area of the temporal tracer profile can be obtained through Equation 2.48.

The centroid of the temporal tracer profile can be obtained as:

$$\bar{t} = \frac{M_1}{M_0} \tag{2.56}$$

Where $\bar{t}$ is the centroid of the tracer profile.

And the variance of the temporal profile can be obtained as:

$$\sigma_t^2(x) = \frac{M_2}{M_0} - \bar{t}^2 \tag{2.57}$$

Where $\sigma_t^2(x)$ is the profile's temporal variance at position x.

By assuming the frozen cloud approximation, the assumption that no dispersion has take place in the time it takes for the solute colud to pass a chosen site, on the basis of the temporal variance the longitudinal dispersion coefficient can be obtained as [Rutherford, 1994]:

$$D_{xx} = \frac{\bar{u}^2}{2}\frac{d}{dt}[\sigma_t^2(x)] \tag{2.58}$$

2.10.2 Routing Procedures

Once an estimate of the longitudinal dispersion coefficient has been obtained through the method of moments, the estimate of the longitudinal dispersion coefficient can be improved by optimising through a routing procedure, with respect to experimental data [Rutherford, 1994]. A routing procedure predicts a downstream concentration profile on the basis of the experimentally obtained upstream concentration profile, the travel time (difference between centroid of each temporal concentration profile) and the estimate of the longitudinal dispersion coefficient. The values of the longitudinal dispersion coefficient and travel time obtained through the method of moments are used as initial values, which can then be optimised to best fit the downstream experimental data. One such method is [Rutherford, 1994]:

$$c(x_2, t) = \int_{-\infty}^{\infty} \frac{c(x_1, \lambda)\bar{u}}{\sqrt{4\pi D_{xx}\bar{t}}} \exp\left[-\frac{\bar{u}^2(\bar{t} - t + \lambda)^2}{4D_{xx}\bar{t}}\right] d\lambda \tag{2.59}$$

Where λ is an integration variable, or pseudo time.

This method assumes the frozen cloud approximation, and effectively takes each element of the upstream profile, transfers it down stream in accordance with advection, and distributes it assuming a Gaussian profile. Through superposition, the downstream profile can be obtained as the sum of each of the downstream profiles created from each upstream element.

The use of a routing procedure, such as Equation 2.59, has been shown to improve the estimate of the longitudinal dispersion coefficients from experimental data, and should also reduce the effects of non-Fickian behavior of the tracer profile from the calculation [Rutherford, 1994].

2.11 Experimental Findings for the Longitudinal Dispersion Coefficient in Steady Pipe Flow for $2000 < Re < 50000$

Fowler and Brown [1943] recorded tracer data that was used by Levenspiel [1958] to obtain the longitudinal dispersion coefficient for $2000 < Re < 100000$. Their measurements were made on 1.5 to 32 metre lengths of glass pipe with internal diameters of 3.15 and 7.95 mm. A flow of water was established within the pipe, which was replaced with a salt solution (0.139 $NNaCl$) at a given time. A longitudinal dispersion coefficient could be obtained from the experiment by analysing how the leading edge of the salt solution mixed with the trailing edge of the water. For each run, small beakers of fluid were collected at a recorded time. By titrating the solution in the beakers, the salt content could be determined, from which the ratio of fluids could be obtained, and thus a measure of how the two fluids were mixing could be proposed.

Taylor [1954] measured the longitudinal dispersion coefficient using a 16.3 metre stainless steel pipe with an internal diameter of 9.53 mm. Salt was injected into the flow of water, and concentration vs. time curves were recorded at 3.22 and 16.3 metres respectively by using conductivity probes to produce a voltage proportional to the concentration of salt in the flow.

Keyes [1955] measured the longitudinal dispersion coefficient in a 2.438 metre glass pipe with an internal diameter of 15.5 mm. The longitudinal dispersion coefficient was obtained by measuring the concentration of CO_2 gas injected into air with a thermal conductivity cell.

Flint and Eisenklam [1969] measured the longitudinal dispersion coefficient in a 23.45 metre brass pipe with an internal diameter of 27.7 mm. The longitudinal dispersion coefficient was obtained by measuring the concentration of gas (either C_2H_4, A or He) injected into oxygen free N_2. The concentration of the injected gas was measured using a Katharometer, a thermal conductivity device.

The results of Fowler and Brown [1943], Taylor [1954], Keyes [1955] and Flint and Eisenklam [1969] are shown in Figure 2.26.

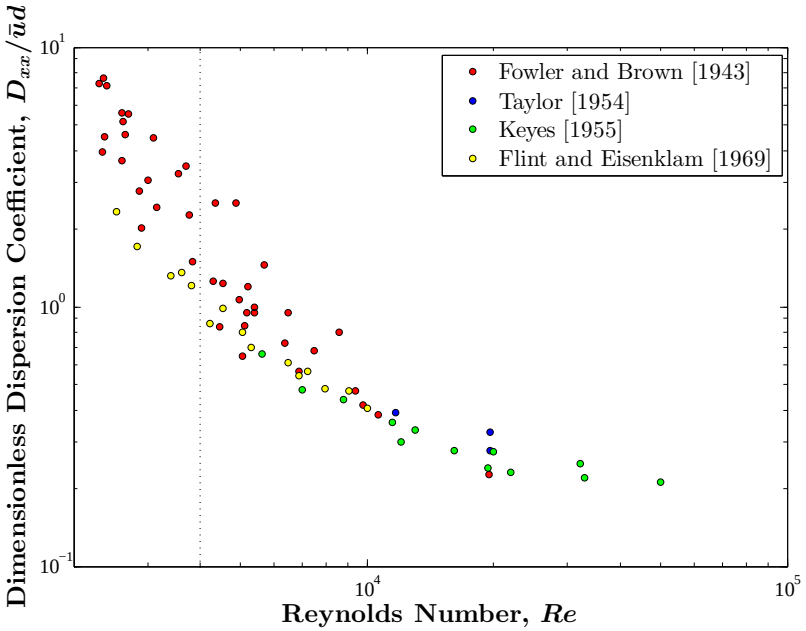

Figure 2.26: *Comparison between the experimental data of Fowler and Brown [1943], Taylor [1954], Keyes [1955] and Flint and Eisenklam [1969].*

2.12 Predicting the Longitudinal Dispersion Coefficient within Steady Pipe Flow

2.12.1 Taylor's Equations for the Longitudinal Dispersion Coefficient

Laminar Flow

Equation 2.31 gives the radial concentration distribution of a solute introduced into a flow. Taylor [1953] solved Equation 2.31 analytically by assuming the velocity profile as the analytical laminar velocity profile, as given in Equation 2.5, and the radial diffusion coefficient as being equivalent to molecular diffusion, i.e. $D_r = D_m$. Through this, Taylor showed that within laminar flow, the longitudinal dispersion coefficient can be analytically obtained as:

$$D_{xx} = \frac{a^2 \bar{u}^2}{48 D_m} \tag{2.60}$$

Equation 2.60 assumes that tracer is cross-sectionally well mixed, such that the following condition had been obtained:

$$T = \frac{D_m t}{a^2} > 0.5 \tag{2.61}$$

For the initial time period, Lee [2004] proposed the longitudinal dispersion coefficient within laminar flow as:

$$D_{xx}(t) = \frac{a^2 \bar{u}^2}{48 D_m} \left[1 - exp\left(-\frac{t}{\tau_0} \right) \right] \tag{2.62}$$

Where $\tau_0 = a^2/16D_m$.

Turbulent Flow

For turbulent flow, Taylor [1954] considered the differential equation governing the radial concentration distribution in the form:

$$\frac{\partial}{\partial r}\left(D_r r \frac{\partial c}{\partial r} \right) = r\left(u_x(p)\frac{\partial c}{\partial x} + \frac{\partial c}{\partial t} \right) \tag{2.63}$$

Taylor assumed the radial diffusion coefficient as the turbulent diffusion coefficient, such that:

$$D_r = D_t \tag{2.64}$$

Taylor defined the turbulent diffusion coefficient by considering it in terms of Reynolds analogy, i.e. the assumption that the transfer of matter, heat and momentum are analogous, such that:

$$D_r = \frac{\tau_t}{\rho \frac{\partial u_x(p)}{\partial r}} \tag{2.65}$$

Where:

$$\tau_t = \tau p \tag{2.66}$$

Where τ_t is the turbulent shear stress.

Taylor assumed a 'universal' velocity distribution, of the form:

$$\frac{u_c - u_x(p)}{u_*} = f(p) \tag{2.67}$$

Where $f(p)$ is a geometric relationship for the velocity distribution as a function of dimensionless position p.

Taylor derived the values of $f(p)$ as the mean value of the data of Stanton and Pannell [1953] and Nikuradse [1932], as shown in Figure 2.27. For the range 0.9

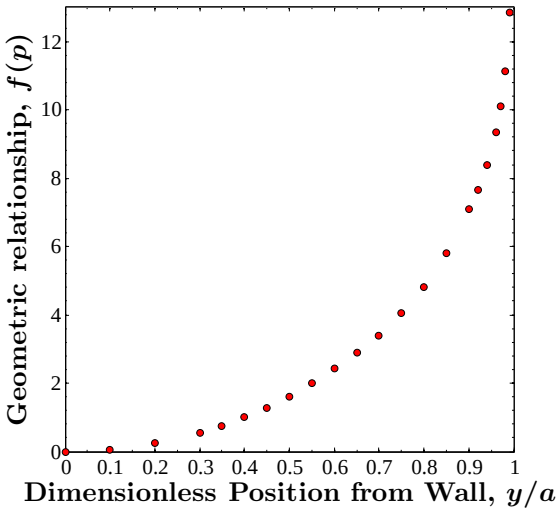

Figure 2.27: *Relationship between dimensionless position p and geometric relationship for the velocity distribution f(p) as derived by Taylor [1954], as the mean values of the data of Stanton and Pannell [1953] and Nikuradse [1932].*

$< p < 1$, Taylor proposes the following relationship for the function $f(p)$:

$$f(p) = 1.35 - 2.5ln(1-p) \tag{2.68}$$

For $0 < p < 0.9$, Taylor relies upon the experimental values, as shown in Figure 2.27.

In addition, Taylor proposes a relationship for the maximum velocity as:

$$u_c = \bar{u} + (4.25u_*) \tag{2.69}$$

Taylor's velocity profile can be defined by using Equation 2.67 in conjunction with the relationship $f(p)$, as shown in Figure 2.27, and the maximum velocity as defined by Equation 2.69. A comparison between Taylor's velocity profile and the data of Durst et al. [1995] is shown in Figure 2.28.

The data of Stanton and Pannell [1953] and Nikuradse [1932], which Taylor used to derive his velocity profile, are both highly turbulent. Thus, Taylor's profile neglects a laminar sub-layer and buffer zone, as shown in Figure 2.28.

Taylor used his definition of the radial diffusion coefficient and velocity profile to solve Equation 2.63 to give the following expression for the longitudinal dispersion

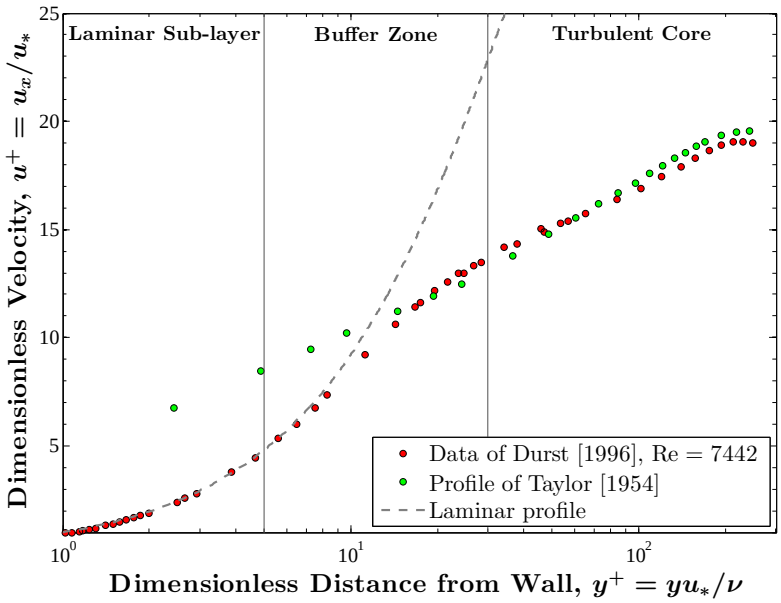

Figure 2.28: *Comparison between the experimental data of Durst et al. [1995] the profile of Taylor [1954], as defined by Equation 2.67 using values of $f(p)$ shown in Figure 2.27, and a laminar profile, as defined by Equations 2.5.*

coefficient within turbulent flow.

$$D_{xx} = 10.1au_* \tag{2.70}$$

Figure 2.29 shows a comparison between the prediction made by Equation 2.70 and experimental data.

From Figure 2.29 it can be seen that because Taylor's velocity profile neglects a laminar sub-layer and buffer zone, his expression for the longitudinal dispersion coefficient is only valid for $Re > 20000$, the portion of the range where the laminar sub-layer and buffer zone become negligible.

2.12.2 Subsequent Work on Predicting the Longitudinal Dispersion Coefficient for $2000 < Re < 50000$

From Figure 2.29 it can be seen that the expression for the longitudinal dispersion coefficient of Taylor [1954] fails to predict experimental data for $Re < 20000$, due to the influence of the laminar sub-layer and buffer zone upon the longitudinal dispersion coefficient for this region.

Tichacek et al. [1957] revisited Taylor's analysis by solving Equation 2.63 using the experimental velocity profiles of Deissler [1950] and Reichardt [1951]. In

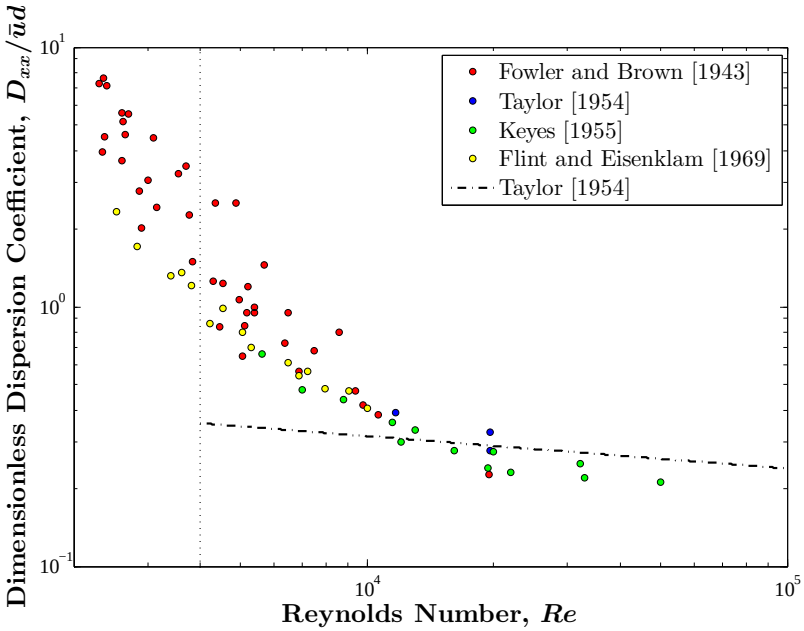

Figure 2.29: *Comparison between the experimental data of Fowler and Brown [1943], Taylor [1954], Keyes [1955], Flint and Eisenklam [1969] and the expression of Taylor [1954], as defined by Equation 2.70.*

addition, they include the contribution to radial diffusion of molecular diffusion, such that:

$$D_r = D_t + D_m \tag{2.71}$$

By assuming that the turbulent transport of mass is equivalent to the turbulent transport of momentum, from Equation 2.71, Tichacek et al. [1957] show that the radial diffusion coefficient can be considered as:

$$D_r = -\frac{\tau_t}{\rho}\frac{\partial r}{\partial u_x} - \nu\left(1 - \frac{1}{S_c}\right) \tag{2.72}$$

Where ν and S_c are the kinematic viscosity and the Schmidt number respectively. The Schmidt number quantifies the ratio of viscous to molecular transport, and is thus defined as:

$$Sc = \frac{\nu}{D_m} \tag{2.73}$$

By solving Equation 2.63 with the experimental velocity profiles of Deissler [1950] and Reichardt [1951], and by assuming the radial diffusion coefficient as defined in Equation 2.72, Tichacek et al. [1957] propose the following expression for the

longitudinal dispersion coefficient:

$$\frac{D_{xx}}{\bar{u}d} = \frac{2}{f_f}\int_0^1 \left[\frac{1}{-\frac{\partial p}{\partial(u_x/\bar{u})} - \frac{32}{Re}\left(1 - \frac{1}{Sc}\right)}\right]\frac{dp}{p}\left[\int_0^p \left(\frac{u_x}{\bar{u}} - 1\right)dp'\right]^2 \tag{2.74}$$

Flint and Eisenklam [1969] revisited Taylor's analysis by reconsidering his Equation, as defined in Equation 2.70, in the form:

$$D_{xx} = Gau_* \tag{2.75}$$

Where G is a constant.

Taylor's analysis found G to be constant with respect to Reynolds Number and equal to 10.1. However, since Taylor's analysis assumes a highly turbulent velocity profile, the values of G are only valid for $Re > 20000$. Flint and Eisenklam [1969] solved Equation 2.63 using the velocity profiles of Flint [1967], a profile which does include a laminar sub-layer and buffer zone, as defined in Equations 2.16, 2.17 and 2.21. From this, they computed values of G between $2500 < Re < 100000$, and thus proposed a model for the longitudinal dispersion coefficient within this range.

Ekambara and Joshi [2003] solved Equation 2.63 using a low Reynolds Number $\kappa - \varepsilon$ CFD model. Within the model, the radial diffusion coefficient included the contribution of molecular diffusion, as in Equation 2.71. The molecular and turbulent radial diffusion coefficient are defined as:

$$D_m = \frac{\nu}{Sc} \tag{2.76}$$

And:

$$D_t = \frac{\nu_t}{Sc_t} \tag{2.77}$$

Where ν_t and Sc_t are the turbulent kinematic viscosity and turbulent Schmidt number respectively. Within the model, the turbulent Schmidt number is assumed to be 0.9. The turbulent kinematic viscosity is obtained through the CFD model as a function of the turbulent kinetic energy per unit mass, κ, and the turbulent energy dissipation rate per unit mass, ε.

Figure 2.30 shows a comparison between experimental data and the models of Taylor [1954], Tichacek et al. [1957], Flint and Eisenklam [1969] and Ekambara and Joshi [2003].

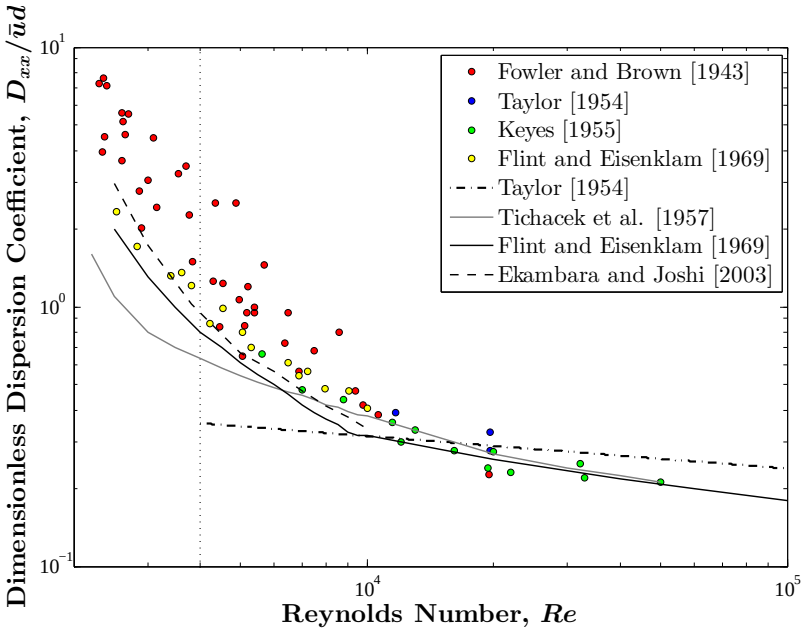

Figure 2.30: *Comparison between experimental data and the models of Taylor [1954], Tichacek et al. [1957], Flint and Eisenklam [1969] and Ekambara and Joshi [2003].*

2.13 The Zonal Model for Predicting the Longitudinal Dispersion Coefficient

2.13.1 Introduction

Within Section 2.12, several methods for predicting the longitudinal dispersion coefficient were discussed. This section will consider a further method for predicting the longitudinal dispersion coefficient, a 'zonal model', which will be considered in some detail as this is the method that will be adopted within the present work to predict the longitudinal dispersion coefficient on the basis of a given velocity distribution and radial diffusion coefficient.

The zonal model predicts the longitudinal dispersion coefficient by dividing the flow into zones, each of which is considered well mixed with its own corresponding concentration and mean velocity. In addition, the diffusion exchange between the zones is accounted for. The zonal model first appeared as a two zone model [Thacker, 1976; Smith, 1982; Chikwendu and Ojiakor, 1985]. An example of the two zone model, for simplicity considered in open channel flow, is given in Figure 2.31, where h_1 and h_2 and u_1 and u_2 are the thickness and mean velocity for zones 1 and 2 respectively. D_y is the diffusion coefficient between zones, accounting for exchange

in the y direction, and in this example is analogous to the radial diffusion coefficient D_r for pipe flow. The velocity terms u_1 and u_2 are the zonal mean velocity and thus are the mean velocities of zone 1 and 2 respectively.

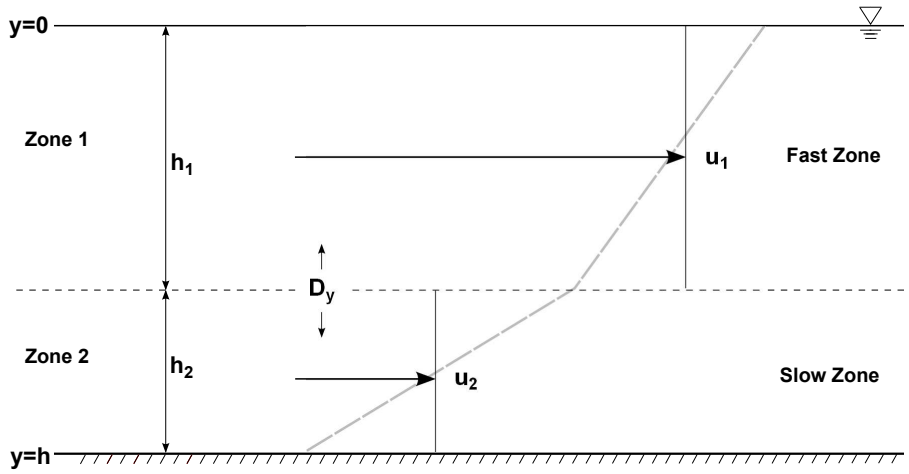

Figure 2.31: *Two zone model within open channel flow*

For the two zone model, the longitudinal dispersion coefficient can be obtained through Chikwendu [1986]:

$$D(2)_{xx} = \frac{(h^2)(q_1 + q_2)(q_1 q_2)^2(u_1 - u_2)^2}{2D_y} \tag{2.78}$$

Where $q_1 = h_1/h$ and $q_2 = h_2/h$, where h is the height of the flow. Within this expression, the term $u_1 - u_2$ accounts for the effect of differential advection, as the term quantifies the difference between the mean velocity of the fast and slow zones.

The two zone model calculates the longitudinal dispersion coefficient by considering the difference in mean velocity between the fast and the slow zone and the vertical exchange between the zones, hence the differential advection term in the expression is the mean velocity of zone 1, the fast zone, less the mean velocity of zone 2, the slow zone. The model can be further extended into a three zone model, as shown in Figure 2.32.

In the case where three zones are considered, the expression becomes more complex. It is now necessary to consider a particular point j, directly below the zone corresponding to it's number (i.e. for j=2, j is a point directly below zone 2). For the three zone model two cases are considered, $j = 1$ and $j = 2$, as there is no flow below zone 3. For $j = 1$ the fast zone is zone 1, the only zone above point j, and the slow zone is zones 2 and 3, the two zones below point j. For this case the

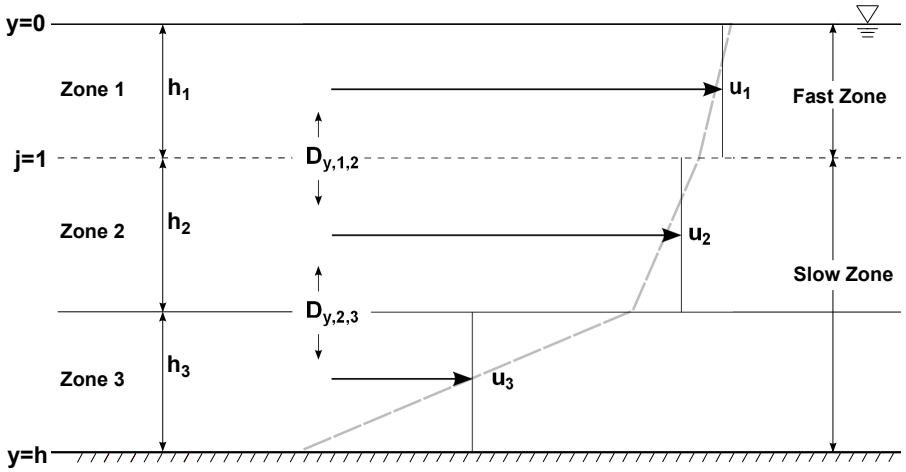

Figure 2.32: *Three zone model within open channel flow, where j=1.*

fast zone velocity is the mean velocity of zone 1, whereas the slow zone velocity is the mean velocity of zones 2 and 3. For the case $j = 2$, the fast zone is zones 1 and 2, the two zones above point j, and the slow zone is zone 3, the zone below point j. Again the fast zone velocity is the mean velocity of zones 1 and 2, whereas the slow zone velocity is the mean velocity of zone 3. The longitudinal dispersion coefficient is the sum of the cases where $j = 1$ and $j = 2$, and can be expressed as:

$$D(3)_{xx} = \sum_{j=1}^{2} \frac{(h^2)(q_j + q_{j+1})(q_1 + q_2 + ... + q_j)^2[1 - (q_1 + q_2 + ... + q_j)]^2[u_{f,1\to j} - u_{s,j\to 3}]^2}{2D_{y,j,(j+1)}} \tag{2.79}$$

Where $u_{f,1\to j}$ is the fast zone velocity, the mean velocity of zones above point j, and $u_{s,j\to 3}$ is the slow zone velocity, the mean velocity of zones below point j. Chikwendu [1986] extended the zonal method to any number of zones N, as shown in Figure 2.33.

For the case where the number of zones is N the number of cases considered, or points j, is $N - 1$. For the N zone case, the same procedure is followed as the three zone case, so for any point j the fast zone velocity is the mean velocity of the zones above the point j and the slow zone velocity is the mean velocity of the zones below the point j. Thus, at each point j, the effect of differential advection is quantified. In addition, at each point j, the expression takes account of the diffusion exchange between adjacent zones, $D_{y,j,j+1}$. The longitudinal dispersion coefficient is the sum of the cases at point j between the limits of $j = 1$ to $j = N - 1$, such

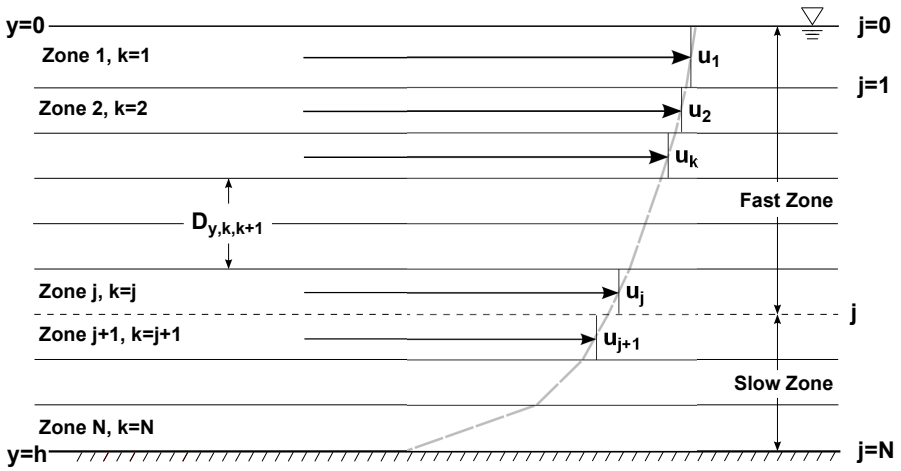

Figure 2.33: *N zone model within open channel flow*

that:

$$D(N)_{xx} = \sum_{j=1}^{N-1} \frac{(h^2)(q_j + q_{j+1})(q_1 + q_2 + ... + q_j)^2[u_{f,1\to j} - u_{s,j\to N}]^2}{2D_{y,j,(j+1)}} \tag{2.80}$$

Where $u_{f,1\to j}$ is the mean velocity between the points $k = 1$ and $k = j$, and $u_{s,j\to N}$ is the mean velocity between the points $k = j + 1$ and $k = N$.

As N tends towards infinity, the sum of the terms at point j becomes an integral expression, such that:

$$D(\infty)_{xx} = h^2 \int_0^1 \frac{q^2(1-q)^2}{D_y(q)}[u_f(q) - u_s(q)]^2 dq \tag{2.81}$$

Where:

$$u_f(q) = \frac{1}{q}\int_0^q u(q')dq' \tag{2.82}$$

And:

$$u_s(q) = \frac{1}{(1-q)}\int_0^q u(q')dq' \tag{2.83}$$

Where $u(q)$ is the velocity at the dimensionless position q, where $q = y/h$ where y is distance from the flow's free surface.

2.13.2 Chikwendu's N Zone Model for Pipe Flow

Chikwendu [1986] extended the the N zone model to pipe flow, so that Equation 2.80 becomes:

$$D(N)_{xx} = \sum_{j=1}^{N-1} \frac{a^2 p_j^4 (1-p_j^2)^2 [u_{f,1\to j} - u_{s,j\to N}]^2}{4D_{r,j,(j+1)}} (W_j + W_{j+1}) \tag{2.84}$$

Where $W_j = p_j - p_{j-1}$.

The main difference between the expressions is that for pipe flow, the longitudinal dispersion coefficient is calculated for the geometry of a pipe, hence Equation 2.84 is expressed in terms of radial position from the pipe's centreline r and dimensionless position from the centreline p, where $p_j = r_j/a$, as shown in Figure 2.34 .

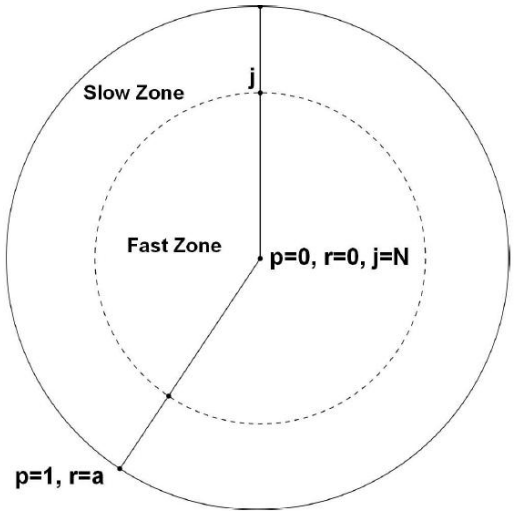

Figure 2.34: *N zone model for pipe geometery*

For pipe flow, the fast and slow zone velocities can be found as:

$$u_{f,1\to j} = \frac{1}{p_j^2} \sum_{k=1}^{j} q_k u_k \tag{2.85}$$

And:

$$u_{s,j\to N} = \frac{1}{1-p_j^2} \sum_{k=j+1}^{N} q_k u_k \tag{2.86}$$

Where $q_j = (r_j^2 - r_{j-1}^2)/a^2$.

Again, as N tends towards infinity, the sum of the terms at point j becomes

an integral expression, such that:

$$D(\infty)_{xx} = a^2 \int_0^1 \frac{p^4(1-p^2)^2}{2pD_r(p)}[u_f(p) - u_s(p)]^2 dp \tag{2.87}$$

Where:

$$u_f(p) = \frac{1}{p^2} \int_0^p 2p' u(p') dp' \tag{2.88}$$

And:

$$u_s(p) = \frac{1}{1-p^2} \int_p^1 2p' u(p') dp' \tag{2.89}$$

2.13.3 The Velocity Term in Chikwendu's Model for Pipe Flow

Laminar Flow

For laminar flow, the velocity profile is parabolic, and from Equation 2.5 and 2.7, it can be seen that the velocity at dimensionless distance from the centreline p can be described through:

$$u(p) = u_c(1-p^2) = 2\bar{u}(1-p^2) \tag{2.90}$$

Hence, the fast and slow zone velocities are:

$$u_f(p) = \frac{1}{p^2} \int_0^p 2p' 2\bar{u}(1-p^2) dp' \tag{2.91}$$

And:

$$u_s(p) = \frac{1}{1-p^2} \int_p^1 2p' 2\bar{u}(1-p^2) dp' \tag{2.92}$$

From this, it can be seen that:

$$u_f(p) = \bar{u}(2-p) \tag{2.93}$$

And:

$$u_s(p) = \bar{u}(1-p) \tag{2.94}$$

From which, it can be seen that for laminar flow:

$$u_f(p) - u_s(p) = \bar{u} \tag{2.95}$$

Therefore, the term $u_f(p) - u_s(p)$ in Equation 2.87 become a constant, $\bar{u}$, thus the velocity term can be taken out of the integral within Equation 2.87, such that:

$$D(\infty)_{xx} = a^2\bar{u}^2 \int_0^1 \frac{p^4(1-p^2)^2}{2pD_r(p)}dp \tag{2.96}$$

Furthermore, within laminar flow the radial diffusion coefficient $D_r(p) = D_m$, the molecular diffusion coefficient. The molecular diffusion coefficient is constant with respect to p, thus is can also be taken outside the integral, such that:

$$D(\infty)_{xx} = \frac{a^2\bar{u}^2}{D_m} \int_0^1 \frac{p^4(1-p^2)^2}{2p}dp \tag{2.97}$$

By integrating Equation 2.97 with respect to p, the expression becomes:

$$D_{xx} = \frac{a^2\bar{u}^2}{D_m}\frac{1}{48} \tag{2.98}$$

Which is equivalent to Equation 2.60, the same result as Taylor [1953] for laminar flow.

Turbulent Flow

For turbulent flow, the differential velocity term $u_f(p) - u_s(p)$ is not constant with respect to dimensionless position p, and is also a function of Reynolds Number. Furthermore, the radial diffusion coefficient $D_r(p)$ is now defined as $D_r(p) = D_t(p) + D_m$, and is also not constant with respect to dimensionless position p. Thus, in order to use the model within turbulent flow, a prediction of the velocity profile $u(p)$ and the turbulent diffusion coefficient $D_t(p)$ is required as a function of both dimensionless position p and Reynolds Number.

2.14 Predicting the Longitudinal Dispersion Coefficient Within Unsteady Flow

The majority of studies undertaken for dispersion within unsteady flow have been for low gradient oscillatory of pulsating flow.

Fischer [1973] reports results for longitudinal dispersion experiments within low gradient oscillatory pipe flow, where the longitudinal dispersion coefficient was 'the same as if the flow had been steady with a velocity equal to the mean absolute velocity'. Bowden [1965] also showed that a steady model can be used to predict the longitudinal dispersion coefficient within unsteady, oscillatory flow. Okubo [1967] and Holley et al. [1970] showed that the dispersion coefficient is pseudo-steady in oscillatory flow if the period of the oscillation is small when compared to the time scale for the solute to become cross-sectionally well mixed. Lee [2004] investigated longitudinal dispersion within pulsating laminar flow, using a set of Equations derived to account for the dispersion memory from previous pulses. He showed that for relatively short duration pulses within laminar flow, dispersion may be greater than for a steady flow with the same mean velocity.

To the author's knowledge, no studies have been undertaken for longitudinal dispersion within high gradient, transient, turbulent and transitional flow, of the type that may be encountered within unsteady periods in the dead-end regions of water distribution networks. The findings of Fischer [1973] and Bowden [1965] for oscillatory flow suggest that below a certain discharge gradient, a steady model may be applicable for unsteady, transient flow.

2.15 The Residence Time Distribution

So far the mixing characteristics of a system have been considered in terms of the longitudinal dispersion coefficient, a coefficient that quantifies the longitudinal mixing characteristics of a system on the basis of the assumption of the Fickian model.

The Residence Time Distribution (RTD) shows the actual mixing response of a system to an idealised slug injection, in terms of the exit age distribution of each particle [Danckwerts, 1953; Levenspiel, 1962]. The Cumulative Residence Time Distribution (CRTD) shows the integral of the RTD at at given time, thus representing the mass of tracer that has exited the system at that given time.

The advantage of using RTDs and CRTDs to quantify the mixing response of a system is that the method shows the actual mixing response of the system, rather than the response on the basis of some assumptions, such as the Fickian model.

Figure 2.35 shows several example CRTDs provided by Danckwerts [1953], for several types of flow. Here the CRTDs are plotted as cumulative fraction against dimensionless time.

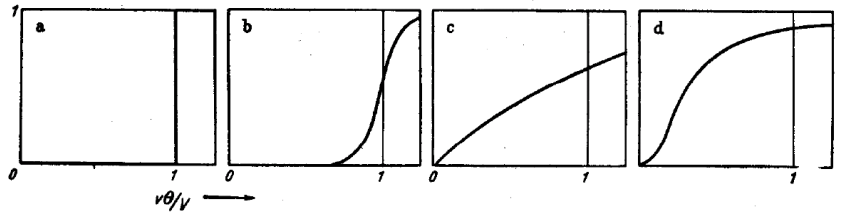

Fig. 1. *F*-diagrams.

(*a*) Piston flow; (*b*) Piston flow with some longitudinal mixing; (*c*) Complete mixing; (*d*) Dead water.

Figure 2.35: *Example CRTDs for variety of mixing cases. Reproduced from Danckwerts [1953]*

Although the RTD is useful in terms of characterising a system's response, it is difficult to obtain RTDs from laboratory data, as it is difficult to produce a instantaneous, cross sectionally well mixed slug injection under laboratory conditions.

The relationship between a non-idealised, measured upstream concentration distribution, the measured downstream concentration distribution and the system's RTD is given through the following expression [Stovin et al., 2010]:

$$c(x_2, t) = \int_0^t c(x_1, t - \lambda) E(\lambda) d\lambda \tag{2.99}$$

Where $c(x_1, t)$ is the upstream concentration distribution, $E(\lambda)$ is the system's RTD and $c(x_2, t)$ is the downstream concentration distribution, which is the convolution integral of the upstream distribution and the RTD.

Thus, if the up and the downstream concentration profiles are measured, the data can be 'deconvolved' to give the system's RTD.

Madden et al. [1996] undertook a comparison of six possible deconvolution techniques for solving Equation 2.99. Of the six approached, they concluded that the best in terms of overall performance was 'maximum entropy deconvolution', based on a technique developed by Skilling and Bryan [1982].

Stovin et al. [2010] and Guymer and Stovin [2011] applied maximum entropy deconvolution to data for tracer studies within manholes. For these studies, the RTD was constrained to be as smooth as possible whilst having an output that gives the best possible fit to the measured downstream data. The smoothness was

maximised on the basis of an entropy function:

$$S(\hat{h}) = -\sum_{j=1}^{N} p_j ln(p_j/\hat{h}_j) \tag{2.100}$$

Where $\hat{h}$ is the estimated RTD, $S(\hat{h})$ is the value for entropy and:

$$p_j = \hat{h}_j / \sum \hat{h} \tag{2.101}$$

Goodness of fit was measured by:

$$R_t^2 = 1 - \frac{\sum (y_i - f_i)^2}{\sum y_i^2} \tag{2.102}$$

Where y_i and f_i are the measured and predicted downstream concentration distributions respectively.

Thus, two functions for the RTD were considered, one constrained by the entropy function, $S(\hat{h})$, and one constrained by the goodness of fit to the downstream data, $R_t^2(\hat{h})$. The final RTD is identified on the basis of both functions, through the Lagrangian function:

$$L(\hat{h}, \xi) = R_t^2(\hat{h}) + \xi S(\hat{h}) \tag{2.103}$$

Where ξ is a weighting coefficient. Equation 2.103 can be used to give the system's RTD using a standard optimisation routine.

2.16 Summary

The aim of the present work is to experimentally investigate longitudinal dispersion in steady and unsteady flow for $2000 < Re < 50000$, and to propose a model to predict the longitudinal dispersion coefficient for the same range for steady and unsteady flow, that can be experienced in the dead end regions of distribution networks.

For fully developed laminar flow, the longitudinal dispersion coefficient can be predicted analytically Taylor [1953], and a good estimate of the longitudinal dispersion coefficient can be made by Taylor's expression for turbulent flow, for $Re > 20000$ Taylor [1954]. Thus, the present work will focus on turbulent and transitional flow between these points. To cover the range over which Taylor's Equations are not valid, the present work will consider the range $2000 < Re < 50000$.

For experimental investigations of steady flow, several authors have mea-

sured the longitudinal dispersion coefficient for $2000 < Re < 50000$. However, few have covered the whole range in detail, and none have measured detailed hydraulic data on the system in question, such as the velocity profile and the friction factor, in conjunction with tracer data. Furthermore, no previous author has shown the relationship between the system's RTD and Reynolds Number, as the system goes from being fully turbulent to transitonal/laminar. Thus, an aim of the present work is to obtain detailed dispersion data, both in terms of the longitudinal dispersion coefficient and the system's RTDs, for the range $2000 < Re < 50000$, in conjunction with hydraulic data for the system over the same range.

For models for the longitudinal dispersion coefficient within steady flow, previous models have been proposed for $2000 < Re < 50000$. However, each of these models are either analytical solutions to the problems governing differential Equation, or are proposed using CFD, and thus are complex to reproduce. An aim of the present work is to propose a simple, general model that can be used to predict the longitudinal dispersion coefficient for $2000 < Re < 50000$ on the basis of the estimation of a few, simple hydraulic parameters for a given system.

For unsteady flow, it is considered that a simple, repeatable method for initially investigating the types of unsteady flow that may be encountered in distribution networks is to consider various configurations of transient flow. Where flow is accelerated or decelerated between various initial and final discharges.

For experimental investigations of unsteady flow, previous work has focused on low gradient, oscillatory flow. To the author's knowledge, no experimental investigation has previously been carried out in transient, turbulent and transitional flow. Thus, the aim of present work is to investigate the mixing characteristics of a system under such conditions.

For modeling the longitudinal dispersion coefficient within unsteady flow, it has previously been proposed that a steady model for the longitudinal dispersion coefficient can be used for low gradient, oscillatory flow [Fischer, 1973]. Thus, the aim of the present work is to use the model proposed for steady flow within the present work to investigate conditions under which this assumption is valid for high gradient, turbulent and transitional unsteady flow.

Chapter 3

Proposed Numerical Model

3.1 Introduction

This chapter describes the development of a numerical model to predict the longitudinal dispersion coefficient for the range $2000 < Re < 50000$, for steady flow. A framework will also be proposed through which the model may be applicable for unsteady flow.

In his pioneering work, Taylor [1954] produced an expression for the longitudinal dispersion coefficient for turbulent flow. However, his expression was derived assuming a highly turbulent velocity profile, neglecting a laminar sub-layer and buffer zone. As such, his expression is only valid for highly turbulent flow, for $Re > 20000$ (see Chapter 2, Section 2.11.1).

In Section 2.12.1, several other models, proposed since Taylor's original expression were reviewed. Whilst these models build upon Taylor's work, none of them fully describe the data for the whole range $2000 < Re < 50000$. One reason for this is because previous models propose a general prediction for the longitudinal dispersion coefficient, assuming certain hydraulic parameters, such as the critical points for the transition from laminar to turbulent flow, the values for the frictional velocity and the form of the velocity profile. However, these parameters are often system specific, and thus need to be considered as the values for the system upon which the dispersion measurements are being made.

The aim of this Chapter is to investigate the applicability of a relatively simple model, where the longitudinal dispersion coefficient can be obtained as a continuous function of Reynolds Number and some other basic hydraulic parameters, and thus can be applied to any system for which this general hydraulic data is available.

The model used within this Chapter is the 'Zonal' model of Chikwendu [1986], as described in Chapter 2, Section 2.13. Chikwendu's model provides a longitudinal dispersion coefficient on the basis of a mean velocity profile and a radial diffusion coefficient. Hence, the purpose of this Chapter is to propose a framework through which an appropriate velocity profile and radial diffusion coefficient can easily be estimated for a given system, for the range $2000 < Re < 50000$.

The model will first be used to reproduce Taylor's expression, by assuming his parameters. Improved descriptions of the velocity profile will then be used to predict the longitudinal dispersion coefficient in a manner more consistent with previous experimental data for $2000 < Re < 50000$.

Within this Chapter, the parameters will be proposed on the basis of previous hydraulic data, and will be compared to previous dispersion data. In addition, the flow will be assumed laminar for $Re < 2000$ and turbulent for $Re > 4000$. The hydraulic parameters used within this Chapter, as well as these critical points, are very general assumptions for the purpose of an initial investigation of the model's validly. Within Chapter 5, the model's parameters will then be validated and revised on the basis of hydraulic data recorded within the present work, and compared to dispersion data of the present work.

3.2 Numerical Model

The zonal model of Chikwendu [1986] is defined in Equation 2.84, and discussed in Chapter 2, Section 2.13.

Chikwendu's model provides an analytical solution for the longitudinal dispersion coefficient, on the basis of a velocity profile and the radial diffusion coefficient. Taylor [1954] defined the radial diffusion coefficient through Reynolds analogy (Equation 2.65) where the primary parameter in the definition of the radial diffusion coefficient is the velocity profile. Thus, if the radial diffusion coefficient is defined within Chikwendu's model in this manner, a prediction of the longitudinal dispersion coefficient can be made on the basis of an estimate of the velocity profile and the frictional velocity for a given Reynolds Number. Unless otherwise stated, the frictional velocity will be calculated on the basis of the friction factor, through Equation 2.10.

Within this Chapter, Chikwendu's model is used with the number of zones $N = 5000$. See Appendix A for justification of the number of zones, which shows that the model's output is independent of the number of zones for all parameters for $N \geq 5000$.

3.3 Model Parameters and Results for Steady Flow

3.3.1 Turbulent flow

Taylor [1954] defined the turbulent velocity profile using a 'universial velocity profile', (Equation 2.67) on the basis of a geometric relationship $f(p)$ (See Chapter 2, Section 2.12.1). See Appendix B for an explanation of how Taylor's velocity profile was reproduced within the present work.

Figure 3.1 shows a comparison between Taylor's velocity profile and the experimentally obtained velocity profile of Durst et al. [1995].

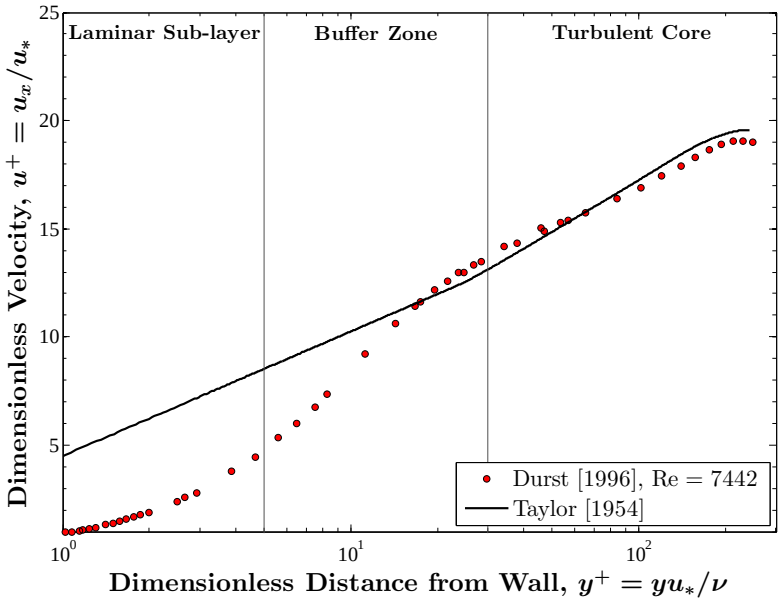

Figure 3.1: *Comparison between the theoretical velocity profile of Taylor [1954] and the experimentally obtained velocity profile of Durst et al. [1995].*

It can be seen that Taylor's velocity profile provides a reasonable prediction of the velocity profile's turbulent core, for $y^+ > 30$, but fails to predict the laminar sub-layer and buffer zone, for $y^+ < 30$.

Figure 3.2 shows the results from Chikwendu's model using Taylor's velocity profile. In addition, frictional velocity is calculated in the same manner as Taylor, using the the friction factor of Blasius [1911] (Equation 2.25).

It can be seen that for highly turbulent flow, assuming Taylor's velocity profile, the model provides a reasonable prediction of the longitudinal dispersion coefficient. However, for $Re < 20000$, Taylor's expression under predicts the dispersion data, which is increasing in magnitude whilst his expression remains relatively

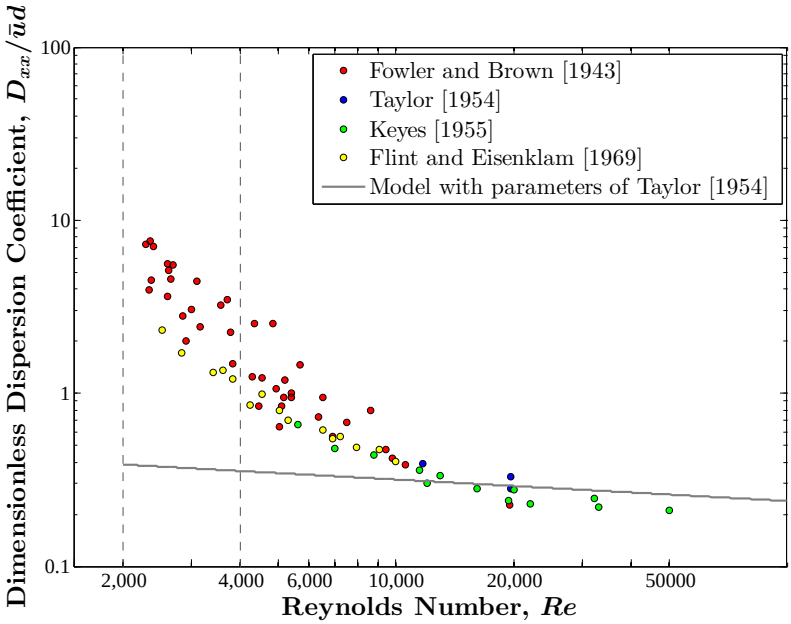

Figure 3.2: *Comparison between results for the longitudinal dispersion coefficient from the model with the parameters of Taylor [1954], and the experimental data of Fowler and Brown [1943], Taylor [1954], Keyes [1955] and Flint and Eisenklam [1969].*

constant.

Reichardt [1951] proposed an expression for the laminar sub-layer and buffer zone, the non-turbulent portion of a turbulent velocity profile. Figure 3.3 shows a comparison between Taylor's profile, the experimentally obtained velocity profile of Durst et al. [1995], and the laminar sub-layer and buffer zone of Reichardt [1951] (Equation 2.14). It can be seen that the laminar sub-layer and buffer zone of Reichardt [1951] provides a reasonable prediction of the velocity profile's boundary layer, for $y^+ < 30$.

The turbulent velocity profile of the present work was composed using Taylor's velocity profile for the turbulent core, for $y^+ > 30$, and the velocity profile of Reichardt [1951] for the laminar sub-layer and buffer zone, for $y^+ < 30$. Thus, using this velocity profile within the model simply highlights the effect of adding a laminar sub-layer and buffer zone to Taylor's velocity profile, where all other parameters are the same as used for Taylor's original analysis.

From Figure 3.3, it can be seen that the two profiles do not converge exactly at $y^+ = 30$. Thus, to produce a smooth continuous velocity profile, the velocity profile of the present work smoothly links the two profiles between $y^+ = 25$ and $y^+ = 50$.

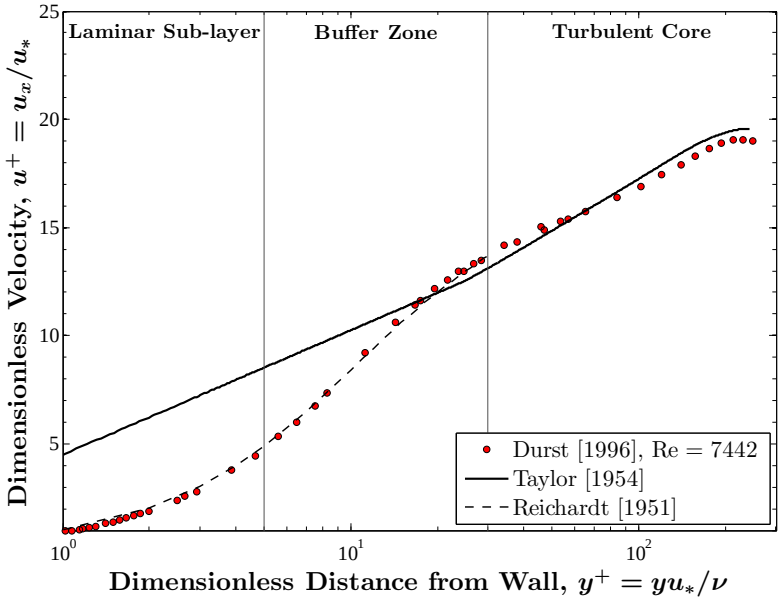

Figure 3.3: *Comparison between the theoretical velocity profiles of Taylor [1954] and Reichardt [1951], and the experimentally obtained velocity profile of Durst et al. [1995].*

Figure 3.4 shows a comparison between the turbulent velocity profile of the present work, and the experimental data of Durst et al. [1995], from which it can be seen that the velocity profile of the present work provides a reasonable prediction of the entire velocity profile, and accounts for the non-turbulent portion of the turbulent velocity profile.

Figure 3.5 shows the results from Chikwendu's model using the turbulent velocity profile of the present work, and the frictional velocity, as defined by Taylor [1954]. It can be seen that for highly turbulent flow, the prediction of the longitudinal dispersion coefficient of the model assuming the turbulent velocity profile of the present work tends towards Taylor's prediction. This is because at high Reynolds Numbers, the length of the laminar sub-layer and buffer zone becomes negligibly small, and thus tends towards Taylor's expression which assumes no laminar sub-layer or buffer zone. However, for low turbulent flow, for $Re < 20000$, the influence of the growing boundary layer defined in the velocity profiles of the present work causes the longitudinal dispersion coefficient to increase in magnitude, in a manner more consistent with the experimental data. The prediction of the model with the low Reynolds Number turbulent velocity profile suggests that the increase in the magnitude of the longitudinal dispersion coefficient with decreasing Reynolds Numbers for turbulent flow is caused by the increase in differential advection, caused

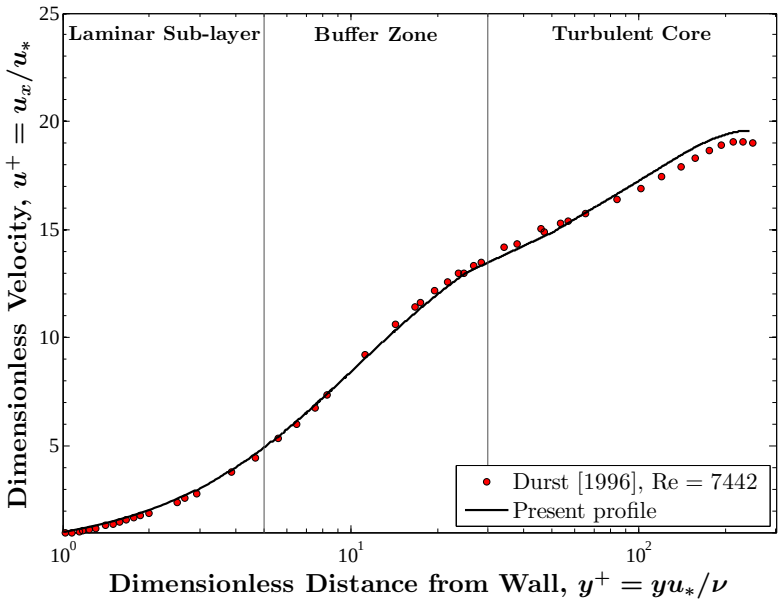

Figure 3.4: *Comparison between the turbulent velocity profile of the present work, and the experimentally obtained velocity profile of Durst et al. [1995].*

by the laminar sub-layer and buffer zones effect on the uniformity of the velocity profile, as the growing boundary layer with decreasing Reynolds Number causes an increases in differential advection, the magnitude of the longitudinal dispersion coefficient increases.

3.3.2 Laminar Flow

Figure 3.5 shows the prediction made by Chikwendu's model with the turbulent velocity profile of the present work, that accounts for the growing non-turbulent portion of a turbulent velocity profile with decreasing Reynolds Number. Whilst the model assuming this velocity profile accounts reasonably well for the trend in the data for turbulent flow, it can be seen that the prediction fails to account for the increase in the longitudinal dispersion coefficient for transitional and laminar flow. This section will consider the prediction assuming a laminar velocity profile.

From Figure 3.5, it can be seen that between $Re = 50000$ and $Re = 4000$, there is an increase in the longitudinal dispersion coefficient by a factor of approximately 3. However, between $Re = 50000$ and $Re = 2000$, there is an increase by a factor of approximately 10. This rapid increase in the magnitude of the longitudinal dispersion coefficient is caused by the rapid transition of the flow from a relatively uniform profile for turbulent flow, to a relatively non-uniform parabolic profile for

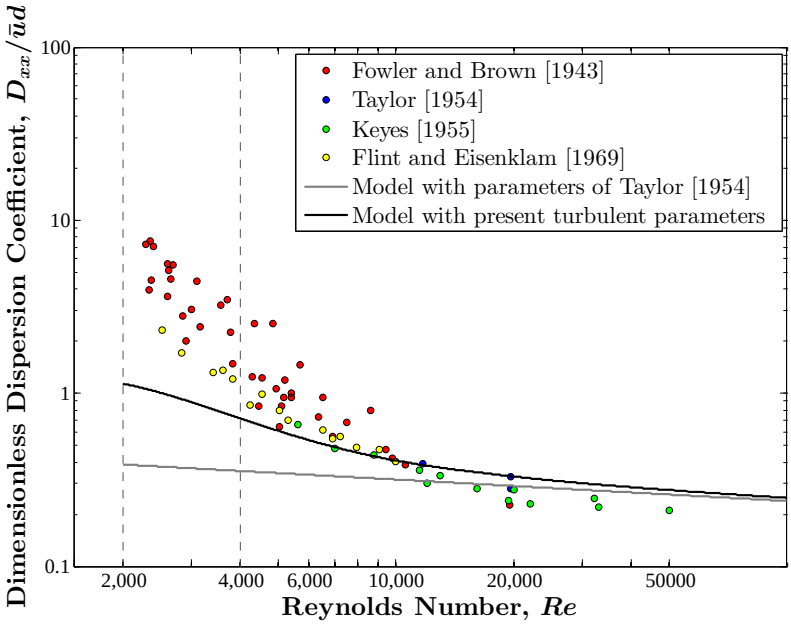

Figure 3.5: *Comparison between results for the longitudinal dispersion coefficient from the model with the parameters of the present work for turbulent flow, and Taylor [1954], and the experimental data of Fowler and Brown [1943], Taylor [1954], Keyes [1955] and Flint and Eisenklam [1969].*

laminar flow.

The parabolic velocity profile for laminar flow can be predicted analytically through the expression presented in Equation 2.5.

Figure 3.6 shows the results from Chikwendu's model, assuming the analytically derived laminar velocity profile, as defined in Equation 2.5, and the frictional velocity on the basis of the analytically derived friction factor for laminar flow, as defined in Equation 2.24. It can be seen that the prediction of the longitudinal dispersion coefficient on the basis of a laminar velocity profile predicts the relatively high value for the longitudinal dispersion coefficient for $Re \approx 2000$.

3.3.3 Transitional Flow

From Figure 3.6, it can be seen the when Chikwendu's model is used assuming turbulent parameters, it makes a reasonable prediction of the experimental data for turbulent flow for $Re > 4000$. Furthermore, when the model is used assuming laminar parameters, it makes a reasonable prediction of the experimental data for laminar flow for $Re \approx 2000$.

For transitional flow, for $2000 < Re < 4000$, the two trends form boundaries

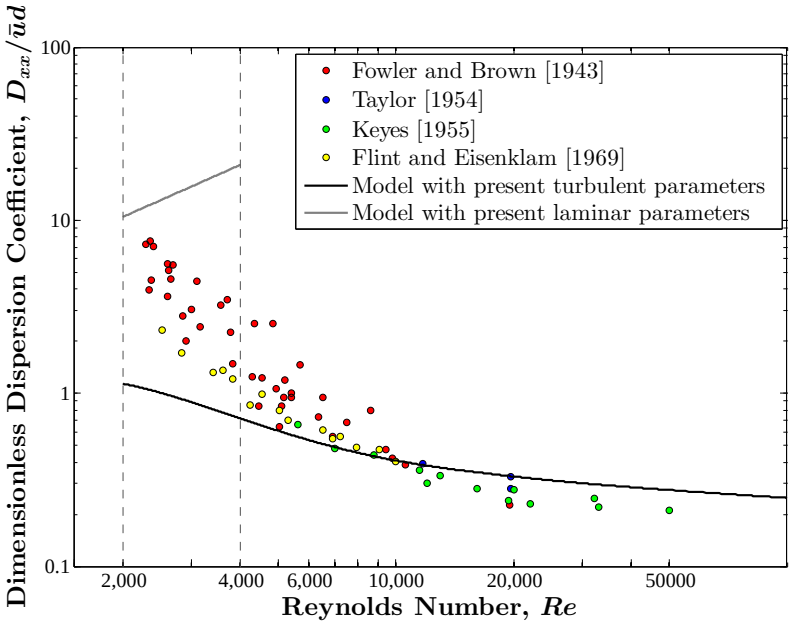

Figure 3.6: *Comparison between results for the longitudinal dispersion coefficient from the model with the parameters of the present work for laminar and turbulent flow, and the experimental data of Fowler and Brown [1943], Taylor [1954], Keyes [1955] and Flint and Eisenklam [1969].*

within which all transitional data falls. However, to provide a more accurate estimation the longitudinal dispersion coefficient within the region, it is necessary to estimate how the velocity profile transitions from a relatively flat profile for turbulent flow, to a parabolic profile for laminar flow.

One possible method for achieving this is by using a transitional expression for the velocity profile, of the form:

$$\frac{u_x}{u_c} = \alpha u_T + (1-\alpha)u_L \tag{3.1}$$

Here, the velocity distribution is defined as a combination of a laminar profile, u_L, the distribution at the critical point for laminar to transitional flow, and a turbulent profile, u_T, the distribution at the critical point for transitional to turbulent flow. The relative contribution made to the transitional distribution by each profile is governed by the transition factor, α, where, if $\alpha = 0$, the profile is fully laminar, and if $\alpha = 1$, the profile is fully turbulent. Thus, to provide an estimation of the velocity profile within transitional flow, and the corresponding longitudinal dispersion coefficient, an estimation of the transitional factor α needs to be made as a function of Reynolds Number.

Figure 3.7 shows the results from Chikwendu's model if the transitional factor α is assumed linear between $2000 < Re < 4000$, the assumed critical points for the transition from laminar to turbulent flow. In addition, the frictional velocity is assumed to vary with α.

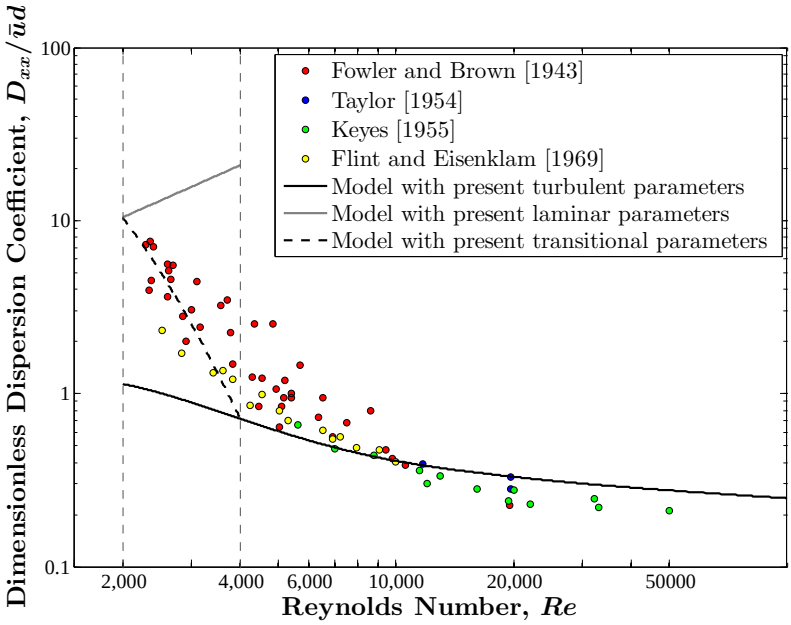

Figure 3.7: *Comparison between results for the longitudinal dispersion coefficient from the model with the parameters of the present work for laminar and turbulent flow, the present work for transitional flow assuming a linear variation in α, and the experimental data of Fowler and Brown [1943], Taylor [1954], Keyes [1955] and Flint and Eisenklam [1969].*

From Figure 3.7 it can be seen that whilst assuming the transition factor, α, linear gives a general estimation of the longitudinal dispersion coefficient within the transitional region, a more accurate prediction may be possible by using experimental data to suggest the trend in α as a function of Reynolds Number for a given system.

Within Chapter 5, analysis of experimental velocity profiles obtained within the present work are presented, from which the trend in α is suggested for the facility used for the experimental tests undertaken within this work.

3.4 Proposed Model for Unsteady Flow

Within Chapter 2, Section 2.14, it was suggested that it is possible to estimate the longitudinal dispersion coefficient within unsteady flow by assuming the longitudinal

dispersion coefficient as the mean of the values for steady flow, at each discrete point in time for a time-varying flow.

Through the model proposed in this Chapter, the longitudinal dispersion coefficient can be estimated as $D_{xx} = f(Re)$. If the flow is unsteady, then $Re = f(t)$, and thus the longitudinal dispersion coefficient be be predicted as:

$$\overline{D_{xx}} = \frac{1}{n} \sum_{i=t_1}^{i=t_2} D_{xx}(t_i) \tag{3.2}$$

Where $\overline{D_{xx}}$ is the mean longitudinal dispersion coefficient, n is the number of data points, t_1 and t_2 are the averaging period start and end times, and $D_{xx}(t_i)$ is the longitudinal dispersion coefficient predicted at time t_i as a function of the Reynolds Number at t_i. Here, the model assumes a constant time step.

3.5 Summary

In this Chapter it has been suggested that Taylor's expression for the longitudinal dispersion coefficient within turbulent flow fails to predict the trend in dispersion data for $Re < 20000$ due to his assumption of a highly turbulent velocity profile, that neglects a laminar sub-layer and a buffer zone.

Though the use of the model of Chikwendu [1986], it was shown that when a laminar sub-layer and buffer zone are included within the turbulent velocity profile, the model predicts the increase in the longitudinal dispersion coefficient for decreasing Reynolds Number for turbulent flow. This suggests that the growing boundary layer with decreasing Reynolds Number is the cause of the increase in magnitude of the longitudinal dispersion coefficient.

It was also suggested that the relatively large magnitude of the longitudinal dispersion coefficient for near laminar flow can be attributed to the parabolic velocity profile in this region, and that the increase in magnitude between turbulent and laminar flow can be explained in terms of the relatively flat turbulent profile transitioning into a non-uniform laminar profile.

On the basis of the velocity profiles proposed within this Chapter, the model can be used to predict the longitudinal dispersion coefficient for a given system, on the basis of an estimation of the frictional velocity for laminar and turbulent flow, the critical points for the transition from laminar to turbulent flow and an estimation of the transition factor, α. Within Chapter 5, the model for steady flow will be validated against dispersion data for steady flow in conjunction with hydraulic data for the facility used to undertake the tests for dispersion.

It was further suggested that the model may be applicable for unsteady flow. Within Chapter 6, the proposed model for unsteady flow will be validated against dispersion data for unsteady flow.

Chapter 4

Experimental Setup and Data Acquisition

4.1 Introduction

This chapter describes the experimental facility used for all experimental tests undertaken within this work, as well as the test programs, data acquisition and pre-analysis data processing of all data.

Three main test series were conducted for this work. An experimental investigation of the hydraulics of steady flow, longitudinal dispersion within steady flow and longitudinal dispersion within unsteady flow. All tests were conducted over a range of discharges corresponding to Reynolds Numbers $2000 < Re < 50000$.

4.2 General Notes on Data Analysis

Within this and subsequent Chapters, some basic equations are used to evaluate the data considered. Although these equations are well known, some ambiguity can arise by the use of slightly different forms of these equations. The following section gives definitions of the equations used.

Where the goodness of fit R^2 is quoted, this refers to the coefficient of determination:

$$R^2 = 1 - \frac{\sum(y_i - f_i)^2}{\sum(y_i - \bar{y})^2} \tag{4.1}$$

Where y_i and f_i are the observed and predicted values respectively, and $\bar{y}$ is the mean of the observed values.

Where standard deviation is quoted, this refers to the standard deviation calculated on the basis of:

$$s = \sqrt{\frac{1}{N-1}\sum_{i=1}^{N}(x_i - \bar{x})^2} \tag{4.2}$$

Where N is the number of samples, x_i are the observed values and $\bar{x}$ is the mean of the observed values.

Unless otherwise stated, error bars shown on graphs in this thesis represent ± 1 standard deviation.

4.3 Experimental Facility

4.3.1 Layout and Specification

The facility used for all tests within this work was a re-circulating system with a sump volume of approximately 2500 litres. The main test section constituted a 17.8 metre long perspex pipe, with an internal diameter of 24 mm.

Three types of measurement were undertaken; head loss, velocity profile and tracer measurements. Head loss measurements were made using 3 pressure tappings, with specific measurements undertaken between any 2 tappings, set-up to two manometers. Velocity profile measurements were undertaken using a Laser Doppler Anemometry (LDA) system in conjunction with a cubic glass test section surrounding the pipe, filled with water. Tracer measurements were undertaken using 6 fluorometers, an injection point and a peristaltic pump for dye injections.

The start point of all tests, i.e. the first pressure tapping for head loss, the water box for LDA measurements and the dye injection point for tracer measurements, were all located at a distance downstream on the main test section estimated as being sufficient for the flow to be fully developed for all flow rates considered. The estimation was made on the basis of the expression given by [White, 2008], for the length required for fully developed laminar and turbulent flow to be obtained, as defined in Equations 2.3 and 2.11 respectively. Tracer tests were conducted before the installation of pressure tappings, so that no interference to the flow field occurred throughout the main test section during the tracer tests. Figure 4.1 gives a schematic of the layout.

When initial tests were conducted, it was discovered that the system's pump could not maintain a stable discharge for long periods of time at very low operating speeds. This problem was particularity important with respect to velocity profile

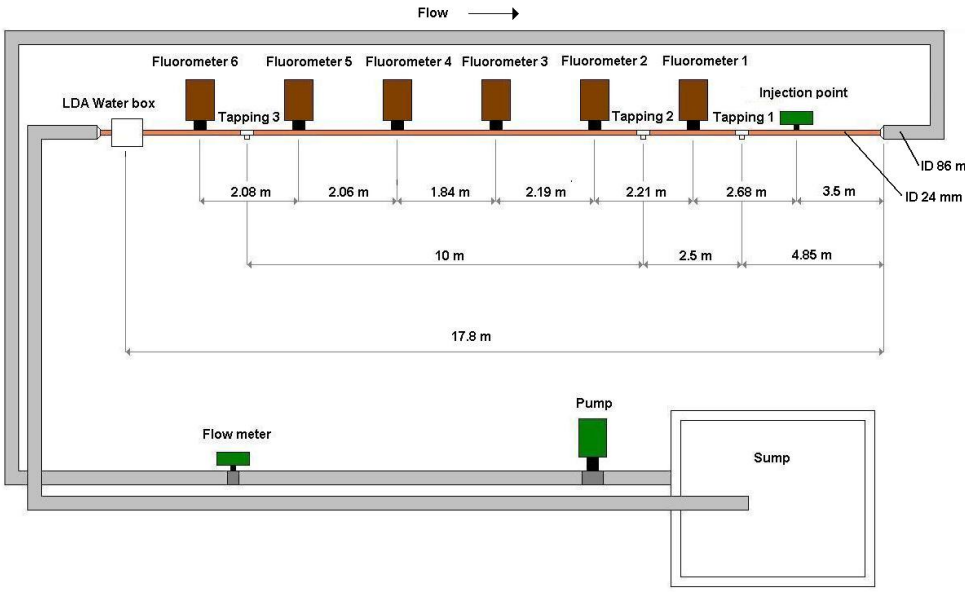

Figure 4.1: *Schematic of facility layout.*

measurements. In some cases it took up to an hour for a single profile to be obtained, during which time a noticeable change in discharge was observed.

To solve this problem, a bypass was installed where the flow was split, so that a portion of the flow went to the main test section, and a portion returned to the sump. The portion of the flow going to the main test section could be regulated by a sluice gate on the bypass's outlet pipe.

This modification meant that low discharges could be obtained whilst the pump was still being operated at a relatively high speed, thus enabling a stable flow to be maintained for long periods of time.

For all steady flows, the discharge was measured before and after each test, to ensure that the flow rate was steady for the entire duration of all tests conducted. Figure 4.2 shows a diagram of the bypass layout.

4.3.2 Discharge Measurements

Two methods were used for measuring the discharge, a volumetric method and a electro magnetic flow meter.

The volumetric method was used to calibrate the electro magnetic flow meter, and for the steady tracer and velocity profile tests, as the length of time for each run of these tests required the use of the bypass system, which meant the electro magnetic flow meter could not be used, as it was located before the bypass junction.

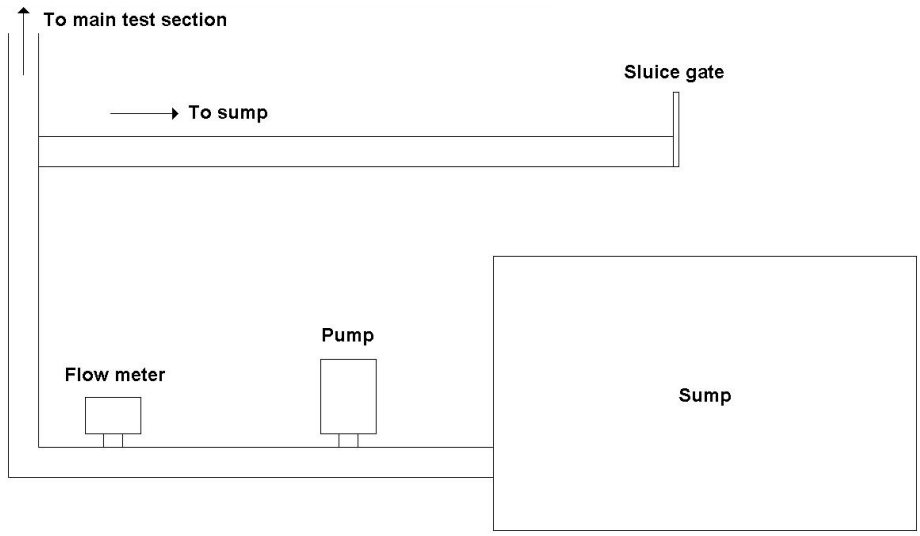

Figure 4.2: *Diagram of the bypass layout from side.*

The electro magnetic flow meter was use for all unsteady tests. In addition, it was used for steady head loss tests, as the duration of these tests was sufficiently small for the flow to remain stable without the bypass system.

Volumetric

Volumetric discharge measurements were obtained by measuring the volume of water collected at the system's output over a certain period of time.

Volumes were measured between $1 < l < 12.5$, where the volume could be measured to the nearest 20 ml. Volumes were collected over 10, 20 or 30 second periods depending on the discharge, where the time to fill a certain volume could be regulated to within approximately 0.5 seconds.

A test was conducted to investigate the repeatability of the volumetric method, where 3 repeat measurements were taken for 18 discharges between $2000 < Re < 50000$. The error was calculated for each discharge as the standard deviation of the 3 repeats, as a percentage of the mean value for that discharge. The mean value for the error for all 18 discharges was $1.3\% \pm 1.2\%$.

Electromagnetic Flow Meter

In addition to the volumetric method, discharges were measured using an electro magnetic flow meter. The flowmeter comprised of a Siemens Sitrans FM Magflo MAG 5100W flowmeter and a Siemens MAG 6000 transmitter. The approximate location of the flow meter on the facility can be seen in Figure 4.1.

The flow meter outputs a voltage as a linear response to the discharge. The instrument was calibrated by recording the voltage output of the instrument for 300 seconds at a known discharge, where the flow rate was obtained volumetrically. This process was repeated several times for a range of flow rates corresponding to $2000 < Re < 50000$. For each test program using the electro magnetic flow meter, the flow meter was calibrated before the test series to obtain the calibration relationship, and after the test series to ensure that the calibration relationship had been maintained. Figure 4.3 shows an example of a calibration for the electro magnetic flow meter.

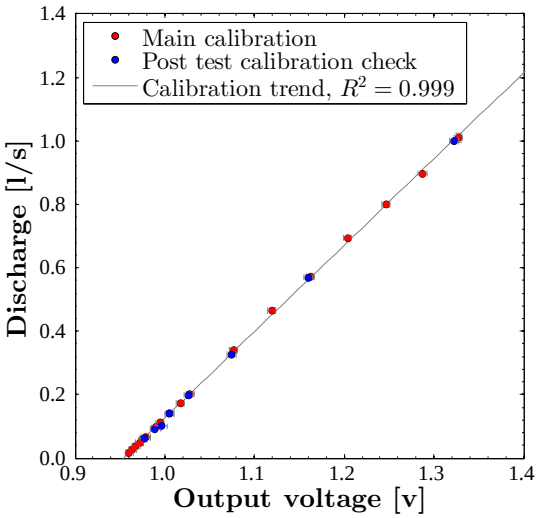

Figure 4.3: *Example calibration of electromagnetic flow meter.*

On the basis of information provided in the flow meter's manual, the percentage error of the flow meter for ≥ 0.5 m/s is $\pm 0.25\%$. The manual provides a relationship for the percentage error for < 0.5 m/s, from which the percentage error for the lowest discharge within all test series was calculated as $\pm 1.3\%$.

4.3.3 Head Loss Measurements

Head loss measurements were made using two manometers mounted upon a wooden plate. A scale between the two manometers enabled the head from each manometer to be read to the nearest mm.

4.3.4 Velocity Profile Measurements

Velocity profiles were obtained using a two beam, 1D LDA system. The system was used to measure longitudinal velocity time series at a particular radial location. The device was traversed to various radial locations across the pipe, from which a mean velocity profile could be obtained. Table 4.1 summarises the system's specification.

Laser wavelength, λ_L	$632.8 \times 10^{-6} mm$
Laser focal length, f_L	400 mm
Beam expansion factor, E_b	0
Beam diameter, b_D	1.68 mm
Beam separation, b_s	38 mm
half-intersection angle of beams, θ	2.72^o

Table 4.1: *Summary of specification of LDA system.*

The point velocity provided by the LDA system was an effective mean velocity of the flow within the instrument's measuring volume. The measuring volume is the volume over which the two laser beams cross, and the length and depth of the measuring volume can be calculated through [Durst et al., 1995]:

$$l_m = \frac{4\lambda_L f_L}{E_b \pi b_D cos(\theta)} \tag{4.3}$$

$$d_m = \frac{4\lambda_L f_L}{E_b \pi b_D sin(\theta)} \tag{4.4}$$

Where l_m and d_m are the length and depth of the measuring volume.

From these equations, and the system's specification, as provided in Table 4.1, the length and depth of the system's measuring volume can be calculated as $l_m = 4$ mm and $d_m = 0.2$ mm.

Velocity point measurements were made along the pipe's vertical plane, from the top of the pipe to the bottom. The system was setup so that the measuring volume's length and depth were perpendicular and parallel to this axis respectively, as shown in Figure 4.4. Hence, velocity point measurements are the mean value over 0.2 mm in the radial direction.

The system was aligned using a target system, as depicted in Figure 4.5. Figures 4.4 and 4.5 show the 3 axes in which the LDA system operates, where the x axis is the pipe's longitudinal axis, the y axis is the pipe's transverse axis and the z axis is the axis from the top to the bottom of the pipe, perpendicular to the transverse axis. The LDA system's probe was held in a clamp, which was fixed in the

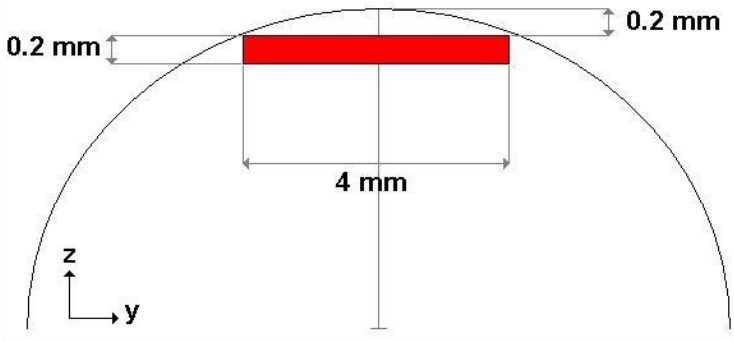

Figure 4.4: *Diagram of LDA systems measuring volume.*

x axis, but allowed for movement in the y and z axes. The goal for the alignment of the system was to align the centre of the measuring volume on the y axis centreline, and to traverse the measuring volume down the z axis, to obtain a velocity profile along the pipe's centreline in the the z axis plane.

The target system, shown in Figure 4.5, consisted of a glass box full with water, through which the main text section of pipe passed. Directly above the main test section of pipe, and on the same centreline in the y axis plane, was an identical section of pipe, with a target plate fixed in the middle of the pipe, i.e. on the pipe's centreline in the y axis. The target was fixed within an identical section of pipe to give the same refractive index as the main test section. The target had two dots on its centreline, a small known distance apart. Hence, these two dots lie on the centreline of the y axis of the main pipe, and centreline of both the y and z axes for the target pipe. To align the system, the LDA probe clamp was first set at the furthest position away from the pipe in y direction. The clamp was then traversed in the z direction, so that both beams lay on the centreline of the target, so that the measuring volume was on the z axis centreline of the target pipe. The clamp was then traversed in towards the pipe in the y direction, so that the two dots of the two laser beams began to come together, to the point that the two beams were over the two target dots. The clamp was then traversed further in, until the beams converged in between the two dots, and the began to separate again. The clamp was traversed further until they were once more over the two dots. The distance traversed between the first and second point that the two beams lied on the two dots was measured. Half this distance corresponds to the point that the measuring volume is on the centreline of the target pipe in both the y and z planes, and thus the y plane for the main pipe.

Once the measuring volume was set to this point, its position was fixed in the y direction, and could be traversed to any desired position in the z axis of the

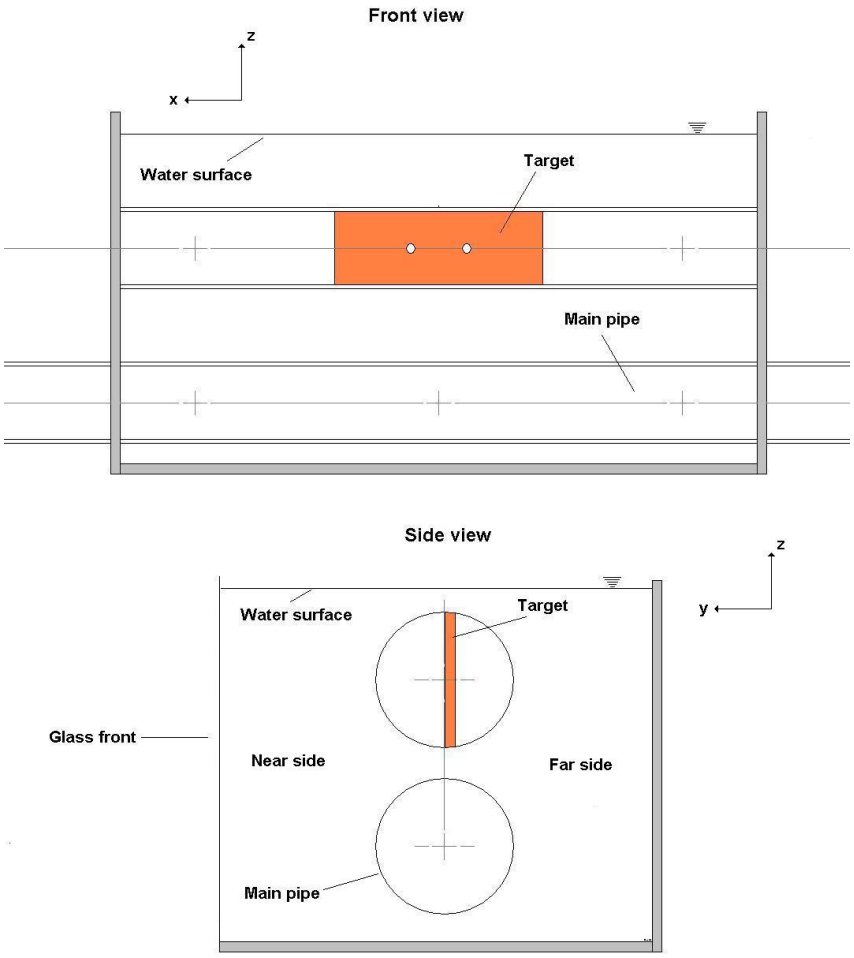

Figure 4.5: *Diagram of LDA target system.*

main test pipe, which was a known distance from the centreline of the target pipe.

Velocities were recorded at various radial positions from the top of the pipe to the bottom, along the z axis. The laser was first taken to the wall of the main pipe, on the basis of the alignment described above, and then traversed down the pipe.

Although the alignment procedure described above was considered sufficient to align the laser on the y axis centreline, positions on the z axis was required to an accuracy of < 0.1 mm, in order to get a precise radial location of the velocity, which was deemed beyond the scope of the target alignment procedure. Profiles were initially recorded in the laboratory on the assumption that the first point at which a velocity could be recorded was $z = 0$. However, as the measuring volume cannot measure up to the wall (see Figure 4.4), a slight offset was present on the velocity data on the basis of this assumption. In theory, this offset should be around

0.2 mm, as this is the distance required for the measuring volume to be completely free of the influence of the wall (see Figure 4.4). However, this assumption does not always hold, since at high flow rates, the data rate is high enough that reasonable measurements can be made even when the measuring volume is partially within the wall, and for very low flow rates, the data rate may be so low that the measuring volume has to be even further from the wall than 0.2 mm to obtain the first reading.

Figure 4.6 (a) shows an example of velocity readings near the wall. It can be seen that the first reading made, initially assumed as being 0 mm from the wall, has a velocity that is small, but non zero. As it is not possible to measure the velocity right up to the wall, some interpolation is required to set the offset, on the assumption that the velocity will be zero at the wall. To achieve this, the velocity profile was compared to a known boundary layer, that of Reichardt [1951], near the wall, as a basis for interpolating the offset. The offset was obtained by comparing the velocity profile near the wall to the known boundary layer on the basis of R^2. Figure 4.6 (b) shows the profile with the offset set on this basis. In this example, the offset was obtained as 0.07 mm.

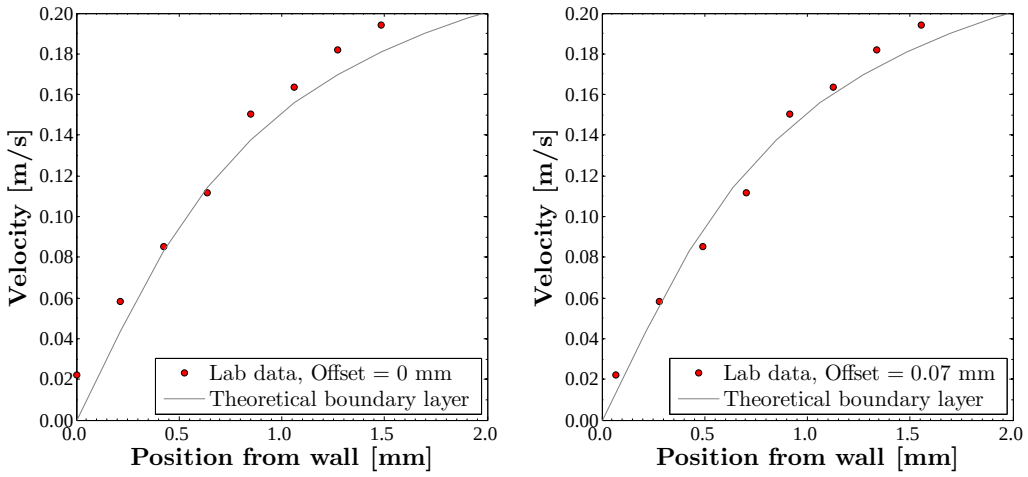

(a) (b)

Figure 4.6: *Example of offset on velocity data.*

The resolution of the LDA system depends on the bandwidth, which could be selected from three possible settings. Table 4.2 summarises the bandwidth settings and the corresponding resolutions.

Bandwidth $[MHz]$	**Range [m/s]**	**Resolution [mm/s]**
1.2	$-4 < u < 4$	26
0.4	$-1.33 < u < 1.33$	12
0.12	$-0.4 < u < 0.4$	4

Table 4.2: *Summary of specification of LDA system.*

4.3.5 Tracer Measurement

Dye Injection

Dye injections were made at the wall of the pipe through a small orifice connected to a peristaltic pump. The pump injected Rhodamine WT through the orifice, in to the flow from a 2 litre sump, for a 1 second period at a speed of 300 rpm.

Concentration Measurements

Measurements of the concentration of the dye within the main test pipe were made using 6 Turner Designs series 10 Fluorometers. Table 4.3 gives the location of the instruments along the main test pipe.

Instrument	1	2	3	4	5	6
Distance from injection [m]	2.68	4.89	7.08	8.92	10.98	13.06

Table 4.3: *Distance of instruments from injection point.*

The instruments provide an output voltage between $0 < v < 5$ as a linear response to the cross-sectional mean concentration of Rhodamine WT in the measuring volume. To relate the output voltage to a concentration, the instruments were calibrated.

To calibrate the instruments, the system was re-circulated with a known concentration of Rhodamine WT, between $0 < ppb < 100$. For each run, dye was added to bring the system to a target concentration. Initial tests showed that the system took approximately 20 minutes to become well mixed. Thus, the system was re-circulated for 25 minutes before the output was logged. The voltage output for all 6 instruments was logged at 30 Hz for 300 seconds after the initial 25 minuets of re-circulation. The concentration of the system was obtained by measuring the concentration of a sample from the sump using a pre-calibrated, bench top Series 10 fluorometer. For each run, six repeat measurements of the sump concentration were made. The sump measurements were made throughout the 300 second log period,

to enure a constant concentration was maintained through the logging period.

For each test program using the 6 fluorometers, the instruments were calibrated before the test series to obtain the calibration relationship, and after the test series to ensure that the calibration relationship had been maintained. Figure 4.7 shows an example of a calibration for all 6 fluorometers.

Initial tests conducted on the fluorometers and data collected for the calibrations showed that the instruments could detect a change in concentration of $< 1ppb$.

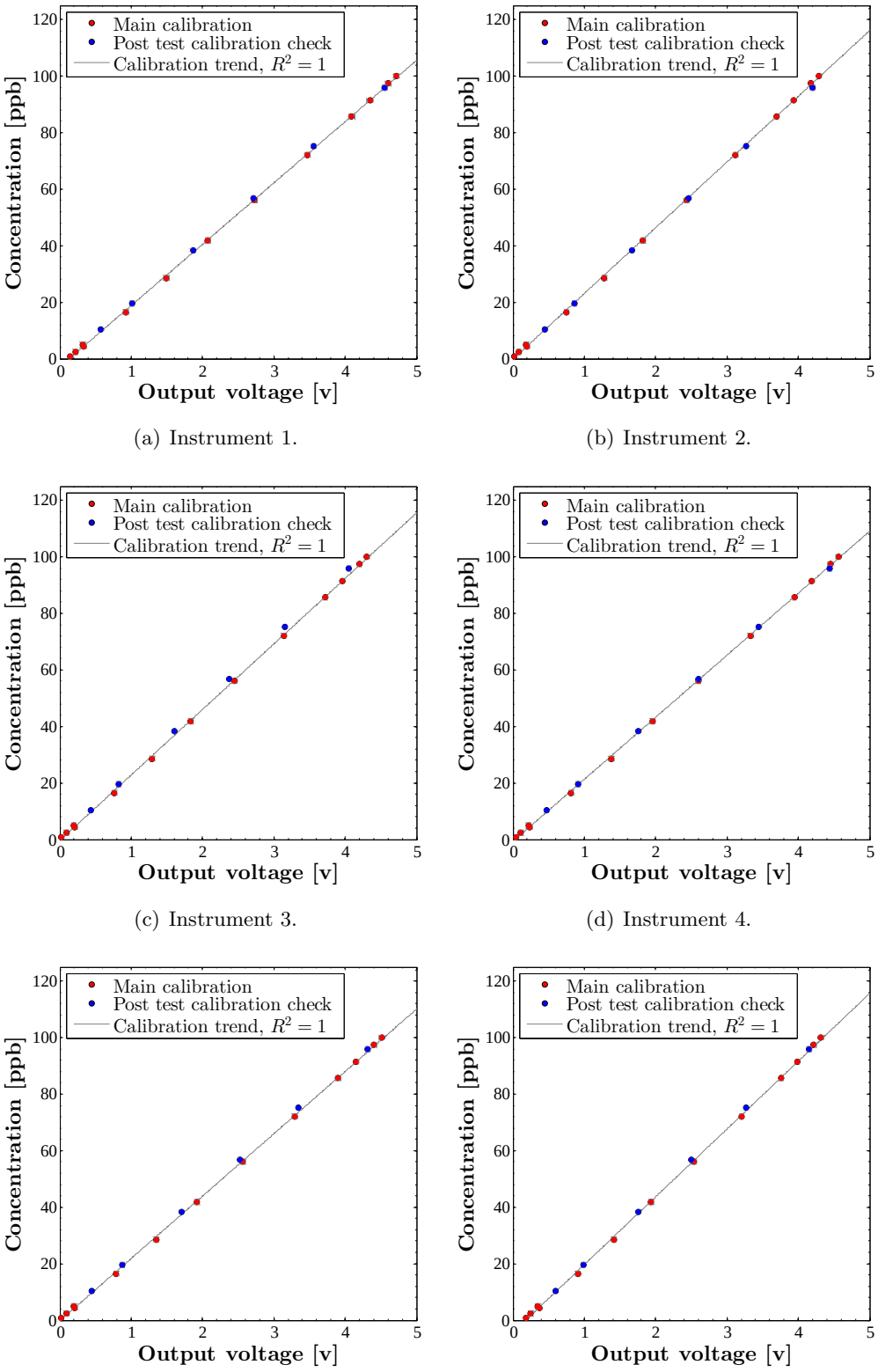

(a) Instrument 1.

(b) Instrument 2.

(c) Instrument 3.

(d) Instrument 4.

(e) Instrument 5.

(f) Instrument 6.

Figure 4.7: *Example calibration of fluorometers.*

4.4 Test Programs

4.4.1 Friction Factor for Steady Flow

Experimental Procedure

The friction factor was calculated on the basis of the static head loss over a length of pipe on the facilities main test section. The static head at a given location was measured using a manometer, which was attached to the pipe through a pressure tapping. Head loss was measured over lengths of 10 and 2.5 metres for a range of discharges. For each run, the up and downstream static head were each measured 5 times, and the head loss was considered as the difference between the mean up and downstream static head. The discharge was obtained using the electromagnetic flow meter, and was considered as the mean discharge recorded over a period of 180 seconds, logged at 30 Hz.

Two main test series were conducted, designated 'Test 1' and 'Test 2'. Test 1 was the primary test, with the head loss calculated over a length of 10 metres. Test 2 was undertaken to obtain head loss at higher discharges than were possible for Test 1, by measuring head loss over a shorter length, 2.5 metres. The maximum possible Reynolds Number at which head losses were obtained was around $Re = 35000$, as above this discharge, the static head at the upstream pressure tapping exceeded the maximum possible evaluation of the manometer. For each test, three repeat trials were conducted. Table 4.4 summariness the test program.

Test	Length [m]	Range	Trial	Number of Runs
SH1	10	$1500 < Re < 27000$	1	47
			2	44
			3	26
SH2	2.5	$4500 < Re < 35000$	1	11
			2	21
			3	13

Table 4.4: *Summary of test series for head loss. 'SH' denotes tests for head loss under steady flow conditions.*

4.4.2 Velocity Profile for Steady Flow

Experimental Procedure

Velocity data were recorded as a longitudinal velocity time series at a particular radial position across the pipe. The recordings were made using the LDA system described in Section 4.3.4.

For each profile, the flow was established, and the discharge was obtained volumetrically 3 times before and 3 times after each test. For each test, the velocity time series was recorded over a certain period of time at various radial locations between the top to the bottom of the pipe.

Seeding particles of 'Timiron super silk' were added at each run to ensure that the minimum data rate did not fall below approximately 100 Hz. Table 4.5 summarises the test programme.

Test	**Reynolds Number**	**Bandwidth** $[MHz]$
SQ1	51910	1.20
SQ2	19740	0.40
SQ3	9590	0.40
SQ4	7900	0.40
SQ5	6020	0.40
SQ6	5030	0.40
SQ7	4890	0.40
SQ8	4070	0.12
SQ9	3230	0.12
SQ10	3000	0.12
SQ11	3000	0.12
SQ12	2620	0.12
SQ13	2500	0.12
SQ14	2440	0.12
SQ15	2210	0.12
SQ16	2170	0.12
SQ17	2000	0.12

Table 4.5: *Summary of test series for the velocity profile. 'SQ' denotes tests for the velocity profile under steady flow conditions.*

Pre-analysis data processing

Figure 4.8 shows 4 examples of the recorded velocity time series, including examples near the wall and near the centreline for a relatively high and relatively low discharge. It can be seen that several outliers are present on the velocity data signals. Outliers were assumed as any value present at +/- 2 standard deviations of the mean value. Figure 4.9 shows the time series with the outliers removed.

The majority of velocity time series were recorded for a period of 60 seconds, with the mean velocity calculated as the mean value over the entire 60 second period. Figure 4.10 (b) - (d) shows values for the mean velocity calculated over increasing periods of time from 0 - 60 seconds. It can be seen that, even at a low flow rate relatively near the wall, the mean velocity has obtained a relatively stable value, independent of averaging time by 60 seconds.

The only exception to the 60 second averaging time was results near the centreline for the velocity profile recorded at $Re = 51909$, the highest flow rate considered. Near the centreline at this flow rate, the data rate was relatively high (around 800 Hz), leading to there being insufficient space to log 60 seconds of data on the data logging device. Thus, in this region, time series were recorded for 45 and 30 second periods, depending on the size of the files produced. From Figure 4.10 (a), it can be seen that, even at 30 seconds, the relatively high data rate meant that the mean velocity obtained a stable value independent of averaging time.

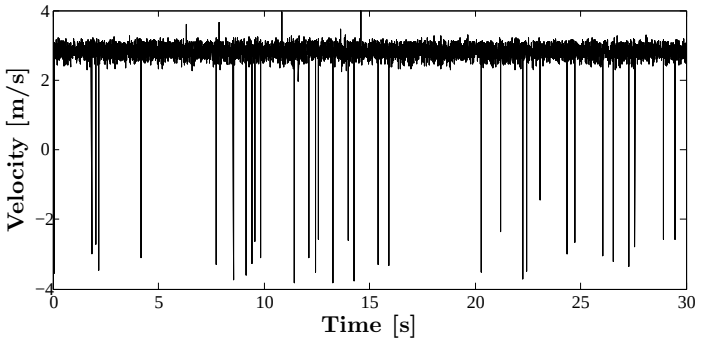

(a) High flow rate, near centreline.

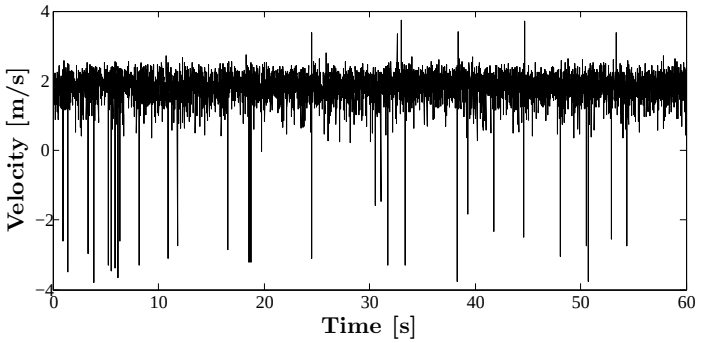

(b) High flow rate, near wall.

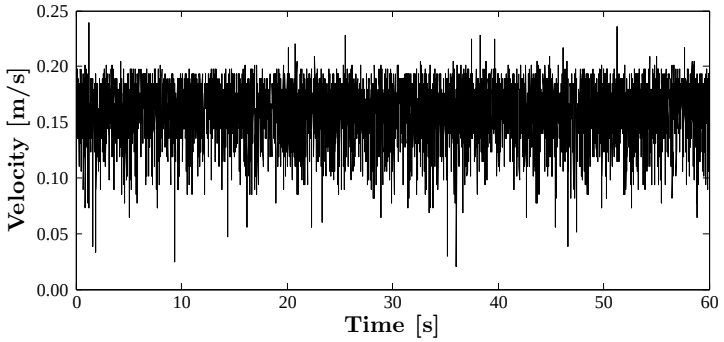

(c) Low flow rate, near centreline.

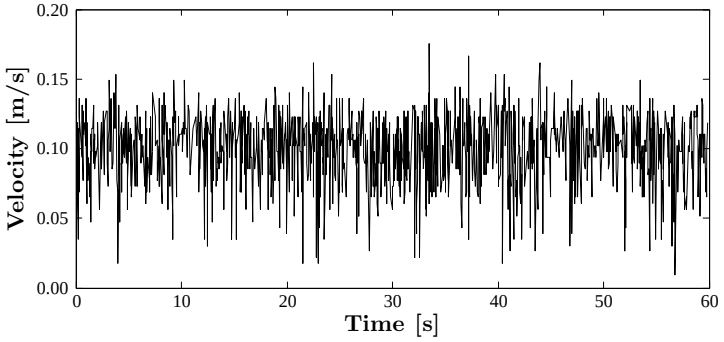

(d) Low flow rate, near wall.

Figure 4.8: *Example of raw velocity time series from LDA system.*

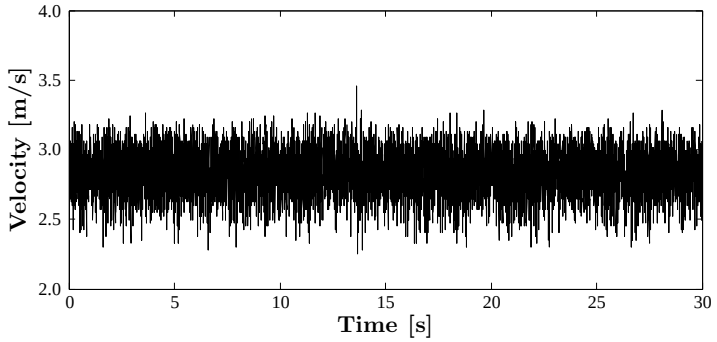

(a) High flow rate, near centreline.

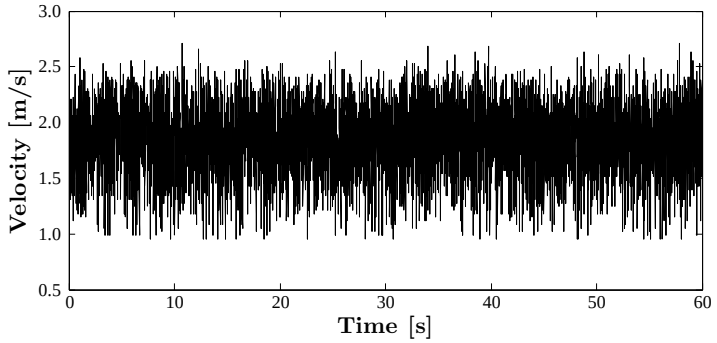

(b) High flow rate, near wall.

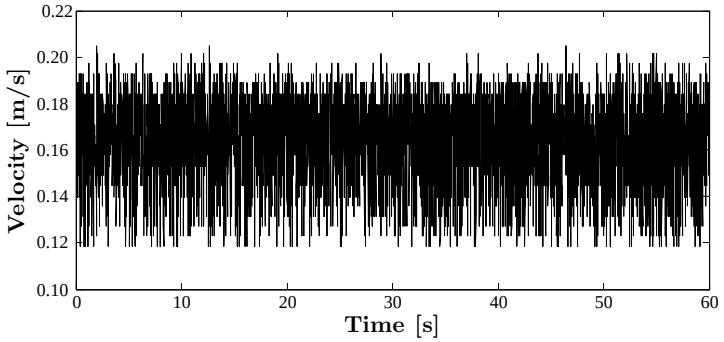

(c) Low flow rate, near centreline.

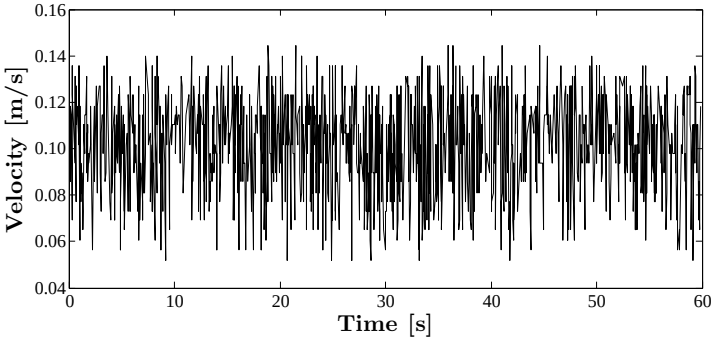

(d) Low flow rate, near wall.

Figure 4.9: *Example of raw velocity time series with outliers removed.*

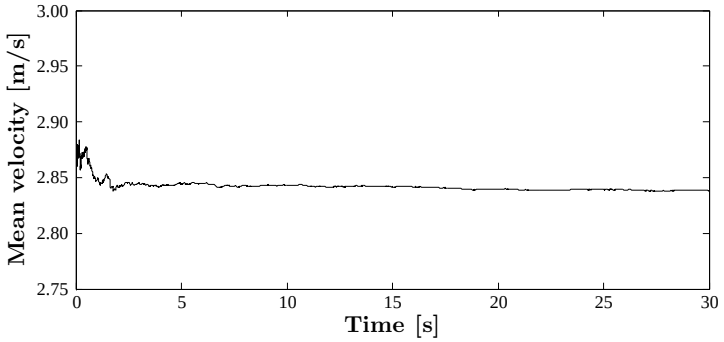

(a) High flow rate, near centreline.

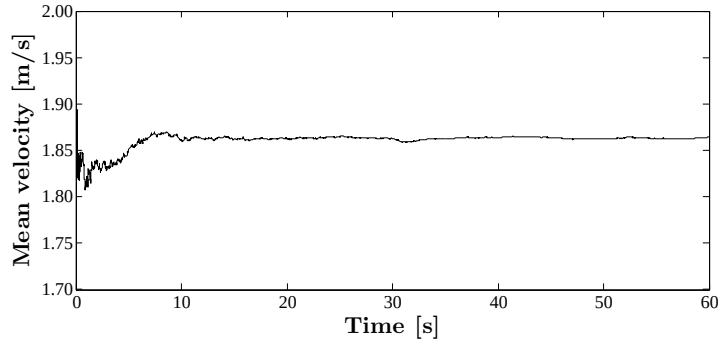

(b) High flow rate, near wall.

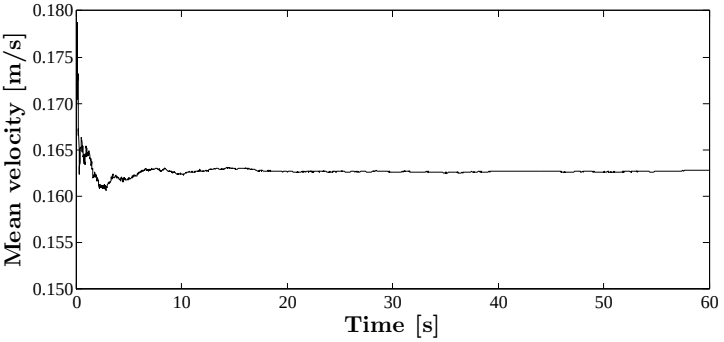

(c) Low flow rate, near centreline.

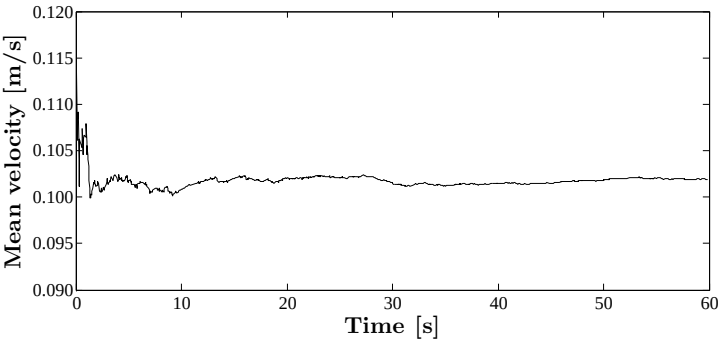

(d) Low flow rate, near wall.

Figure 4.10: *Example of mean velocity averaged over increasing periods of time.*

4.4.3 Tracer Tests for Steady Flow

Experimental Procedure

Concentration vs. time profiles were recorded by injecting a fluorescent dye, Rhodamine WT, into the flow and recording the response of 6 fluorometers to the dye. The instruments were calibrated before and after the test series, to relate the instrument's output voltage to a concentration in ppb (See Section 4.3.5).

For each discharge, three injections were made, thus three profiles were recorded at each instrument for each discharge investigated. The discharge for each test was obtained volumetrically. The discharge was measured three times before and after each set of injections, thus the measurement of the discharge represents the mean value of six repeats. Table 4.6 summariness the test program.

Test	**Reynolds Number**	**Number of Runs**
SC1	50892	3
SC2	32360	3
SC3	20500	3
SC4	20380	3
SC5	14820	3
SC6	10370	3
SC7	8110	3
SC8	8110	3
SC9	5990	3
SC10	5340	3
SC11	3790	3
SC12	3570	3
SC13	3180	3
SC14	2790	3
SC15	2670	3
SC16	2270	3
SC17	2270	3
SC18	2190	3
SC19	1820	3

Table 4.6: *Summary of test series for longitudinal dispersion in steady flow. 'SC' denotes tracer tests under steady flow conditions.*

Pre-analysis data processing

The fluorometers used for concentration measurements output a voltage from $0 < v < 5$ as a linear response to the cross-sectional mean concentration of dye in the instrument's measuring volume. This response was logged at a frequency of 30 Hz. Figure 4.11 (a) shows an example of a raw concentration vs. time profile.

The voltage output from the fluorometers was converted to a concentration in *ppb* by applying a calibration relationship to the output voltage. The calibration relationship was obtained through the procedure described in Section 4.3.5

Figure 4.11 (b) shows an example of a calibrated concentration vs. time profile, once the calibration relationship has been applied to the data.

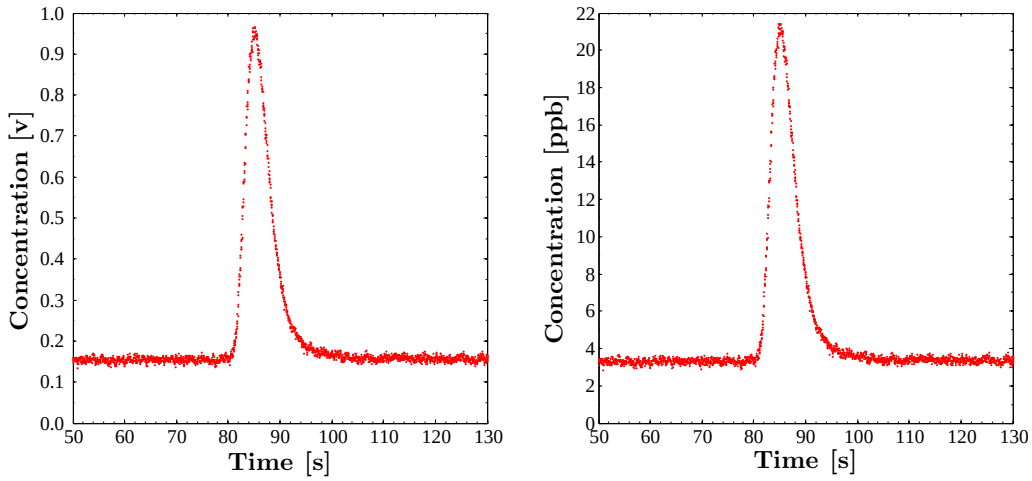

(a) Raw Profile.

(b) Calibrated Profile.

Figure 4.11: *Example of raw and calibrated concentration vs. time profile.*

From Figure 4.11 (b) it can be seen that, even after calibration, there is still a background concentration. This background is a combination of additional fluorescence from the fluid, that is not filtered out by the instrument, and the build up of dye in the system from previous injections. In order to use the profiles for analysis, the background needs to be removed, so that only the concentration profile above the background level remains.

The first step in this process is to remove the background concentration by subtracting the mean background concentration from profile. The mean background concentration was approximately constant for the duration of each test within the series, with a mean difference between the first and last 30 seconds of the trace of

0.03 ppb, with a standard deviation of 0.02 ppb. Therefore, the mean background concentration was assumed as the mean value of the first 30 seconds of each trace, which was subtracted from each profile. Figure 4.12 (a) shows an example profile with the background concentration removed.

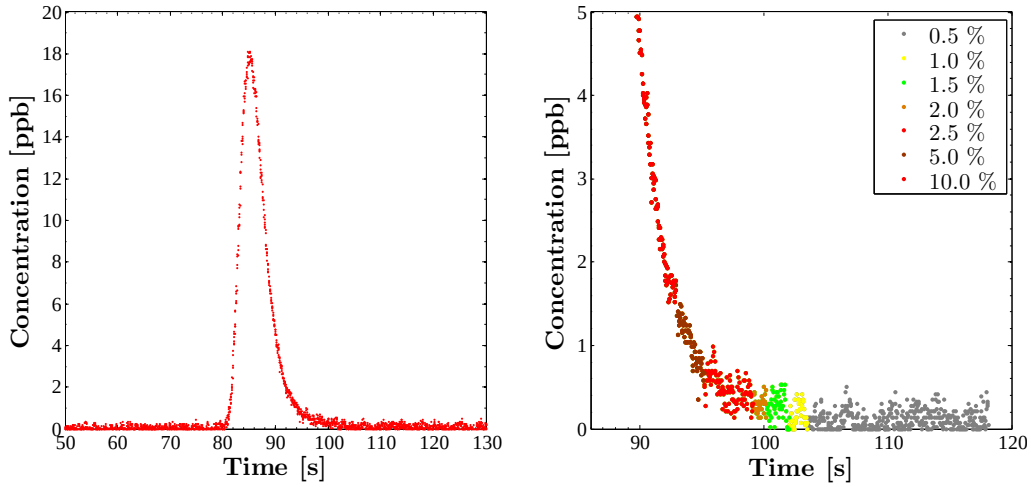

(a) Profile with background removed.

(b) Trailing edge of profile for various cut off percentages.

Figure 4.12: *Example of profile with background removed and trailing edge of profile for various cut off percentages.*

From Figure 4.12 (a), it can be seen that, although removing the mean background concentration removes the majority of the background, a layer of small but non-zero values still remains. These values are scatter above the mean, and thus are not removed by simply subtracting the mean background concentration. To obtain a profile suitable for analysis, a start and end point of the profile has to be defined, however, the scatter makes the determination of a definite start and end of the profile difficult. One method to overcome this problem is by defining the start and end locations as a point at which the signal drops below a certain percentage of the profile's peak concentration. The approach adopted was to define the start and the end locations as the point at which ten consecutive data points fell below a certain percentage of the peak. Figure 4.12 (b) shows an example profile where the cut-off point has been defined as 10, 5, 2.5, 2, 1.5, 1 and 0.5 % of the peak concentration. The goal of choosing what percentage of the peak to use is to find a value that incorporates the whole profile, whilst minimising the amount of background scatter included. From Figure 4.12 (b), it can be seen that when the

cut-off is defined as 10 %, a non-negligible portion of the profile's trailing edge is cut off, whereas when the cut-off is defined as 0.5 %, a large amount of background scatter is incorporated in the profile. Defining the cut-off as 1 % appears a good compromise, incorporating the entire profile, whilst only including a small amount of scatter. For this reason, the default cut-off value for the present analysis was defined as 1 %.

Figure 4.13 shows an example final profile with the background removed, and start and end locations defined through the procedure described above.

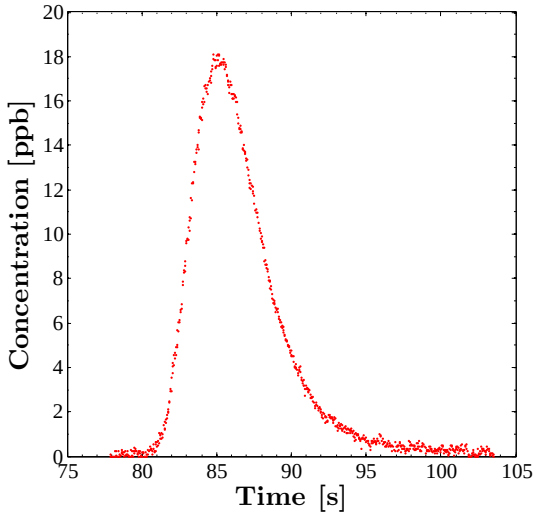

Figure 4.13: *Example profile which has had background removed, and start and end location defined.*

4.4.4 Tracer Tests for Unsteady Flow

Experimental Procedure

For unsteady flow, tracer tests were conducted within various configurations of unsteady discharge transients. The discharge was measured as an instantaneous time series using the electromagnetic flow meter, and was logged at 30 Hz. For each run, an initial discharge was set, and an injection was made into the initial steady discharge. The discharge was then accelerated or decelerated to a final discharge. Injections were then made within the discharge transient, and a final injection was made into the final steady discharge. The discharge transients were controlled by the pump's digital controller, were at a set transient time, the controller instructed the pump to linearly increased or decrease its speed, on the basis of a pre-set gradient. The injections were made by the peristaltic pump described previously, which was computer controlled, and instructed to inject at set times within the discharge transient. Each discharge transient was repeated 5 times, thus for every point an injection was made before, during or after an unsteady transient, 5 concentration profiles were obtained. Table 4.7 summariness the test program.

Test	**Initial Reynolds number**	**Final Reynolds number**	**Approximate transient time**	**Number of injections per run**	**Number of runs per test**
UC1	6500	50000	60	5	5
UC2			10	4	5
UC3			5	4	5
UC4	50000	6500	60	5	5
UC5			10	4	5
UC6			5	4	5
UC7	2700	50000	60	4	5
UC8			10	3	5
UC9			5	3	5
UC10	50000	2700	60	4	5
UC11			10	4	5
UC12			5	4	5

Table 4.7: *Summary of test series for longitudinal dispersion for unsteady flow. 'UC' denotes tracer tests under unsteady flow conditions.*

Pre-analysis data processing

The concentration profile's recorded for unsteady flow were processed through the same procedure described for steady flow.

Figure 4.14 (a) shows an example discharge transient for unsteady flow. From Figure 4.14 (a) it can be seen that the discharge signal is relatively noisy. The final discharge data used for analysis was smoothed using a 31 point moving average, where the discharge single is recorded at a constant time step of dt = 0.0333 s. Figure 4.14 (b) shows a comparison between raw and the smoothed discharge signal.

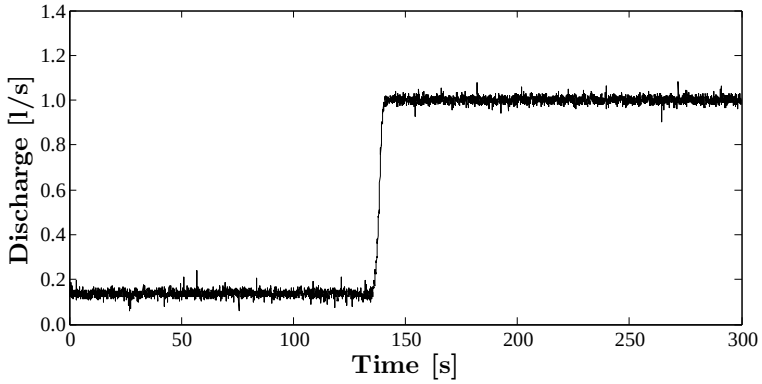

(a) Raw discharge.

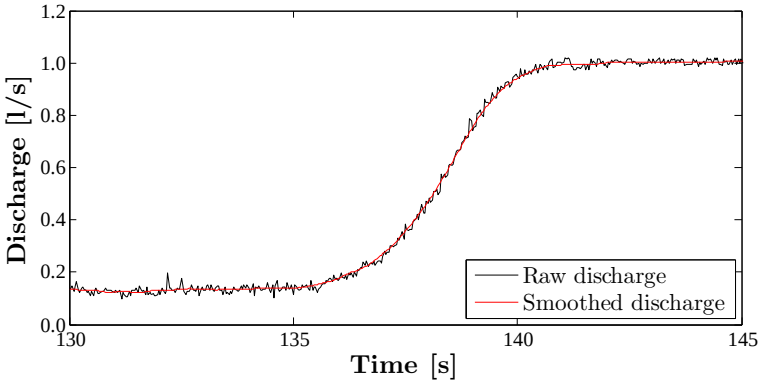

(b) Smoothed discharge.

Figure 4.14: *Example of raw and smoothed discharge signal.*

For each set of injections into a particular discharge transient, 5 repeat readings were taken. Thus, each discharge transient at a given gradient was repeated 5 times. Figure 4.15 shows a comparison between the recorded discharge for 5 repeat discharge transients, for transient times of approximately 5, 10 and 60 seconds, the three cases considered.

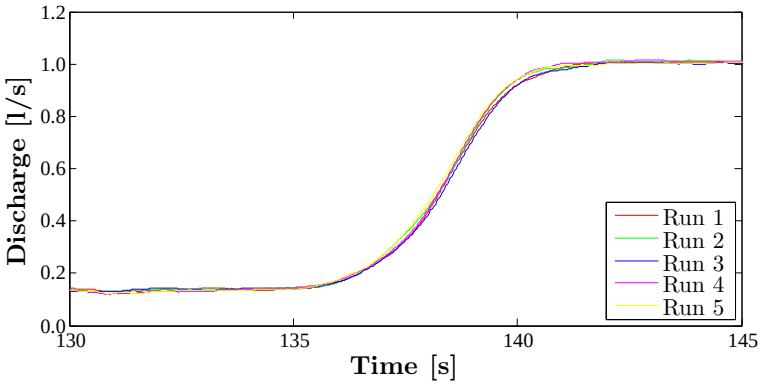

(a) Transit time = 5 seconds.

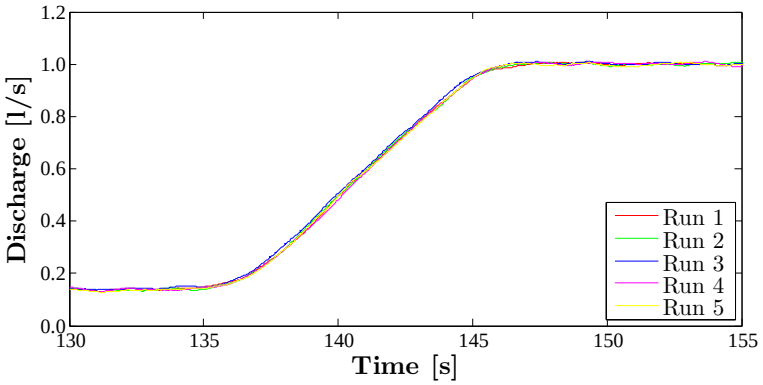

(b) Transit time = 10 seconds.

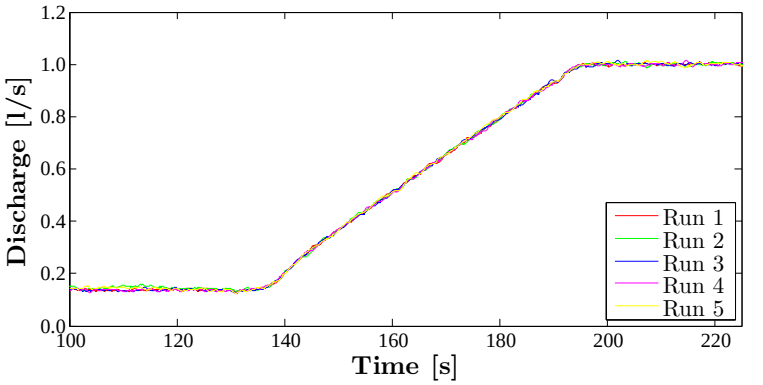

(c) Transit time = 60 seconds.

Figure 4.15: *Comparison between repeat discharge transients.*

Chapter 5

Results, Analysis and Discussion for Steady Flow

—

5.1 Introduction

This chapter presents the results, analysis and some discussion for all the tests undertaken within steady flow for the present work. Section 5.2 considers the hydraulics of steady flow for $2000 < Re < 50000$, within the facility used, and on the basis of the observed data, suggests the critical points for the transitions between laminar, transitional and turbulent flow. Section 5.3 considers the the effects of the Reynolds Number, and thus the changing hydraulics of the flow with Reynolds Number discussed in Section 5.2, on longitudinal dispersion for steady flow, for $2000 < Re < 50000$. Section 5.4 uses the hydraulic data presented in Section 5.2 to validate and modify the parameters used within the numerical model presented in Chapter 3, and to validate the final model against the dispersion data presented in Section 5.3.

5.2 Hydraulics of Steady Flow

This section presents results and analysis for an experimental investigation of the hydraulics of steady pipe flow for the range of discharges corresponding to approximately $2000 < Re < 50000$. As discussed in Chapter 2, the flow's hydraulics have been shown to have a significant impact upon longitudinal dispersion (See Chapter 2, Section 2.11 and 2.12). This section will be used to gain insight into the flow regimes

occurring through out this range of Reynolds Numbers within the experimental facility used for all subsequent experimental tests. The experimental investigation will consider the friction factor and the flow's mean longitudinal velocity profile as indicators of the flow's hydraulic characteristics, with a view to suggesting critical points for the transitions between laminar, transitional and turbulent flow.

5.2.1 Friction Factor

Analysis

The test program for the friction factor for steady flow is described in Chapter 4, Section 4.4.1.

Head loss was calculated for each run at a given discharge as the difference between the mean head of 5 repeat readings from the up and downstream manometers. The mean velocity was obtained from the systems discharge.

For a given head loss and cross-sectional mean velocity, the friction factor can be calculated be re-arranging Equation 2.22, such that:

$$f = h_f \left(\frac{d}{L}\right)\left(\frac{2g}{\bar{u}^2}\right) \tag{5.1}$$

Results

Figure 5.1 shows the results for the friction factor against Reynolds Number for Tests 1 and 2, from which three distinct trends can be seen. A turbulent trend, where the friction factor is relatively high and linear in log-log coordinates, a laminar trend where the fiction is relatively low and linear in log-log coordinates, and a transitional trend, linking the two with a 'S' type shape.

By considering the trends in the friction factor data, critical points can be suggested for the transition from laminar to turbulent flow. The indeterminate nature of flow within the transitional region makes it difficult to estimate definitive thresholds. This can be highlighted by considering each data set alone, from which it can be seen that, to some degree, different critical points and transitional trends occur for each of the three repeat tests conducted within this region. However, it appears that for each run, the flow conforms to a fully turbulent trend for $Re > 5000$, and a fully laminar trend for $Re < 2500$.

To use experimental results for the friction factor to determine the frictional velocity for use with the turbulent velocity profiles discussed in the next section, and to gain further insight into the trends in the data, a trend was fitted to the friction factor data for $2000 < Re < 50000$.

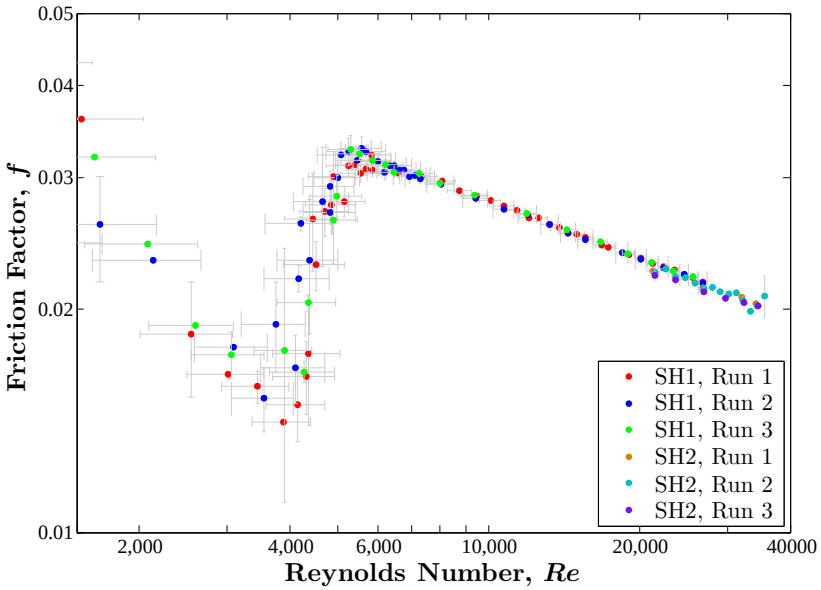

Figure 5.1: *Friction factor vs. Reynolds Number for Test 1 and Test 2.*

Initially, three trends, linear in log-log coordinates, were fitted to the laminar, transitional and turbulent data respectively:

$$P_1 = \frac{50.1}{Re} \tag{5.2}$$

$$P_2 = \frac{2.132 \times 10^{-9}}{Re^{-1.927}} \tag{5.3}$$

$$P_3 = \frac{0.2636}{Re^{0.2442}} \tag{5.4}$$

Trends were fitted to the data between points at which the data appears to unambiguously conform to a certain regime. For laminar flow, P_1 was fitted to data for $1500 < Re < 2500$. For transitional flow, P_2 was fitted to data for $3500 < Re < 5000$. For turbulent flow, P_3 was fitted to data for $Re > 6000$.

Figure 5.2 shows a comparison between the trends presented in Equations 5.2, 5.3 and 5.4 and the experimental data of the present work for the friction factor. The trends provide good fits to the laminar and turbulent data, and a reasonable fit to the transitional data, with a reduced goodness of fit due to the increased scatter caused by the nature of the flow in this region.

The expression proposed by Yang and Joseph [2009], as defined in Equation 2.27, can be used to smoothly link friction factor trends for each regime in a manner

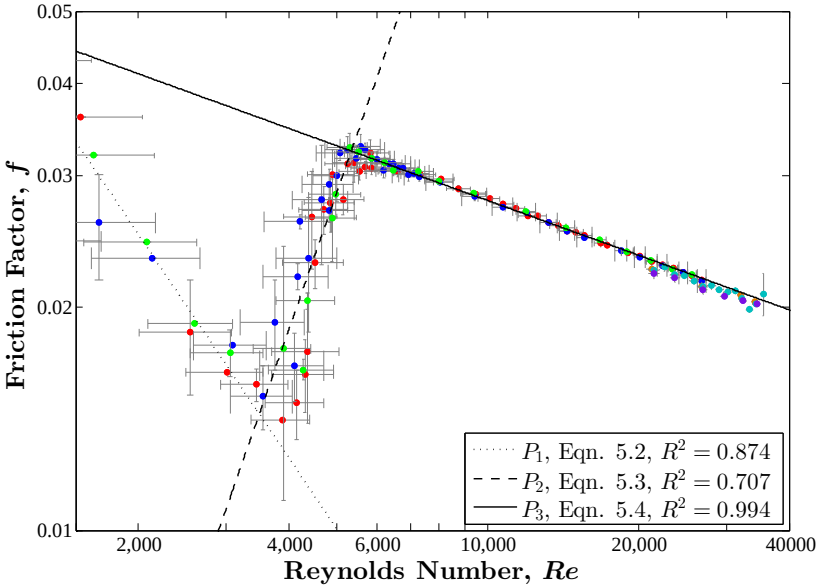

Figure 5.2: *Comparison between trends for the friction factor for laminar, transitional and turbulent flow, as defined in Equations 5.2, 5.3 and 5.6, and the experimental data of the present work.*

consistent with the data (See Chapter 2, Section 2.4.4). For the present work, the expression of Yang and Joseph [2009] was considered in the following form:

$$F_0 = P_1$$

$$F_1 = F_0 + \frac{P_2 - F_0}{[1 + (Re/Re_{c,1})^{-m_1}]^{0.5}}$$

$$f = F_2 = F_1 + \frac{P_3 - F_1}{[1 + (Re/Re_{c,2})^{-m_2}]^{0.5}} \tag{5.5}$$

Using this expression, Re_c and m were optimised to give the best possible fit to the experimental data on the basis of the criteria of fit R^2. The final expression obtained was:

$$F_0 = P_1$$

$$F_1 = F_0 + \frac{P_2 - F_0}{[1 + (Re/4020)^{-16}]^{0.5}}$$

$$f = F_2 = F_1 + \frac{P_3 - F_1}{[1 + (Re/5000)^{-60}]^{0.5}} \tag{5.6}$$

Figure 5.3 shows a comparison between the continuous function for the fric-

tion factor, as described in Equation 5.6, and the experimental data of the present work.

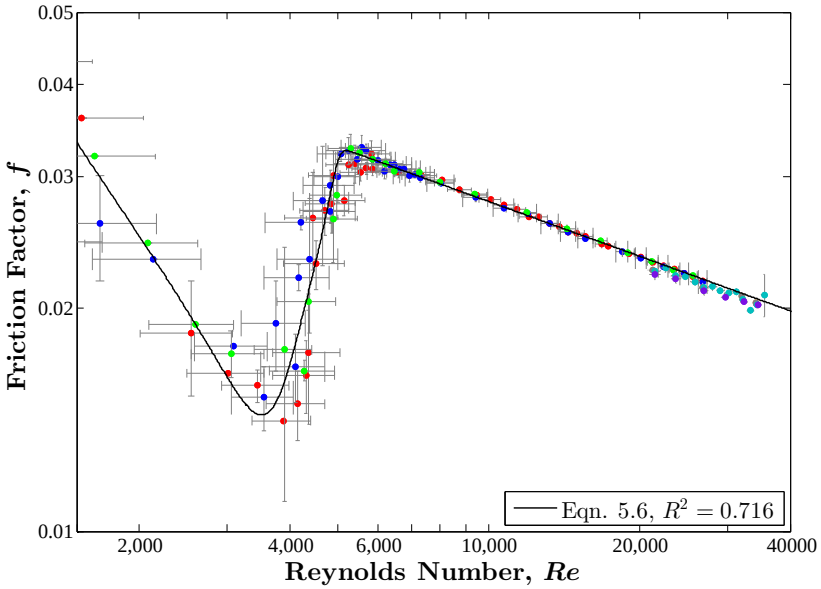

Figure 5.3: *Comparison between the continuous expression for the friction factor, as defined in Equation 5.6, and the experimental data of the present work.*

On the basis of the data for the friction factor presented within this section, it appears that the flow conforms to a fully laminar trend for $Re < 2500$, a fully turbulent trend for $Re > 5000$, and thus is transitional for $2500 < Re < 5000$. The remainder of this section will investigate these critical points further through the results for the mean velocity profile.

5.2.2 Velocity Profile

The test program for the velocity profile for steady flow is described in Chapter 4, Section 4.4.2. The following subsections present results for the mean velocity profiles for turbulent, laminar and transitional flow. For this subsection, the flow will be assumed turbulent for $Re > 5000$, transitional for $2500 < Re < 5000$, and laminar for $Re < 2500$. These critical points are suggested on the basis of the trends from the friction factor data, but will be re-evaluated on the basis of the velocity profiles presented.

Turbulent flow

Figure 5.4 shows the results for the mean velocity profile for turbulent flow for approximately $5000 < Re < 50000$. It can be seen that over this range, the profiles are approximately symmetrical, taking on a conventional 'turbulent flow' shape, with a large velocity gradient near the wall and relatively flat profile in the core. It can also be seen that the gradient of the boundary layer decreases as Reynolds Number decreases, whilst the length of the boundary layer increases.

To highlight this change in gradient and length of the boundary layer, Figure 5.5 shows a comparison between a profile at $Re = 51910$, the highest recorded turbulent profile considered, and a profile at $Re = 5030$, considered the lowest recorded turbulent profile. The results are shown with the velocity term normalised with respect to the maximum velocity, to enable easy comparison between the distribution of the two profiles. It can be seen that for highly turbulent flow, the boundary layer is relatively small and flat, whereas for low turbulent flow, the boundary layer is larger and more non-uniform.

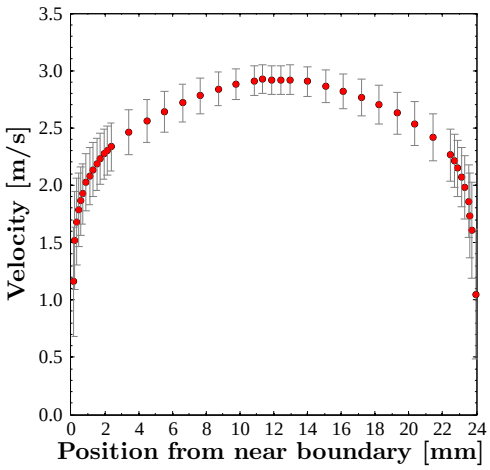

(a) Re = 51910.

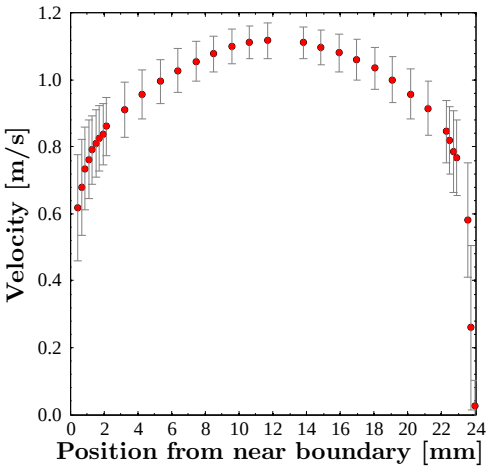

(b) Re = 19740.

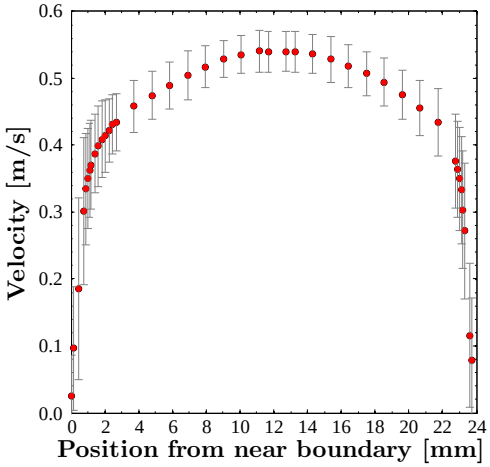

(c) Re = 9590.

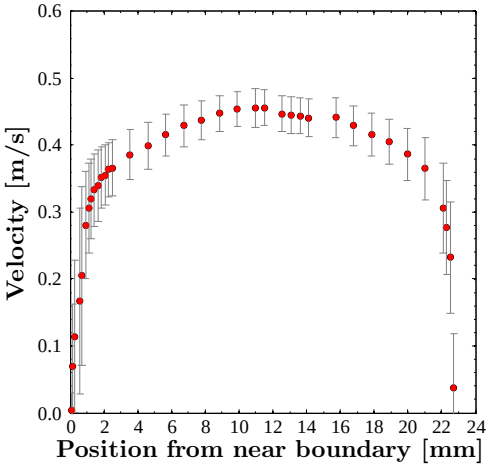

(d) Re = 7900.

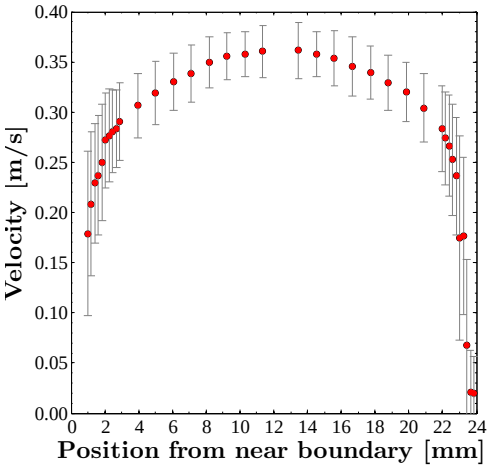

(e) Re = 6020.

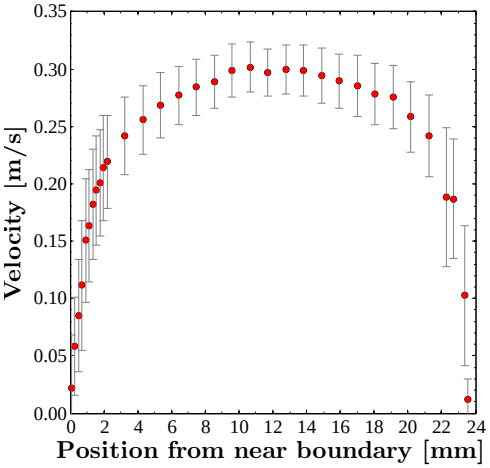

(f) Re = 5030.

Figure 5.4: *Turbulent velocity profiles.*

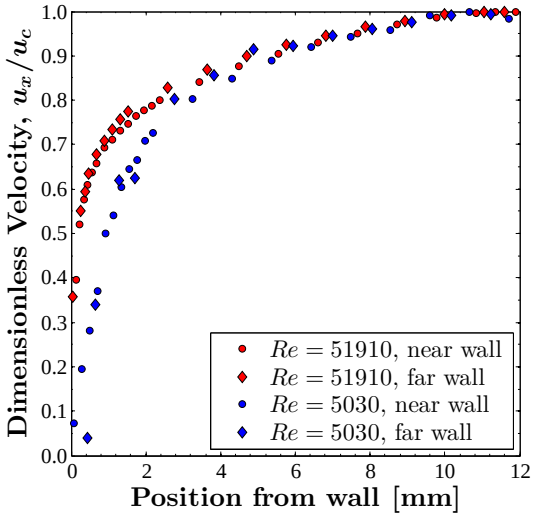

Figure 5.5: *Comparison between high turbulent velocity profile,* $Re = 51910$*, and low turbulent velocity profile,* $Re = 5030$*.*

The profiles presented in this section appear to support the suggestion on the basis of the friction factor data, that the flow is turbulent for $Re > 5000$.

Laminar flow

Figure 5.6 shows the results for the mean velocity profile for laminar flow for approximately $2500 < Re < 2000$. It can be seen that over this range, the profiles conform to approximately the same distribution, as would be expected for laminar flow.

Figure 5.7 shows a comparison between each profile, with the velocity normalised with respect to the maximum velocity, and the analytical laminar profile, as defined in Equation 2.5. Distributions are shown from the wall to the centreline, hence both sides of the profile are plotted together. Profiles are designated either 'near wall', referring to the profile recorded from the top of the pipe to the centreline, and 'far wall', referring to the profile recorded from the centre line to the bottom of the pipe. It can be seen that the profiles conform approximately to the laminar trend through out the range, but for $2500 < Re < 2170$, the profiles are asymmetrical, and thus do not provide a very good fit to the laminar profile. For $Re < 2000$, the profiles appear almost symmetrical and provide a reasonable fit to the laminar profile, thus it could be suggested that some degree of transitional characteristics are present in the profiles for $2500 < Re < 2170$, whilst the flow appears fully laminar at $Re < 2000$.

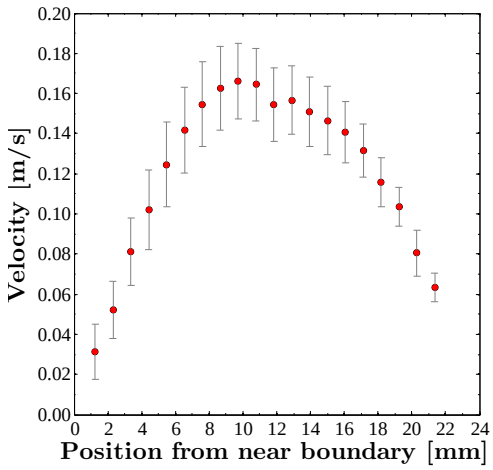

(a) Re = 2500.

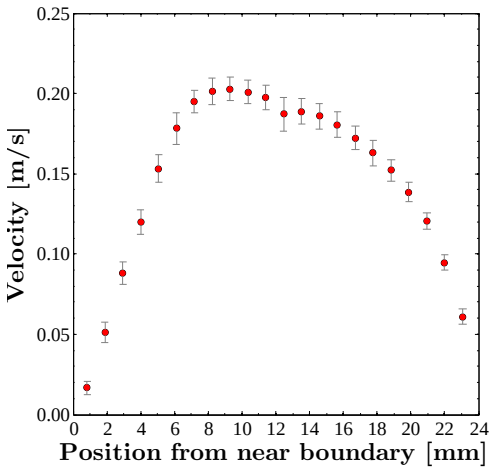

(b) Re = 2440.

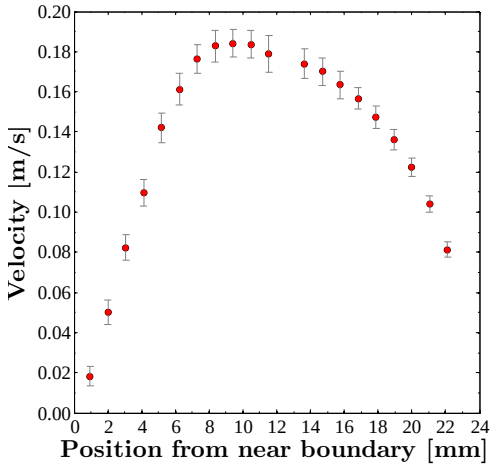

(c) Re = 2210.

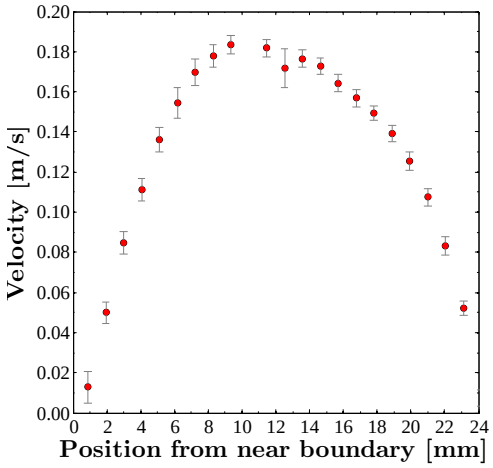

(d) Re = 2170.

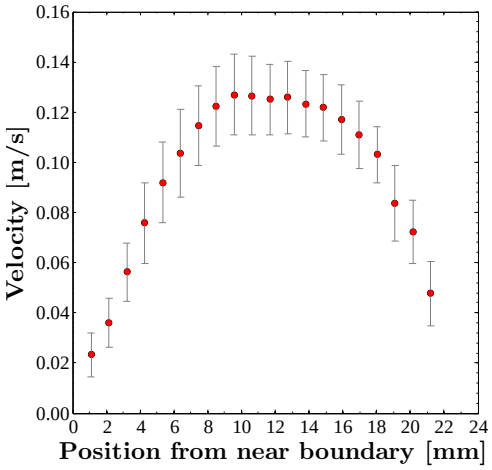

(e) Re = 2000.

Figure 5.6: *Laminar velocity profiles.*

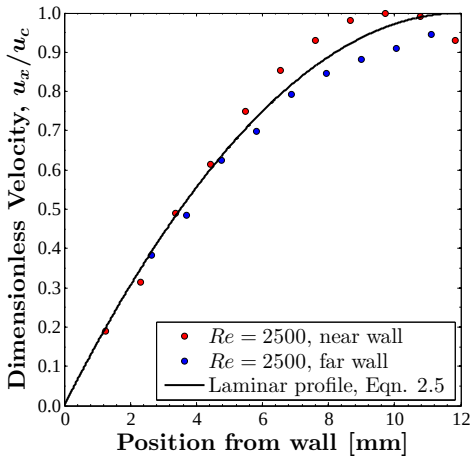

(a) Re = 2500.

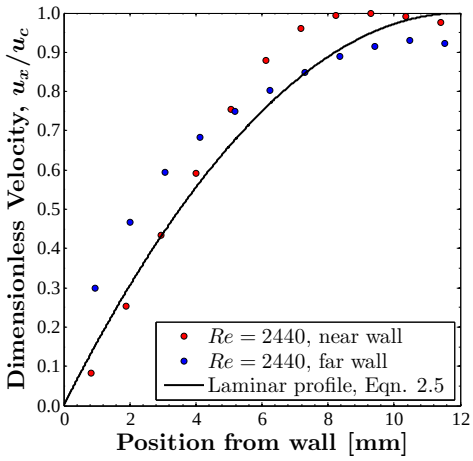

(b) Re = 2440.

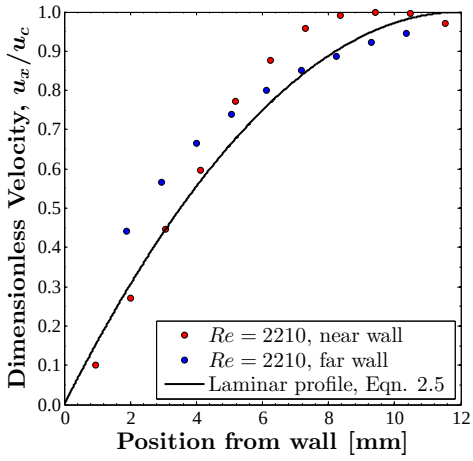

(c) Re = 2210.

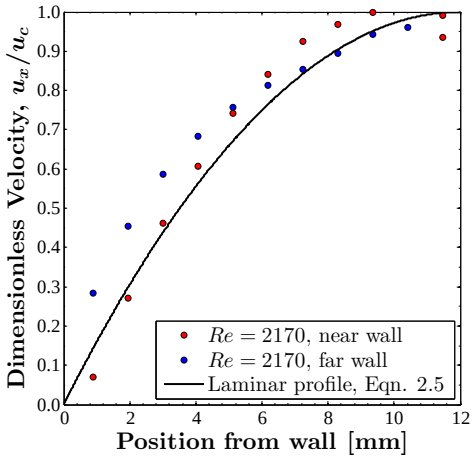

(d) Re = 2170.

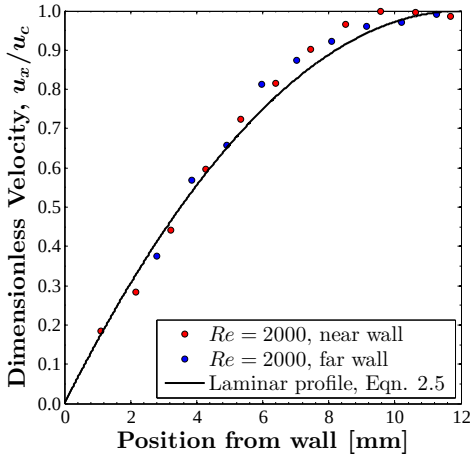

(e) Re = 2000.

Figure 5.7: *Comparison between laminar velocity profiles and analytical laminar velocity profile, as defined in Equation 2.5.*

Figure 5.8 shows a comparison between a profile at $Re = 51910$, considered the highest recorded turbulent profile, a profile at $Re = 5030$, considered the lowest recorded turbulent profile, and a profile at $Re = 2000$, considered a fully laminar profile. The results are shown with the velocity term normalised with respect to the maximum velocity, to enable easy comparison between the distribution of the three profiles.

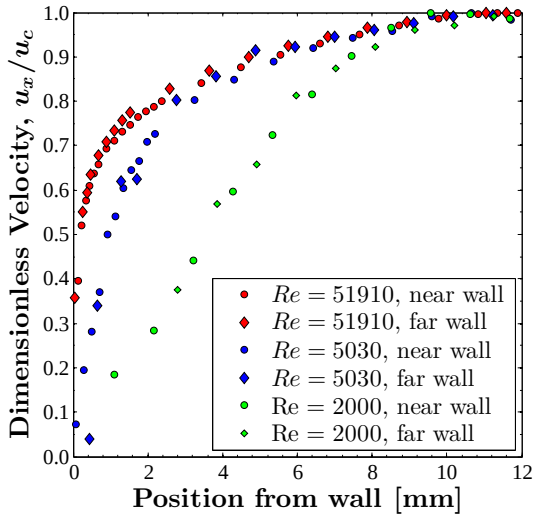

Figure 5.8: *Comparison between high turbulent velocity profile, $Re = 51910$, a low turbulent velocity profile, $Re = 5030$, and a laminar profile, $Re = 2000$.*

It can be seen that there is a large difference between the turbulent and laminar profiles. The laminar profile is far less uniform than the turbulent profiles, with a relatively small velocity gradient near the wall. It can also be seen that, although there is a distinct difference in the distribution near the wall between $Re = 51910$ and $Re = 5030$, it is relatively small when compared to the difference between the profiles at $Re = 5030$ and $Re = 2000$, despite the far smaller difference in discharge. This highlights the distinct change in the flow's hydraulics between $2000 < Re < 5000$, which corresponds to a relatively small change in discharge.

Transitional flow

Figure 5.9 shows the results of the mean velocity profile for transitional flow for approximately $5000 < Re < 2500$.

It can be seen that a variety of non-conventional shaped profiles are present within the transitional region, as might be expected under the influence of transient

turbulence. At $Re = 4890$, as shown in Figure 5.9 (a), the distribution appears to be a reasonably conventional yet distorted turbulent profile, as might be expected at the start of the transitional region. As Reynolds Number further decreases, the profiles are dominated by distinct asymmetry, appearing to be caused by a discontinuity near the centre line, on the far boundary side, leading to an abnormal boundary layer at the far wall.

Figure 5.10 shows the normalised transitional profiles, compared to turbulent and laminar profiles, to highlight the form of the transitional profiles.

The expected distribution of a transitional profile should fall somewhere between the final fully turbulent distribution, assumed as $Re = 5030$, and first fully laminar distribution, assumed as $Re = 2000$. From Figure 5.10 it can be seen that for the majority of the transitional distribution, this prediction is true for the near wall distributions. However, the non-conventional distribution at the far wall fails to fall within these limits.

The discontinuities in the far side distribution could be caused by turbulent structures present in the transitional region, caused by slight discontinuities in the experimental set-up, which do not cause a noticeable effect in fully developed turbulent or laminar flow, but are propagated by the nature of the transient turbulence in the transitional region. These structures also appear to be more pronounced, yet similar in shape, to the asymmetry near the centre line for the higher Reynolds Number 'laminar' profiles, discussed in the previous section. These discontinuities appear to have decayed by $Re = 2000$, suggesting that this is the point at which fully developed laminar flow is obtained.

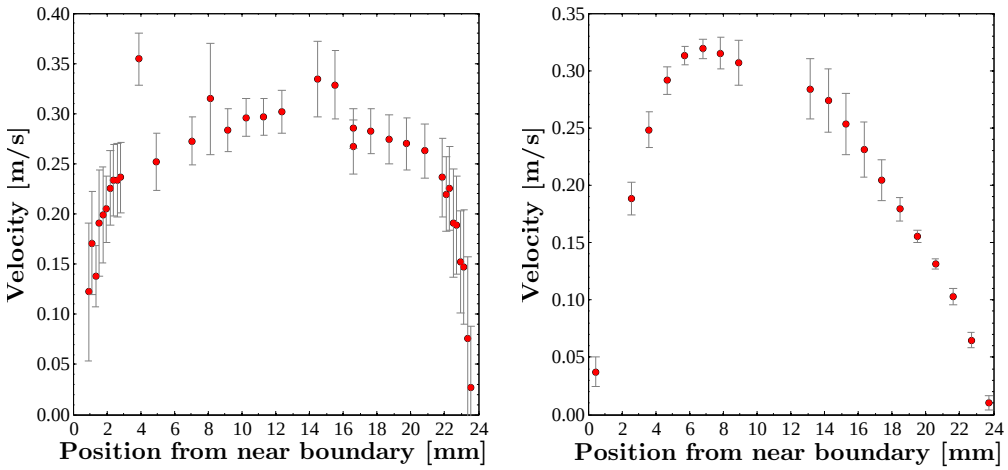

(a) Re = 4890

(b) Re = 4070

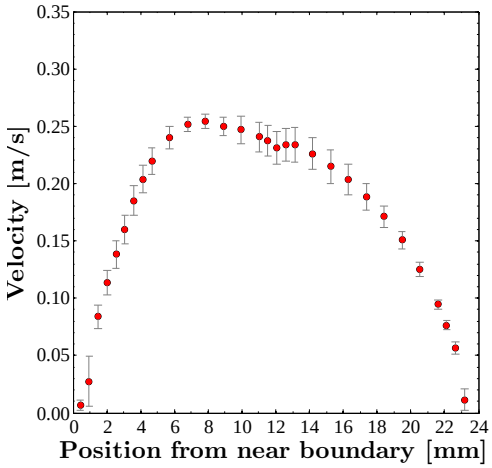

(c) Re = 3230

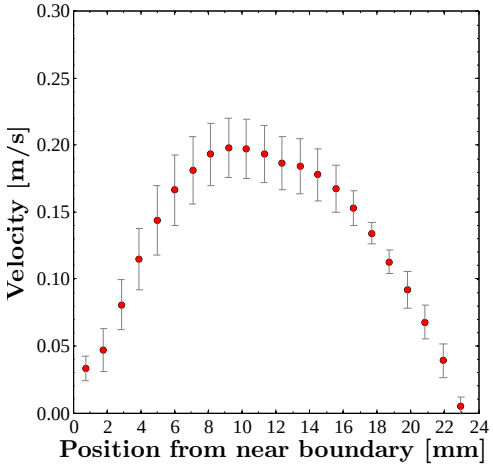

(d) Re = 3000

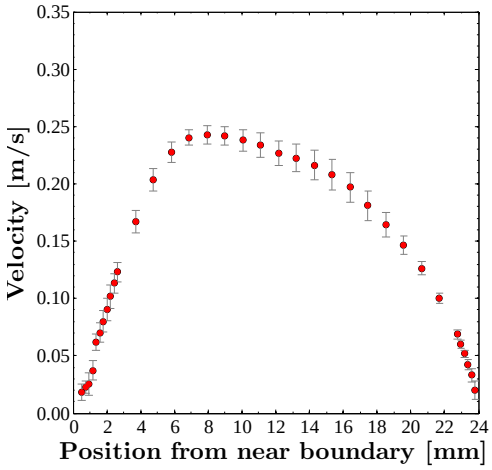

(e) Re = 3000

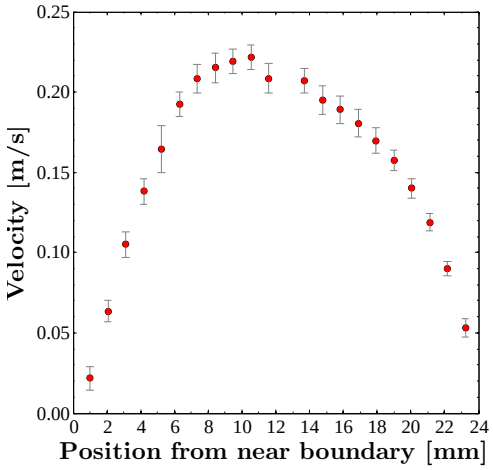

(f) Re = 2620

Figure 5.9: *Transitional velocity profiles.*

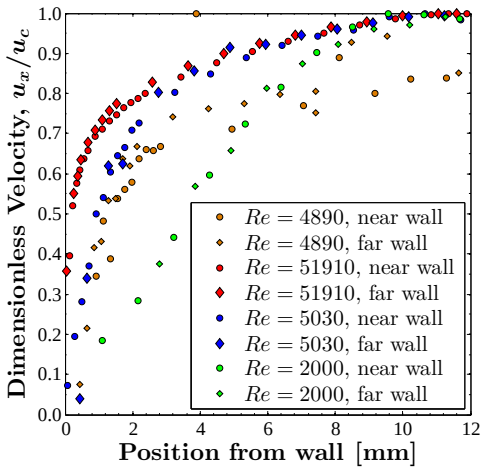

(a) Re = 4890

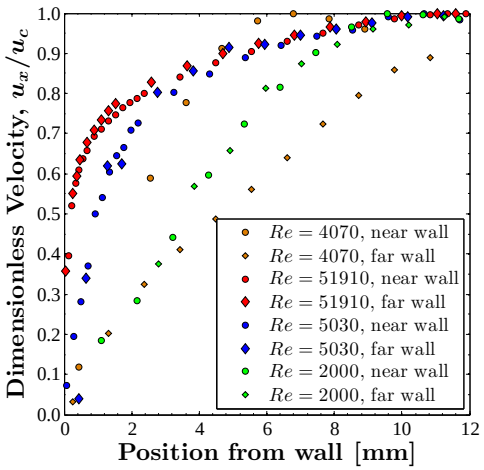

(b) Re = 4070

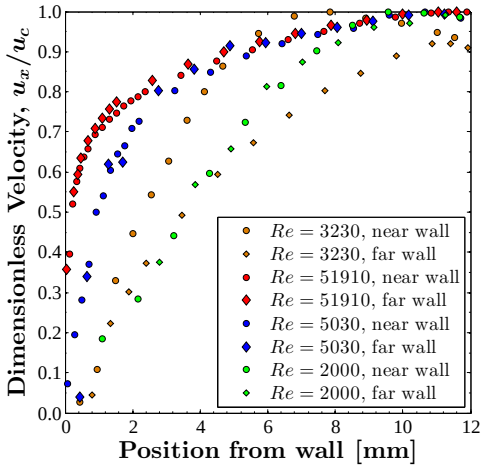

(c) Re = 3230

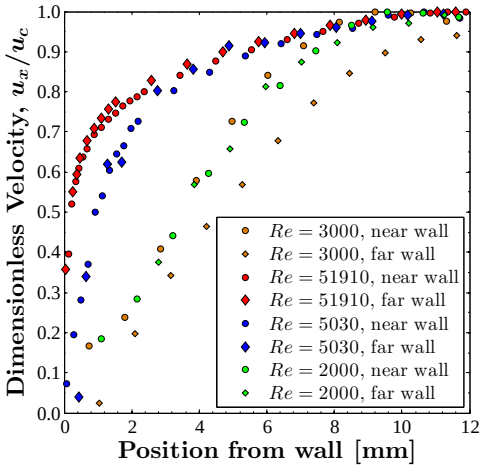

(d) Re = 3000

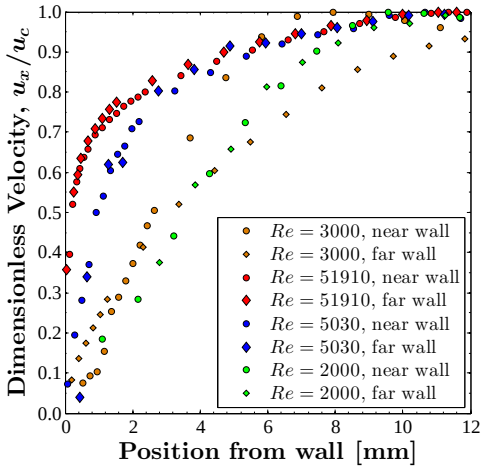

(e) Re = 3000

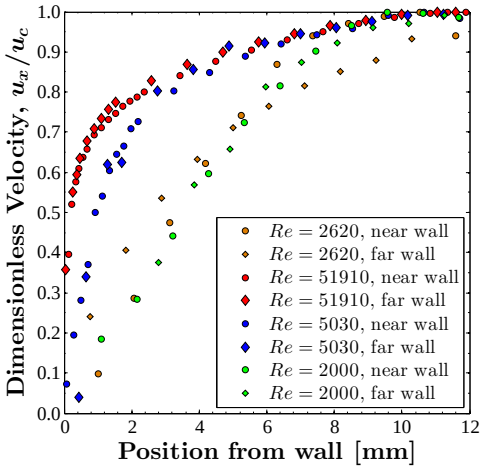

(f) Re = 2620

Figure 5.10: *Comparison between turbulent, laminar and transitional velocity profiles.*

5.2.3 Summary of hydraulic results

The aim of the section was to gain insight into the various flow regimes present within the range of flow rates for which experimental work will be undertaken for the rest of this work. Specifically, with respect to estimating critical points for turbulent, transitional and laminar flow.

The data for the friction factor gives a broad overview of the flows characteristics, and appears to suggest that the flow is turbulent for $Re > 5000$ and laminar for $Re < 2500$, with a corresponding transitional region occurring for $2500 < Re < 5000$.

The data for the velocity profiles provided a more detailed examination of the flow. This data confirmed that fully turbulent velocity profiles occur for $Re > 5000$, and that laminar like velocity profiles occur for $Re < 2500$. However, the data suggests that unambiguously fully developed laminar flow only occurs around $Re < 2000$. The slight discrepancy between the appearance of fully developed laminar flow between the friction factor and the velocity data can be attributed to the fact that the discontinuities in the laminar velocity profile that lead to this conclusion occurs near the centre line, whereas the friction factor quantifies the characteristics of the boundary layer near the wall.

On the basis of all the data considered, flow will be considered laminar for $Re < 2000$, turbulent for $Re > 5000$ and transitional for $2000 < Re < 5000$.

The nature of turbulent and transitional flow means that these limits are not proposed as absolute thresholds, but rather that at $Re < 2000$, the flow will likely be laminar and at $Re > 5000$, the flow will likely be turbulent. It is clear from the data that laminar characteristics sometimes appear at $Re > 2000$, and that turbulent characteristics sometimes appear at $Re < 5000$. However, these limits are proposed as a broad context in which to understand subsequent data collected.

5.3 Steady Tracer Results and Analysis

The following sections present tracer results for the tests investigating longitudinal dispersion for the range $2000 < Re < 50000$. The test program for the tracer tests for steady flow is described in Chapter 4, Section 4.4.3.

The section will first provide qualitative analysis of initial tracer results, and will then go on to discuss the validity of the Fickian model for all tests considered. It will conclude by quantifying the longitudinal dispersion coefficient, assuming the Fickian model is valid.

5.3.1 Pre-analysis data checking

The following subsection considers some basic checks on the quality of the data recorded. For the checks presented, data is considered between instruments 2 and 6, as these are the instruments used for the final analysis, although similar results were observed between all instruments.

Mass recovery

The mean mass recovery between instruments 2 and 6 for all runs undertaken was 98.5 %, with a standard deviation of 9.6 %.

Figure 5.11 shows the relationship between mass recovery and Reynolds Number. It can be seen that a mass recovery of around 100%, with relatively low scatter, is maintained for $5000 < Re < 50000$, the range of flow rates suggested as being fully turbulent by hydraulic data presented previously within this Chapter. However, for $Re < 5000$, the scatter in the data increases, where the mass recovery is approximately $\pm 10 - 15\%$ of the stable value maintained for turbulent flow.

Within this range, it has been suggested that the flow is transitional or laminar. It is suspected that the increase in error of the mass recovery for low transitional and laminar flow is due to the solute cloud not being fully cross-sectionally well mixed, leading to the instruments readings, which assumes a cross-sectionally well mixed measuring volume, not being fully representative of the tracers within the measuring volume.

Repeatability of traces

Figure 5.12 shows a comparison between each of the three repeat injections for a given discharge, for example tests at a range of Reynolds Numbers. Each profile is the furthest downstream profile (profile at instrument 6), normalised with respect to the maximum concentration of the profile at instrument 2. The reason the profiles are normalised with respect to the maximum concentration at instrument 2, rather than with respect to their own maximum concentrations, is so that the repeatability of the mixing process of the whole system is evaluated. In addition, the time axis is normalised with respect to the profile's centroid. Figure 5.12 (a)-(c) shows that for $5000 < Re < 50000$, a range suggested as being fully turbulent, there is good agrement between the three repeat trials. Figure 5.12 (d) shows that for $Re = 3570$, a Reynolds Number suggested as being mid transitional, there is reasonable agreement between the general trend of the profile, with the exception of the leading edge, which is slightly different for each trial. Figure 5.12 (e) shows that for $Re = 2670$, a

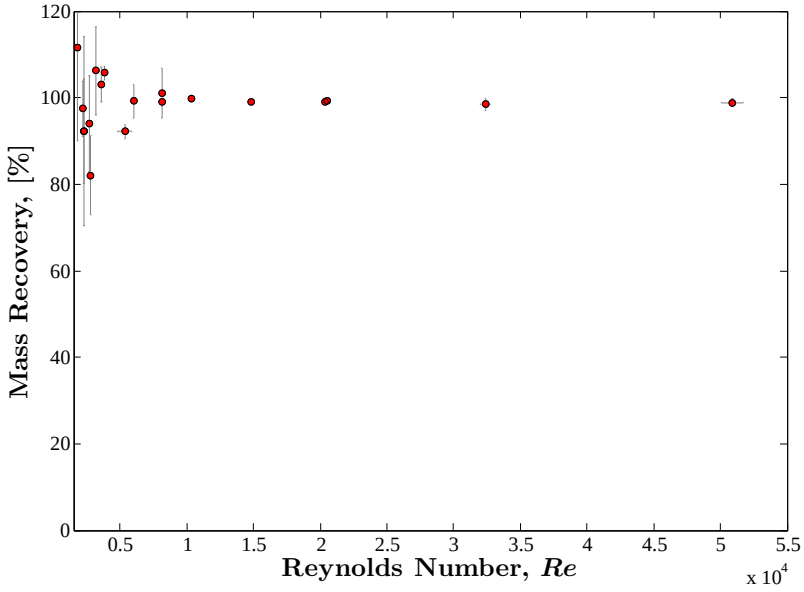

Figure 5.11: *Relationship between mass recovery and Reynolds Number.*

Reynolds Number suggested as being low transitional to laminar, although there is broad agrement between the distributions of each profile, there is some noticeable difference between each profile, in a manner more pronounced than at higher flow rates. Figure 5.12 (f) shows that for $Re = 1820$, a Reynolds Number suggesting the flow is laminar, there is very little repeatability between the distributions of the profiles.

The high agreements between the profiles presented in Figure 5.12 (a)-(c) shows that the system is capable of providing consistant, repeatable results.

The lower repeatability seen for low Reynolds Numbers, as shown in Figure 5.12 (d)-(f), coincides with the previous suggestion that the flow is transitional to laminar for these flow conditions. It is considered that the difference between the distributions in this region is due to the indeterminate, complex nature of the mixing characteristics in this range, rather than the intrinsic irrepeatability of the test, which was demonstrated as being good by the previous examples at higher flow rates.

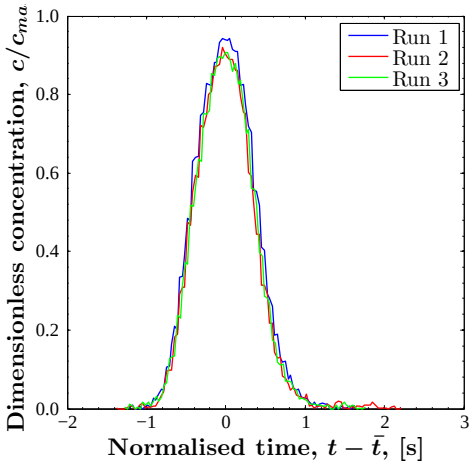

(a) Re = 50890.

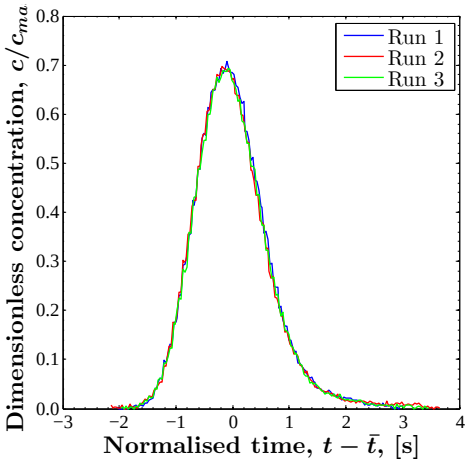

(b) Re = 20500.

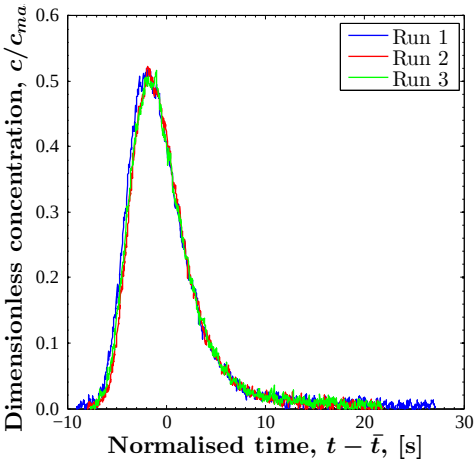

(c) Re = 5990.

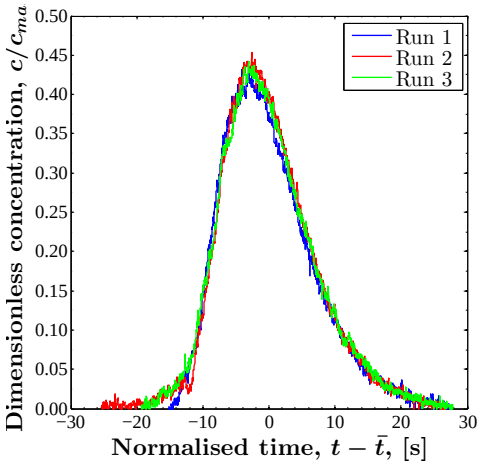

(d) Re = 3570.

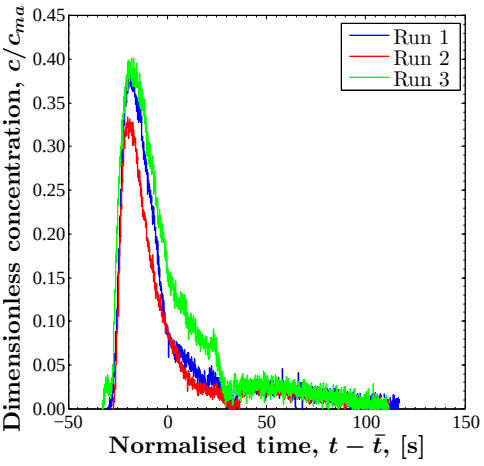

(e) Re = 2670.

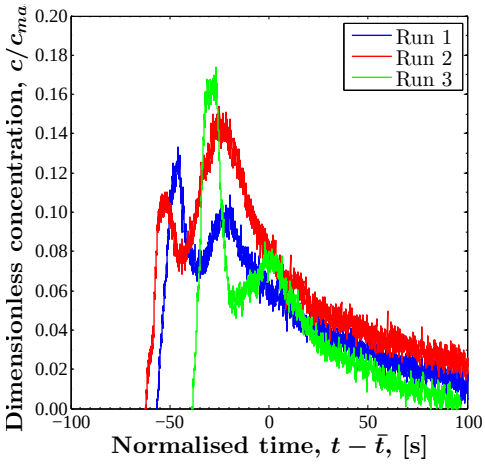

(f) Re = 1820.

Figure 5.12: *Comparison between three repeat traces, furthest downstream traces for a range of Reynolds Numbers.*

5.3.2 Initial Tracer Results

Figure 5.13 shows example results for the concentration vs. time profiles at each instrument, for a range of Reynolds Numbers.

Two general trends can be seen from the data; firstly that the degree to which the profiles have spread as they travel downstream increases with decreasing Reynolds Number. Secondly, that the skewness of the downstream profiles, and thus the degree to which the profile are not Gaussian, also increases with decreasing Reynolds Number.

Some insight into the mechanisms causing these observations can be gained by considering the data presented in Figure 5.13 in conjunction with the hydraulic data presented in the previous section. Figure 5.8 shows a comparison between the velocity profile at $Re = 51910$, considered a highly turbulent flow, $Re = 5030$, considered a low turbulent flow and $Re = 2000$, considered a laminar flow.

Figure 5.13 (a) shows tracer results for a flow at $Re = 50890$, from which it can be seen that at this Reynolds Number, little dispersion takes place as the solute cloud travels downstream. From Figure 5.8 it can be seen that for $Re = 51910$, the velocity profile is highly uniform, and close to the 'plug flow' assumption. For such flow conditions, little differential advection occurs, due to the uniformity of the velocity profile, and the solute cloud is effectively advected downstream unchanged, as shown in Figure 5.13 (a).

Within the previous section it was suggested that the flow is turbulent for $Re > 5000$. From Figure 5.8 it can be seen that between $Re = 51910$, considered a highly turbulent flow, and $Re = 5300$, a low turbulent flow near the transition, the velocity profile remains generally uniform, however as the Reynolds Number decreases, the size of the boundary layer increases, causing an increase in the non-uniformity of the velocity profile. Figure 5.13 (b)-(e), for $20000 < Re < 5000$, it can be seen that as the boundary layer grows, and the velocity profile transitions from the highly turbulent and uniform profile seen for $Re = 51910$ into the more non-uniform profile seen for $Re = 5300$, the degree to which the solute cloud spreads as it travels downstream increases. It can also be noted that whilst the profiles are reasonably symmetrical within this range, the tail of the profiles becomes more elongated as Reynolds Number decreases, as tracer begins to be retained in the laminar sub-layer.

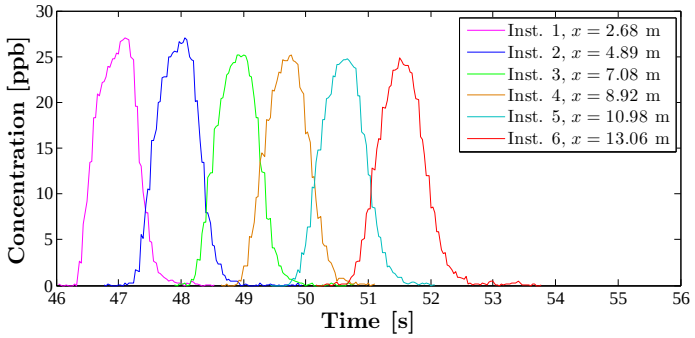

(a) Re = 50890.

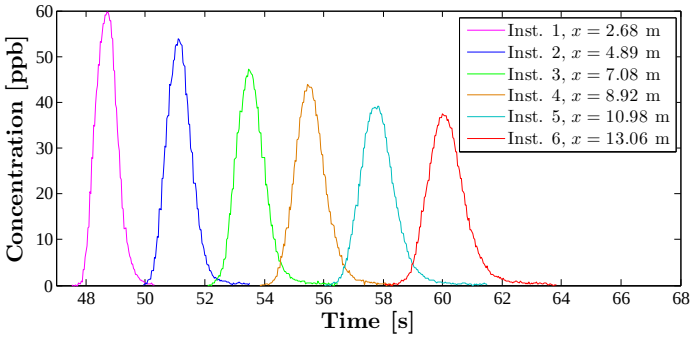

(b) Re = 20500.

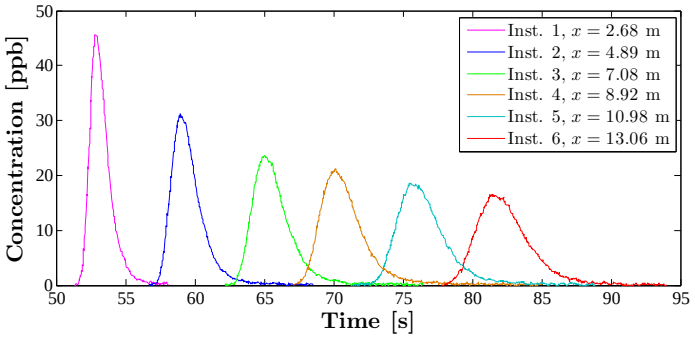

(c) Re = 8110.

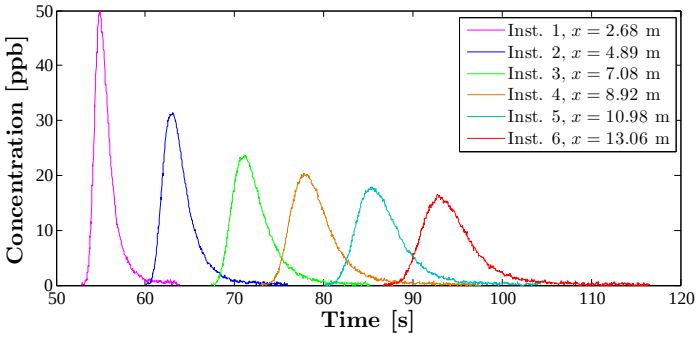

(d) Re = 5990.

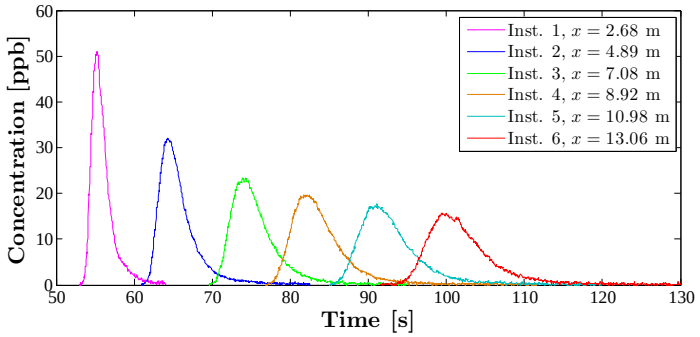

(e) Re = 5340.

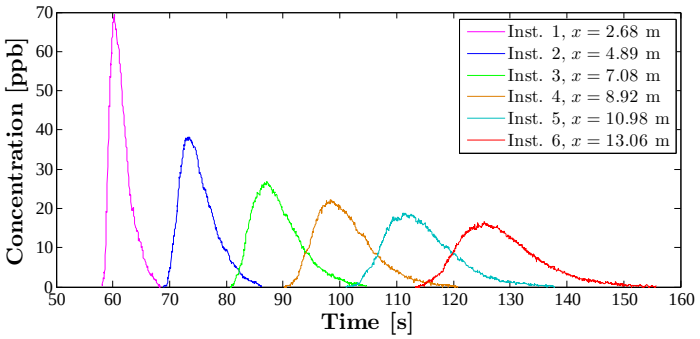

(f) Re = 3570.

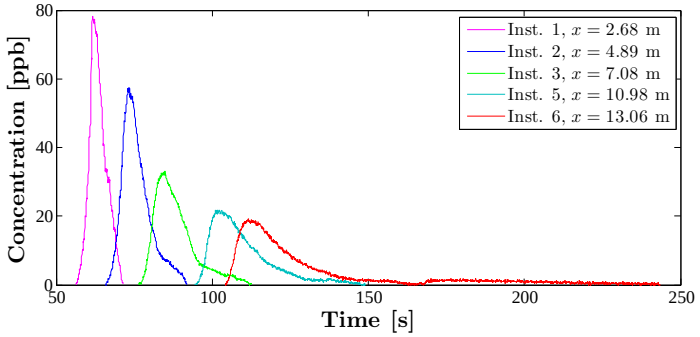

(g) Re = 2670.

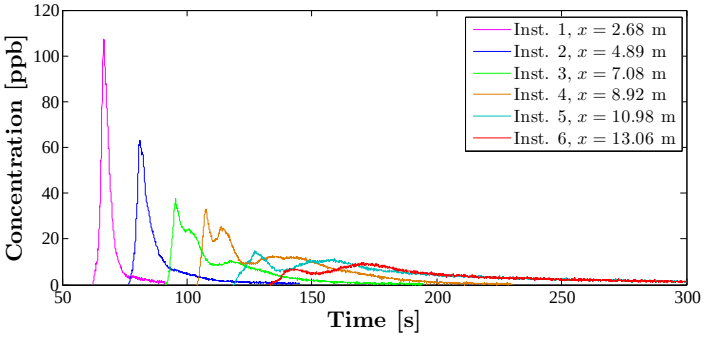

(h) Re = 1820.

Figure 5.13: *Example of concentration vs. time profiles at each instrument, for various Reynolds Number. Note, problem with instrument 4 meant profile is not available for Re* = 2670*, (g).*

Within the previous section it was also suggested that the flow is transitional for $2000 < Re < 5000$. From Figure 5.8 it can be seen that within this region, the flow transitions from being a relatively flat velocity profile at $Re = 51910$, to a non-uniform parabolic profile for $Re = 2000$. From Figure 5.13 (f) it can be seen that up to around $Re = 3500$, a flow considered to be mid-transitional, the general trend and shape of the concentration profile's is similar to that for turbulent flow, with the spreading and length of the trailing edge of the profile's increasing with decreasing Reynolds Number, whilst still maintaining a reasonable degree of symmetry. It could be suggested that within the initial part of the transitional region, the turbulence is generally continuous, leading to similar results in terms of the tracer profile's shape to that for turbulent flow. However, the hydraulic data presented in the previous section is not detailed enough to confirm this suggestion. From Figure 5.13 (g) it can be seen that up to around $Re = 2500$, a flow considered to be low-transitional, the asymmetry of the profile increases sharply, where the whole trailing edge of the profile is skewed. This form could be attributed to tracer getting caught in the relatively large laminar sub-layer at this Reynolds Number. Furthermore, if the level of turbulence is low and non-continuous, the tracer is not easily removed from the laminar sub-layer, and thus an effective dead zone is formed.

From Figure 5.13 (h) it can be seen that at $Re = 1820$, a distinct change occurs in the forms of the tracer profiles. Within the previous section it was suggested that the flow is laminar for $Re < 2000$. Within laminar flow, the length required for the tracer to become cross-sectionally well mixed increases by several orders of magnitude [Lee, 2004]. As such, the seemingly arbitrary profiles seen in Figure 5.13 (h) can be attributed to the solute cloud not being cross-sectionally well mixed.

To provide a clear comparison between an up and a downstream profile, and thus a clear picture of the degree to which the solute cloud has spread, Figure 5.14 shows a comparison between an upstream profile, taken as the profile at Instrument 2, and a downstream profile, taken as the profile at Instrument 6. The distance between the instruments is 8.2 metres. Profiles are presented with the concentration normalised with respect to the maximum concentration for the upstream profile, and time as normalised by subtraction the profiles centriod from the time axis, such that both profile's centroids are set as zero. From Figure 5.14, the increase in dispersion with decreasing Reynolds Number discussed above can clearly be see.

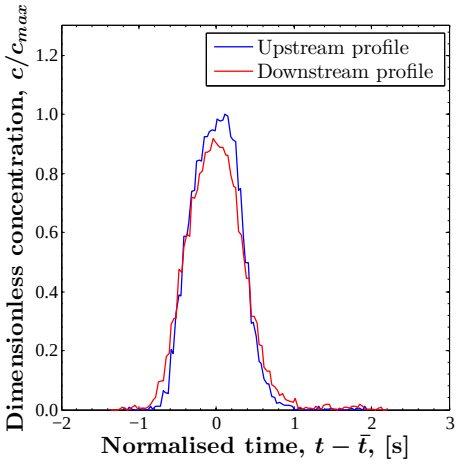

(a) Re = 50890.

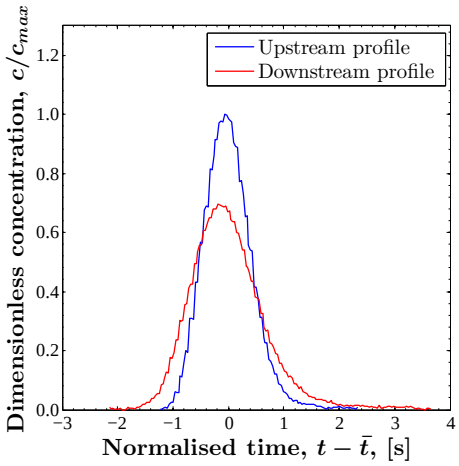

(b) Re = 20500.

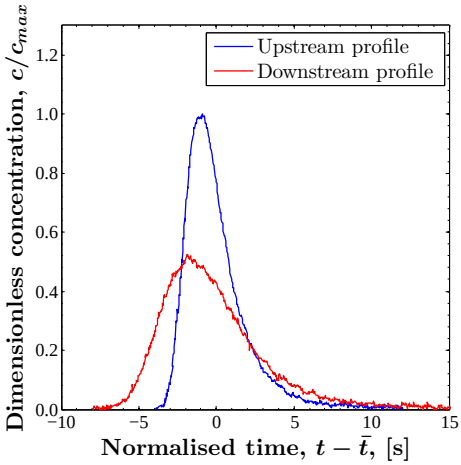

(c) Re = 5990.

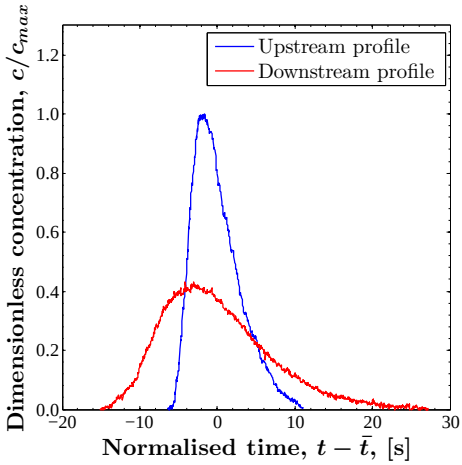

(d) Re = 3570.

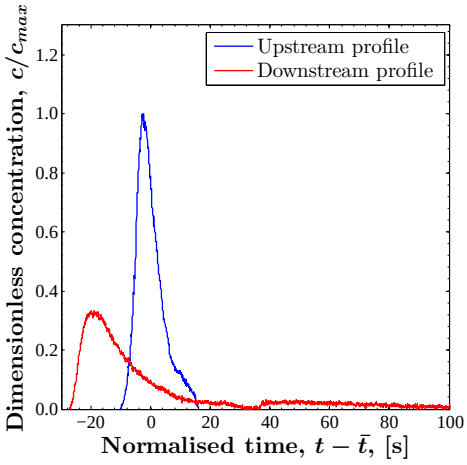

(e) Re = 2670.

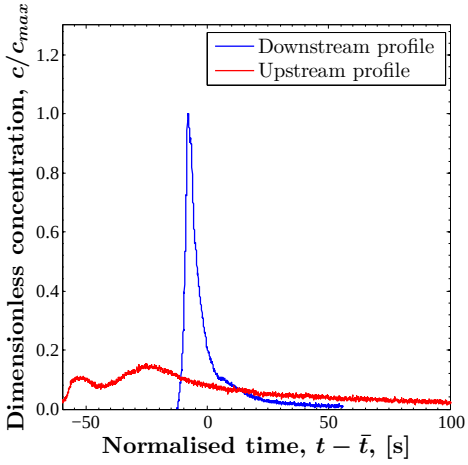

(f) Re = 1820.

Figure 5.14: *Comparison between up and downstream profiles for range of Reynolds Numbers.*

5.3.3 Analysis Methods

ADE Optimisation Code

To obtain longitudinal dispersion coefficients from the laboratory data presented in the previous subsection, an ADE optimisation code was developed (See Chapter 2, Section 2.10.2 for explanation of ADE optimisation).

The code utlises an up and a downstream experimental profile, and a predicted downstream profile. The predicted downstream profile is obtained by routing the upstream experimental profile to the location of the downstream experimental profile on the basis of a travel time and a longitudinal dispersion coefficient. The predicted downstream profile can then be compared to the experimental downstream profile on the basis of a criteria of fit, in this case the coefficient of determination, R^2.

The predicted downstream profile was initially estimated on the basis of the Method of Moments (See Chapter 2, Section 2.10.1). The travel time and Longitudinal Dispersion Coefficient were then optimised to give the best possible value of R^2. The optimisation process ran until there was less than a 1 % difference between the values for both the travel time and the Longitudinal Dispersion Coefficient between the final value and the previous iteration.

Deconvolution Code

In addition to using the ADE optimisation to obtain a longitudinal dispersion coefficient from the lab data, insight was gained into the mixing characteristics of the system by deconvonving the lab data to obtain the systems Residence Time Distribution (RTD), which were presented in the form of cumalative residence time distributions (CRTDs). RTDs were obtained using a pre-developed deconvolution code (See Chapter 2, Section 2.15 and Appendix C for full explanation of code). Appendix C gives a full explanation of the parameters used within the Deconvolution code.

5.3.4 Conditions Under which The Fickian Model is Valid

The optimisation procedure used to obtain longitudinal dispersion coefficients from laboratory data assumes Fickian dispersion, where the profiles are assumed as Gaussian and fully developed, i.e. that the magnitude of the longitudinal dispersion coefficient is independent of downstream distance of the concentration profile. The length required for this condition to be obtained corresponds to the length for the solute cloud to become cross-sectionally well mixed (see Chapter 2, Section 2.9.1).

For turbulent flow, this length is usually small, as the solute becomes rapidly well mixed [Taylor, 1954]. The following section will consider the degree to which this condition is obtained for all the traces undertaken in this work.

One reason for addressing whether the system is conforming to the Fickian model is to determine which instruments the longitudinal dispersion coefficient should be calculated between. The goal is to determine the longest possible length that the dispersion coefficient can be determined over, to give the best possible characterisation of the system's mixing response, whilst being confident that the dispersion process is Fickian over this entire length, and thus conforming to the assumption of the ADE model.

To investigate the development of the longitudinal dispersion coefficient, Figure 5.15 shows examples of the longitudinal dispersion coefficient as obtained between an up and a downstream profile, where the downstream profile was recorded at the furthest instrument downstream, and the upstream profile was recorded at instruments at increasing distance from the injection point, for various values of Reynolds Number (See Table 4.3 for instrument's distance from the injection point).

It can be seen that for $50000 > Re > 3000$, a relatively constant dispersion coefficient is obtained for all lengths, indicating that the longitudinal dispersion coefficient is fully developed at all lengths considered.

For $2000 < Re < 3000$, a variety of cases can be seen. For $Re = 2790$, as shown in Figure 5.15 (j), the longitudinal dispersion coefficient continues to increase in magnitude throughout the range (with the exception of between the final two sites), indicating that the longitudinal dispersion coefficient is never fully developed over the range considered. A similar trend can be seen for $Re = 1820$, as shown in Figure 5.15 (l). For $Re = 2190$, as shown in Figure 5.15 (k), a relatively constant longitudinal dispersion coefficient can be seen, indicating that the longitudinal dispersion coefficient is fully developed. The switch between fully developed and non-developed longitudinal dispersion coefficient in this range can be attributed to the flow being transitional - laminar.

In this region, the flow can switch rapidly from being laminar to turbulent, thus altering the length required for the longitudinal dispersion coefficient to become fully developed by orders of magnitude (See Chapter 2, Section 2.8.2).

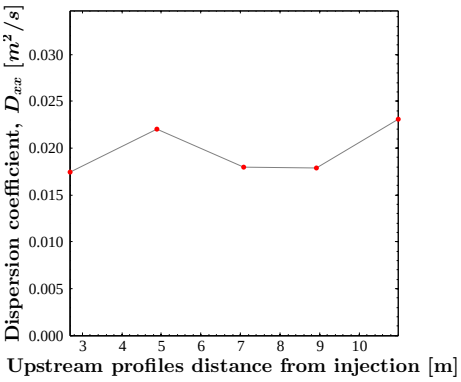

(a) Re = 50890.

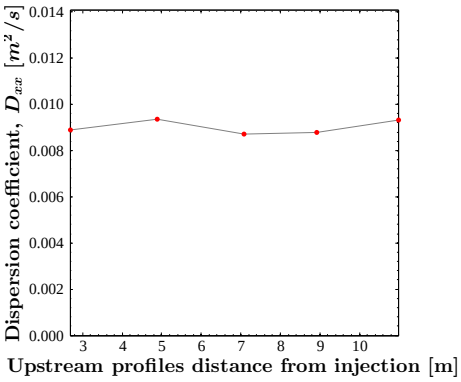

(b) Re = 20500.

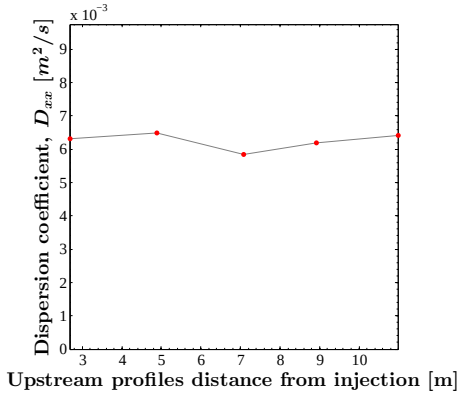

(c) Re = 10370.

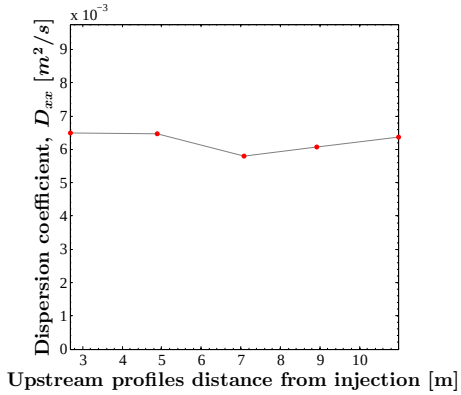

(d) Re = 8110.

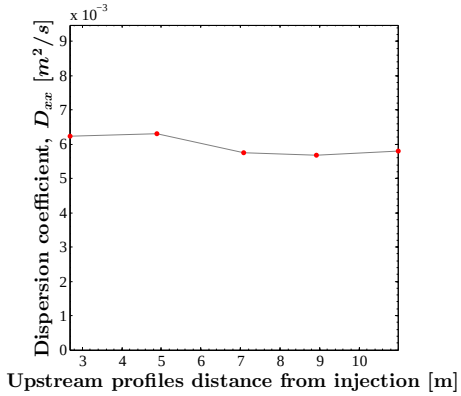

(e) Re = 5990.

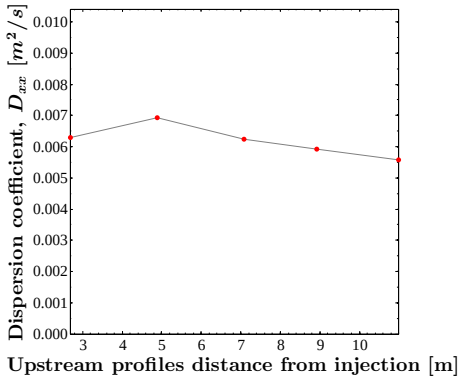

(f) Re = 5340.

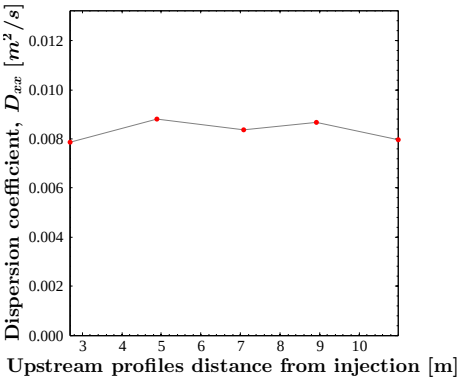

(g) Re = 3780.

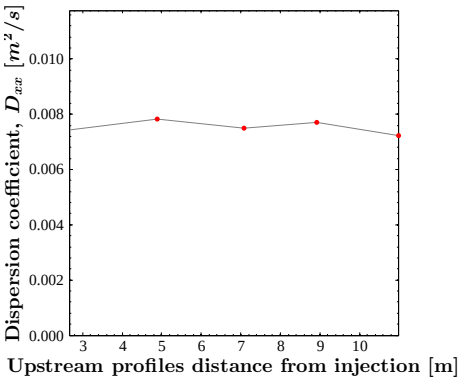

(h) Re = 3570.

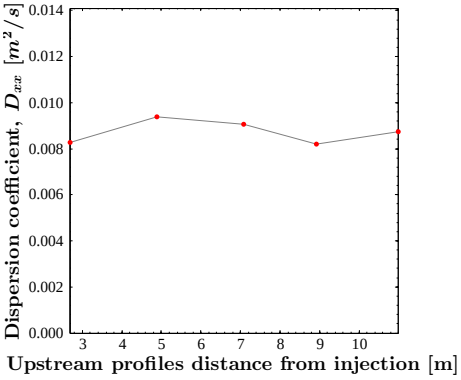

(i) Re = 3180.

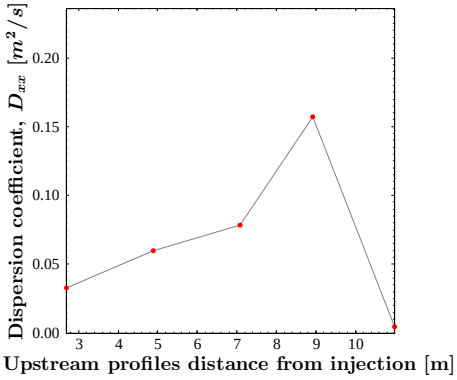

(j) Re = 2790.

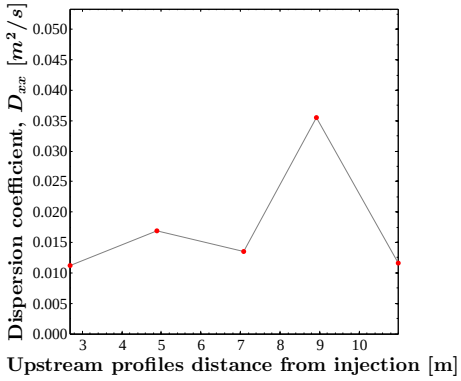

(k) Re = 2190.

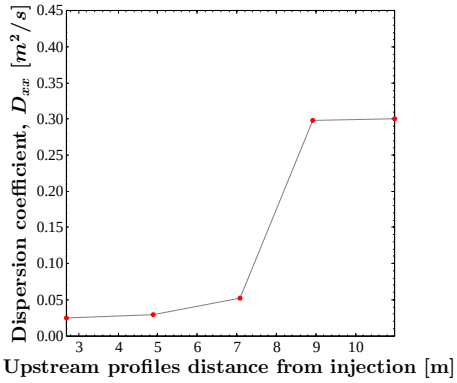

(l) Re = 1820.

Figure 5.15: *Development of the longitudinal dispersion coefficient, showing longitudinal dispersion coefficient calculated with increasing distance between upstream instrument and injection point.*

For the remainder of the chapter, mixing characteristics will be considered between instruments 2 and 6. This length is considered a good compromise, as the upstream profile is a reasonable distance from the injection point (4.9 metres) and the reach length is relatively large (8.2 metres). Furthermore, the data presented in Figure 5.15 shows that for the majority of the data, the longitudinal dispersion coefficient is fully developed over this length. For low transitional and laminar flows, where the longitudinal dispersion coefficient may not be developed, the degree to which the Fickian model is valid in such cases will be assessed further in this section. However, it has been noted that the Fickian model can be a 'useful' assumption for evaluating the mixing response of a system, even outside of the fully developed range [Gill and Sankarasubramanian, 1970].

In addition to assuming that the longitudinal dispersion coefficient is fully developed, the Fickian dispersion model also assumes that the concentration profiles are Gaussian. The ADE optimisation model assumes a downstream Gaussian distribution of each portion of the measured upstream profile. Thus, a good initial indicator of the system's conformity to the Fickian model is the goodness of fit between the measured downstream profile and the final predicted downstream profile through the ADE optimisation model.

Figure 5.16 compares the experimental downstream profile and the final predicted downstream profile from the ADE optimisation. It can be seen that the optimisation model provides a good fit to the experimental downstream profile for $3000 < Re < 50000$ (Figure 5.16 (a - h)), but struggles to accommodate the highly skewed and non-Gaussian nature of the profiles for $2000 < Re < 3000$ (Figure 5.16 (i - l)).

Figure 5.17 summarises the data, showing the relationship between all values of R^2 for the goodness of fit between the experimental and predicted downstream profiles, and Reynolds Number. It can be seen that a relatively high value of R^2 is maintained for all data until around $Re < 3000$, at which point the value sharply drops. A relatively high, stable and consistent value for R^2 is maintained for $Re > 10000$, however the Figure only shows values up to $Re = 15000$, to highlight the trend for low Reynolds Numbers.

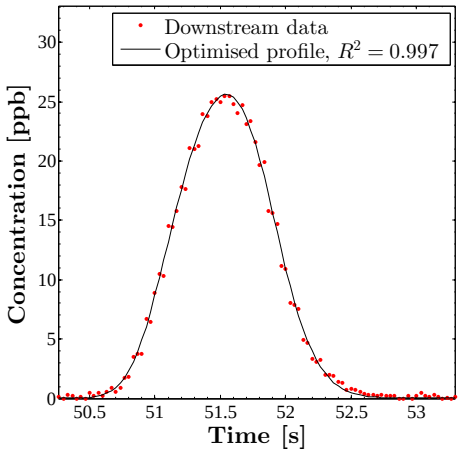

(a) Re = 50890.

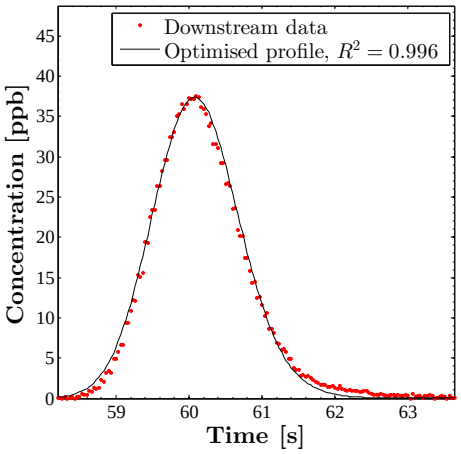

(b) Re = 20500.

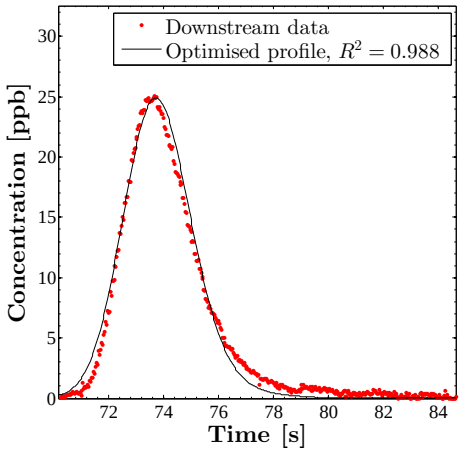

(c) Re = 10370.

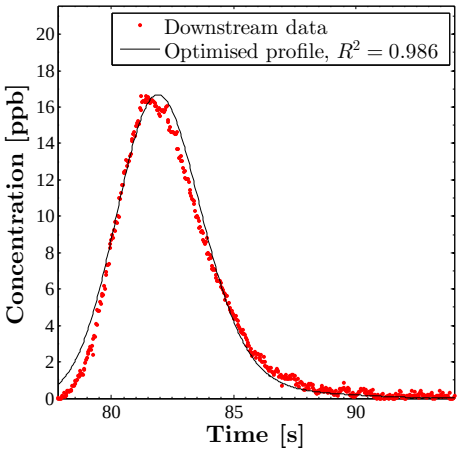

(d) Re = 8110.

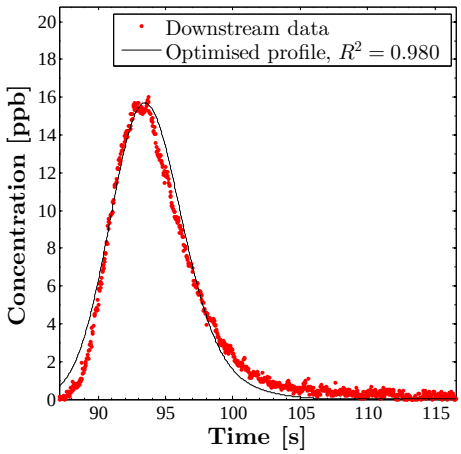

(e) Re = 5990.

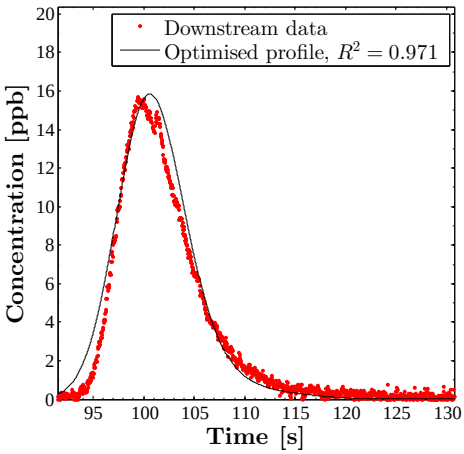

(f) Re = 5340.

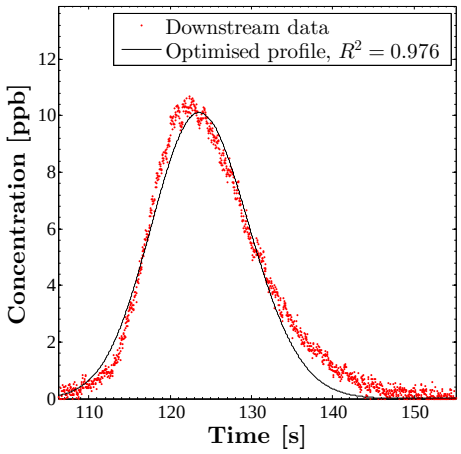

(g) Re = 3780.

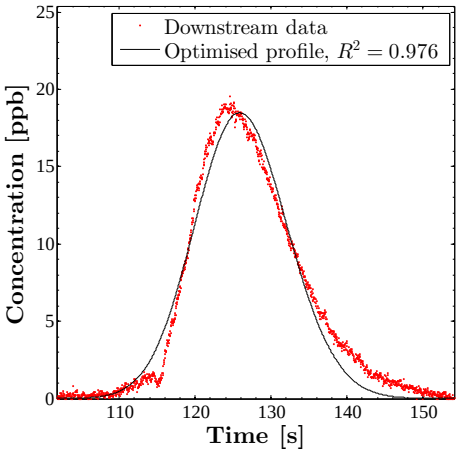

(h) Re = 3570.

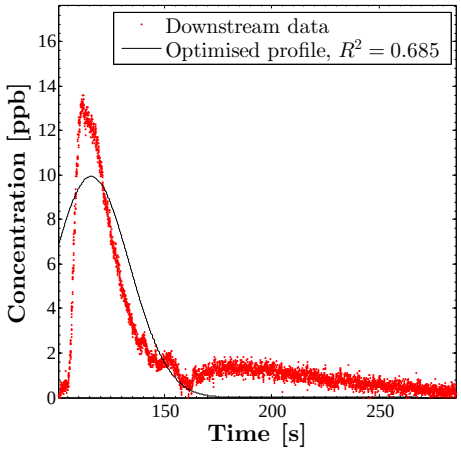

(i) Re = 2790.

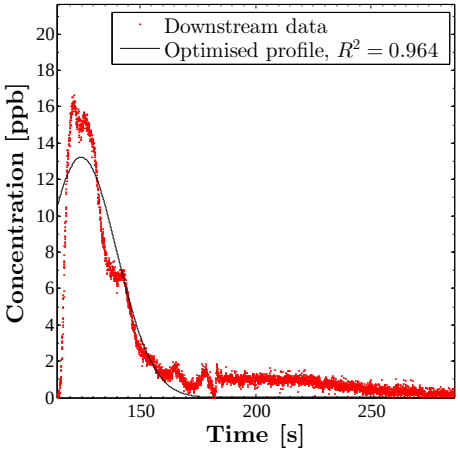

(j) Re = 2270.

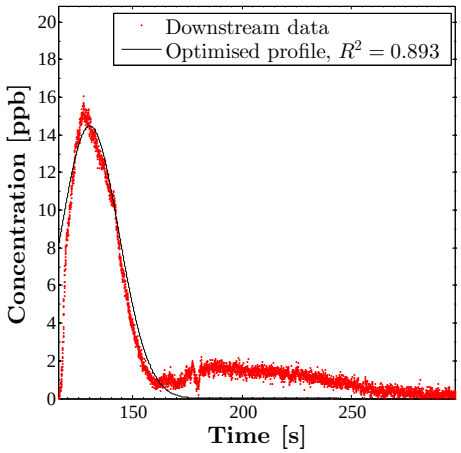

(k) Re = 2190.

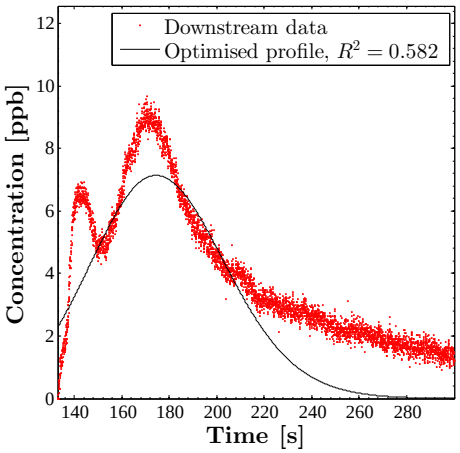

(l) Re = 1820.

Figure 5.16: *Experimentaly obtained downstream profile compared to final predicted downstream profile through ADE optimisation model.*

Although the ADE optimisation assumes a Gaussian mixing response, the final downstream profile represents the sum of each element of the upstream profile, distributed through the Guassian assumption. If the upstream profile was an idealised point injection, then the downstream profiles would be fully Gaussian, but as the model uses a non-idealised measured profile, the final downstream profile can account for non-Gaussian features, such as asymmetry, as see in Figure 5.16.

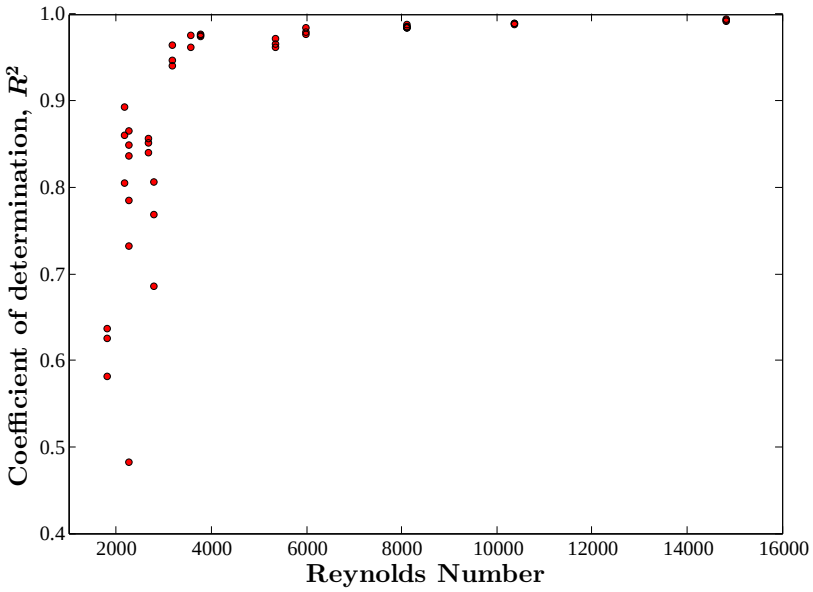

Figure 5.17: *Values of R^2 for comparison between final downstream optimised profile and experimental data.*

To obtain the fundamental mixing response of the system, i.e. the response of the system to an idealised point injection, the laboratory data must be deconvolved to obtain the system RTD. The laboratory data was deconvolved using a pre-developed code, as described in Chapter 2, Section 2.13 and Appendix C.

Figure 5.18 shows the Cumulative Residence Time Distribution (CRTD), obtained by deconvolving experimental data, compared to a predicted downstream profile using the ADE equation assuming an idealised point injection, and the experimentally obtained values for the longitudinal dispersion coefficient obtained through the optimisation procedure. The profiles are both normalised to obtain unity, although in order to see the detail of the profiles distribution, the chart time scales are zoomed in, and thus do not always show the complete profile.

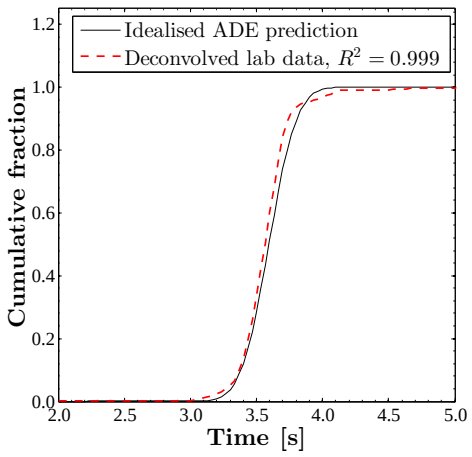

(a) Re = 50890.

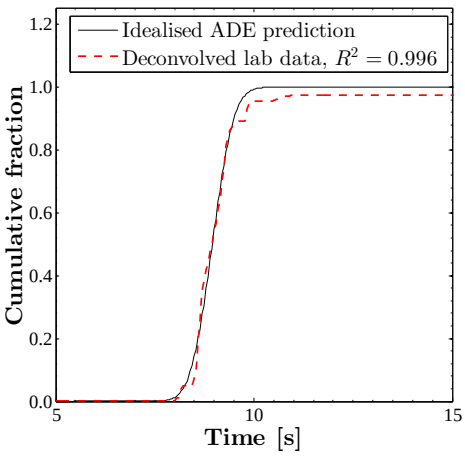

(b) Re = 20500.

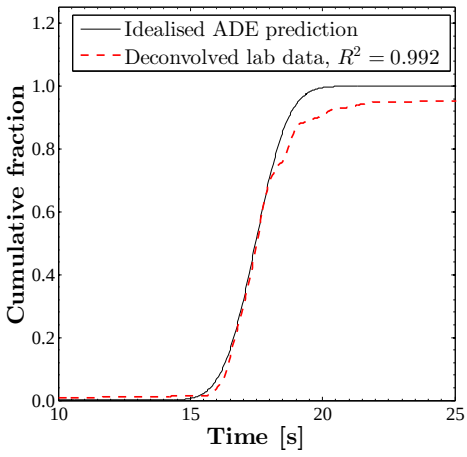

(c) Re = 10370.

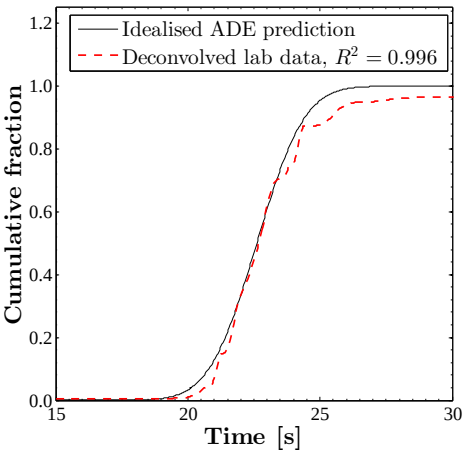

(d) Re = 8110.

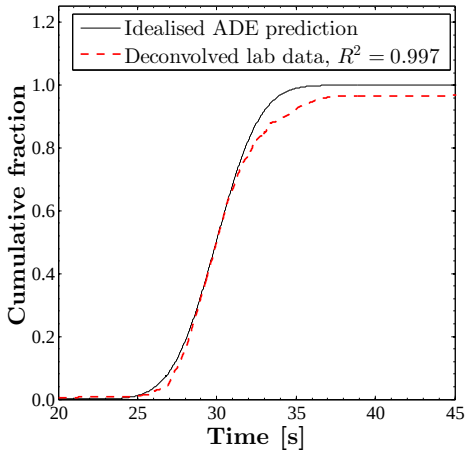

(e) Re = 5990.

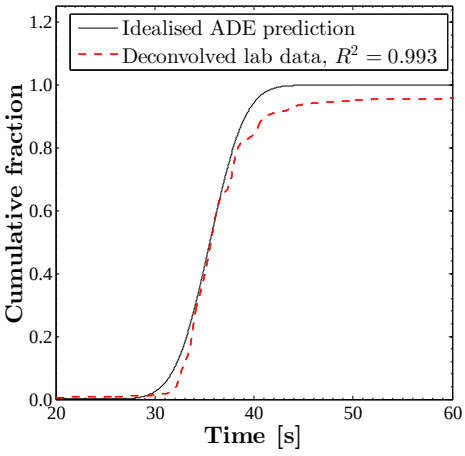

(f) Re = 5340.

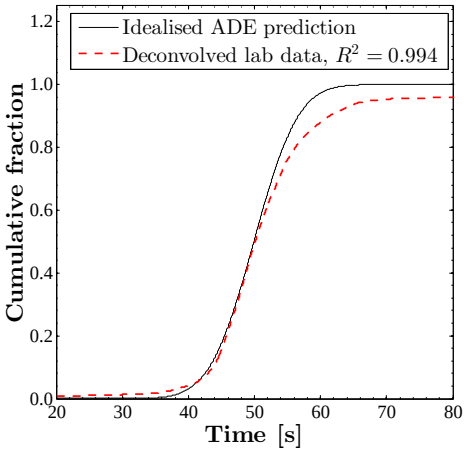

(g) Re = 3780.

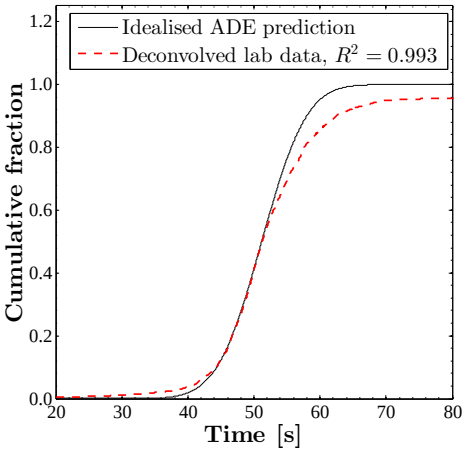

(h) Re = 3570.

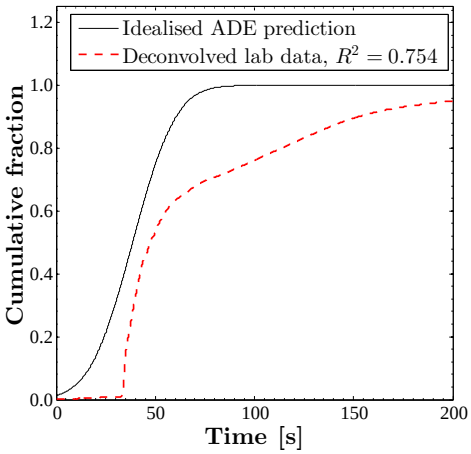

(i) Re = 2790.

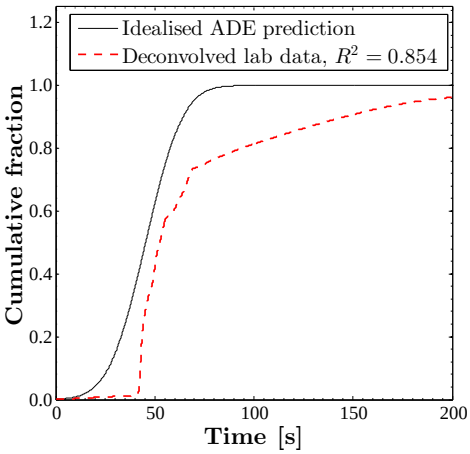

(j) Re = 2270.

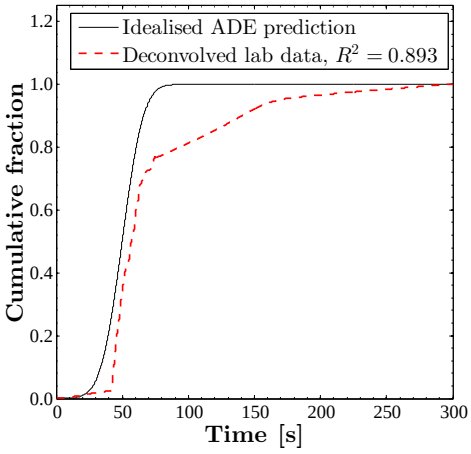

(k) Re = 2190.

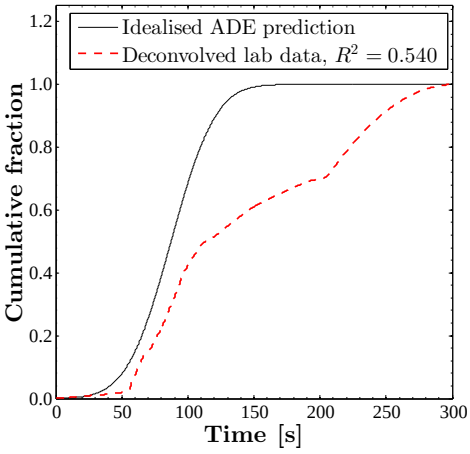

(l) Re = 1820.

Figure 5.18: *Comparison between CRTD's from deconvolved experimental data and ADE prediction for idealised point injection.*

Thus, the figures represent the experimentally obtained response of the system to an idealised point injection (The CRTDs from deconvolved laboratory data), compared to the response of the system to an idealised point injection assuming the mixing characteristics are Fickian (ADE prediction). Through this method, the degree to which the system is conforming to the Fickian model can be assessed in a manner more robust than simply considering the goodness of fit between the optimised ADE prediction and the experimental data.

From Figure 5.18 two general fundamental mixing responses of the system can be suggested.

For $50000 < Re < 3000$, as shown in Figure 5.18 (b)-(h), it can be seen that the system is conforming reasonably well to the Fiackian assumption. Here, the majority of the CRTDs are in agreement with the predicted Gaussian profile, with the exception of the profile's trailing edge, which takes significantly longer to obtain mass balance than that of the predicted profile. This is due to the elongated trailing edge of the profiles, as seen previously in this chapter, which are poorly described by the relatively small number of sample points for the trailing edge of the turbulent profiles (See Appendix C for explanation of sample point distribution for the deconvolution code). It can be noted that the shape of the CRTDs are similar for all profiles in this relatively large range, and that a similar value of R^2 is maintained throughout.

For $2790 < Re < 1820$, as shown in Figure 5.18 (i)-(l), it can be seen that the system is not described well by the Fickian assumption. Here, the CRTDs compare poorly to the predicted Gaussian profiles, and thus the values of R^2 reduce considerably.

Figure 5.19 summaries the data, showing the relationship between all values of R^2 and Reynolds Number. It can be seen that a high and relatively constant value of R^2 is maintained for all data until around $Re < 3000$, at which point the value drops sharply, indicating that the Fickian assumption is valid for $Re > 3000$.

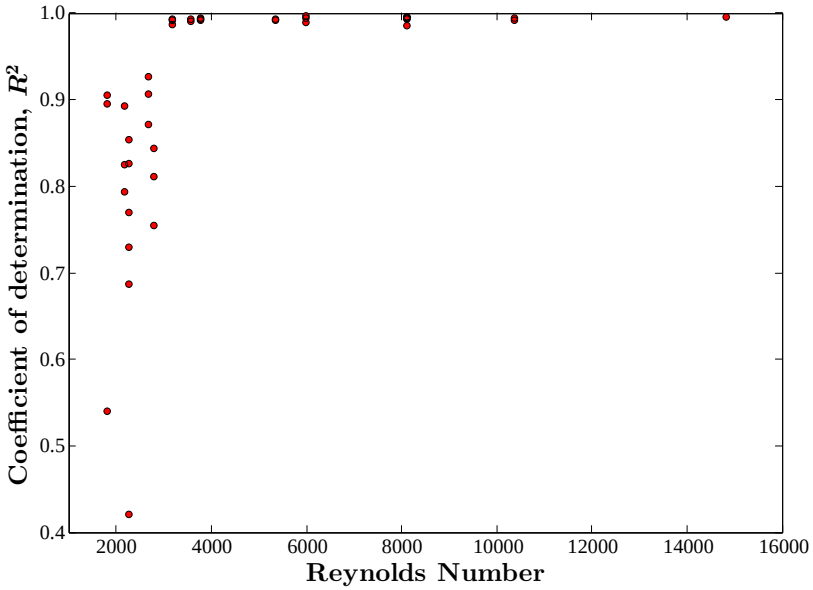

Figure 5.19: *Values of R^2 for comparison between CRTD's from deconvolved experimental data and ADE prediction for idealised point injection.*

5.3.5 Generalised CRTDs

To provide a clear comparison between the system's fundamental mixing response for all Reynolds Numbers considered, Figure 5.20 shows a comparison between CRTDs for every run in the test series, plotted against normalised time, $\hat{T} = tQ/V$. The normalise time is derived so that $\hat{T} = 1$ is the profile's centroid, where if the solute cloud was an idealised slug injection, where no dispersion had taken place, the cumulative fraction would be a step change from 0 to 1 at $\hat{T} = 1$. The data has been sub-divided into Reynolds Number bands to provided easy comparison between the various regimes. For the sub-divisions, $50000 > Re > 20000$ is considered highly turbulent flow, $2000 > Re > 8000$, turbulent flow, $8000 > Re > 5000$, low turbulent flow, $5000 > Re > 3000$, high transitional flow, $3000 > Re > 2500$, low transitional flow, $2500 > Re > 2000$, transitional to laminar flow and $Re < 2000$, laminar flow.

From Figure 5.20, for $5000 < Re < 50000$, the range considered turbulent, the system's CRTD appears to conform to a relatively consistent, general shape. However, it can be noted that a slight change occurs between high turbulent flow for $20000 < Re < 50000$, and low turbulent flow for $8000 < Re < 20000$, where for the low turbulent flow, the profile's trailing edge is slightly elongated, under the influence of the growing boundary layer.

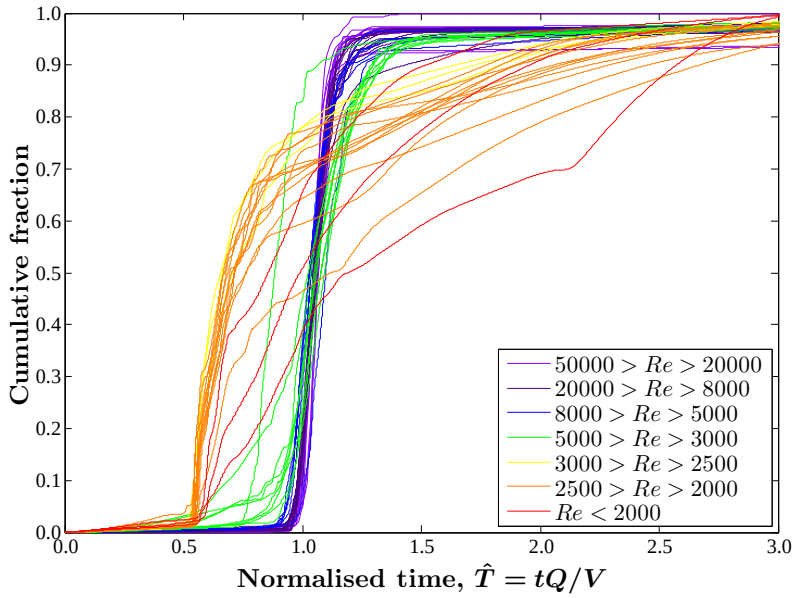

Figure 5.20: *Comparison between normalised CRTDs for all trials.*

For the initial portion of the transitional region, for $3000 < Re < 5000$, the system's CRTDs again appear to conform to a consistent general shape throughout the range, however in this region, the tail of the CRTDs are further elongated, as the boundary layer grows further.

For low transitional flow, for $2500 < Re < 3000$, a distinct change occurs in the mixing characteristics of the system, with a complete change in the form of the CRTDs, as the flow transitions from being turbulent to laminar. However, despite the profiles not converging exactly, there is still a general shape to the profiles in this region.

For low transitional to laminar flow, for $Re < 2500$, it can be seen that some of the profiles conform to the shape observed for $2500 < Re < 3000$, whilst some conform to a seemingly arbitrary distribution, as the flow switches from being turbulent to laminar.

It can also be noted that for $Re < 5000$, a large change in the first arrival time occurs. The first arrival time for $Re > 5000$ is around $\hat{T} > 0.8$, and the first arrival time for $Re < 3000$ is around $\hat{T} = 0.5$. This change can be understood with reference to the discussion of laminar velocity profile's in Chapter 2, Section 2.3.2, where it was shown analytically in Equation 2.6 that the mean to maximum velocity ratio for a laminar velocity profile is 0.5. Thus, the centreline velocity for a laminar profile is $2\bar{u}$, and thus tracer at the centre of the flow will arrive twice as quickly

as the concentration profile's centroid, traveling at the mean velocity of the flow, as shown for results for $Re < 3000$. For turbulent flow, the velocity profile is more uniform, with a typical mean to maximum velocity radio of around 0.8 [Benedict, 1980], again, confirmed by for results for $Re > 5000$. Thus, the normalised CRTDs provide a good representation of the sharp change in differential advection between turbulent and laminar flow.

5.3.6 Longitudinal Dispersion Coefficient Assuming The Fickian Model

So far within this chapter, it has been proposed that the Fickian model is a reasonable assumption for $3000 < Re < 50000$. The following section will assume the validity of the Fickian model for the whole range of Reynolds Numbers considered, i.e. $2000 < Re < 50000$, on the basis that it is valid for $3000 < Re < 50000$, and can at least be a useful assumption for indicating the mixing processes for $2000 < Re < 3000$, the range in which its validity is questionable.

Figure 5.21 shows the relationship between Reynolds Number and the dimensionless longitudinal dispersion coefficient, $D_{xx}/\bar{u}d$, for $2000 < Re < 50000$. The longitudinal dispersion coefficient was obtained through the ADE optimisation procedure described previously in this chapter. Each longitudinal dispersion coefficient represents the mean value of 3 repeat tests.

It is again useful to consider the results in light of the hydraulic data presented previously in this chapter. It can be seen that for highly turbulent flow, for $20000 < Re < 50000$, the longitudinal dispersion coefficient is relatively small and constant as the flat, uniform velocity profile observed for these flow rates, as seen for $Re = 51910$ in Figure 5.8, leads to little dispersion.

For turbulent flow, for $5000 < Re < 20000$, the longitudinal dispersion coefficient increases gradually, as the effect of the boundary layer grows, causing the velocity profile to be more non-uniform, as seen in Figure 5.8, where the uniform velocity profile seen for $Re = 51910$ develops into a more non-uniform profile, with a larger boundary layer at $Re = 5030$.

For transitional flow, for $2000 < Re < 5000$, the longitudinal dispersion coefficient increase more significantly with Reynolds Number, to the point that at $Re \approx 2000$, the value for the longitudinal dispersion coefficient is approximately a factor of 50 greater than at $Re > 20000$. The changes in the velocity profile between these limits can be seen in Figure 5.8, where the velocity profile develops from a relatively flat turbulent profile at $Re = 5030$, to a non-uniform parabolic profile at $Re = 2000$, leading to a sharp increase in magnitude of the longitudinal dispersion

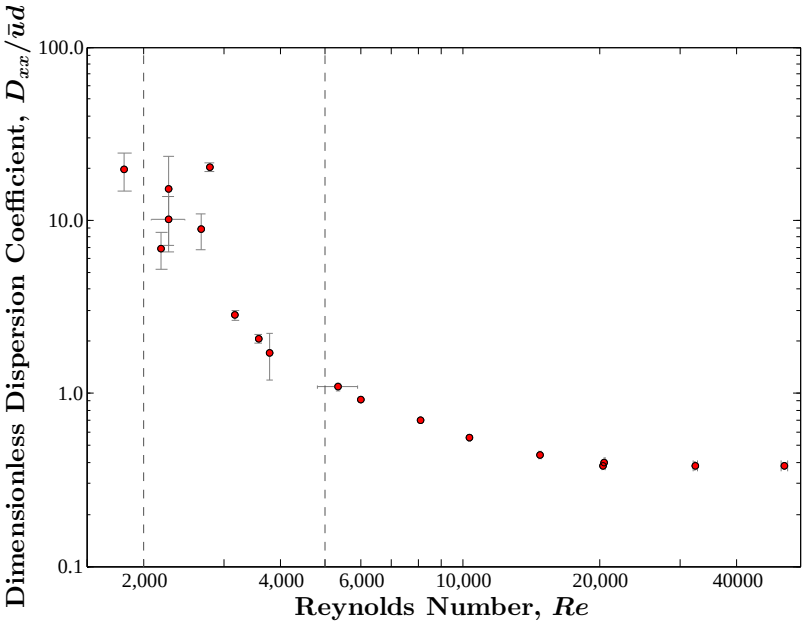

Figure 5.21: *Relationship between dimensionless longitudinal dispersion coefficient and Reynolds Number.*

coefficient.

It can also be seen that for turbulent flow, the scatter in the data is relatively small, to the point that the error bars are not always visible. However, within transitional flow, the scatter is greater, with visible and relatively larger error bars as the mixing characteristics in this region are less repeatable, as shown in Figure 5.12.

5.3.7 Summary of Steady Flow Tracer Results

Within this Section tracer data has been used to consider longitudinal dispersion processes for the range of Reynolds Numbers $2000 < Re < 50000$. Through all of the results presented, it was shown that longitudinal dispersion increases with decreasing Reynolds Number. Further more, through the use of ADE optimisation and deconvolution codes, it was shown that the longitudinal dispersion coefficient is fully developed, and conforms well to the Fickian assumption reasonably, for $3000 < Re < 50000$. It was also shown that a distinct change in the mixing characteristics of the system occurs between $2000 < Re < 5000$, as the flow transitions from being turbulent to laminar. Assuming the Fickian model holds over the whole range, the relationship between longitudinal dispersion and Reynolds Number was investigated, where it was proposed that the value of the longitudinal dispersion

coefficient increases in magnitude as Reynolds Number decreases and approaches laminar flow.

5.4 Validation of Numerical Model for Steady Flow

Within Chapter 3, it was suggested that the numerical model proposed could be applied to a specific system on the basis of an estimation of the turbulent and laminar frictional velocity, an estimation of the critical points for the transition from turbulent to laminar flow, and an estimation of the transition factor α.

This section will consider the model, where these parameters are used on the basis of the hydraulic data presented at the start of this Chapter. The model will then be compared to the longitudinal dispersion coefficients obtained in the previous section.

5.4.1 Parameters and Results for Turbulent Flow

Within Chapter 3, a turbulent velocity profile was proposed that accounts for the laminar sub-layer and buffer zone. Figure 5.22 shows a comparison between the theoretical and experimental velocity profile of the present work, for $Re = 51910$ and $Re = 5030$, considered the highest and the lower recorded turbulent velocity profile. For the data presented in Figure 5.22, the frictional velocity is calculated on the basis of the expression for friction factor presented earlier in this chapter, derived on the basis of the experimental data of the present work, as defined in Equation 5.6.

From Figure 5.22 it can be seen that there is good agreement between the theoretical turbulent velocity profile and the experimentally obtained turbulent velocity profiles of the present work.

Figure 5.23 shows the results from Chikwendu's model assuming the turbulent parameters of the present work, where the velocity profile is the turbulent velocity profile of the present work, and the frictional velocity is calculated on the basis of the expression for the turbulent fraction factor of the present work, as defined in Equation 5.4. In addition, Figure 5.23 shows the results from Chikwendu's model assuming Taylor's velocity profile and the frictional velocity calculated on the basis of the expression for the turbulent fraction factor of the present work.

It can be seen that for highly turbulent flow, the prediction of the longitudinal dispersion coefficient of the model assuming the velocity profile of the present work tends towards Taylor's prediction, as at high Reynolds Numbers, the length of the laminar sub-layer and buffer zone becomes negligibly small, and thus tends towards

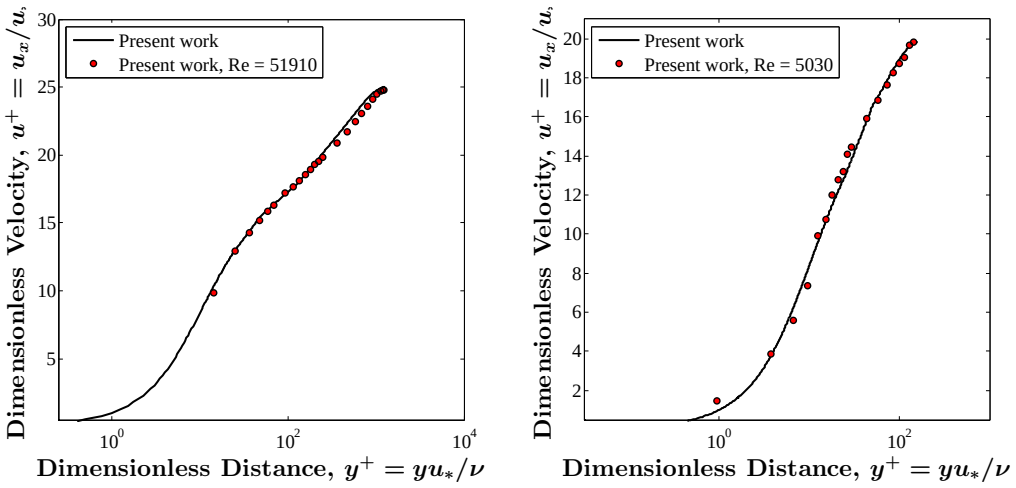

(a) Re = 51910. (b) Re = 5030.

Figure 5.22: *Comparison between experimental turbulent velocity profiles of present work and theoretical turbulent velocity profile of the present work.*

Taylor's expression which assumes no laminar sub-layer or buffer zone. The model also predicts the relatively low and constant trend in the dispersion data for $Re >$ 20000, due to the highly uniform velocity profile.

For low turbulent flow, for $Re < 20000$, the influence of the growing boundary layer defined in the velocity profiles of the present work causes the longitudinal dispersion coefficient to increase in magnitude.

5.4.2 Parameters and Results for Laminar Flow

The parabolic velocity profile for laminar flow can be predicted analytically through the expression presented in Equation 2.5. Figure 5.7 (e) shows a comparison between the velocity profile predicted through Equation 2.5, and experimental data of the present work for laminar flow, from which it can be seen that there is good agreement between the prediction made by the analytical profile and the experimental data of the present work.

Figure 5.24 shows the results from Chikwendu's model, where the velocity profile is the analytical, laminar velocity profile, as defined in Equation 2.5, and where the frictional velocity is calculated on the basis of the expression for the laminar friction factor of the present work, as defined in Equation 5.2.

From Figure 5.24, it can be seen that the prediction of the longitudinal dispersion coefficient on the basis of a laminar parameters of the present work predicts the relatively high value for the longitudinal dispersion coefficient at Reynolds

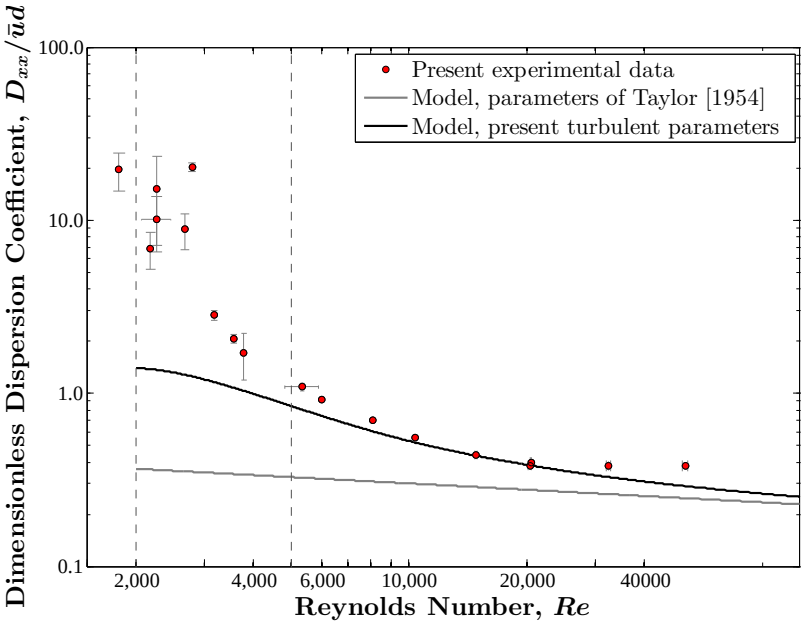

Figure 5.23: *Comparison between the experimental longitudinal dispersion coefficient of the present work and the model with the parameters of Taylor [1954] and the turbulent parameters of the present work.*

Numbers around $Re = 2000$, the point at which the flow transitions to being fully laminar.

5.4.3 Parameters and Results for Transitional Flow

From Figure 5.24, it can be seen the when Chikweund's model is used assuming turbulent parameters of the present work, it makes a reasonable prediction of the experimental data for turbulent flow for $Re > 5000$. Furthermore, when the model is used assuming laminar parameters of the present work, it makes a reasonable prediction of the experimental data for laminar flow at around $Re = 2000$.

For transitional flow, for $2000 < Re < 5000$, it can be seen that the two trends form boundaries, within which all transitional data falls. However, to provide a more accurate estimation the the longitudinal dispersion coefficient within the region, it is necessary to estimate how the velocity profiles transition from a relatively flat profile at $Re = 5000$, to a parabolic profile at $Re = 2000$.

Within Chapter 3 a transitional expression was proposed, as defined in Equation 3.1. This expression assumes a laminar profile, u_L, and a turbulent profile u_T, where the relative contribution made to the transitional distribution by each profile is governed by the transition factor, α, where, if $\alpha = 0$, the profile is fully laminar,

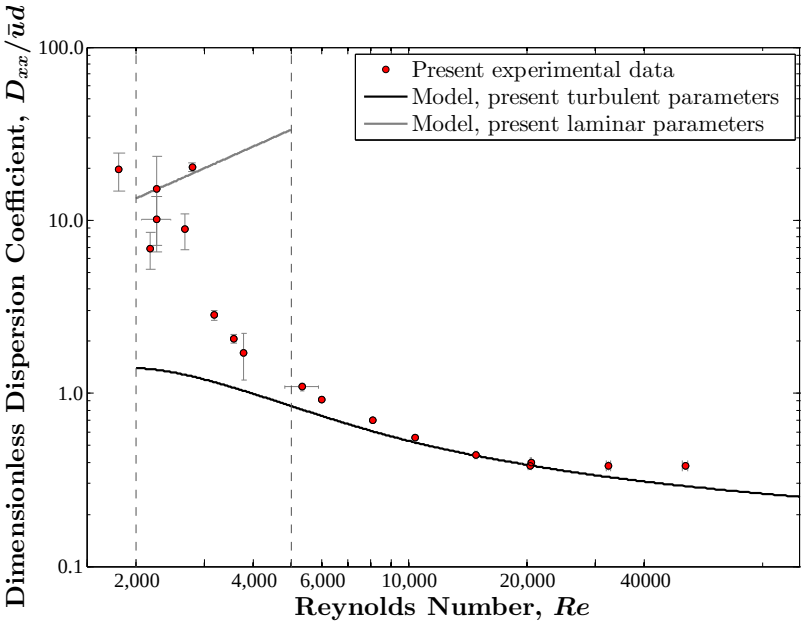

Figure 5.24: *Comparison between the experimental longitudinal dispersion coefficient of the present work and the model with the turbulent and laminar parameters of the present work.*

and if $\alpha = 1$, the profile is fully turbulent.

In the context of the present work, u_L is assumed as the laminar profile proposed in Section 5.4.3 at $Re = 2000$, and u_T is assumed as the turbulent profile of the present work proposed in Section 5.4.2 at $Re = 5000$.

Values for α were obtained by optimising the transitional expression as defined in Equation 3.1, assuming the profiles discussed above, against experimentally obtained velocity profiles, to obtain the optimal value of α for each profile. The velocity profiles used were the experimentally obtained velocity profile of the present work, from the near wall to the centre line, for each profile within the transitional region.

Figure 5.25 shows a comparison between the experimental transitional velocity profiles of the present work, and the optimised transitional velocity profile through Equation 3.1, optimising for α.

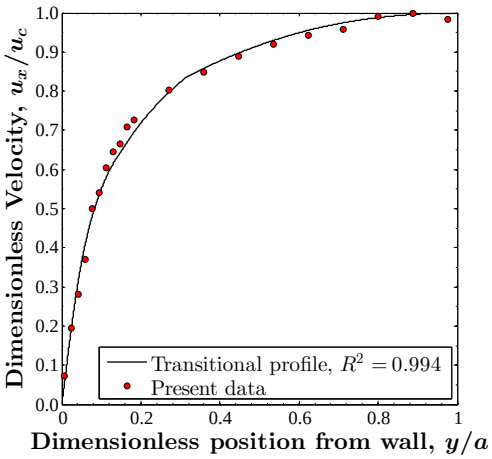

(a) Re = 5030.

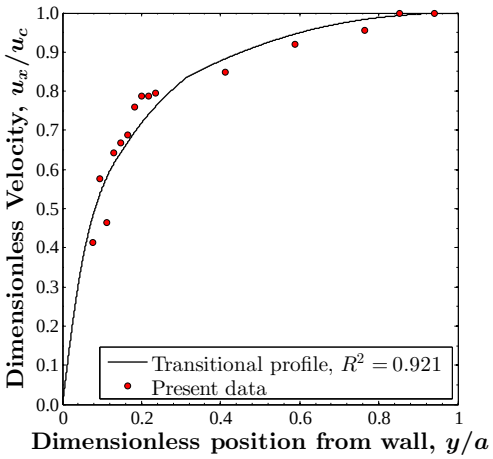

(b) Re = 4890.

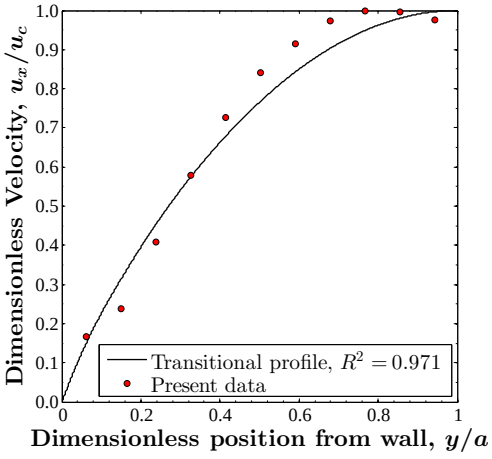

(c) Re = 3000.

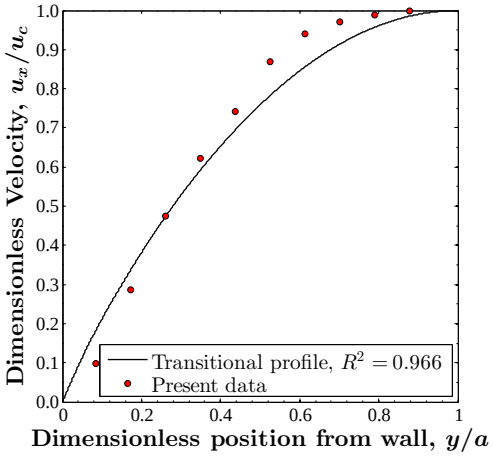

(d) Re = 2620.

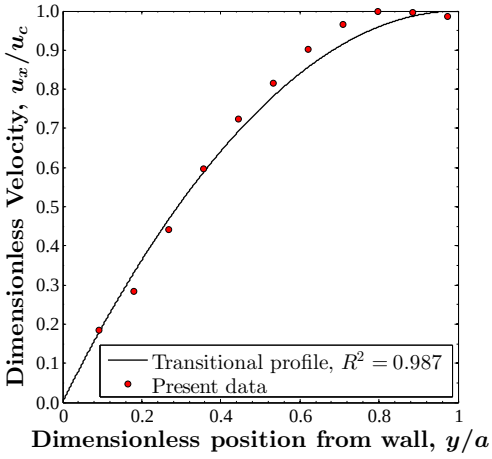

(e) Re = 2000.

Figure 5.25: *Comparison between optimised transitional velocity profile and experimental data.*

Figure 5.26 shows the relationship between α and Reynolds Number for all the experimental transitional profiles of the present work. The trend of the transition from a turbulent to a laminar profile appears to conform to a sigmoidal type trend, as is common for transitional phenomenon [Yang and Joseph, 2009]. Thus, to produce a continuous expression for α that could be used to predict the transitional velocity profile for the whole range, a sigmoidal function was fitted to the data, of the form:

$$\alpha = \frac{a}{a + e^{b\zeta}} \tag{5.7}$$

Where $a = 1.124$, $b = -4.288$ and:

$$\zeta = \left[\frac{Re - 2000}{1500}\right] - 1 \tag{5.8}$$

Figure 5.26 shows a comparison between the sigmoidal trend and the experimentally obtained values for α.

Figure 5.27 shows examples of predicted transitional velocity profiles for the range $2000 < Re < 5000$, through the transitional velocity profiles as defined in Equation 3.1, assuming the values of α as predicted through Equation 5.7.

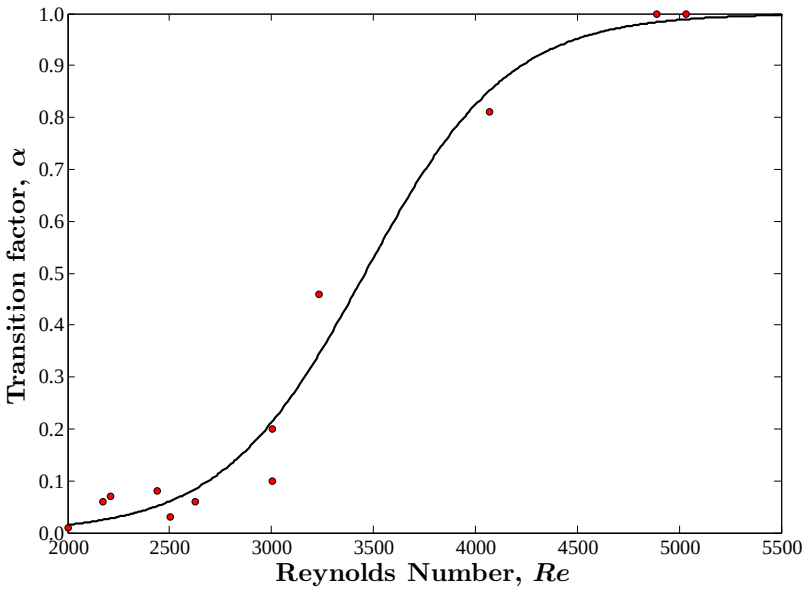

Figure 5.26: *Relationship between velocity profile transition factor, α, and Reynolds Number.*

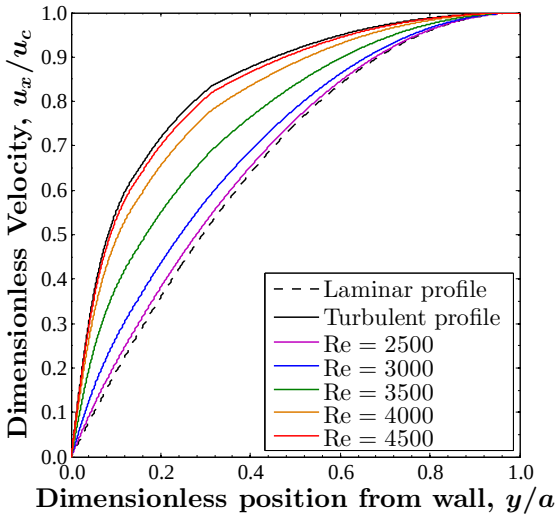

Figure 5.27: *Examples of predicted transitional velocity profiles of present work.*

Figure 5.28 shows the results from Chikwendu's model assuming the transitional velocity profile of the present work, where both the velocity profile and the frictional velocity vary with α.

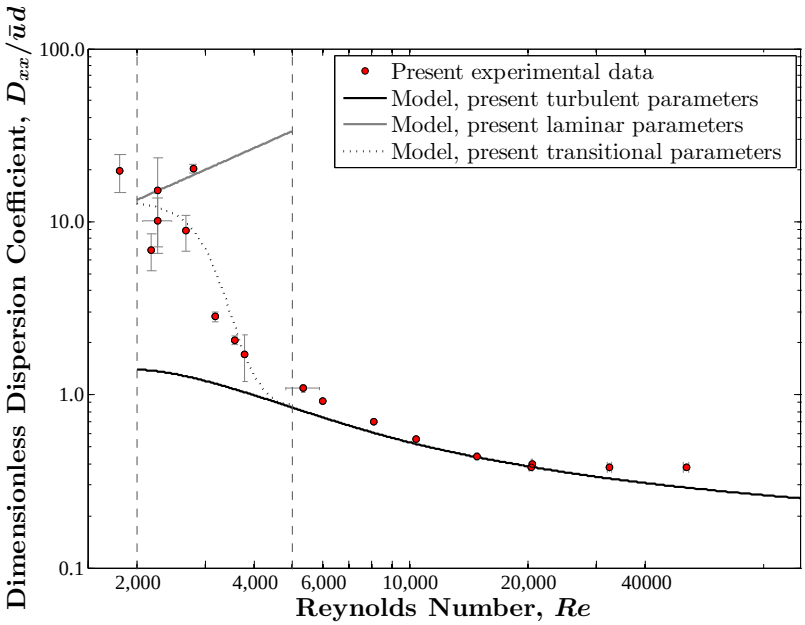

Figure 5.28: *Comparison between the experimental longitudinal dispersion coefficient of the present work and the model with the turbulent, laminar and transitional parameters of the present work..*

From Figure 5.28, it can be seen that as the velocity profile transitions from being the uniform turbulent shape at $Re = 5000$ to the parabolic shape at $Re = 2000$, as shown in Figure 5.27, the longitudinal dispersion coefficient also increases from the relatively low value at $Re = 5000$, to the relatively high value at $Re = 2000$, in a manner consistent with the experimental data.

From Figure 5.28 it can be seen that when Chikwendu's model is used with the laminar, turbulent and transitional parameters of the present work, it provides a good prediction of the longitudinal dispersion coefficient when compared to the experimental data of the present work for the whole range $2000 < Re < 50000$.

Figure 5.29 shows a comparison between the experimental data of the present work and previously obtained experimental data, previous models for the longitudinal dispersion coefficient, and the model of the present work. From Figure 5.29 it can be seen that the experimental data of the present work compares well to previous data, and that the numerical model makes a superior prediction of the data over the whole range, when compared to previous models.

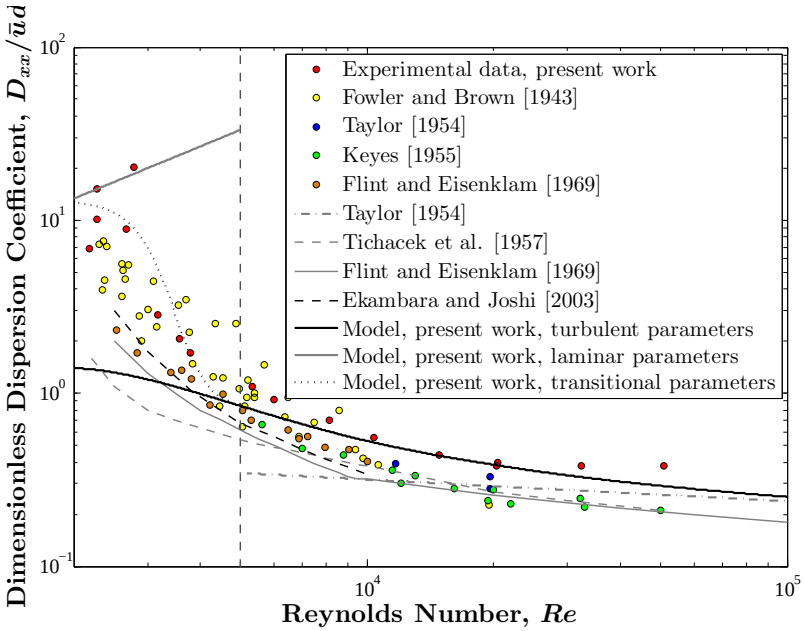

Figure 5.29: *Comparison between the experimental longitudinal dispersion coefficient of the present work and the numerical model of the present work, compared to previously obtained experimental data and previous models.*

5.5 The Use of the Numerical Model in Conjunction with the ADE Model

So far in this section, the model of Chikwendu [1986] has been used in conjunction with a variety of parameters to highlight the dependency of the longitudinal dispersion coefficient on Reynolds Number.

This section will use the values of the longitudinal dispersion coefficient, predicted through the model with the various parameters discussed in this section, to predict a downstream concentration profile, which will be compared to experimental data to highlight the effect of the longitudinal dispersion coefficient on the prediction of a downstream profile.

The downstream profile will be predicted by using an ADE routing procedure to route an upstream experimental profile to downstream experimental data, on the basis of an optimised travel time, as obtained in this chapter through the ADE optimisation procedure, and a value of the longitudinal dispersion coefficient, as predicted through Chikwendu's model using the various parameters discussed in this chapter.

5.5.1 Turbulent Flow

Figure 5.30 shows experimental downstream data, compared to two predicted profiles, one on the basis of the longitudinal dispersion coefficient predicted through Taylor's expression, and the other on the basis of the longitudinal dispersion coefficient predicted through the application of Chikwendu's model, assuming the turbulent parameters of the present work.

From Figure 5.30 (a) for $Re = 50890$, a flow considered to be highly turbulent, it can be seen that both Taylor's expression and the parameters of the present work predict a similar concentration profile, which is consistent with the experimental data.

Figure 5.30 (b) - (f), for $5000 < Re < 20000$, a range considered to be turbulent, a number of observations can be made. The concentration profiles predicted on the basis of Taylor's expression consistently under-predicts the spreading of the experimental concentration profile, due to the assumption of a highly turbulent velocity profile, which leads to low dispersion. The degree to which the concentration profiles predicted on the basis of Taylor's expression under-predicts the spreading of the concentration profiles increases with decreasing Reynolds Number. For lower Reynolds Numbers, the laminar sub-layer and buffer-zone are growing, causing an increase in dispersion, whereas Taylor's universal velocity distribution maintains a consistent highly uniform turbulent velocity profile, independent of Reynolds Number. It can also be seen that when the velocity profile of the present work is used, the predicted downstream concentration profile provides a much better fit to the downstream data, and accounts for the increase in dispersion as Reynolds Number decreases.

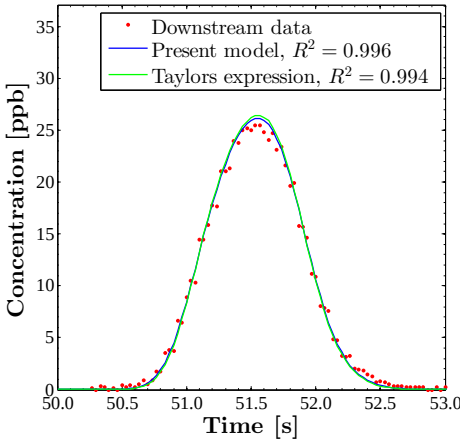

(a) Re = 50890.

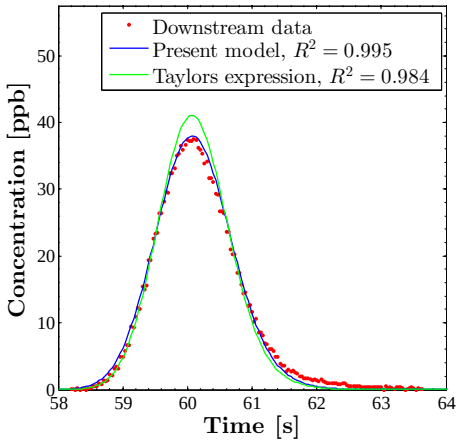

(b) Re = 20500.

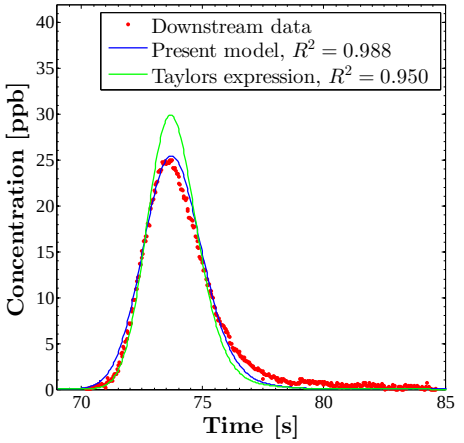

(c) Re = 10370.

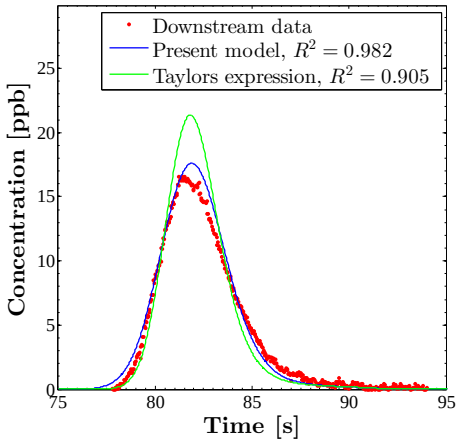

(d) Re = 8110.

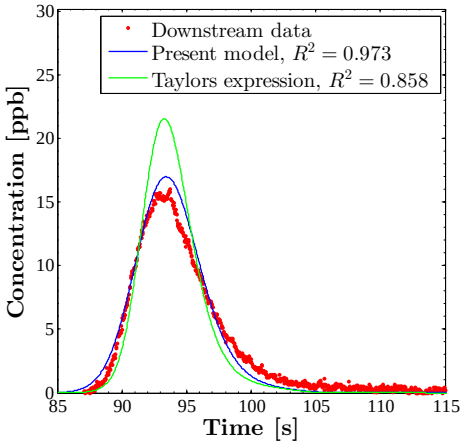

(e) Re = 5990.

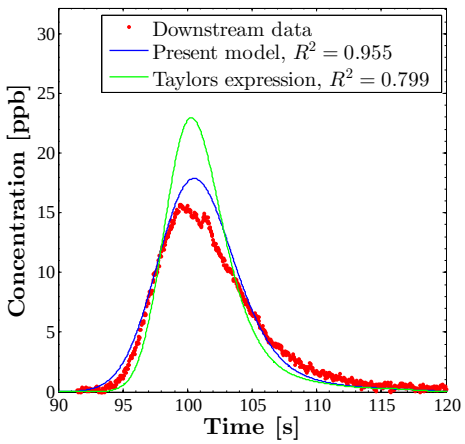

(f) Re = 5340.

Figure 5.30: *Comparison between downstream profiles and ADE prediction using longitudinal dispersion coefficient from model, using turbulent parameters present work and Taylor.*

5.5.2 Laminar and Transitional Flow

Figure 5.31 shows experimental downstream data, compared to three predicted profiles, predicted on the basis of the longitudinal dispersion coefficient from Chikwendu's model, assuming the turbulent, laminar and transitional parameters of the present work.

It can be seen that for all predicted concentration profiles within the transitional range, the predicted concentration profile on the basis of turbulent parameters predicts a relatively low level of dispersion, whereas the prediction on the basis of the laminar parameters predicts a relatively high level of dispersion. The prediction on the basis of the transitional parameters predicts a profile somewhere in between the turbulent and the laminar profile, on the basis of the value for α. The transitional profile, in general, provides the best fit to the transitional data, and provides a reasonable prediction of the downstream profiles for $3000 < Re < 5000$. For $2000 < Re < 3000$, whilst the transitional parameters predict the spreading of the profile, the goodness of fit is reduced by the non-Gaussian distributions of the concentration profiles.

5.5.3 Summary of Results for Numerical Model for Steady Flow

Within this section it has been shown that when the model presented in Chapter 3 is used with the turbulent and laminar parameters of the present work, the model predicts the trends for the experimentally obtained data of the present work for the longitudinal dispersion coefficient for both turbulent and laminar flow. Further more, the two predicted trends form boundaries in which transitional data falls. The transition of the velocity profile from a turbulent to a laminar profile was proposed on the basis of the experimental data of the present work, and provided parameters for transitional flow. When the transitional parameters were used within the model, the model provided a good prediction of the experimental data of the present work for the longitudinal dispersion coefficient within transitional flow.

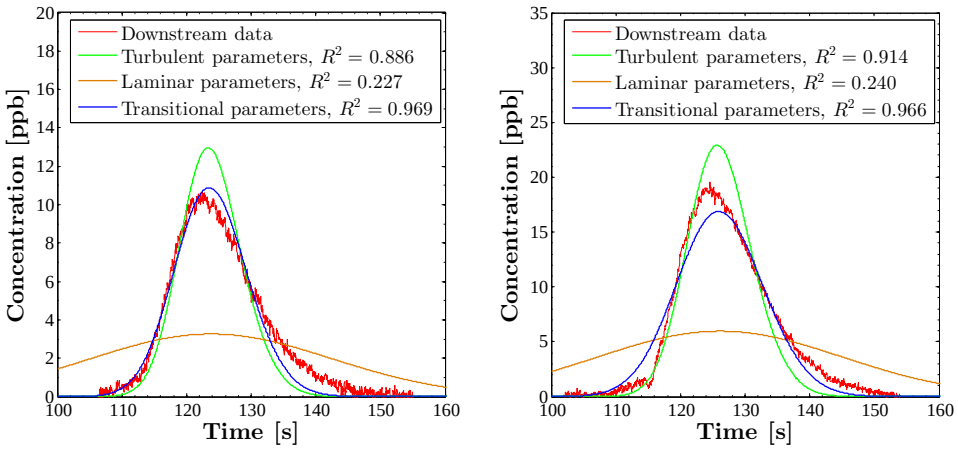

(a) Re = 3780.

(b) Re = 3570.

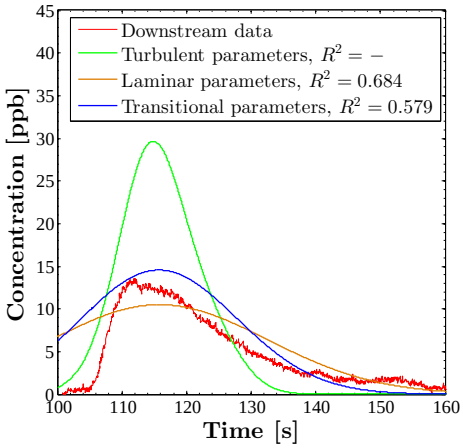

(c) Re = 2790.

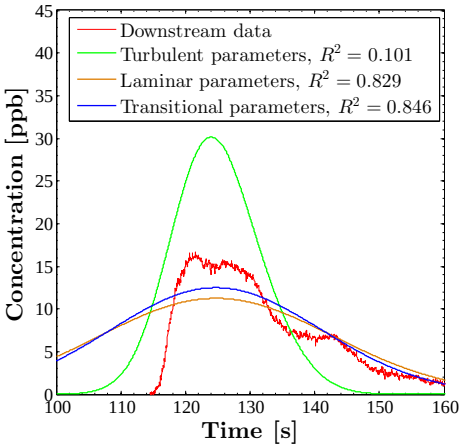

(d) Re = 2270.

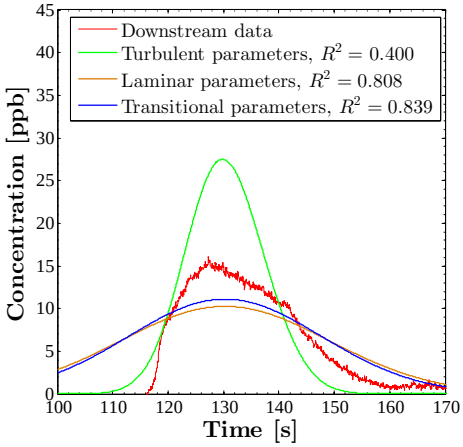

(e) Re = 2190.

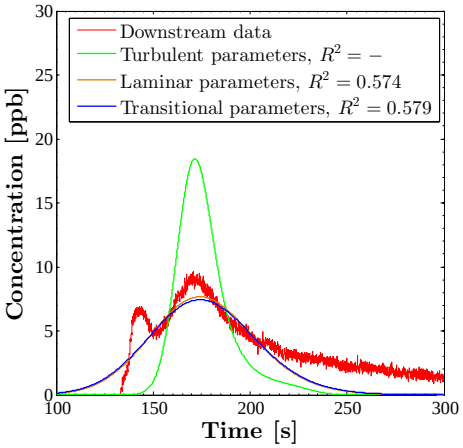

(f) Re = 1820.

Figure 5.31: *Compassion between downstream profiles and ADE prediction using longitudinal dispersion coefficient predicted through model, using laminar, turbulent and transitional parameters.*

5.6 Summary

Within this chapter experimental data for the friction factor and velocity profile were used to suggest that flow within the experimental facility used for all tests for the present work is turbulent for $Re > 5000$, laminar for $Re < 2000$ and thus transitional for $2000 < Re < 5000$.

Experimental results from tracer tests were also presented, which show that longitudinal dispersion increases with decreasing Reynolds Number, and that the trend can be explained in terms of the changing form of the velocity profile with Reynolds Number, on the basis of the hydraulic data presented. It was also shown that the Fickian model is valid for $Re > 3000$ for the facility of the present work.

The numerical model presented in Chapter 3 was used on the basis of the hydraulic data presented in this Chapter. With parameters consistent with the hydraulic data presented, the model was shown to provide a good prediction of the longitudinal dispersion coefficient compared to experimental data of the present work for $2000 < Re < 50000$.

Chapter 6

Results, Analysis and Discussion for Unsteady Flow

6.1 Introduction

This chapter presents the results, analysis and some discussion for all tests undertaken for unsteady flow.

Within Chapter 5, it was shown that the Fickian model is valid for the facility used for $3000 < Re < 50000$, and can provide useful insight into mixing characteristics for $Re < 3000$. It was also shown that a distinct change in the system's mixing characteristics occurs for transitional flow, for $2000 < Re < 5000$.

Within this Chapter, the Fickian model will be assumed, and longitudinal dispersion coefficients obtained using the ADE optimisation procedure discussed in Chapter 5. Longitudinal dispersion coefficients will then be compared to pseudo-steady longitudinal dispersion coefficients, to investigate conditions under which a steady model can be used to predict the longitudinal dispersion coefficient within unsteady flow.

6.2 Analysis Method for Unsteady Flow

Previously in this work, concentration profiles have been considered as concentration vs. time profiles, where the longitudinal dispersion coefficient quantifies the change in temporal variance between an up and a downstream profile.

For unsteady flow conditions, this approach becomes problematic. For example, if the discharge increases between measuring the up and downstream profile, there may be an apparent reduction in temporal variance of the profile due to the

changing discharge [Bennett, 2012].

To address this problem, profiles can be considered as concentration vs. cumulative volume profiles. The volume passing through a site at a given time step is:

$$v = Qdt \tag{6.1}$$

Thus, the cumulative volume, which can be used as an effective time, is:

$$\sum v = \sum Qdt \tag{6.2}$$

The discharge in Equation 6.2 accounts for the effect of changing discharge upon the tracer cloud.

Employing concentration vs. cumulative volume profiles allows an illustrative value for the longitudinal dispersion coefficient to be obtained in an analogous manner to that from the temporal profiles. [Bennett, 2012].

If the flow is steady, and the longitudinal dispersion coefficient is calculated on the basis of cumulative volume profiles, dimensional analysis can be used to show that the longitudinal dispersion coefficient is the same as if calculated from temporal profiles, divided by the discharge, such that:

$$D_{xx}(v) = D_{xx}(t)\frac{1}{Q} \tag{6.3}$$

Where $D_{xx}(v)$ and $D_{xx}(t)$ are the longitudinal dispersion coefficient as a function of cumulative volume and time respectively.

Thus, Equation 6.3 can be re-arranged to give the longitudinal dispersion coefficient in conventional units as:

$$D_{xx}(t) = D_{xx}(v)Q \tag{6.4}$$

Within unsteady flow, the discharge is a function of time. Thus, the discharge needs to be considered as the mean discharge over a time period, where the time period is the time over which the two profiles are considered:

$$\bar{Q} = \frac{1}{t_2 - t_1}\sum_{i=t_1}^{i=t_2} Q(t_i) \tag{6.5}$$

Where t_1 is the first measurement of the upstream profile, and t_2 is the final measurement of the downstream profile.

Thus, the effective longitudinal dispersion coefficient within unsteady flow,

calculated between two concentration vs. cumulative volume profiles, can be considered as:

$$D_{xx}(t) = D_{xx}(v)\bar{Q} \tag{6.6}$$

In addition to the mean discharge, the mean temporal cross-sectional mean velocity, $\bar{\bar{u}}$, and mean Reynolds Number, $\bar{Re}$, can be calculated from the mean discharge.

For the injections made into unsteady flow considered in this Chapter, the longitudinal dispersion coefficient was obtained through the optimisation method discussed in Chapter 5. The only modifications made were to use cumulative volume rather than time, and the temporal mean cross-sectional mean velocity $\bar{\bar{u}}$.

6.3 Model Formation for Unsteady Flow

The framework used within this Chapter to predict the longitudinal dispersion coefficient within unsteady flow was discussed in Chapter 3, Section 3.4. It was proposed that the longitudinal dispersion coefficient can be estimated within unsteady flow by predicting the longitudinal dispersion coefficient at discrete times within the unsteady flow, as if the flow was steady, or 'pseudo-steady', and then estimate a mean longitudinal dispersion coefficient from these discrete values. This Chapter will consider conditions under which this framework is valid.

To use the model proposed in Chapter 3 for unsteady flow, an estimate for the longitudinal dispersion coefficient as a function of Reynolds Number needs to be made for steady flow, so that the longitudinal dispersion coefficient can be estimated at each discrete velocity, as if the flow was steady. Within this Chapter, two methods for predicting the longitudinal dispersion coefficient as a function of Reynolds Number for steady flow will be used; an empirical and a numerical method.

For the numerical method, the longitudinal dispersion coefficient will be predicted on the basis of the numerical model proposed for predicting the longitudinal dispersion coefficient within steady flow, proposed in Chapters 3 and 5, to predict the longitudinal dispersion coefficient as a function of Reynolds Number.

The empirical method will use a fit to steady dispersion data to predict the longitudinal dispersion coefficient as a function of Reynolds Number. The fits performed to the steady data to give an expression for the longitudinal dispersion coefficient as a function of Reynolds Number are presented in Appendix D. Whilst the numerical model is presented as the actual model for unsteady flow within this work, as it is predictive and independent of any tracer data collected. The empirical model is used as a control to highlight cases where the numerical model for unsteady flow is failing to predict the data because it does not fit the steady data well, rather

than the unsteady data. As the empirical model provides a very good fit to the steady data, it provides the best possible framework for predicting the longitudinal dispersion coefficient within unsteady flow to evaluate the numerical model against.

To predict the mean longitudinal dispersion coefficient within unsteady flow using either of the models, the longitudinal dispersion coefficient was predicted at each Reynolds Number of a measured discharge time series for the duration of the trace considered, i.e. from the time the first measurement of the upstream profile was made to the time that the final measurement of the downstream profile was made. The mean longitudinal dispersion coefficient for unsteady flow was then calculated as the mean value for all of the values predicted at each discrete Reynolds Number over this time period.

6.4 Pre-analysis Data Checking

Pre-analysis data checks, such as mass recovery between profiles and repeatability of traces for all tests considered showed similar results to the checks presented for steady data in Chapter 5.

6.5 Results for Longitudinal Dispersion within Transient Turbulent Flow

For turbulent flow, discharge transients were considered for accelerating flow between $Re = 6500$ and $Re = 47000$, and decelerating flow between $Re = 47000$ and $Re = 6500$. The flow was accelerated or decelerated by setting a gradient at which the pump changed speed from the initial discharge to the final discharge. The acceleration or deceleration rates were calculated to give target transient times, T, as 60, 10 and 5 seconds, as high, medium and low transient times. The lowest transient time, $T = 5$ seconds, was selected on the basis of it being the highest possible acceleration rate achievable by the pump.

The instruments between which the concentration profiles were used to calculated the longitudinal dispersion coefficient were selected to give a good characterisation of mixing characteristic within the high gradient transients, i.e. that the up and the downstream profiles were both within the transient, and were within it for the maximum time possible. For accelerating flow, the up and downstream profiles are from instruments 1 and 3, whereas for decelerating turbulent flow, the up and downstream profiles are used between instruments 2 and 4.

The main results are presented in Figures 6.1 to 6.3, which show the discharge transient, on which for each injection, the time of the first measurement of the upstream profile is shown with a solid coloured line, and the final measurment of the downstream profile is shown with a dashed line of the same colour. The time between these points is the time over which the mean Reynolds Number and longitudinal dispersion coefficient are calculated. The figures also shows downstream profiles for representative injections. The downstream experimental data is shown as a concentration vs. cumulative volume plot, and is compared to three profiles, an optimised profile and two unsteady modelled profiles. The optimised profile is obtained through the optimisation procedure described in Chapter 5, where the upstream profile is routed onto the downstream profile on the basis of an optimised longitudinal dispersion coefficient and travel time. The two modelled profiles show the same profile but with the longitudinal dispersion coefficient predicted on the basis of the unsteady model discussed previously in this Chapter, with the longitudinal dispersion coefficient calculated on the basis of the trend fitted to the steady data (Unsteady empirical model) and through the numerical model (Unsteady model).

When considering transient flow, a useful parameter to consider is the dimensionless discharge gradient, γ, as proposed by He and Jackson [2000], and defined in Equation 2.28. He and Jackson [2000] derived the gradient in a manner that if $\gamma < 1$, the flow is considered to behave as steady flow at each discrete velocity, hence the flow is deemed 'pseudo-steady'. If $\gamma > 1$, then the flow is considered to deviate from pseudo-steady characteristics. One limitation of the gradient is that it only provides a value that is pseudo-steady with respect to unity for accelerating flow.

Figure 6.1 shows an example of results for accelerating turbulent flow between $Re = 6500$ and $Re = 47000$, with a transient time of $T = 60$ seconds, the highest transient time considered and thus the lowest discharge gradient. This configuration corresponds to a mean discharge gradient of $\gamma = 0.132$, thus it is expected that the flow should be pseudo-steady. From Figure 6.1 (c) and (d), it can be seen that the numerical model provides a very good prediction of the longitudinal dispersion coefficient within the unsteady transient, suggesting that under such conditions the unsteady model is valid and the mixing processes are pseudo-steady.

Figure 6.3 shows an example set of results for accelerating turbulent flow between $Re = 6500$ and $Re = 47000$ with a transient time of $T = 5$ seconds, the smallest transient time considered and thus the highest discharge gradient. This configuration corresponds to a mean discharge gradient of $\gamma = 1.442$, thus it is expected that the flow should be none pseudo-steady to some degree. From Figure 6.3 (c), it can be seen that the numerical model provides a reasonable prediction

of the longitudinal dispersion coefficient within the unsteady transient, however, it can be seen that the model over predicts the downstream concentration.

Figure 6.2 shows an example set of results for accelerating turbulent flow between $Re = 6500$ and $Re = 47000$ with a transient time of $T = 10$ seconds. This configuration corresponds to a mean discharge gradient of $\gamma = 0.735$, thus it is expected that the flow should be pseudo-steady, although close to the none pseudo-steady case. From Figure 6.2 (c), it can be seen that the numerical model provides a good prediction of the longitudinal dispersion coefficient within the unsteady transient, suggesting that under such conditions the unsteady model is valid. However, it can be seen that the numerical model over predicts the concentration to a very small degree, in a similar but less pronounced manner than for the case where $T = 5$ seconds.

Similar downstream concentration profiles were observed for decelerating turbulent flow.

Table 6.1 summarises the entire test series for transient turbulent flow. Within Table 6.1, the 'Optimised' column shows the mean observed longitudinal dispersion coefficient on the basis of the ADE optimisation procedure. The 'Numerical Model' column shows the value for the longitudinal dispersion coefficient obtained through the unsteady model with the longitudinal dispersion coefficient predicted on the basis of the steady numerical model. It also shows the percentage error between the models value and the optimised value. The 'Empirical Model' column gives the value for the longitudinal dispersion coefficient obtained through the unsteady model with the longitudinal dispersion coefficient predicted on the basis of the value from the fit to the steady data, as well as the percentage error between the modeled value and the observed value. The reason for including the model where the longitudinal dispersion coefficient is predicted through the fit to the steady data is to highlight cases where error is caused by the numerical model failing to predict steady data, rather than the unsteady data, i.e. it operates as a control on the unsteady numerical model. Where values for γ are quoted, the flow is unsteady, where values are not quoted, the flow is steady.

From Table 6.1, it can be seen that for both accelerating and decelerating turbulent flow where the transient time is 60 seconds, i.e. the lowest discharge gradient of $\gamma = 0.132$ for accelerating flow, the mean error between the longitudinal dispersion coefficient predicted through the numerical model and the observed value obtained through the optimisation procedure is $< 10\%$ for all unsteady cases. This is a similar result to the value for steady flow, suggesting that the numerical model is valid for such discharge conditions and thus the longitudinal dispersion coefficient

is pseudo-steady.

From Table 6.1, it can be seen that for both accelerating and decelerating turbulent flow where the transient time is 5 seconds, i.e. the highest discharge gradient of $\gamma = 1.442$ for accelerating flow, the mean error between the longitudinal dispersion coefficient predicted through the numerical model and the observed value obtained through the optimisation procedure is $\approx 35\%$ for all unsteady cases. The error corresponds to the model under predicting the longitudinal dispersion coefficient for accelerating flow, and over predicting the longitudinal dispersion coefficient for decelerating flow. He and Jackson [2000] suggest that when $\gamma > 1$, there is a delay in the response of the turbulence. This idea would explain the error for both cases. For accelerating flow, the model would predict a velocity profile increasing in uniformity as Reynolds Number increases. However, if there was a delay in the formation of the turbulence, a low Reynolds Number velocity profile would exist temporarily at higher Reynolds Numbers within the acceleration, causing an increase in dispersion than would normally be observed for such Reynolds Numbers. Thus a higher longitudinal dispersion coefficient than would be predicted by the model. Further, the reverse would be true for high gradient decelerating flow, where the velocity profile would remain relatively flat until the high levels of turbulence had decayed, and the viscous effects had had time to allow the low turbulent velocity profile to form, causing a reduction in dispersion, and thus a lower longitudinal dispersion coefficient than would be predicted by the model. However, it should be noted that despite the $\approx 35\%$ error between the longitudinal dispersion coefficient of the model and the observed value, the prediction made by the numerical model still provides a reasonable prediction of the downstream concentration profile, as can be seen in Figure 6.3 (c), and by the fact that the value for R^2 for the numerical model is relatively high for all unsteady cases. For accelerating and decelerating turbulent flow, where the transient time is 10 seconds, corresponding to a discharge gradient of $\gamma = 0.735$, a similar yet far less pronounced trend can be seen, where the error is around $\approx 13\%$. Thus the numerical model provides a very good prediction for transient flow where $\gamma < 1$, and a reasonable prediction for up to $\gamma = 1.442$, the highest gradient considered.

For all cases, the injections into the final steady flow show fully steady characteristics, suggesting that fully developed steady flow is obtained relatively quickly after the end of the discharge transients. Thus suggesting a small relax time after the discharge transients, as would be expected for turbulent flow.

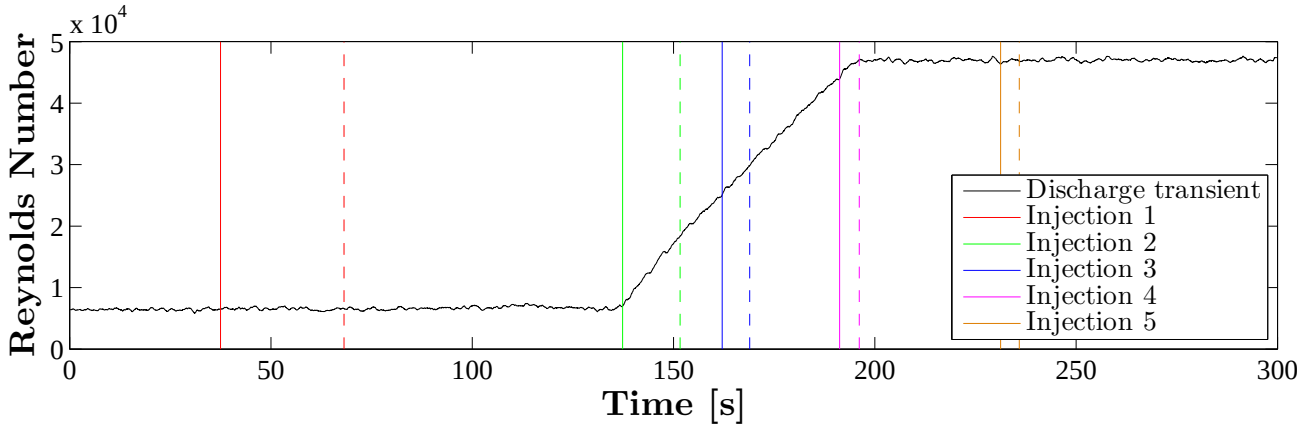

(a) Flow conditions.

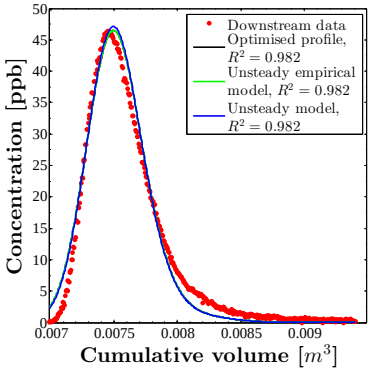

(b) Injection 1.

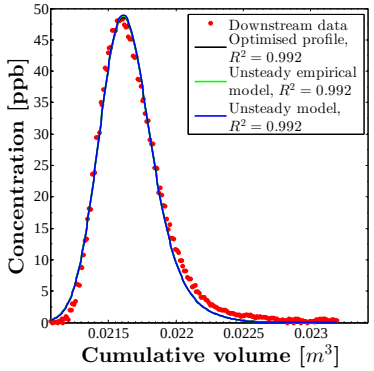

(c) Injection 2.

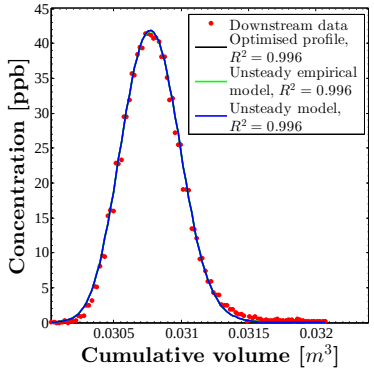

(d) Injection 3.

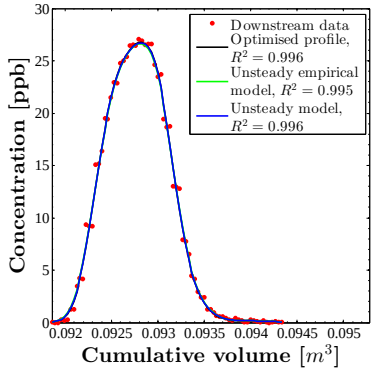

(e) Injection 5.

Figure 6.1: *Results for* $Re = 6500$ - $Re = 47000$ *for target transient time of* $T = 60$ *seconds.*

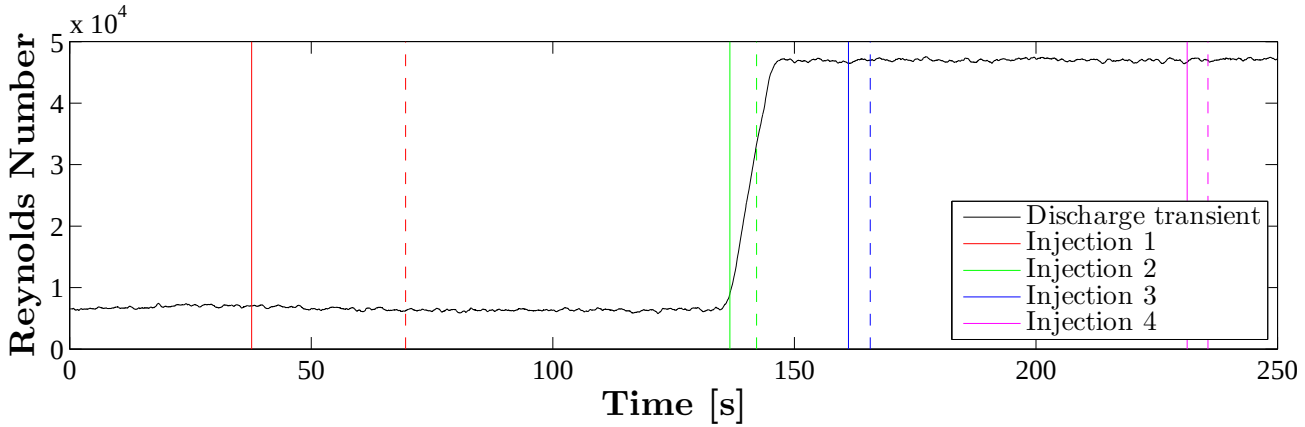

(a) Flow conditions.

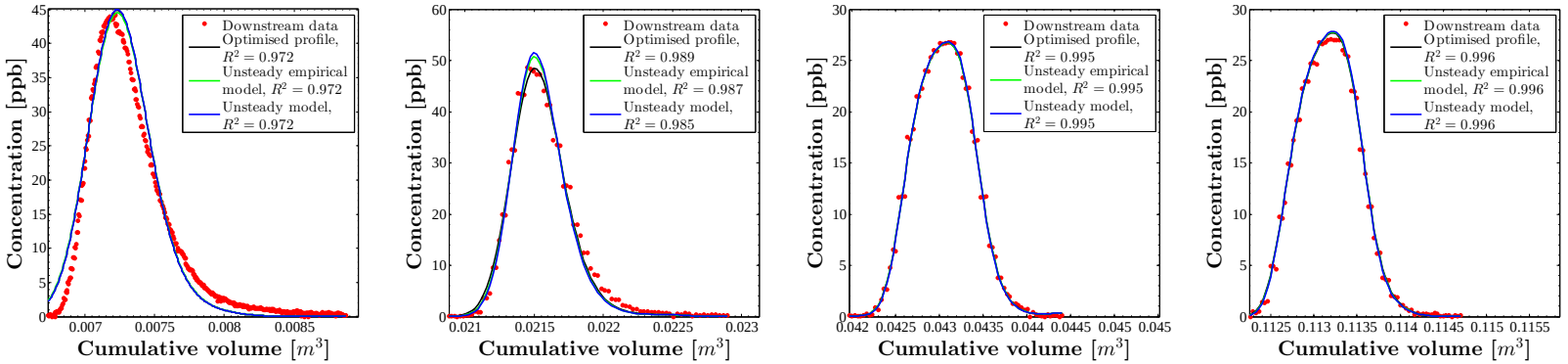

(b) Injection 1. (c) Injection 2. (d) Injection 3. (e) Injection 4.

Figure 6.2: *Results for* $Re = 6500$ - $Re = 47000$ *for target transient time of* $T = 10$ *seconds.*

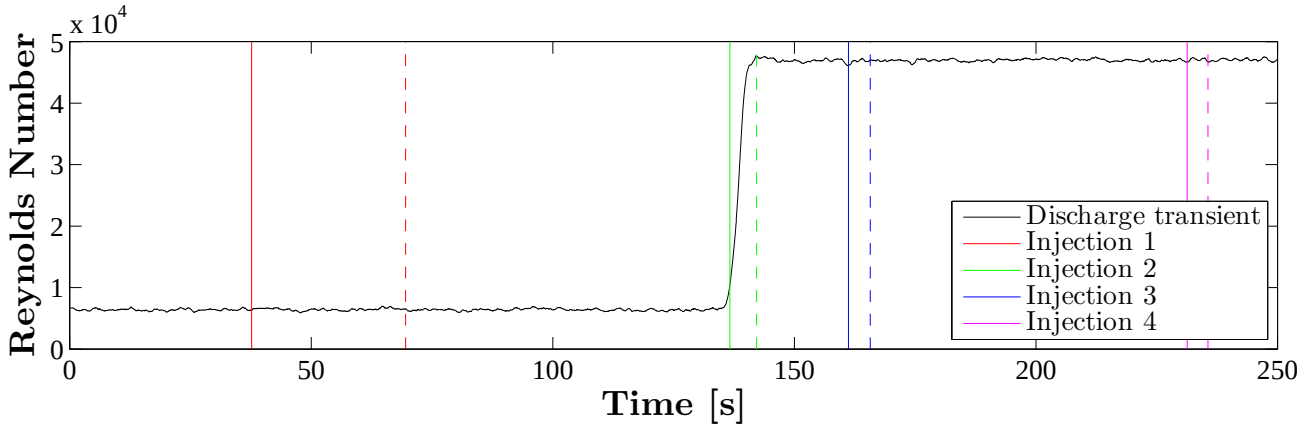

(a) Flow conditions.

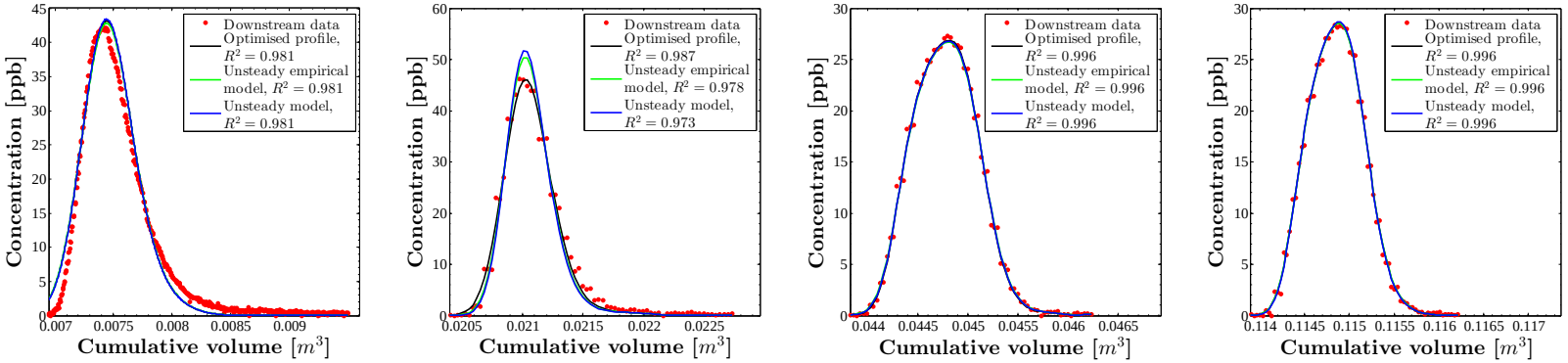

(b) Injection 1. (c) Injection 2. (d) Injection 3. (e) Injection 4.

Figure 6.3: *Results for* $Re = 6500$ - $Re = 47000$ *for target transient time of* $T = 5$ *seconds.*

Re_I	Re_F	**T [s]**	**Inj.**	γ	$\bar{Re}$	**Optimised**		**Empirical Model**			**Numerical Model**		
						$D_{xx}/\bar{\bar{u}}d$	R^2	$D_{xx}/\bar{\bar{u}}d$	R^2	Error [%]	$D_{xx}/\bar{\bar{u}}d$	R^2	Error [%]
6500	47000	60	1	-	6500	0.717 ± 0.022	0.980	0.733	0.980	2.1	0.703	0.980	2.0
			2	0.132	12900	0.465 ± 0.012	0.991	0.469	0.991	0.9	0.483	0.991	3.7
			3	0.132	27600	0.348 ± 0.005	0.996	0.348	0.996	0.0	0.345	0.996	1.0
			4	0.132	45900	0.296 ± 0.020	0.996	0.326	0.996	8.9	0.298	0.996	0.6
			5	-	46900	0.273 ± 0.026	0.996	0.325	0.996	15.6	0.297	0.996	7.9
6500	47000	10	1	-	6500	0.705 ± 0.028	0.978	0.725	0.978	2.8	0.698	0.978	1.0
			2	0.735	25000	0.428 ± 0.010	0.991	0.378	0.989	13.3	0.379	0.987	13.1
			3	-	47000	0.314 ± 0.020	0.996	0.325	0.996	7.4	0.297	0.996	5.9
			4	-	47000	0.314 ± 0.036	0.996	0.325	0.996	3.3	0.297	0.996	6.0
6500	47000	5	1	-	6500	0.705 ± 0.010	0.979	0.734	0.979	3.9	0.704	0.979	0.1
			2	1.442	34000	0.477 ± 0.017	0.987	0.355	0.979	34.4	0.344	0.974	38.7
			3	-	47000	0.297 ± 0.028	0.996	0.325	0.996	8.7	0.297	0.996	0.0
			4	-	47000	0.282 ± 0.045	0.996	0.325	0.996	13.2	0.296	0.996	4.9
47000	6500	60	1	-	47000	0.324 ± 0.021	0.997	0.363	0.997	10.6	0.296	0.997	9.6
			2	-0.003	46000	0.337 ± 0.034	0.997	0.363	0.997	7.2	0.298	0.997	12.9
			3	-0.003	25000	0.362 ± 0.017	0.998	0.381	0.998	5.0	0.356	0.998	1.9
			4	-0.003	6500	0.742 ± 0.014	0.989	0.767	0.989	3.2	0.700	0.989	6.1
			5	-	6500	0.725 ± 0.018	0.989	0.758	0.988	4.3	0.695	0.988	4.4
47000	6500	10	1	-	47000	0.349 ± 0.039	0.997	0.363	0.997	3.8	0.296	0.996	17.8
			2	-0.012	39000	0.275 ± 0.034	0.998	0.367	0.998	25.1	0.313	0.998	12.1
			3	-	6500	0.742 ± 0.016	0.985	0.765	0.985	3.0	0.699	0.985	6.2
			4	-	6500	0.745 ± 0.022	0.989	0.760	0.989	2.0	0.696	0.988	7.1
47000	6500	5	1	-	47000	0.359 ± 0.025	0.987	0.363	0.997	0.9	0.296	0.997	21.4
			2	-0.017	25000	0.264 ± 0.020	0.997	0.419	0.996	36.9	0.396	0.996	33.2
			3	-	6500	0.771 ± 0.019	0.983	0.756	0.983	2.0	0.693	0.982	11.1
			4	-	6500	0.749 ± 0.023	0.987	0.752	0.987	0.4	0.691	0.987	8.3

Table 6.1: *Summary unsteady data for transient turbulent flow.*

6.6 Longitudinal Dispersion within Transient Turbulent and Transitional Flow

For turbulent to transitional flow, discharge transients were considered for accelerating flow between $Re = 2700$ and $Re = 47000$, and decelerating flow between $Re = 47000$ and $Re = 2700$. Transient times were again set as 60, 10 and 5 seconds.

The instruments between which the two concentration profiles were used to calculate the longitudinal dispersion coefficient were instruments 1 and 3 for acceleration transitional to turbulent flow, and instruments 2 and 4 for decelerating turbulent to transitional flow. The main results for turbulent to transitional transient flow are presented in Figures 6.4 - 6.6.

Figure 6.4 shows an example set of results for accelerating transitional to turbulent flow between 2700 and 47000 with a transient time of $T = 60$ seconds, the highest transient time considered and thus the lowest discharge gradient. This configuration corresponds to a mean discharge gradient of $\gamma = 0.665$. From Figure 6.4 two main observations can be made. Firstly, that for the two injections made into the discharge transient, as shown in Figure 6.4 (c) and (d), there is very good agreement between the prediction of the numerical model and the main body of the downstream profile. Secondly, for the first injection made into the transient flow, as shown in Figure 6.4 (c), an injection made into transitional/laminar acceleration, although there is good agrement between between the prediction made by the numerical model and the main body of the profile, there is a non-conventional form to the profile's leading and trailing edge, where a small bump can be seen on the leading edge, and a small secondary profile can be seen on the trailing edge. Figure 6.7 (a) shows the development of the concentration profile at each instrument within the transient. It can be seen that the profile begins as a single conventional concentration vs. cumulative volume profile at instrument 1. By instrument 3, it has split into two distinct profiles, a main profile, and a small secondary profile. After instrument 3, the secondary profile approaches the main profile, to the point that by instrument 6, the two profiles are conjoined.

Given the lack of hydraulic data within unsteady flow for the present work, it is beyond the scope of the present work to provide a substantiated argument as to the cause of this phenomenon. However, some insight can be gained by considering previous investigations into the hydraulics of accelerating low Reynolds Number laminar/transitional flow. Kurokawa and Morikawa [1986] presented velocity profiles for flow accelerated from stationary to a highly turbulent Reynolds Numbers over several transient times, a flow configuration similar to the discharge transient of

the present case, i.e. low gradient laminar/transitional to turbulent acceleration, where the transition to turbulent flow occurs within the acceleration. Figure 2.15 (b) shows an acceleration for a transient time of $T = 25$ seconds, the closest match to the presently discussed acceleration configuration. From 2.15 (b) it can be seen that in the initial period of laminar acceleration, leading up to the transition to turbulence, a large discrepancy can be seen within the laminar velocity profile, where the velocity of the boundary layer remains relatively small, whereas the velocity at the core is relatively large. This segregation continues to the point that just before the transition, a large step in the profile can be seen between the region of high velocity in the core, and a region of low velocity in the boundary layer. After the transition, the disparity quickly decays and the flow field obtains a conventional turbulent distribution. If this large step was to appear in the velocity profile during the laminar/transitional acceleration phase, the conventional concentration profile seen just after injection at instrument 1 could split under the extreme differential advection caused by having a large step between the very high velocity at the core, and very small velocity at the boundary. This could lead to the main portion of the profile being transported in the core, and a secondary section of tracer left in the boundary layer. As the flow transitions to being turbulent, the tracer residing in the boundary layer would become quickly well mixed, and thus would form a secondary profile, as seen at instrument 3. As the disparity in the velocity profile decays after the transition, and the velocity profile obtains a fully turbulent distribution, the two profiles would begin to converge, as is seen as the profile travels beyond instrument 3.

Figure 6.6 shows an example set of results for accelerating transitional to turbulent flow between 2700 and 47000 with a transient time of 5 seconds, the lowest transient time considered and thus the highest discharge gradient. This configuration corresponds to a mean discharge gradient of $\gamma = 10.583$. Again, two main observations can again be made. Firstly, that for the injections made into the transient flow, as shown in Figure 6.6 (c), the numerical model makes a reasonable general prediction of the concentration distribution, but noticeably over predicts the concentration distribution in a similar, yet more pronounced manner to what was seen in the previous section for high gradient turbulent flow. This would be expected for the gradient $\gamma = 10.583$, the highest gradient considered. Secondly, for the injection made into the transient flow, the downstream profile again has discrepancies at the leading and trailing edge, and a secondary profile on its trailing edge. Figure 6.7 (c) shows the development of the concentration profile at each instrument within the transient. It can be seen that the form of the profile is similar

to the low gradient laminar/transitional acceleration seen in 6.7 (a), however, the profiles re-converge more rapidly than for the low gradient case. In the context of the explanation for the phenomenon suggested for the previous case, this would be understood as being due to the fact that for the high gradient transient, the shorter transient time would lead to a shorter period of laminar/transitional acceleration, and a longer period of turbulent acceleration. Thus, the period of exposure to the segregated laminar profile would be shorter, and the period of conventional turbulent profile in which the concentration profiles could re-converge would be greater.

Figure 6.5 shows an example set of results for accelerating transitional to turbulent flow between $Re = 2700$ and $Re = 47000$ with a transient time of 10 seconds. This configuration corresponds to a mean discharge gradient of $\gamma = 4.354$. From Figure 6.5 it can be seen that the results for the mid transient time 10 seconds fall in between the results for the high and low transient gradients. From Figure 6.5 (c) it can be seen that the numerical model over predicts the downstream concentration profile in a similar manner to that observed for the high gradient case, but to a lesser degree. Figure 6.7 (b) shows the development of the concentration profile at each instrument within the transient, from which it can be seen that the secondary profile re-converges with the main profile more quickly than for the low gradient flow, but slower than for the high gradient flow.

Similar downstream profiles were observed for decelerating turbulent to transitional flow as for accelerating and decelerating turbulent flow.

Table 6.2 summarises the entire test series for transient turbulent and transitional flow.

From Table 6.2 it can be seen that for both accelerating and decelerating turbulent to transitional flow where the transient time is $T = 60$ seconds, i.e. the lowest discharge gradient of $\gamma = 0.665$ for accelerating flow, the mean error between the longitudinal dispersion coefficient predicted through the numerical model and the observed value obtained through the optimisation procedure is $< 12\%$ for all unsteady cases, which is a similar result to the value for steady flow, suggesting that the numerical model is valid for such discharge conditions. However, it should be noted that the low error for accelerating transitional to turbulent flow does not account for the non-conventional profiles, as the optimised and modelled profiles both give a very good fit the main profile, and thus the failure of the optimised and modelled profiles to predict the secondary profile is not well demonstrated by the value for R^2.

From Table 6.2 it can be seen that for both accelerating and decelerating turbulent to transitional flow where the transient time is $T = 5$ seconds, i.e. the

highest discharge gradient of $\gamma = 10.583$ for accelerating flow, the mean error between the longitudinal dispersion coefficient predicted through the numerical model and the observed value obtained through the optimisation procedure is $\approx 40\%$ for all unsteady cases. The error again corresponds to the model under predicting the longitudinal dispersion coefficient for accelerating flow, and over predicting the longitudinal dispersion coefficient for decelerating flow. This error is again suggested as being due to the flow having a discharge gradient of $\gamma > 1$, where there is a delay in the response of the turbulence. Again, the results do not account for the non conventional profiles for accelerating transitional to turbulent flow.

A further interesting result can be seen from Table 6.2 for results for the injection into the final steady flow. For the deceleration from $Re = 47000$ to $Re = 2700$ at the lowest transient time $T = 5$ seconds, corresponding to the highest discharge gradient $\gamma = 10.583$, two injections were made into the final steady flow of $Re = 2700$, after the discharge transient. It can be seen that despite the fact that the discharge is steady, and the same for both injections, the magnitude of the longitudinal dispersion coefficient increases from the first injection to the second by a factor of approximately 1.8. Furthermore, the standard deviation increases from a value approximately 10% that of the mean longitudinal dispersion coefficient for the first injection to around 100% that of the mean longitudinal dispersion coefficient for the second injection, and the goodness of fit between the ADE optimisation model decreases from $R^2 = 0.975$ for the first injection to $R^2 = 0.781$ for the second injection. The fact that the first injection has a relatively low longitudinal dispersion coefficient, low standard deviation and high goodness of fit, compared to the second injection into the same discharge which has a relatively high longitudinal dispersion coefficient, high standard deviation and low goodness of fit suggests that for the first injection, the flow is still turbulent, whereas for the second injection, the flow is transitional to laminar. Similar results can be seen for $T = 10$ seconds. These results suggest that when the flow is decelerating from turbulent to transitional to laminar flow at a high gradient, where $\gamma > 1$, there is a relatively long relax time required for the flow to recover from the discharge transient, and resume the flow characteristics that would be expected for that Reynolds Number.

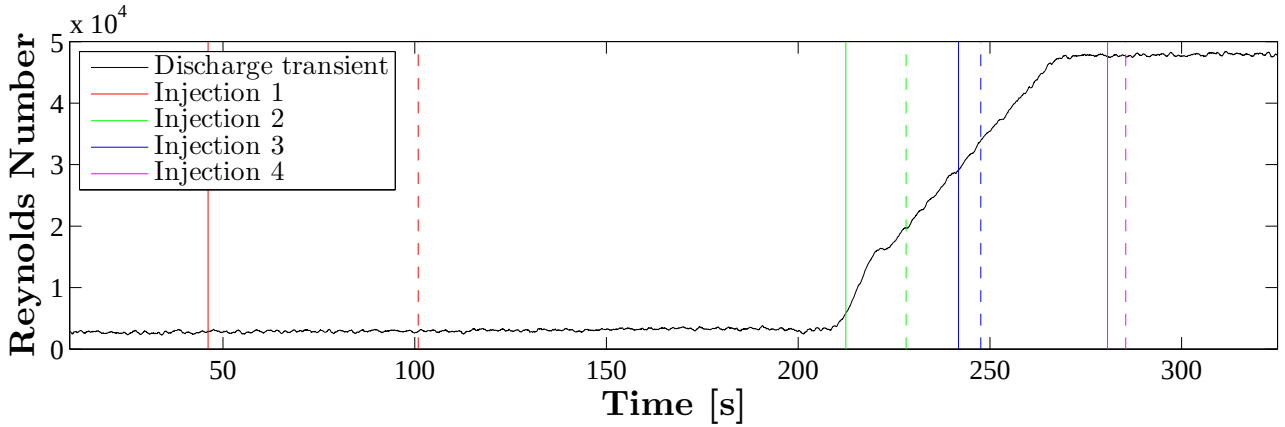

(a) Flow conditions.

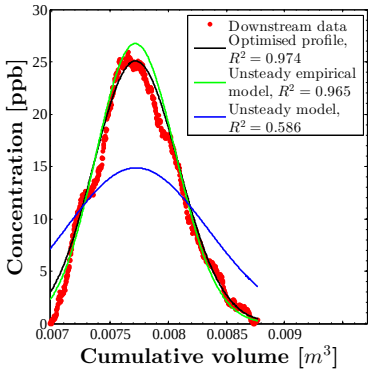

(b) Injection 1.

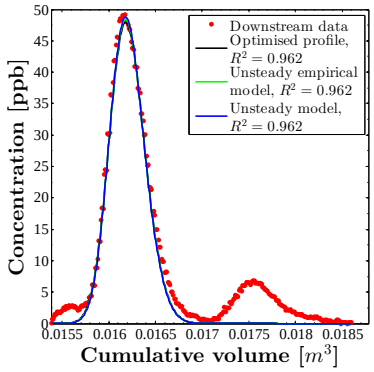

(c) Injection 2.

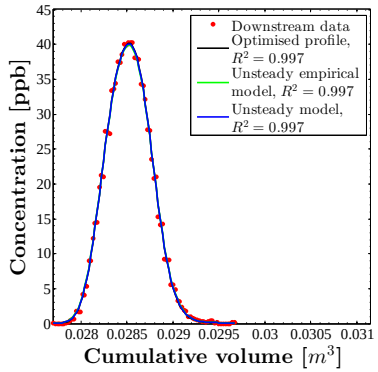

(d) Injection 3.

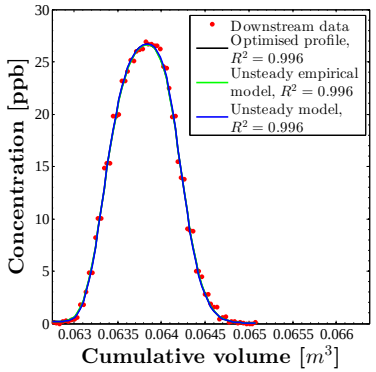

(e) Injection 5.

Figure 6.4: *Results for* $Re = 2700$ - $Re = 47000$ *for* $T = 60$ *seconds.*

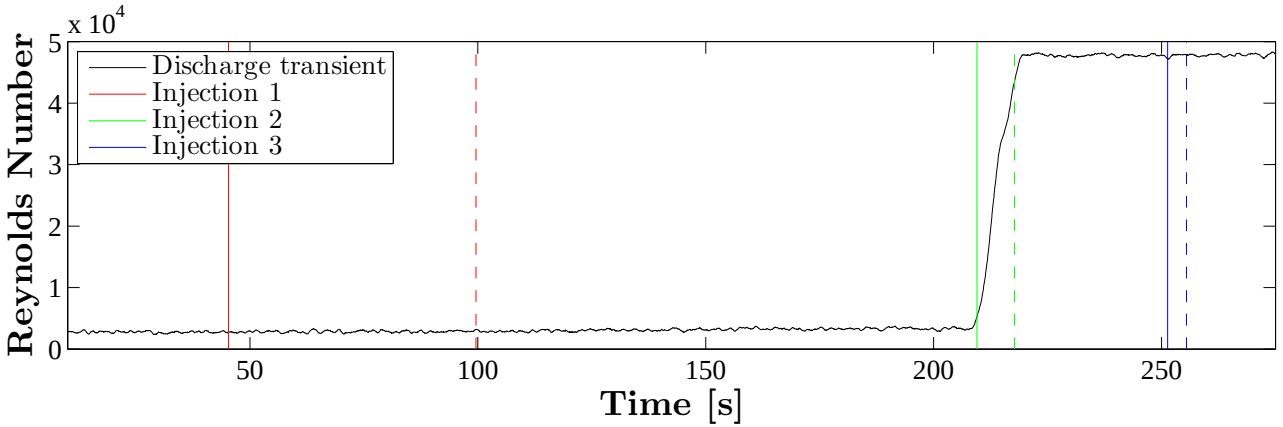

(a) Flow conditions.

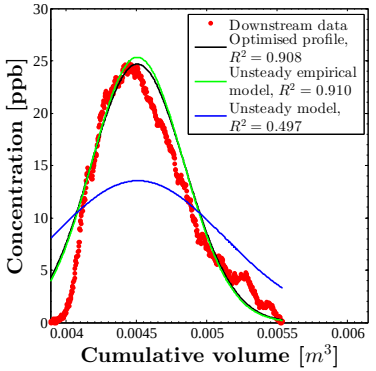

(b) Injection 1.

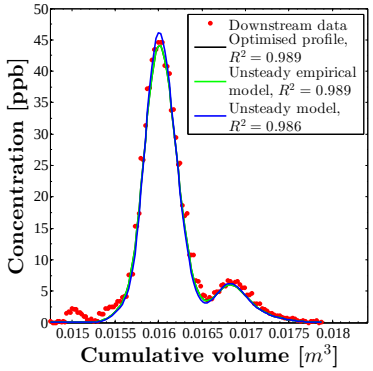

(c) Injection 2.

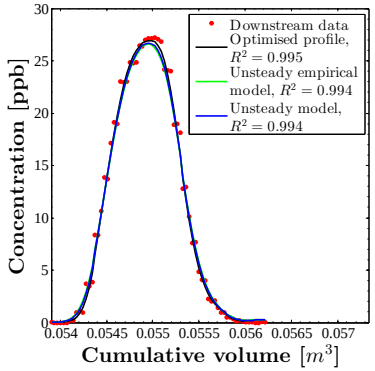

(d) Injection 3.

Figure 6.5: *Results for* $Re = 2700$ - $Re = 47000$ *for* $T = 10$ *seconds.*

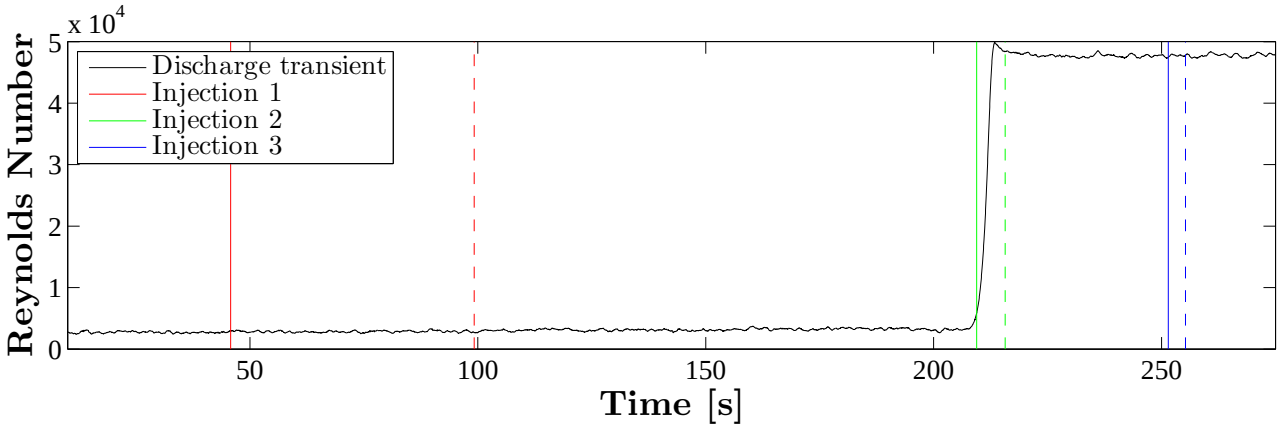

(a) Flow conditions.

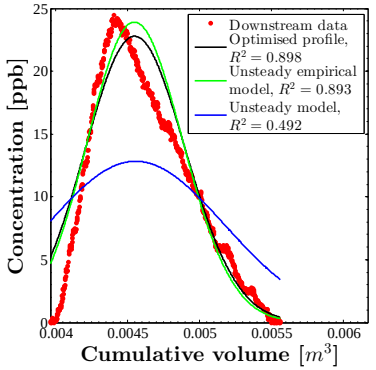

(b) Injection 1.

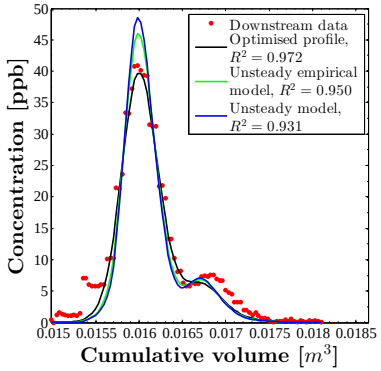

(c) Injection 2.

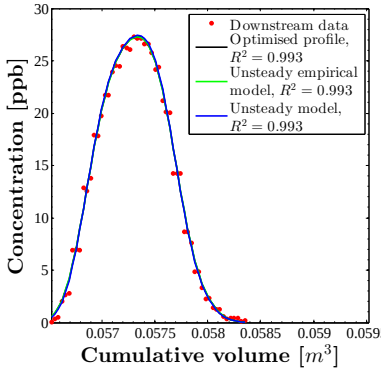

(d) Injection 3.

Figure 6.6: *Results for* $Re = 2700$ - $Re = 47000$ *for* $T = 5$ *seconds.*

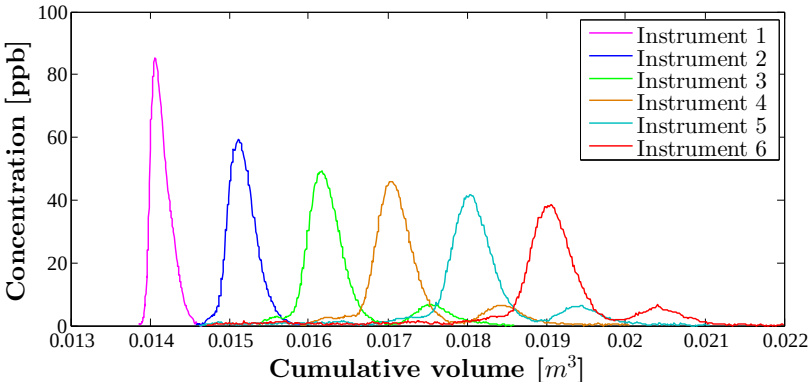

(a) $T = 60$.

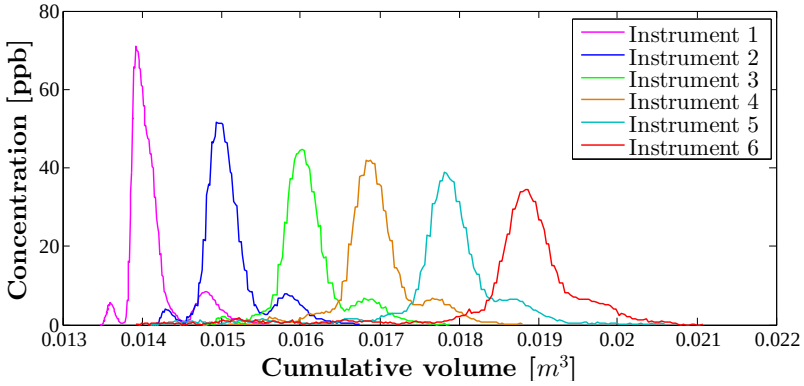

(b) $T = 10$.

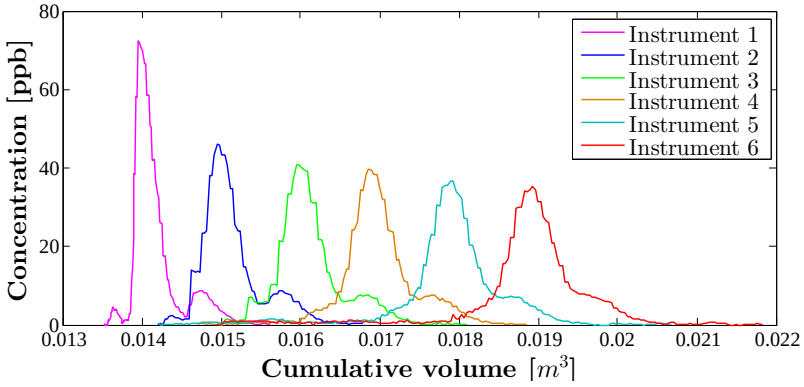

(c) $T = 5$.

Figure 6.7: *Example of concentration profiles at each instrument for laminar/transitional acceleration.*

Re_I	Re_F	**T [s]**	**Inj.**	γ	$\bar{Re}$	**Optimised**		**Empirical Model**			**Numerical Model**		
						$D_{xx}/\bar{\bar{u}}d$	R^2	$D_{xx}/\bar{\bar{u}}d$	R^2	Error [%]	$D_{xx}/\bar{\bar{u}}d$	R^2	Error [%]
2700	47000	60	1	-	2700	3.049 ± 1.420	0.872	2.033	0.819	50.0	8.107	0.586	62.4
			2	0.665	13000	0.485 ± 0.052	0.959	0.496	0.959	2.2	0.506	0.960	4.2
			3	0.665	32000	0.324 ± 0.024	0.996	0.347	0.996	6.7	0.330	0.996	1.8
			4	-	47000	0.268 ± 0.035	0.995	0.334	0.995	19.6	0.295	0.995	9.2
2700	47000	10	1	-	2700	3.041 ± 1.271	0.865	2.035	0.777	49.5	8.150	0.589	62.7
			2	4.354	25000	0.499 ± 0.159	0.980	0.437	0.986	14.1	0.428	0.983	16.6
			3	-	47000	0.245 ± 0.080	0.983	0.334	0.982	26.7	0.295	0.983	17.2
2700	47000	5	1	-	2700	3.551 ± 1.272	0.834	2.021	0.673	75.7	8.036	0.628	55.8
			2	10.583	35000	0.535 ± 0.069	0.973	0.389	0.964	37.8	0.368	0.952	45.4
			3	-	47000	0.300 ± 0.023	0.994	0.334	0.994	10.0	0.295	0.994	1.7
47000	2700	60	1	-	47000	0.337 ± 0.036	0.996	0.311	0.996	8.2	0.295	0.996	14.0
			2	-0.003	46000	0.330 ± 0.028	0.997	0.312	0.997	6.0	0.298	0.997	11.1
			3	-0.003	24000	0.366 ± 0.015	0.998	0.340	0.998	7.7	0.362	0.998	1.1
			4	-	2700	2.583 ± 0.231	0.972	1.758	0.959	46.9	8.500	0.840	69.6
4700	2700	10	1	-	47000	0.354 ± 0.049	0.997	0.311	0.997	13.7	0.295	0.997	19.9
			2	-0.011	39000	0.293 ± 0.024	0.998	0.317	0.998	7.4	0.312	0.998	6.1
			3	-	2700	2.645 ± 0.503	0.972	1.791	0.952	47.7	8.040	0.768	67.1
			4	-	2700	3.648 ± 3.621	0.849	1.978	0.745	84.5	5.771	0.729	36.8
47000	2700	5	1	-	47000	0.387 ± 0.027	0.996	0.311	0.996	24.4	0.295	0.996	31.1
			2	-0.016	23000	0.274 ± 0.040	0.997	0.442	0.996	38.09	0.445	0.996	38.5
			3	-	2700	2.378 ± 0.205	0.975	1.814	0.967	31.1	7.805	0.787	69.5
			4	-	2700	4.389 ± 4.974	0.781	1.984	0.668	121.2	5.639	0.667	22.2

Table 6.2: *Summary unsteady data for transient transitional to turbulent flow.*

6.7 Summary

Within this Chapter tracer data has been considered for various configurations of discharge transients for turbulent and transitional flow.

The mean longitudinal dispersion coefficient within discharge transients for accelerating and decelerating turbulent flow was compared to the mean longitudinal dispersion coefficient, predicted by the numerical model for steady flow presented in Chapters 3 and 5. It was shown that the numerical model makes a very good prediction of the data for discharge gradients of $\gamma < 1$, and reasonable predictions for up to $\gamma = 1.442$. These results shows that when the dimensionless discharge gradient is $\gamma < 1$, the longitudinal dispersion coefficient is pseudo-steady, and thus can be predicated through a steady model.

For discharge transients for accelerating flow between transitional and turbulent flow, it was shown that the numerical model makes a very good prediction of the main concentration profile for discharge gradients of $\gamma < 1$, and reasonable predictions for up to $\gamma = 10.583$. However, non-conventional concentration profiles were observed for all accelerating transitional to turbulent flow, which were not predicted by the model. It was suggested that these profiles were caused by non-conventional velocity profiles within accelerating laminar/transitional flow. The results show that whilst a pseudo-steady model can make useful predictions with such flows, the form of the concentration profiles suggest that the mixing processes are non-pseudo steady. For decelerating turbulent to transitional flow similar results were observed than for transients within turbulent flow, with the exception of a longer relax time after the transient, for the flow to resume fully developed steady characteristics.

Chapter 7

Conclusions

For steady pipe flow, experimental data has shown that the longitudinal dispersion coefficient increases in magnitude as Reynolds Number decreases for $Re < 20000$. Hydraulic data collected on the same facility indicated that this trend is due to the increase in non-uniformity of the velocity profile. For turbulent flow, the increase in non-uniformity is caused by the velocity profile's growing boundary layer. For transitional flow, a more pronounced increase in the longitudinal dispersion coefficient is caused by the relatively flat velocity profile seen for turbulent flow transitioning into a relatively non-uniform parabolic profile for laminar flow. By considering the systems CRTDs, it was also shown that a distinct change occurs in the fundamental mixing response of the system for transitional flow, where the CRTDs deviate significantly from the relatively consistent shape maintained for the turbulent range.

It was also shown that for steady pipe flow, the Fickian model for longitudinal dispersion is valid for turbulent flow, and the initial portion of the transitional range. The point at which the Fickian model appears to become invalid corresponds to the point at which the system's CRTDs deviate from the relatively consistent shape maintained for turbulent flow, to a more non-conventional shape for transitional flow. For low transitional to laminar flow, the Fickian model provides poor predictions of the downstream concentration profiles for a given upstream injection, but can still be a useful assumption for estimating the general mixing characteristics of a system.

The expression of Taylor [1954] for turbulent flow fails to predict the longitudinal dispersion coefficient for $Re < 20000$, due to his assumption of a highly turbulent velocity profile, which does not include a laminar sub-layer or buffer zone. If Taylor's parameters are used within the model of Chikwendu [1986], but with a turbulent velocity profile that includes a laminar sub-layer and buffer zone, and a transitional velocity profile that accounts for the velocity profile transitioning from

a turbulent profile to a laminar profile, the model makes a good prediction of the longitudinal dispersion coefficient for steady flow for $2000 < Re < 50000$. This is due to the better defined velocity profile accounting for the increase in differential advection as the velocity profile becomes more non-uniform with decreasing Reynolds Number. The model provides a very good prediction of the longitudinal dispersion coefficient for turbulent flow, and a reasonable, but reduced fit to the data for transitional flow, as the standard deviation of the longitudinal dispersion coefficient increases for transitional flow, making it intrinsically more difficult to predict the mixing characteristics, as the flow transitions from being laminar to turbulent. The model also provides a very good prediction of the downstream concentration distributions on the basis of the predicted longitudinal dispersion coefficient for turbulent flow, but fails to account for the non-Gaussian downstream profiles observed for transitional flow. The model does, however, broadly account for the spreading of the profiles for transitional flow.

For unsteady pipe flow, it was shown that using a representative mean longitudinal dispersion coefficient, assuming the Fickian model, can provide useful insight into the mixing characteristics of a system for unsteady, transient flow. On this basis, a steady model for the longitudinal dispersion coefficient can provide a very good estimate of the longitudinal dispersion coefficient within unsteady, transient flow, for discharge gradients of $\gamma < 1$. Where $\gamma > 1$, a steady model for the longitudinal dispersion coefficient typically under predicts the dispersion coefficient for accelerating flow, and over predicts the longitudinal dispersion coefficient for decelerating flow. However, the model was shown to provide a reasonable prediction of the mixing characteristics of the flow for up to $\gamma = 10$, where the under or over estimation of the longitudinal dispersion coefficient only leads to small discrepancies between the predicted and measured downstream concentration profiles.

For accelerating laminar/transitonal flow, a non-conventional concentration distribution was observed, where discontinuities appear on the leading and trailing edge of the concentration profile. The discontinuity on the trailing edge is pronounced enough to appear to be a secondary profile, which re-converges within the main profile as the flow becomes turbulent. It was suggested that this phenomenon may be due to a non-conventional velocity profile within accelerating laminar/transitional transient flow, as has previously been observed by Kurokawa and Morikawa [1986]. However, measurements of the velocity profile for the discharge transient in question on the system used for the present work would be required to confirm this suggestion.

Chapter 8

Further Work

The study of longitudinal dispersion within steady flow within the present work provided a good overview of the mixing charctersitics of the system for turbulent and transitional flow, with respect to the flow's hydraulics through these regimes. However, a more comprehensive analysis could be possible with more detailed laboratory results. For the tracer tests, more insight could be gained, particularity for transitional and laminar flow, by measuring the point concentration of the solute cloud at multiple radial positions rather than as a cross-sectional mean result. This data would provide a better picture of the form of the tracer cloud when the solute is not cross-sectionally well mixed. For the hydraulic data, the ability to measure the velocity at several radial positions simultaneously, and thus obtain an entire velocity profile simultaneously, would allow for the flow's hydraulics to be obtained at the same time as tracer data, which would provide a clearer picture of the nature of the specific flow being investigated.

For modeling steady flow, it was shown that whilst the Fickian model is a reasonable assumption for turbulent and high transitional flow, it was observed that the validity of the model decreases for low turbulent and transitional flow. If the fundamental mixing characteristics of the flow at these Reynolds Numbers, quantified by the systems CRTDs presented in this work, could be incorporated into a steady model, the model would predict the downstream concentration distribution in a manner that would better facilitate the skewed profiles at theses flow rates.

For unsteady flow, better insight into the characteristics of the system for various discharge transients could be gained by collecting hydraulic data, such as the velocity profile and friction factor, for the configurations of unsteady flow considered in this work. Within this work it was suggested that a delay in the response of the turbulent occurs for $\gamma > 1$, and that a non-conventional velocity profile occurs for

transitonal/laminar acceleration. Both of these suggestions could be substantiated with suitable hydraulic data. If detailed hydraulic data were collected, an empirically based model could be developed to account for the delay in the turbulence of the longitudinal dispersion coefficient at high discharge gradients.

Further insight and predictive capabilities could be gained by developing a CFD model in conjunction within the tracer data presented within this work, and new hydraulic data for unsteady, transient flow. Such a model may be able to provide better understanding of the nature of non-pseudo-steady flow for high discharge gradients.

Bibliography

Acheson, D J. *Elementary Fluid Dynamics*. Oxford University Press, 1990.

Avila, K; Moxey, D; de Lozar, A; Avila, M; Barkley, D, and Hof, B. The onset of turbulence in pipe flow. *Science*, 333:192–196, 2011.

Avila, M; Willis, A P, and Hof, B. On the transient nautre of localized pipe flow turbulence. *Journal of Fluid Mechanics*, 646:127–137, 2010.

Benedict, R P. *Fundamentals of Pipe Flow*. John Wiley and Sons, 1980.

Bennett, P. *Evaluation of the Solute Transport Characteristics of Surcharged Manholes using a RANS Solution*. PhD thesis, 2012.

Blackburn, H M and Sherwin, S J. Formulation of a galerkin spectral element-fourier method for three-dimensional incompressible flows in cylindrical geometries. *Journal of Computational Physics*, 197:759–778, 2004.

Blasius, P R H. The law of similarity applied to friction phenomena. 1911.

Blokker, E J M; Vreeburg, J H G; Buchberger, S G, and van Dijk, J C. Importance of demand modelling in network water quality models: A reivew. *Drinking Water Engineering and Science*, 1:27–38, 2008.

Blokker, E J M; Vreeburg, J H G; Beverloo, H; Arfman, M Klein, and van Dijk, J C. A bottom-up approach of stochastic demand allocation in water quality modelling. *Drinking Water Engineering and Science*, 3:43–51, 2010.

Bowden, K F. Horizontal mixing in the sea due to a shearing current. *Journal of Fluid Mechanics*, 21:83–95, 1965.

Buchberger, S G; Carter, J T; Lee, Y, and Schade, T G. Random demands, travel times and water quality in deadends. *American Water Works Association Research Foundation*, Report 90963F:470, 2003.

Chikwendu, S C. Calculation of longitudinal shear dispersivity using an n-zone model as n $\rightarrow \infty$. *Journal of Fluid Mechanics*, 167:19–30, 1986.

Chikwendu, S C and Ojiakor, G U. Slow-zone model for longitudinal dispersion in two-dimensionl shear flows. *Journal of Fluid Mechanics*, 152:15–38, 1985.

Colebrook, C F. Turbulent flow in pipes, with particular reference to the transition region between smooth and rough pipe laws. *Journal of the Institution of Civil Engineers*, 11:133–156, 1939.

Danckwerts, P V. Continuous flow systems distribution of residence times. *Chemical Engineering Science*, 2(1):1–13, 1953.

Darbyshire, A and Mullin, T. Transition to turbulence in constant-mass-flux pipe flow. *Journal of Fluid Mechanics*, 289:83–114, 1995.

Deissler, R G. Analytical and experimental investigation of adiabatic turbulent flow in smooth tubes. *NACA Technical Memorandum*, 2138, 1950.

Durst, F; Jovanovic, J, and Sender, J. Lda measurements in the near-wall region of a turbulent pipe flow. *Journal of Fluid Mechanics*, 295:305–335, 1995.

Eckhardt, B. Introduction. turbulence transition in pipe flow: 125th anniversary of the publication of reynolds' paper. *Philosophical Transactions of the Royal Society*, 367:449–455, 2009.

Eckhardt, B. A critical point for turbulence. *Science*, 333:165–166, 2011.

Ekambara, K and Joshi, J B. Axial mixing in pipe flows: Turbulent and transition regions. *Chemical Egnineering Science*, 58:2715–2724, 2003.

Faisst, H and Eckhardt, B. Sensitive dependence on initial conditions in transition to turbulence in pipe flow. *Journal of Fluid Mechanics*, 504:343–352, 2004.

Fischer, H B. Longitudinal dispersion and turbulent mixing in open channel flow. *Annual Review of Fluid Mechanics*, 5:59–78, 1973.

Flint, L F. On the velocity profile for turbulent flow in straight pipe. *Chemical Engineering Science*, 22:1127–1131, 1967.

Flint, L F and Eisenklam, P. Longitudinal gas dispersion in transitional and turbulent flow through a straight tube. *The Canadian Journal of Chemical Engineering*, 47:101–106, 1969.

Fowler, F C and Brown, G G. Contamination by successive flow in pipe lines. *American Institute of Chemical Engineers*, 39:491–516, 1943.

Gill, W N and Sankarasubramanian, R. Exact analysis of unsteady convective diffusion. *Proceedings of the Royal Society of London*, 316(1526):341–350, 1970.

Greenblatt, D and Moss, E A. Rapid temporal acceleration of a turbulent pipe flow. *Journal of Fluid Mechanics*, 514:65–75, 2004.

Guymer, I and Stovin, V R. One-dimensional mixing model for surcharged manholes. *Journal of Hydraulic Engineering*, 137(10):1160–1172, 2011.

He, S and Jackson, J D. A study of turbulence under conditions of transient flow in a pipe. *Journal of Fluid Mechanics*, 408:1–38, 2000.

He, S; Ariyaratne, C, and Vardy, A E. A computational study of wall friction and turbulence dynamics in accelerating pipe flows. *Computers and Fluids*, 37: 674–689, 2008.

He, S; Ariyaratne, C, and Vardy, A E. Wall shear stress in accelerating turbulent pipe flow. *Journal of Fluid Mechanics*, 685:440–460, 2011.

Hof, B; Lozar, A; Kuik, D J, and Westerweel, J. Repeller or attractor? selecting the dynamical model for the onset of turbulence in pipe flow. *Physical Review Letters*, 101:214–501, 2008.

Holley, J R; Harleman, D R F, and Fischer, H B. Dispersion of pollutants in estuary type flows. *Journal of the Hydraulics Division Proceedings of the American Society of Civil Engineers*, 96(8):1691–1709, 1970.

Jung, N S; Boulos, P F, and Wood, D J. Pitfalls of water distrubtions model skeletonization for surge analysis. *American Water Works Association*, 99(12): 87–98, 2007.

Jung, S Y and Chung, Y M. Large-eddy simulation of accelerated turbulent flow in a circular pipe. *Journal of Heat and Fluid Flow*, 33(1):1–8, 2011.

Keyes, J J. Diffusion film characteristics in turbulent flow: Dynamic response method. *American Institute of Chemical Engineers*, 1:305–311, 1955.

Kuik, D J; Poelma, C, and Westerweel, J. Quantitative measurement of the lifetime of localized turbulence in pipe flow. *Journal of Fluid Mechanics*, 645:529–539, 2010.

Kurokawa, J and Morikawa, M. Accelerated and decelerated flows in a circular pipe. *The Japan Socitey of Mechanical Engineers*, 249:249–216, 1986.

LeChevallier, M W; Gullick, R W; Mohamma, R K; Friedman, M, and Funk, J E. The potential for health risks from intrusion of contaminants into the disstribution system from pressure transients. *Journal of Water and Health*, 1:3–14, 2003.

Lee, Y. *Mass Dispersion in Intermittent Laminar Flow.* PhD thesis, 2004.

Leite, R. An experimental investigation of the stability of poiseuille flow. *Journal of Fluid Mechanics*, 5:81–96, 1958.

Levenspiel, O. Longitudinal mixing of fluids flowing in circular pipes. *Industrial and engineering Chemistry*, 50(2):343–346, 1958.

Levenspiel, O. *An Introduction to the Design of Chemical Reactors.* John Wiley and Sons, 1962.

Lindgren, E. *The Transition Process and Other Phenomena in Viscous Flow.* PhD thesis, 1957.

Madden, F N; Godfrey, K R; Chappell, M J; Hovorka, R, and Bates, R A. A comparison of six deconvolution techniques. *Journal of Pharmacokinetics and Biopharmaceutics*, 24(3):283–299, 1996.

Mathieu, J and Scott, J. *An Introducton to Turbulent Flow.* Cambridge University Press, 2000.

McKeon, B J; Swanson, C J; Zagarola, M V; Donnelly, R J, and Smits, A J. Friction factors for smooth pipe flow. *Journal of Fluid Mechanics*, 511:41–44, 2004.

Meseguer, A and Trefethen, L N. Linearized pipe flow to reynolds number 10000000. *Journal of Computational Physics*, 186:178–197, 2003.

Moody, L F and Princenton, J N. Friction factors for pipe flow. *Transactions of the ASME*, 66:671–684, 1944.

Nikuradse, J. English translation: Laws of turbulent flow in smooth pipes. *NACA Technical Memorandum*, 359, 1932.

Nikuradse, J. English translation: Laws of turbulent flow in rough pipes. *NACA Technical Memorandum*, 1292, 1933.

Okubo, A. The effect of shear in an oscillataory current on horizontal diffusion from an instanatous source. *International Journal of Oceanology and Limnology*, 1(3): 194–204, 1967.

Pfenniger, W. *Transition in the Inlet Length of Tubes at High Reynolds Numbers, In Boundary Layer and Flow Control (ed. GV Lachman).* Pergamon, 1961.

Reichardt, H Z. Complete representation of the turbulent velocity distribution in smooth pipes. 31:208–219, 1951.

Reynolds, O. An experimental investigation of the circumstances which determine whether the motion of water shall be direct or sinuous, and of the law of resistance in parallel channels. *Philosophical Transactions of the Royal Society*, (174):935–982, 1883.

Reynolds, O. On the dynamical theory of incompressible viscous fluids and the determination of the criterion. *Philosophical Transactions of the Royal Society*, (186):123–164, 1894.

Rutherford, J C. *River Mixing.* John Wiley and Sons, 1994.

Salwen, H; Cotton, F W, and Grosch, C E. Linear stability of poiseuille flow in a circular pipe. *Journal of Fluid Mechanics*, 98(2):273–284, 1980.

Saph, V and Schoder, E W. An experimental study of the resistance to the flow of water in pipes. *Transactions of the American Society of Civil Engineers*, 51: 253–330, 1903.

Sayre, W W. *Dispersion of Mass in Open Channel Flow.* PhD thesis, 1968.

Senecal, V E and Rothfus, R R. Transition flow of fluids in smooth tubes. *Chemical Engineering Progress*, 49(10):533–538, 1953.

Skilling, J and Bryan, R K. Maximum entropy image reconstruction general algorithm. *Monthly Notices of the Royal Astronomical Society*, 211:111–124, 1982.

Smith, R. Non-uniform discharges of a contaminants in shear flows. *Journal of Fluid Mechanics*, 120:71–89, 1982.

Stanton, T E and Pannell, J. Dispersion of soluble matter in solvent flowing slowly through a tube. *Proceedings of the Royal Society*, 219(1137):186–203, 1953.

Stovin, V R; Guymer, I; Chappell, M J, and Hattersley, J G. The use of deconvolution techniques to identify the fundamental mixing characteristics of urban drainage structures. *Water Science and Technology*, 61(8):2075–2081, 2010.

Taylor, G I. Dispersion of soluble matter in solvent flowing slowly through a tube. *Proceedings of the Royal Society*, 219(1137):186–203, 1953.

Taylor, G I. The dispersion of matter in turbulent flow througha a pipe. *Proceedings of the Royal Society*, 223(1155):446–468, 1954.

Thacker, W C. A solvable model for shear dispersion. *Journal of Physical Oceanography*, 6:66–75, 1976.

Tichacek, L J; Barkelew, C H, and Baron, T. Axial mixing in pipes. *American Institute of Chemical Engineers*, 3(4):439–442, 1957.

Tzatchkov, V G; Aldama, A A; Arreguin, F I, and Buchberger, S G. Advective-dispersion transport in water distribution networks within intermittent flow. *Transactions on Ecology and the Environment*, 48:217–226, 2001.

Tzatchkov, V G; amd Z Li, Steven G. Buchberger; Romero-Gomez, P, and Choi, C. Axial dispersion in pressurized water distribution networks a review. *International Symposium on Water Management and Hydraulic Engineering*, 2009.

White, F M. *Fluid Mechanics*. McGraw-Hill International, 2008.

Willis, A P and Kerswell, R R. Turbulent dynamics of pipe flow captured in a reduced model: Puff relaminarization and localized 'edge' states. *Journal of Fluid Mechanics*, 619:213–233, 2009.

Wygnanski, I J and Champagne, F H. On transition in a pipe. part 1. the orgin of puffs and slugs and the flow in a turbulent slug. *Journal of Fluid Mechanics*, 59 (2):281–335, 1973.

Yang, B H and Joseph, D D. Virtual nikuradse. *Journal of Turbulence*, 10(11):1–28, 2009.

Appendix A

Justification for Resolution of Numerical Model

The zonal model of Chikwendu [1986], used for the model for the longitudinal dispersion coefficient within the present work, is define by Equation 2.84. From Equation 2.84, it can be seen that the number of zones, N, needs to be defined. This parameter both sets the resolution of the radial parameters, such as the velocity profile, and the number of zones over which the calculation for the longitudinal dispersion coefficient is made (see Section 2.13 for full explanation of the zonal model).

Within the present work, the number of zones was set as $N = 5000$. This value was set on the basis of being a good compromise between the models output achieving a stable value, independent of number of zone, whilst still only requiring moderate amount of time to run simulations.

Figure A.1 shows the models output as a function of number of zones N, for several different parameter configurations. 'Turbulent parameters, $Re = 50000$' is the highest Reynolds Number the turbulent parameters were considered for, 'Turbulent parameters, $Re = 5000$' is the lowest Reynolds Number turbulent parameters were considered for, and the highest Reynolds Number transitional parameters were considered for, as at $Re = 5000$, turbulent and transitional parameters are the same (as $\alpha = 1$). 'Transitional parameters, $Re = 3500$' is a Reynolds Number mid way through the transitional range, and 'Transitional parameters, $Re = 2000$' is the lowest Reynolds Number at which transitional parameters were considered. The results from the model are shown as the the longitudinal dispersion coefficient predicted by the model as a percentage of the models output for the maximum number of zones considered, $N = 10000$, the point at which the model's output is considered fully stable.

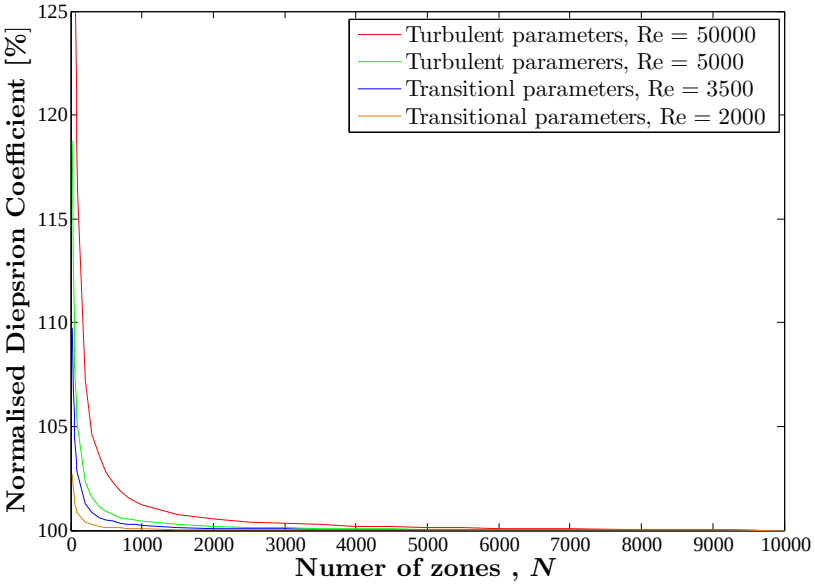

Figure A.1: *Relationship between number of zones for model of Chikwendu [1986] and models output, as percentage of final value.*

From Figure A.1 it can be see that for $N = 5000$, the models output is stable, with a difference from the final output of $< 2\%$ for all parameter configurations considered.

Appendix B

Reproduction of Taylor's Velocity Profile

Taylor [1954] defined his turbulent velocity profile using a 'universial velocity profile', as defined by the expression given in Equation 2.67, on the basis of a geometric relationship $f(p)$ (See Chapter 2, Section 2.11.1).

For $0.9 < p < 1$, Taylor proposes an expression for $f(p)$, as defined in Equation 2.68. However, for $0 < p < 0.9$, Taylor only gives 14 experimentally derived values of $f(p)$, thus for these values of p, his velocity profile can only be used at 14 points. To use Taylor's velocity profile at a higher resolution within the numerical model of the present work, an expression was fitted to his values of $f(p)$ for $0 < p < 0.9$. The expression used was the following 6th order polynomial:

$$f(p) = 69.56p^6 - 139.5p^5 + 103.1p^4 - 31.68p^3 + 10.05p^2 - 0.1943p + 0.0001672 \quad \text{(B.1)}$$

Using a higher order polynomial allows for a very good fit to Taylor's profile, with a goodness of fit $R^2 = 1$.

In addition, $f(p)$ was assumed linear very near the wall, for $0 < p < 0.02$, as Equation B.1 gives negative values for $f(p)$ very near the wall.

Appendix C

Deconvolution Code

The deconvolution code used within the present work to obtain RTDs from experimental data was a developed at The University of Sheffield, and based on the code used for Stovin et al. [2010] and Guymer and Stovin [2011] (See Chapter 2, Section 2.15).

The only difference between the code used within the present work and the code used for Stovin et al. [2010] and Guymer and Stovin [2011] is the manner in which the RTD, $\hat{h}$, is initially estimated. For the original code, a base-line prediction of the RTD is made using nearest neighbor moving average prediction. This method provided very noisy RTDs for the data sets of the present work. The code was modified so that instead of using a base-line prediction of the RTD, using a nearest neighbor moving average, a Gaussian approximation of the RTD was used. The initial Gusssian curve was estimated on the basis of the location of the profiles peak and standard deviation.

Within the deconvolution code, four main parameters need to be defined; the number of sample points, the sample point distribution, the number of iterations and the constraint function used. The number of sample points used was 40, where the sample points were distributed using a 'slope based' distribution, which distributes the sample points so more points are allocated to the portions of the RTD where the slope is higher. The number of iterations was set as 150 and the constraint function used was R_t^2. All parameters were set after discussion with the code's developers at The University of Sheffield.

Appendix D

Fit to Steady Dispersion Data

In order to predict the longitudinal dispersion coefficient as a function of Reynolds Number for use within the unsteady model, a trend was fitted to all steady data sets.

It was found that a simple three parameter power function could give a very good fit the turbulent data, and a reasonable fit to transitional data. The expression was of the form:

$$\frac{D_{xx}}{\bar{u}d} = aReb + c \tag{D.1}$$

The expression was fitted to 3 ranges of Reynolds Numbers; $5000 < Re < 50000$, as a fit to the turbulent data, $3000 < Re < 50000$, as a fit to the data over which the Fickian model was shown to be valid and $2000 < Re < 6000$, as a fit to the transitional data. Tables D.1, D.2 and D.3 show the results for the fits to each data set.

Figure D.1 shows two example fits to data for the longitudinal dispersion coefficient between instruments 1 and 6, where fits are for the the ranges $5000 < Re < 50000$ and $2000 < Re < 5000$.

Upstream instrument	**Downstream instrument**	a	b	c	R^2
1	2	1.103×10^4	-1.182	0.2294	0.970
1	3	5.976×10^5	-1.614	0.3077	0.990
1	4	2.776×10^6	-1.781	0.3179	0.993
1	5	6.301×10^5	-1.595	0.2885	0.995
1	6	9.537×10^5	-1.637	0.3064	0.993
2	4	1.171×10^4	-1.126	0.1868	0.885

Table D.1: *Expression constants for Equation D.1, for* $5000 < Re < 50000$.

Upstream instrument	Downstream instrument	a	b	c	R^2
1	2	6.297×10^4	-1.389	0.2518	0.946
1	3	1.404×10^6	-1.718	0.3207	0.954
1	4	7.244×10^6	-1.902	0.3359	0.962
1	5	9.291×10^6	-1.917	0.3282	0.960
1	6	1.806×10^8	-2.268	0.3788	0.951
2	4	8.063×10^6	-1.900	0.3007	0.947

Table D.2: *Expression constants for Equation D.1, for* $3000 < Re < 50000$.

Upstream instrument	Downstream instrument	a	b	c	R^2
1	2	1.34×10^{-10}	2.4590	1.0060	0.157
1	3	-0.1128	0.4150	5.1690	0.522
1	4	178.3	-0.5388	-0.7505	0.454
1	5	8.621×10^9	-2.7070	0.3993	0.662
1	6	1.429×10^{11}	-3.0460	0.4960	0.706
2	4	-0.0001013	1.0740	2.1690	0.591

Table D.3: *Expression constants for Equation D.1, for* $2000 < Re < 6000$.

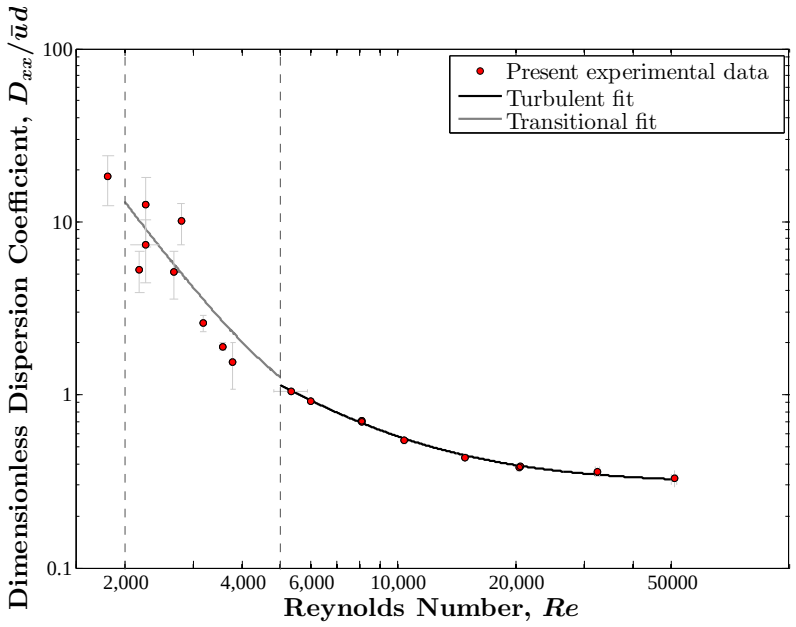

Figure D.1: *Example of fits to steady data for the longitudinal dispersion coefficient using fits between instruments 1 and 6, for the ranges* $5000 < Re < 50000$ *and* $2000 < Re < 5000$.

Appendix E

Sensitivity Analysis and Radial Variation of Velocity Fluctuations

E.1 Sensitivity of Numerical Model to Main Parameters

A sensitively analysis was conducted to determine the dependance of the model's output on three main parameters, the magnitude of the velocity profile, the frictional velocity and the radial diffusion coefficient. The magnitude of the velocity profile was varied by increasing or decreasing the maximum velocity, u_c, by $\pm 10\%$. The magnitude of the velocity profile was found to have a small effect on the models output, with the $\pm 10\%$ variation leading to around $\pm 0.1\%$ effect on the model's output. This result was expected, as the model primarily measures differential advection, thus as the velocity magnitude does not effect the velocity profiles distribution, it has little effect upon dispersion. The magnitude of the frictional velocity was also varied by increasing or decreasing its magnitude by $\pm 10\%$. The variation of the frictional velocity was found to have non-negligible effect on the models output, with the $\pm 10\%$ variation leading to around $\pm 5\%$ effect on the model's output. The larger dependence of the model on the frictional velocity is due to the frictional velocity's effects on the velocity profiles distribution and size of the boundary layer, thus leading to a non-negligible effect on differential advection and thus the model's output. Finally, the magnitude of the radial diffusion coefficient, D_r, was varied by increasing or decreasing its value by $\pm 10\%$. It was found that the model's output is inversely proportional to the magnitude of the radial diffusion coefficient, with

+10% increase in the radial diffusion coefficient leading to a reduction of exactly −10% of the models output, and vice versa. This results was expected, as the final result from the model comprises of the quantification of differential advection from the velocity profile, factored by $1/D_r$, thus the magnitude of the radial diffusion coefficient has a direct effect upon the model's output.

E.2 Radial Variation of Velocity Fluctuations

Due to the limitations of the data collected, it was not possible to directly measure the radial diffusion coefficient on the facility used for the experimental work of the present work. However, Figure E.1 shows the radial distribution of the standard deviation of the velocity time series's, from the data used to produce the mean velocity profiles. Although this parameter is not the same as the radial diffusion coefficient, the standard deviation of the velocity data time series's provides a simple demonstration of the radial distribution of the flow's turbulence, in a similar manner to a turbulent intensity, which is related to radial diffusion.

For laminar to transitional flow, as shown in Figures E.1 (a) - (c) the data is relatively noisy, but a trend can be observed where the turbulence decreases near the wall. It can also be noted that a similar asymmetry is seen for these profiles as for the transitional velocity profiles shown in Figure 5.9.

For turbulent flow, as shown E.1 (d) - (f) it can be seen that the turbulence is relatively constant in the profile's core, but increases to a peak value as the radial position approaches the wall, before reducing at the near wall boundary layer.

Some doubt over the validity of the use of the velocity standard deviation data to show the turbulence characteristics can be attributed to the relatively low resolution of the LDA system (see Table 4.2). Whilst it has been shown that the resolution is sufficient for a mean velocity profile (see Figure 4.10), the relatively low resolution may be insufficient obtain detailed turbulence characteristics. Whilst this make it difficult to experimentally validate the radial distribution of the radial diffusion coefficient, the numerical models output is only dependant on the distribution of the radial diffusion coefficient to around 15%, with the most important parameter being the cross-sectional mean radial diffusion coefficient obtained from the radial diffusion coefficient's profile.

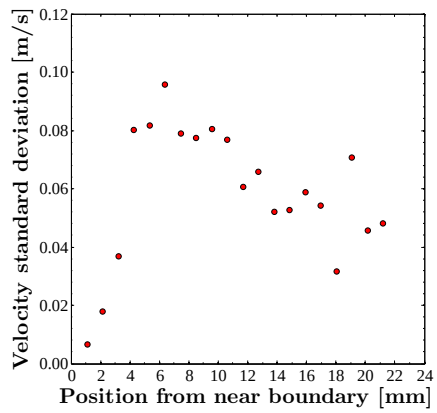

(a) Re = 2000.

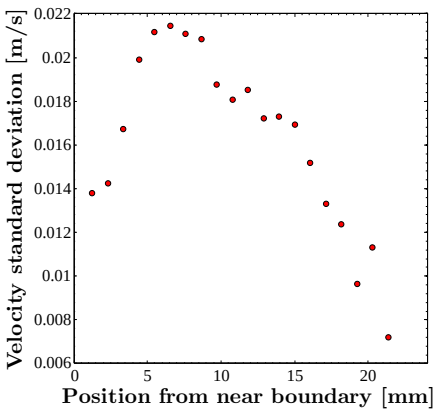

(b) Re = 2500.

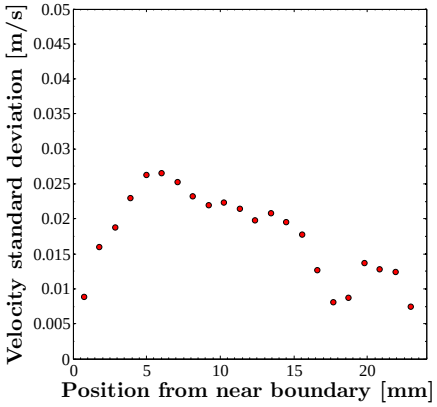

(c) Re = 3000.

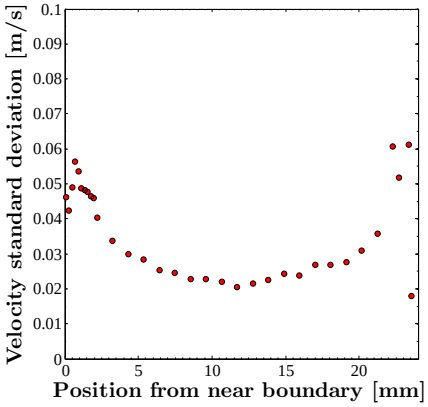

(d) Re = 5030.

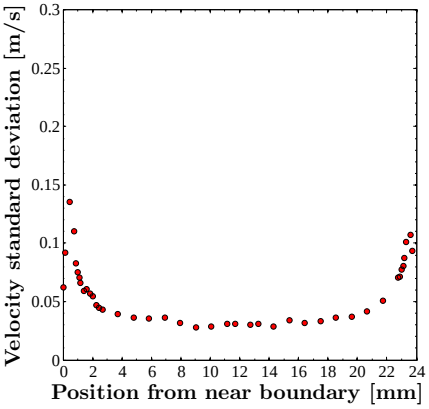

(e) Re = 9590.

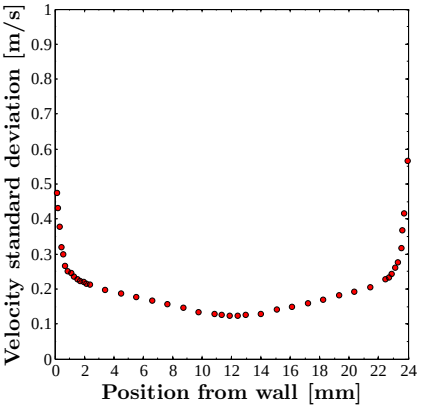

(f) Re = 51910.

Figure E.1: *Radial distribution of velocity time series standard deviation.*